Tiago André Cunha Reis

Mestre em Engenharia Química e Bioquímica

Universidade do Minho

Three-Dimensional Electrospun Constructs for Wound Healing Applications

Dissertação para obtenção do Grau de Doutor em
Sistemas de Bioengenharia (MIT-Portugal)

TÉCNICO
LISBOA

Orientador: Prof.ª Doutora Ana Isabel Nobre Martins Aguiar
Oliveira Ricardo,
Universidade Nova de Lisboa

Co-orientadores: Prof.ª Doutora Paula Therese Hammond,
Massachusetts Institute of Technology

Prof. Doutor Ilídio Joaquim Correia
Universidade da Beira Interior

Presidente: Prof. Doutor Manuel Nunes da Ponte

Arguentes: Prof. Doutor Lino Silva Ferreira
Prof. Doutor Nuno João Meleiro Alves das Neves

Vogais: Prof. Doutora Ana Isabel Nobre Martins Aguiar Oliveira Ricardo
Prof. Doutor João Pedro Conde

FACULDADE DE
CIÊNCIAS E TECNOLOGIA
UNIVERSIDADE NOVA DE LISBOA

Outubro 2016

THREE-DIMENSIONAL ELECTROSPUN CONSTRUCTS FOR WOUND HEALING APPLICATIONS

To my family: Vasco, Natália,
Diogo and Sofia

Acknowledgements

Family always comes first. Pai, obrigado por ensinares-me os valores da vida e de que nunca devemos desistir. Mãe, obrigado pelo esforço e sacrifício de uma vida, que mesmo assim levou-te a ajudar e muito este teu filho. Diogo, thank you for being an awesome and loyal brother that I can rely no matter what or when. Sofia, you are the best part of all this MIT-Portugal experience. Thank you for the support and love that we share.

I would like to thank my supervisor Prof. Ana Aguiar Ricardo (FCT-UNL). I would also like to thank Prof. Paula T. Hammond (MIT) for the unique opportunity to conduct part of my research in her lab. Her co-supervision was key in many moments of this thesis, something that she would always add her smile and outstanding analytical capabilities. Thank you Professor!

I have to say a few words about Prof. João Paulo Borges (FCT-UNL), a man that I deeply respect for his personality and professionalism. Prof. João Paulo Borges is the type of a Professor that inspires his students to be better, and if today I am deeply in love with material science is because of him. Thank you Professor!

In my mind, polymer science is equal to Prof. Ana Ramos (FCT-UNL). I miss so much her lectures and the way that she introduces her students to this fascinating field. Attending the polymer science course was one of the best decisions in my life. I recall that I had already exceeded the maximum number of courses that one could attend during a master’s program, but I attended her course anyway. Once again, one of the best decisions in my life. Thank you Professor!

There are others that take an important role in my life – not only during my PhD – being role models regarding their ethics, personality and engineering skills. These are my role models: Prof. Pedro Simões (FCT-UNL), Prof. João Paulo Crespo (FCT-UNL), Prof. Rui Oliveira (FCT-UNL) and Prof. Manuel Carrondo (FCT-UNL). Thank you all!

I would also thank Prof. Ana M. Rego (IST-UL) for her support regarding the use and interpretation of the XPS analysis. It was a pleasure to meet you and work with you. Thank you Professor!

Someone that is truly underappreciated by the MIT-Portugal Program is Prof. José Silva Lopes. Prof. José Silva Lopes was outstanding in interacting with the MIT-Portugal Program PhD students. His dedication is beyond any doubt. Thank you Professor!

I am also thankful to meet people like: Rita Restani and Steven Castleberry, thank you both for the friendship.

I need to thank to the American Red Cross. If there is a written thesis today is because I survived a house fire while I was in the United States. Although this traumatic experience was hard to deal with, the American Red Cross staff was always present to help me. Among previous tears and blood, thank you!

As someone that never attended private schools, it is a privilege to acknowledge the Portuguese Government for providing me a costless education with high standards of quality since 1992. Finally, I thank the financial support from Fundação Calouste Gulbenkian, Fundação para a Ciência e a Tecnologia (FC&T), through the projects PEst-C/EQB/LA0006/2013, MIT-Pt/BS-CTRM/0051/2008, PTDC/EMETME/103375/2008, the doctoral grant SFRH/BD/51188/2010, MIT-Portugal Program (Bioengineering Systems Focus Area) FEDER and FSE.

Abstract

This thesis embraces the opportunity to develop a wound dressing substrate that not only attends the functional requirements of a wound dressing, but also avoids the need of secondary dressings. Novel electrostatically driven self-assembled fibrous based materials made of poly(ε-caprolactone) are manufactured, resulting in asymmetrical materials with enhanced topographies. Such constructs are characterized by a flat bottom side and a top side populated with fibrous-based microsized protrusions, which have a median inter-protusion distance of 528 µm and a median peak density of 73 peaks per cm^2. For the first time, it is provided a full explanation of the underlying fabrication phenomena, suggesting new routes to other polymers such as gelatin or chitosan. After the characterization of the proposed substrates, such materials are functionalized by *layer-by-layer*. Several combinations of polyelectrolytes (chitosan, gelatin, alginate, hyaluronic acid, poly-1, linear polyethyleneimine and dextran sulphate) and layer numbers (n = 1, 3, 5 or 10) are tested regarding the physicochemical properties of the generated multi-layered films, as well as the cellular adhesion on these constructs. It is intended to formulate, test and control, the underlying phenomena that avoids the cellular adhesion and proliferation within the used dressing. As prepared these materials are capable of withstanding $(11.0 \pm 0.3)\times10^4$ kg per m^2 after 14 days of hydration. Their unique asymmetry promotes unidirectional liquid uptake (from the top side towards the inner structure of the materials), while being impermeable to potential external liquid-forms of infection at its bottom side. Nevertheless, such constructs also observed the high porosity (89.9%) and high surface area (1.44 $m^2.g^{-1}$) characteristic of traditional electrospun mats. The selected coating reduced cellular adhesion on the constructs throughout the generation of a rubbery film layer, which would also provide a means to tailor water vapor transmission and swelling ratio for different wound environments specifications (e.g. ischemic wounds, I/II/III-degree burns, etc.). As a showcase, functionalized wound dressing substrates were able to achieve 90 ± 0.5 % of wound closure within 48 hours.

Keywords: wound dressing, electrospinning, layer-by-layer, self-assembly.

Resumo

Esta tese abraça a oportunidade de desenvolver uma base para pensos de feridas que não só atende aos requisitos funcionais de um penso, mas que também evita a necessidade de pensos secundários. São fabricados novos materiais fibrosos auto-formados electrostaticamente de poli(ε-caprolactona), os quais resultam em materiais assimétricos com topografias melhoradas. Tais construções caracterizam-se por uma base plana e uma parte superior preenchida com microssaliências fibrosas, as quais têm uma distância inter-saliência média de 528 µm e uma densidade média de picos de 73 picos por cm^2. Pela primeira vez, é fornecida uma explicação completa dos fenómenos da fabricação subjacente, sugerindo novas vias para outros polímeros como a gelatina ou o quitosano. Após a caracterização dos substratos propostos, tais materiais são funcionalizados segundo a técnica camada-a-camada. Várias combinações de polieletrolitos (quitosano, gelatina, alginato, ácido hialurónico, poli-1, polietileneimina linear e sulfato de dextrano) e números de camada ($n = 1, 3, 5$ ou 10) são testados quanto às propriedades físico-químicas dos revestimentos em multicamadas gerados, bem como quanto à adesão celular sobre estas construções. Pretende-se formular, testar e controlar, os fenómenos subjacentes que evitem a adesão celular e proliferação dentro do penso utilizado. Como preparado, estes materiais são capazes de suportar $(11,0 \pm 0,3) \times 10^4$ kg / m^2 após 14 dias de hidratação. A sua assimetria única promove a absorção unidirecional de líquidos (do lado superior em direção à estrutura interna dos materiais), sendo impermeável a potenciais formas líquidas de infeção externas no seu lado inferior. No entanto, tais construções também observaram uma porosidade elevada (89,9%) e uma área superficial elevada (1,44 $m^2.g^{-1}$), as quais são características de materiais eletrofiados tradicionais. O revestimento selecionado reduziu a adesão celular nestes materiais, segundo a geração de uma película de viscosa, a qual também fornece um meio adequado à transmissão de vapor de água e absorção de líquidos para diferentes especificações de feridas (feridas isquémicas, por exemplo, feridas, queimaduras I/II/III grau, etc.). Além disso, o penso melhorado foi capaz de alcançar 90 ± 0,5% de oclusão da ferida num período de 48 horas.

Palavras-chave: penso para feridas, eletrofiação, camada-a-camada, auto-formação.

Table of Contents

Index of Figures

Index of Tables

1

Wound Pathophysiology and Wound Dressing Conceptualization

SUMMARY[1]

The wound healing phenomena is a multipart and orchestrated process of bioevents and cell lineages. In addition to its complexity, wound repair is also deeply affected by external conditions that can compromise the healing rate of the injured tissue. The proper designed of a wound dressing is challenging, since such constructs must attend a set of multivariable and dynamic requirements in order to avoid the generation of non-functioning mass of fibrotic tissue or a chronic wound healing stage. Herein, it is reviewed the most important aspects of wound pathophysiology while highlighting the most important requirements to be fulfilled by a wound dressing in a wound dressing.

---

[1] This Chapter was partially submitted for publication (Tiago C. Reis, “*Wound Pathophysiology and Wound Dressing Conceptualization*”).

1.1 WOUND PATHOPHYSIOLOGY AND REPAIR

1.1.1 The human skin anatomy and wound pathophysiology

The human skin is the largest organ in the body, consisting of three layers: (i) *epidermis*; (ii) *dermis*, and (iii) *hypodermis* (**Figure 1.1**). The epidermis is a multi-layered epithelium that starts from the interface with the dermis and is about 80-100 µm thick, comprising four sublayers: the *stratum basalis*, the *stratum spinosum*, the *stratum granulosum* and the *stratum corneum*. The epidermis is deprived of extracellular matrix (ECM), with the exception of its *stratum basalis*, a cellular configuration which its progenitor cells undergo a continuous self-renewal and differentiation to keratinocytes. As the keratinocytes migrate towards the surface of the skin, they suffer a terminal differentiation and maturation, resulting in a keratinized layer of dead cells which confers the main barrier properties of the skin in its *stratum corneum*. The dermis is positioned bellow the epidermis, being a connective tissue that encompasses vascular endothelial cells, ECM, fibroblasts and skin appendages such as sweat glands, hair follicles, etc., and it is responsible for most of the mechanical properties and resilience of the human skin. Among the several dermis constituents, fibroblasts play an important role on modulating the skin mechanical strength and elasticity, throughout the secretion of collagen and elastin, respectively. The tensile strength of the dermis can range from 3.4 MPa to 68.9 MPa,[1] depending on the type of species, orientation of the skin specimen tested and the location on the body. Finally, underneath the dermis one will find the hypodermis, an adipose like tissue that its main role is to act as an insulator and cushioning layer between the skin and skeletal structures as muscles and bones.

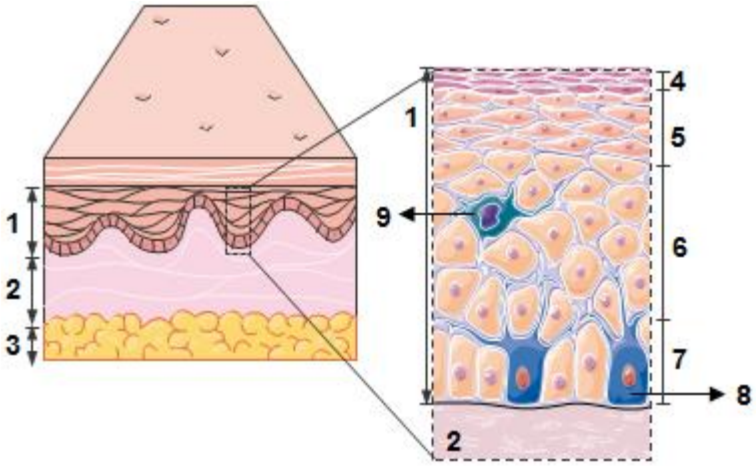

Figure 1.1 Basic skin anatomy. **1**, Epidermis. **2**, Dermis. **3**, Hypodermis. **4**, Stratum corneum. **5**, Stratum granulosum. **6**, Stratum spinosum. **7**, Stratum basalis. **8**, Melanocyte. **9**, Langerhans cell.

As the outer covering of the body, the human skin is frequently exposed to different sources of danger, which may contribute to the development of wounds. Wounds are within the main unresolved medical needs that affect treatment results, quality of life, length of hospital stay and reimbursement rates in healthcare.[2] A wound is defined as a disruption of normal anatomic structure and function.[3] In the specific case of skin wounds, this category of wounds comprises surgical and accidental lacerations, burns, pressure ulcers, diabetic and venous ulcers. Just in the United States, wound treatment and complications thereof surpasses $ 20 billion per year,[4] whereas chronic wounds are especially costly since they require repetitive treatments. In a similar fashion, the National Health Service of the United Kingdom spends annually £ 1 billion in the treatment of wounds, being venous leg ulcerations, pressure wounds and diabetic foot ulcerations the most expensive types of wounds to treat.[5] In the case of Portugal, Furtado *et al.*[6] estimated that 1.42 out of 1000 Portuguese citizens has a chronic wound, and that number will increase due to an existing correlation between poor healing and an aging society.[7] Furthermore, chronic wounds are predisposed to complications that also have impact on the time of the reparative process. Such complications of chronic wounds include infections, malignant transformation and functional limitations. Cellulitis, osteomyelitis, abscess formation, gangrene and sepsis can result from an infected wound, while some chronic wounds can potentially observe a malignant transformation (for example, Marjolin ulcers).[8, 9] In addition, functional limitations include, for instance, gait impairment.[10]

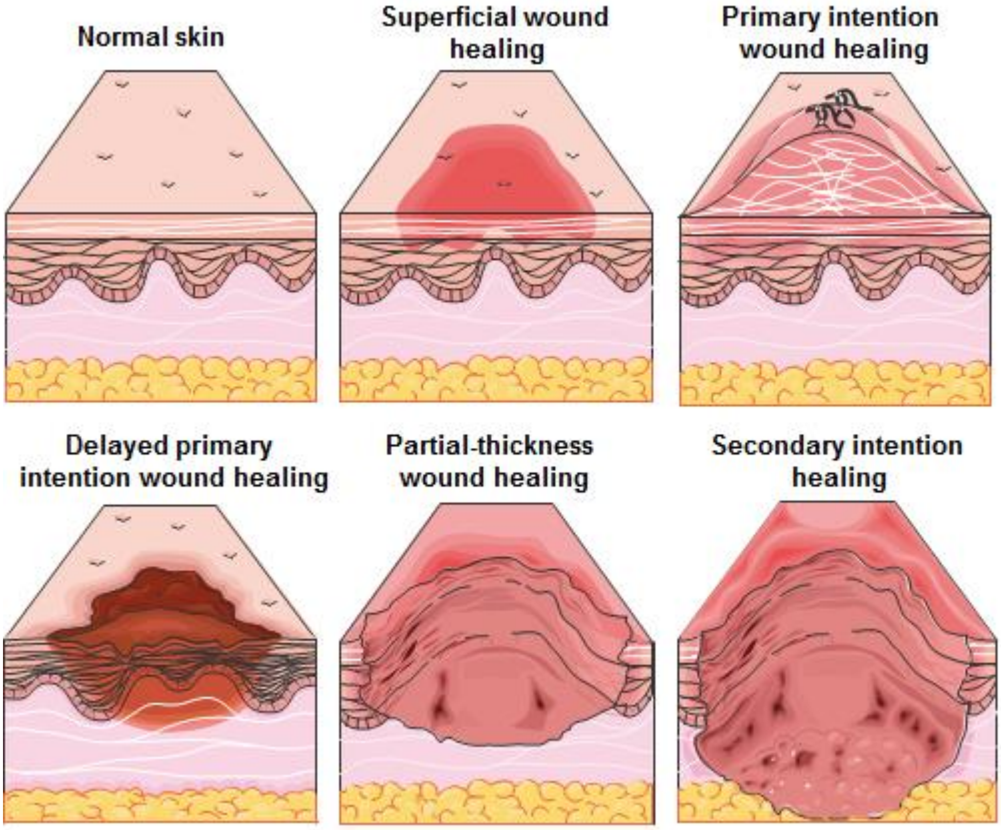

Figure 1.2 Schematics of the five basic models of healing and corresponding wound depth.

By definition, a chronic wound is a lesion of a tissue that failed to continue through an timely and orderly reparative process – named *wound healing* – which aims to restore and produce the anatomic and functional integrity of the injured tissue, leading to a stage of pathologic inflammation. In this way, the healing process is interrupted, delayed and therefore incomplete, resulting in a poor anatomical and functional outocome.[11] Currently, there are five basic models of healing and one can find similarities in all, whereas such similarities guide the development of better wound dressings.[12] The five basic healing models are: (i) superficial wound healing; (ii) primary intention wound healing; (iii) delayed primary intention wound healing; (iv) partial-thickness wound healing, and (v) secondary intention healing (**Figure 1.2**).

Superficial wound healing: An inflammatory repair process can result as an alteration of the skin's surface either by pressure (which includes friction and shearing, typically stage I pressure ulcers), contusions and first-degree burns. The involvement of the skin surface may be associated with deep tissue death, and consequently the tissue ruptures and generates a deep cavity, a common problem observed in pressure ulcers and grade I neuropathic ulcers. This wounds usually shows several alterations in the skin such in its temperature (warmth followed by coolness, an imperative indication of tissue death), color, tension and sensation, all of them leading a clinician to conclude tissue congestion. Despite soft tissues heal by themselves over time, medical intervention for this type of wounds (for example, though the use of ultrasounds for reabsorption of hematoma) boosts the recovery over functional activities and mobility.

Primary intention wound healing: This healing model consists in bringing closer the edges of a wound in order to promote closure, a model frequently employed in surgical lacerations. Thus, the usage of this healing model avoids the loss of subcutaneous tissue and the possible contamination of the wound bed with microorganisms or debris. The outcome is a minimal residual scarring with a full closure within 3-7 days for patients without functional impairments.

Delayed primary intention wound healing: However, when a wound is contaminated with microorganism or other foreign bodies, or where a significant tissue loss occurred and the employment of the primary intention wound healing model would outcome in unbearable tissue tension, the delayed primary intention wound healing model is preferential. Despite stiches are used in the subcutaneous and fascial layers, in this model the wound is left open. After the risk of infection is mitigated, or tissue loss is partially recovered, the wound will self-close within 5-7 days for patients without functional impairments.

Partial-thickness wound healing: Partial-thickness wounds are skin injuries where partial-thickness loss of the dermis occurred. Examples of this type of wounds are skin tears, second-degree burns, abrasions and stage II pressure ulcers. The existent cavity is healed accordingly to the resurfacing of the wound bed environment by new epidermal cells. The novel epidermal cells at the wound edges and from the locally present dermal appendages (e.g. sweat glands), tend to migrate towards the wound interior in order to repopulate the empty space.[13]

Secondary intention healing: This healing model diverges from the previous, since it is only employed in wounds where full-thickness loss of the dermis occurred and such loss may also be extended to the underlying tissues. The secondary intention healing model, or also commonly found in the literature as the contraction healing, results when myofibroblasts generate contractile forces that draw together the wound. This healing approach leads to minimal epitheliazation and to the production of scar tissue, and therefore the skin anatomic functionality and structure is not replaced. Moreover, a wound that heals throughout secondary intention healing present elasticity or tensile strength that does not match the native properties of the surrounding tissue. The contraction healing is the process commonly observed during the healing of chronic wounds, which can be extended up to 6 months to 2 years.

Since the conception of wound dressings for non-healing partial-thickness wounds and non-healing full-thickness wounds is one of the main goals of this thesis, the reparative process of these wounds it will be properly introduced and detailed in the Section 1.1.2 – Acute wound repair. Moreover, **Table 1.1** shows the differential diagnosis of the underlying etiology of a non-healing wound, whereas 70 % of ulcers are caused by ischemia, secondary to diabetes mellitus, venous stasis, and pressure.[14]

Table 1.1 Differential diagnosis of non-healing wounds.

Chronic wound category	Etiology
● **Vascular**	▨
Arterial	Atherosclerosis, arteriovenous malformation
Lymphatic	Lymphedema
Mixed (Venous-Arterial)	▨
- Vasculitis	Systemic lupus erythematosis, rheumatoid arthritis, scleroderma, polyarteritis nodosa, Wegener's granulomatosis
- Venous	Venous stasis
● **Pressure**	Spinal cord injury, bedbound, elderly
● **Neuropathic**	Diabetes, peripheral neuropathy
● **Hematologic**	Polycythemia rubra vera, sickle cell disease
● **Traumatic**	Burns, cold injury, radiation, factitious
● **Neoplastic**	Basal carcinoma, squamous cell carcinoma, melanoma,
● **Others**	Marjolin's ulcer, Bowen's disease Sarcoidosis, obesity, tropical ulcer, pyoderma gangrenosum, necrobiosis lipoidica diabetecorum

1.1.2 Chronic wound repair

The inflammatory process associated with chronic wounds is significantly different from that associated with acute wounds (**Figure 1.3**). In the acute healing process, the inflammation is a self-limiting biochemical cascade of events that aims to remove necrotic tissue, debris, microorganisms and theirs contaminates, while it triggers the recruiting and activation of fibroblasts.[15] On the other hand, in the case of chronic wounds, the inflammation process is not self-limiting, i.e., it is responsible to further injure the wounded tissue while continuously reactivating and promoting novel routes of inflammation. For example in chronic wounds, tissue trauma by continuous *in situ* pressure, leucocyte trapping, bacterial populations or ischemic reperfusion injury, are potential causes for recruiting and keeping neutrophils at the wounded site throughout long periods of time (months up to years). This phenomenon leads to the up-regulation of the inflammatory cascade and consequent abnormal inflammatory profile, while in comparison with acute wounds the neutrophils are only present in the first 72 h,[16] allowing the continuation of the wound healing cascade without further problems. The presence of activated neutrophils at wound bed of a chronic wound triggers the production of local ECM degradative matrix metalloproteinases (MMPs), calcium-dependent zinc-containing endopeptidases that are capable of degrading extracellular matrix components.[17] While in acute wounds such MMPs are locally inhibited (e.g. by the nonspecific proteinase inhibitor α2-macroglobulin) in proper stoichiometric ratios, at non-healing chronic wounds the stoichiometric MMP:inhibitor ratio is unbalanced leading to the wound bed degradation.[17-19] Therefore, the secretion rate of ECM components, such as collagen, by fibroblasts, is lower than the rate of degradation of these components, and consequently these cells are incapable to make progress in depositing ECM.[19] Moreover, the extended inflammatory environment in chronic wounds contributes to the predominant presence of cytokines (e.g. tumor necrosis factor α), important biochemical cues for cell signaling.[20] As a result, it is observed a considerable reduction of endogenous factors that should promote the proliferation of novel epidermal cells at the wound edges (e.g. platelet-derived growth factor).[21] Other reported difference between the acute and chronic reparative processes is in the fibroblasts themselves. Brem *et al.* demonstrated that fibroblasts within a chronic wounded environment have premature senescence, which disrupts their normal functioning.[22] As a result, such fibroblasts report impaired migration capacity as well as reduced response to local growth factors. In summary, the pathologic inflammation of chronic wounds results in more inflammation, turning out in an interrupted, delayed and therefore incomplete healing process, due to intermittent feedback events that converge towards an uncontrolled inflammatory positive feedback loop.

So far, it was only introduced the main differences between acute and chronic healing specially in association with local inflammation. Nevertheless, the wound healing process is far more complex, it is indeed a complex cascade of biochemical events that is orderly synchronized. The understanding of each stage contributes to the development of better wound dressings, since their imperative requisites become known and therefore can be attended from a dressing conception point-of-view. The wound healing process can be divided into 4 overlapping stages: (i) *hemostasis*, (ii) *inflammation*, (iii) *proliferation* and (iv) *remodeling* (**Figure 1.4**). This tissue reparative process involves complex interactions of ECM constituents, different cellular phenotypes, soluble mediators and infiltrating cooperative cells. Nevertheless, and accordingly to this PhD thesis framework and intent, it is avoided the extensive biological detailed information over these stages, since the main goal at this point it is only to contextualize the reader with the general panorama of the wound healing process and to guarantee future references understanding. Proper literature was selected and quoted in order to provide a source of information for those whom seek more detail.

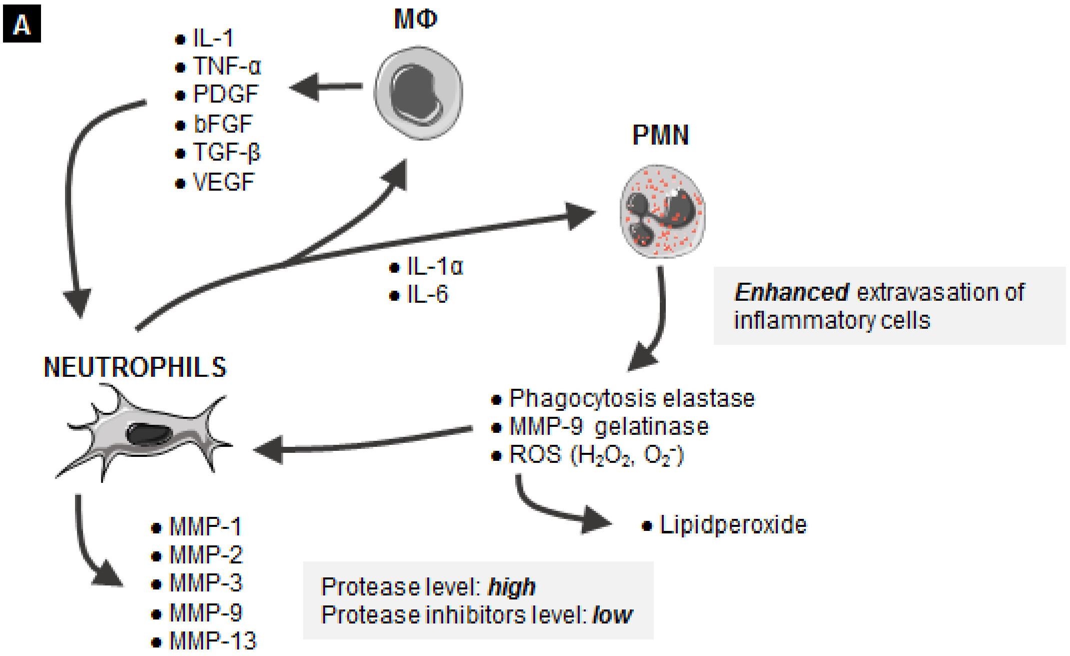

B

	Acute healing	**Etiology**
• **Mitogenic activity**	High	Low
• **Fibroblasts**	Normal	With Premature Senescence
• **MMP/TIMP ratio**	Normal	High
• **ECM deposition**	Normal	Low
• **Inflammation**	Self-limiting	Uncontrolled
• **Healing time**	Normal	Delayed

Figure 1.3 Acute wound healing model and comparison between the acute healing *versus* the chronic healing processes. **A,** Multivariable molecular and cellular model of a chronic wound in a chronic inflammatory staged characterized by abundant platelets and polymorphonuclear leucocytes (PMN) and macrophage (Mϕ) infiltration. The presence of abundant inflammatory cells triggers the production of proinflamatory cytokines (TNF-α, IL-1 and IL-6) inducing a pro-oxidant milieu, which leads to the degradation of ECM structural proteins (collagen) and to the degradation of excreted growth factors. The attracted leukocytes, mainly neutrophils, are a rich source of reactive oxygen species (H_2O_2, O_2^-) whereas those species can actively overregulate the production of matrix metallic proteinases (MMP-1, MMP-2, MMP-3, MMP-9 and MMP-13). Moreover, in a bacterial context, excreted bacterial compounds such as the extracellular adherence protein (Eap) may impair the repair mechanics by interfering with the current cell-matrix interactions and therefore extend the inflammatory response. **B,** Summary of the acute versus chronic wound healing disequilibrium and healing stages comparison.

Tissue injury is often linked to the disruption of blood vessels and consequent extravasation of blood constituents. After wounding, it is observed that the injured blood and lymphatic vessels undergo a process called vasoconstriction, which allows to achieve local hemostasis within few minutes.[23, 24] At this moment, *in situ* attracted platelets are activated by adhesive matrix proteins (e.g., collage and fibronectin) in the vascular wall, while thus adhering and aggregating in order to form a platelet plug. In parallel, platelets are continuously excreting soluble mediators (thromboxane A_2, serotonin and adenosine diphosphate) and other adhesive proteins (thrombospodin, factor VIII, etc.),[23] causing the stimulation of local thrombin production. It is this serine protease that converts local fibrinogen in fibrin and consequently generates a fibrin clot. Later on, the fibrin clot is plasmin cleaved.[25] The next stage of the wound healing process is inflammation, an important step where chronic wounds accordingly to the above reported features cannot surpass. This stage is characterized by the early recruitment of neutrophils and monocytes, which evade from surrounding capillaries into the wound bed. The recruitment process is based in the local present chemotactic factors previously generated by the platelets (e.g., kallikrein), and once in the wounded environment the neutrophils are responsible to kill and phagocyte bacteria.[26] On the other hand, local monocytes differentiate to macrophages and therefore are responsible to kill and phagocyte bacteria, scavenge tissue debris and destroy residual neutrophils.[27] In the absence of infection, it is observed a gradual decrease in the number of local neutrophils.[28, 29] The wound healing process moves towards the execution of the biochemical events associated with the proliferation stage, a phase that comprises the most prominent events of the healing process. This phase tends to occur after 4-5 days of the wounding and may last up to several weeks in patients with acute wounds.[30] The proliferation stage can be subdivided in the following subsequent sub phases: *granulation tissue formation*, *re-epithelization* and *ECM reorganization*. The granulation tissue comprises collagen type III and acts as ground substance for fibroblasts, macrophages and the newly replicated endothelial cells.[31] At this point, several capillaries populate the novel tissue while fibroblasts are continuously producing glycoproteins (fibrin, fibronectin and hyaluronic acid) that will reinforce the novel extracellular matrix. The cooperative roles of fibroblasts and blood vessels allow to support cell in growth and oxygen and nutrient supply, whereas the macrophages are mainly responsible to produce growth factors (such as the platelet-derived growth factor (PDGF) and the transforming growth factor β1 (TGF-β1).) that continuously stimulate fibroplasia and angiogenesis. The provisional extracellular matrix generated by the fibroblast is then hypothetical remodeled by TGF-β1 and/or TGF-β2, ensuring a more stable collagen based matrix.[14, 17, 32] After achieving a viable cellular scaffold within the wound bed, keratinocytes migrate towards the wound bed and consequently proliferate and differentiate *in situ*. Within 24 h, these epidermal cells are adjacent to the wound margin and become gradually flattened, while demonstrating pseudopodium-like projections that will support their migration towards the wound matrix. Due to the extensive amount of stimulatory growth factors in the newly fabricated wound matrix previously provided by the macrophages, the keratinocytes proliferate and differentiate in order to surface cover the wound through an epithelium layer. Posteriorly, the fibroblasts will differentiate into a myofibroblast phenotype that is responsible to compact the connective tissue and for further wound contraction. As briefly stated above, TGF-β1 and/or TGF-β2, as well as PDGF, are hypothetically the main growth factors responsible to stimulate tissue remodeling through the integrin receptors and cross-links between individual bundles of collagen.[33, 34] Nevertheless, collagen remodeling from granulation tissue (collagen type III) to scar tissue (collagen type I), depends on the continuous fabrication of collagen by the present subpopulation of fibroblasts, as well as on its catabolic metabolization controlled by the local matrix metallic proteinases. In addition, it is also observed in this tissue remodeling phase the proper reorientation of collagen fibers, leading to a partial restoration of the wound original mechanical strength. However, a scar is only 70 % as strong as normal skin.[30]

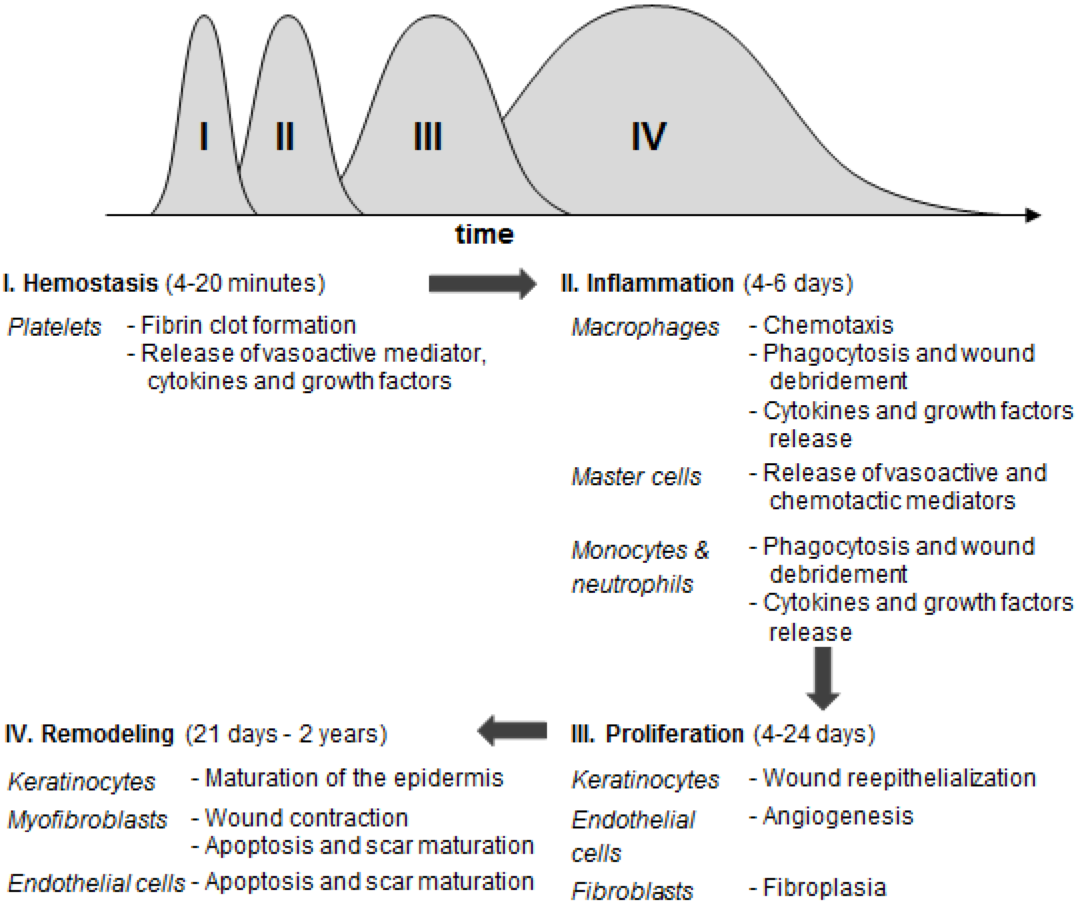

Figure 1.4 Wound healing overlapping phases and inter- and intracorrelation. Cell phenotypes and their effects on acute healing.

1.2 FUNCTIONAL REQUIREMENTS OF A WOUND DRESSING

Several strategies have been developed in order to better manipulate the wound repair process. Such strategies comprise different approaches as the use of scaffolds,[35, 36] physical manipulation of the wounded environment by negative pressure[37] or electrical stimulation,[38] administration of small molecules,[39] gene-therapy approaches,[40] and cell-based strategies such as the local administration of stem cells.[41, 42] While all of these strategies have demonstrated their potential benefit on *in vitro* and *in vivo* models,[43] many of them are being employed in combination with constructs – named *wound dressings* – which are conceptualized to partially fulfil the main skin functions. For example, Kim *et al.*[44] demonstrated that alginate wound dressings can be used to customize negative pressure wound therapy for intractable auricular defects. On the other hand, Shan *et al.*[45] reported the *in vivo* use of silk fibroin/gelatin wound dressings functionalized with astragaloside IV to elicit anti-scar effects on partial-thickness burn wounds, whereas Wen *et al.*[46] demonstrated that bacterial cellulose dressing containing uniform silver sulfadiazine nanoparticles for burn wound healing can promote a better epithelialization progress. In addition, Falanga *et al.*[47] verified that autologous bone marrow–derived cultured mesenchymal stem cells delivered in a fibrin dressing, were capable to boost the healing process either in murine and human cutaneous wounds. In all of these examples, the usage of wound dressings provides a protective environment for the injured tissue.[48] Nevertheless, there is a set of functional requirements that a wound dressing must attend:

1.2.1 Biocompatibility, non-antigenicity and non-cytotoxicity

Peremptorily, a wound dressing must be biocompatible, non-antigenic and non-cytotoxic, in order to guarantee the absence of inflammatory, immunogenic and/or cytotoxic phenomena in the wounded and surrounding tissues. As previously introduced, inflammation corresponds to an abnormal migration and accumulation of phagocytic cells, aiming to eradicate bacteria or other foreign bodies throughout an immune response. An extensive immune response can result in the wound dressing rejection.[49] After the contact between a wound dressing and the injured tissue, the material tends to quickly adsorb a layer of host proteins such as albumin, immunoglobulin G and fibrinogen, which in turn will denature or partially denature.[50, 51] For example, it is believed that fibrinogen plays an important role in acute inflammatory responses.[52] Pre-coated materials with fibrin or fibrinogen have been reported to attract large populations of phagocytic cells when subcutaneously and intraperitoneally used.[53] Upon adsorption on a material, fibrinogen may denature according to the surface chemistry of the material, exposing previously hidden epitopes that potentially interact with locally present inflammatory cells, enhancing therefore the recruiting process of neutrophils and monocytes. In this way, Zhou *et al.*[54] by properly coating a material surface with glycosaminoglycans, and therefore altering the fibrinogen adsorption process, observed that inflammatory responses were greatly reduced on all coated substrates in terms of macrophage adhesion, spreading, foreign body giant cells formation, β1 integrin expression as well as proinflammatory cytokine IL-1β production. Sánchez *et al.*[55] by assessing biomaterial-induced macrophage activation, cell-mediated immune response and oxidative stress in 169 patients with soft-tissue dermal fillers, concluded that subjects treated with fillers based on calcium hydroxyapatite, methacrylate, acrylamides and silicone, have higher plasma concentrations of myeloperoxidase (3.9-fold) and the chitinase-like proteins chitotriosidase (2.5-fold) and YKL-40 (2.0-fold), biomarkers of innate cell-related immune response,[56-58] in comparison with non-filler subjects. On the other hand, hyaluronic acid alone elicited a small immune response. Besides the potential inflammatory and immunogenic behavior of a wound dressing, its cytotoxicity is also a key parameter one must control. Highly toxic wound dressings can lead to bulk tissue necrosis due to apoptotic cell death in the surrounding tissues, which is further stimulated by ongoing autophagy and pyroptosis.[59] These cell death events are highly regulated throughout signaling networks caused by foreign chemical compounds, which can be the end product of the wound dressing degradation process. Typically, their effects increase the production of reactive oxygen species within the cell, leading to the oxidation of protein thiols and a shift in cellular redox signaling.[60] Moreover, the effects of such end products are mediated by disruption/modulation of cellular Ca^{2+} homeostasis. Ca^{2+} depletion or modifications in the Ca^{2+} transport systems, are directly linked to the endoplasmic reticulum stress through the activation of procaspase-12, an enzyme that acts on effector caspases to induce apoptosis.[61]

1.2.2 Exudate management

The wound exudate, also named as “wound fluid” or “wound drainage”, consists on a complex mixture of water, soluble inflammatory mediators, proteases, growth factors and electrolytes, which are continuously leaked from local capillaries. The exudate leaking rate depends on the capillaries’ permeability and hydrostatic and osmotic pressure across the capillary walls, a known correlation designated as the Starling’s hypothesis.[62] Abnormal wound exudate production can be associated with increased capillary permeability during the inflammation stage after the skin injury, malignancy, wound bed infection, lymphorrhea, chronic healing, tissue oedema regarding intravenous fluid overload or low blood protein levels, and transudate caused by increased capillary pressure in lower limbs.[63-65] Excessive amounts of exudate at the wound are the main consequence of tissue maceration and excoriation in the periwound region. The local retention of exudate causes the keratinocytes swelling and immediate *stratum corneum* weakening, which in turn can be easily ruptured by external forces such as those caused by the dressing removal or those associated with limb movement.[66] An excessive amount of exudate is also responsible to impair the cellular migration towards the wound bed, avoiding proper tissue replacement and extending therefore the healing period. Moreover, the wound exudate comprises many detrimental biochemical compounds that hinder the healing phenomena as previously mentioned. One example are the MMPs, secreted endopeptidases that remodel the ECM components. Thus, wound exudate accumulation at the wound bed leads to the cumulative concentration of these proteolytic enzymes, increasing the ECM degradation rate comparatively to the ECM synthesis rate. For example, MMP-9 is overexpressed in diabetic patients being present in an abnormally high concentration at the plasma of these patients,[67] and therefore its local accumulation at the wound bed has been reported as one of the main causes of diabetic foot ulcers.[68] Nevertheless, the wound exudate also comprises several biochemical agents that have a positive effect on the regenerative mechanisms, such as fibroblast growth factors, epithelial growth factors and platelet-derived growth factors.[43] While from one end proper exudate absorption and sequestration of detrimental compounds is advised, on the other end one must guarantee a moist environment and the local provision of the beneficial healing agents already present in the wound exudate. In addition, a dressing absorptive capacity must also be optimized in order to reduce the number of wound dressing changes, enhancing patient comfort and compliance while reducing the needed healthcare services.

1.2.3 Moisture management

The moisture levels at the wound bed result throughout a dynamic balance between wound exudate production, the dressing absorptive capacity and its permeability for water vapor. According to the wound phenotype, the wound exudate production differs from wound to wound type. For example, in the case of venous leg ulcers, a chronic wound example, the continuous inflammatory stage promotes the wound exudate production through the mechanisms previously reported.[69] On the other hand, in the case of diabetic foot ulcers, wound bed moisture levels are depleted.[70] The absence of proper restoration of the wound bed moisture leads to the adherence of the dressing applied, whereas new blood vessels and granulation tissue can grow into the dressing structure. Therefore, a good moisture management strategy is strictly linked to the underlying wound pathology. Upon the dressing absorptive capacity, commonly designated in the literature as swelling capacity, wound dressings are classified into three classes: moisture absorbing, moisture maintaining and moisture donating. Moisture absorbing dressings tend to absorb 15 to 20 times their weight of fluid, being ideally for highly exuding scenarios.[71] In contrast, moisture donating dressings, also designated as hydrocolloids, are characterized by a matrix of insoluble polymers comprising up to 90 % water content, which enables the delivery of water molecules in poorly exuding wounds.[72, 73] Besides the importance of wound pathology in the exudate production, different wound types have shown different water vapor transmission rates. Water loss at a wounded site arises from the rupturing effect of the semipermeable protein layer in the *stratum corneum*, which breakdown promotes profuse water loss through the wound. While the dermis comprises about 80 % water, the *stratum corneum* comprises about 40 % and about 15 % in its inner and outermost layers.[74] Nevertheless, water has a large latent heat of evaporation of 2.3 $MJ.kg^{-1}$ [75] and consequently, local temperature increasing leads to water vapor transmission across the wound interface. Therefore, according to the wound pathophysiology, different wound types represent different needs in terms of moisture balance. For example, granulating wounds show a water vapor transmission rate of 214.1 ± 8.4 $g.m^{-2}.h^{-1}$, while first, second and third degree burns show values of 11.6 ± 1.1 $g.m^{-2}.h^{-1}$, 178.1 ± 5.5 $g.m^{-2}.h^{-1}$ and 143.2 ± 4.5 $g.m^{-2}.h^{-1}$ respectively.[76] More recently, Yan *et al.*[77] have reported the following values of water vapor transmission rate for granulating wounds (89.0 ± 8.4 $g.m^{-2}.h^{-1}$) and first degree burns (8.5 ± 0.5 $g.m^{-2}.h^{-1}$). In addition to the wound water vapor transmission rate, it is also important the water vapor transmission rate value of the wound dressing. After the absorption of the exudate by the dressing, water vapor transmission stills occurring through the dressing itself. Unmatching the wound exudate production rate, the exudate absorption rate and the dressing water vapor transmission rate, can conduct to a subsequent exudate accumulation in the wounded environment or to dry out the wound. For example, it has been suggested[77] for the case of granulating wounds that a value of water vapor transmission rate between 83.3 and 104.2 $g.m^{-2}.h^{-1}$, would be adequate to provide a proper moisture environment and avoiding exudate accumulation in granulating wounds.

1.2.4 pH management

The keratinocytes present in the epidermis are continuously secreting organic compounds that acidify the intact skin tissue, turning it to a naturally occurring acidic medium with a pH ranging from 4 to 6, a proactive action to avoid fungi and bacterial development. When the skin is injured, and consequently local blood and lymphatic vessels are disrupted, the wound pH increases to 7.4. According to the wound pathophysiology, acute wounds tend to become acidic while chronic wounds tend to become alkaline.[78] An alkaline pH is responsible to impair healing by favoring bacterial colonization and proliferation ($pH > 6$), and proteolysis mediated by the *in situ* host and bacterial proteases kinetically suppresses the healing bioevents.[79] Due to the wound pH role in the healing period, the clinical community have relied in topical formulations and wound dressings to control or modify the wound pH. In parallel with their thermal insulation provision, wound dressings are mainly conceptualized to control pH through the prevention of the respiratory alkalosis by preventing the loss of CO_2 from the wounded environment, which in turn contributes to lower the wound pH. Nevertheless, upon on the chosen wound dressing type, the wound pH tends to evolve differently. The wound exudate of chronic wounds under non-permeable dressings is frequently observed as more acidic, in comparison with chronic wounds were a permeable dressings is utilized. Wilson *et al.*[80] studied the clinical outcome of tailored dressings into two groups both suffering from chronic venous leg ulcers, whereas group 1 was set for a pH value 7.3 and group 2 was set for a pH value 6.0. Group 2 reported a rate of healing 3-fold higher than group 1. Regarding the listing process of the functional requirements for a wound dressing, pH management is a crucial one. In this way, local titration of the wound pH is currently understood as a beneficial feature to accelerate the wound healing process. It is suggested that more acidic wounds heal better, since a low pH value leads to an increase of local oxygen to the cells, a common observation described in literature as the Bohr-effect.[81]

1.2.5 Gaseous exchange

The metabolic pathways in the wound healing events are often associated with oxygen consumption and carbon dioxide production. Therefore, oxygen supply as well as carbon dioxide release must be guaranteed. In atraumatic skin tissues, it is observed that deep tissue layers report a partial pressure of oxygen (pO_2) around 5 %, while in the superficial layers pO_2 is established around 1 %.[82] Indeed, in wounded skin tissues pO_2 values as low as 1 % are still recorded at the wound surface, suggesting that atmospheric oxygen can oxygenate the wound bed.[83] The generated hypoxia due to the locally damaged skin microvasculature leads the cells to execute anaerobic metabolism, which increases the local production of lactic acid, reduces pH and stimulates the up-regulation of vasodilatory factors.[84, 85] Moreover, the pH reduction lowers the hemoglobin affinity for oxygen, further reducing the oxygen delivery.[81] Several studies have linked the oxygen presence as essential for the phagocytosis of external microorganisms,[86, 87] referring the positive effect of an *in situ* oxygen tension for the overall wound rate closure. Also, the locally generated hypoxia-inducible factors are utilized in many proangiogenic mechanisms through the vascular endothelial growth factor[88] and nitric oxide[89, 90] signaling. In this way, it is being observed an increase of treating modalities that balance the provision of oxygen into the wound bed, such as the hyperbaric oxygen therapy[91, 92] and topical oxygen therapy.[93] On the other hand, the carbon dioxide tension in a wound bed tends to increase as the healing processes moves forward. The partial pressure of carbon dioxide (pCO_2) rises from 60 to 75 mmHg at the second week, and such increase is related to higher metabolic activity and deficient diffusion over the damaged vascular network.[82] It has been demonstrated that high levels of local carbon dioxide can down-regulate genes related to innate immunity,[94] while resulting in reduced phagocytic activity due to a lower NFκB cellular activity.[95] Tsuji *et al.*[96] reported that endothelial cells under hypoxia conditioning were capable to proliferate at high levels of CO_2, suggesting that local pCO_2 mediates the cellular events regardless the local pH or oxygen values. These newly observations over the potential use of CO_2 in wound healing have deeply contribute to new therapeutic approaches. For instance, in a clinical study Brandi *et al.*[97] treated patients affected by chronic wounds through the subcutaneously administration of CO_2, concluding that comparatively to the control group (no CO_2 administration) such patients could observe an increase in microcirculation and in the tissue oxygenation values. Despite their different roles in the wound healing process, oxygen and carbon dioxide must be able to freely permeate a wound dressing, while keeping minimal tension values that can beneficially stimulate the wound regeneration process.

1.2.6 Prevention and Infection control

Wounds are prone to colonization by a diverse microbial flora that appears mainly from three different sources: (a) endogenous microorganisms from genitourinary, oropharyngeal and gastrointestinal mucous membranes; (b) exogenous microorganisms in the surrounding environment, and (c) microorganisms that are present in the human skin under normal circumstances.[98, 99] The diminished epidermal barrier function caused by a local injury, exposes the subcutaneous tissue to these sources of infection, while in parallel tissue hypoxia enhances the colonization phenomena.[100] Moreover, as a result of the established *in situ* bacterial activity, extracellular adherence proteins, formylmethionyl peptides and N-acetylmuramyl-L-alanyl-D-isoglutamine, tend to accumulate at the wound surface, accelerating the directed neutrophil locomotion or interfering with cell–matrix interactions.[101] At the wound bed, bacteria produce an exopolysaccharide matrix, designated as *biofilm*, in order to function as a protective substrate and barrier for the colony. Kierker *et al.*[102] demonstrated that just in 24 hours, biofilm communities of *Staphylococcus aureus* significantly increased the apoptosis of human keratinocytes. In addition, Zhao *et al.*[103] demonstrated that *Pseudomonas aeruginosa* biofilm-challenged wounds typically heal in approximately 6 weeks, at least 2 weeks longer than nonbiofilm-challenged normal wounds. Therefore, an ideal wound dressing must not only prevent the initial contamination by endogenous and exogenous bacteria, but it must also eradicate infection during the healing period. While the initial contamination prevention can be mainly achieved by proper impermeability to foreign bodies, the clinical community have pursued infection control either by the continuous elution of antimicrobial agents imbibed in the dressing inner structure[104] or the usage of polymeric materials that are antimicrobial by nature.[105] For example, in a randomized comparative study, 20 patients with ulcers of vascular aetiology, wound duration ≥ 6 months and ankle brachial index > 0.6, where treated with a silver-containing hydrofiber dressing, which promoted a bacterial load reduction of 41.6 %.[106] Alternatively, Moghadas *et al.*[107] reported that film-like wound dressings based on chitosan and biofunctionalized montmorillonite could achieve killing efficiencies over 99.6 % and 99.7 % towards *Escherichia coli* and *Staphylococcus aureus* populations respectively. Nevertheless, in the absence of drug eluting systems or natural antibiotic matrixes, proper infection control can be achieved by promoting an adverse environment for bacterial growth. For instance, by inducing a hyperosmotic environment, Connel *et al*.[108] were able to reduce the *Escherichia coli* and *Enterococcus faecalis* bioburden levels by 3 logs within 24 hours, values that were similar to wounds treated with the control silver sulfadiazine. Adverse milieus can be alternatively triggered by modulation of the wound environment pH,[109] or by promoting the *in situ* production of hydrogen peroxide.[110]

1.2.7 Odor management

The decrease of local vascularization and occlusion of blood vessels in a wound bed after a skin injury contributes to reduce tissue oxygenation, leading to a hypoxic environment. The resultant necrotic tissue is favorable to anaerobic bacterial colonization, where such bacteria generated volatile fatty acids (e.g., proprionic, isobutyric, butyric, isovaleric or valeric acid) give rise to a wound's malodor. It has been reported the presence of other proteolytic bacteria that produce a set of amines and diamines, such as putrescine and cadaverine, which also enhance a wound's potential malodor.[111] In addition, Shirasu *et al.*[112] observed the generation of dimethyl sulfide in malignant wounds, an organosulfur compound also found in fermented milk and certain rotten vegetables. Proper odor management practices have been recently explained under the acronym RACE: removal of necrotic tissue, antibacterial agents, odor concealers, and education and support.[113] While the removal of necrotic tissue and posterior infection prevention are key for a better odor management, odor concealers are also essential to capture and neutralize the generated volatile compounds usually under electrostatic interactions. In an international survey conducted by Gethin *et al.*[114] regarding 1444 clinical professionals, activated charcoal dressings were the most used type of wound dressings to manage a wound's malodor (84.9 %). Nevertheless, such constructs present some limitations. For example, these wound dressings are not recommend to be cut or trimmed, otherwise charcoal particles will enter the wound, a constrain that hinders their ideal fit to any wound.[115] Recently, Narayanan *et al.*[116] disclosed the production of a poly(ε-caprolactone) (PCL)/β-cyclodextrin functional nanofibrous wound dressings, which were able to absorb and retain high amounts of odor compounds (butyric and propionic acid), while preserving the typical flexibility of electrospun non-woven mats. Regardless the incorporation of antibacterial compounds in some dressings to control a wound infection, some hydrophilic dressings produce a characteristic odor as they decompose *in situ* after gelling over the wound.[63] Ideal wound dressings are then not only characterized by an appropriate wound exudate and moisture management, but also by their ability to retain and neutralize the malodor agents generated by the wound milieu, especially when a reduced dressing change frequency is desirable.

1.2.8 Reduce adherence

Further trauma to the wounded tissue can be achieved by removing a wound dressing and replacing it by a new one.[117] A wound dressing change is frequently related to one of the following factors: loss of therapeutic benefit, wound dressing rupture and/or the need to visually evaluate the regenerating tissue. Regarding the wound type, the repeated application and removal of a dressing can occur daily or weekly. In this way, avoiding cellular adhesion on the wound dressing is an important requirement. The dressing removal can strip away the new formed epithelium, extending or triggering the inflammatory cascade of events,[118] which can be then expressed as a rubor, calor or a dolor sensation, corresponding to local redness, heat, pain or swelling. In a clinical study, Hollinworth *et al.*[119] reported that 81% of the practitioners noticed that patients experienced most pain when dressing products were removed. Cellular adhesion over wound dressings can be structured as a continuous four-step process: (i) exudate-dressing interactions; (ii) cell-dressing interactions; (iii) biointegration, and (iv) biomaterial response to tissue environment.[120, 121] After placing the wound dressing, the wound exudate will form a layer of moisture on the dressing surface that is consequently preceded by the adsorption of the *in situ* biochemical compounds, reducing the Gibbs free energy of the future cell-dressing interactions.[51] One of the most important aspects of a wound dressing to tune the exudate constituents' adsorption is the dressing hydrophilicity, since hydrophobic materials will impair the formation of the needed moisture layer. For example, Martins *et al.*[122] concluded that by reducing the hydrophobicity of poly(ε-caprolactone)-based fibrous scaffolds through plasma treatment, the fibroblast cellular adhesion (L929 cell line) was significantly enhanced. After the establishment of the moisture layer, the wound bed proteins tend to migrate into the layer by diffusion, whereas protein concentration and solubility at the wound bed take a significant role. For instance in the case of a bloody wound, higher concentrations of fibrinogen, serum proteins and glycoproteins, are present in the wounded microenvironment, and therefore such components diffuse towards the wound dressing ending up to be stabilized at the generated layer of moisture, which significantly increases the tendency for future cellular anchorage. While studying the effect of protein concentration in the *in vitro* cellular adhesion, Koblinski *et al.*[123] found that the presence of low levels of adhesion proteins (fibronectin), together with high concentrations of non-adhesion proteins (osteonectin), could still promote the cells adhesion on U-bottom 96-well plastic plates, while low levels of adhesion proteins by their own were unable to promote cellular adhesion. Another potential driver of protein adsorption is the electrostatic attraction between a charged wound dressing and proteins at the wound site that are bipolar.[124] The moisture layer mediated protein adsorption on a wound dressing is also driven by the wound dressing topography. Despite fibrinogen being recognized as an adhesion protein, Rechendorff *et al.*[125] observed that the fibrinogen adsorption depends on the construct surface topography that it comes in contact with. The authors reported a reinforcement of 70 % on cellular adhesion when increasing the substrate roughness from 2.0 to 32.9 nm. In agreement, Damanik *et al.*[126] also correlated the surface topography and roughness with a better cell attachment, morphology and proliferation, extending their findings to an observed enhancement in the expression profile of proinflammatory (IL-1β, IL-6) and antiflammatory cytokines (TGF-β1, IL-10), as well as in the collagen and elastin expression. In summary, the reduced adherence property – ideally complete non-adherence – of a wound dressing is an important functional requirement, since it contributes to an easy and painless removal.[127] In addition, extending the period of non-adherence or avoiding completely the adherence phenomena, is also a cost-saving measurement, since average nursing time and costs per patient are significantly reduced.[128]

1.2.9 Provision of thermal insulation

Wound overheating has been reported to decrease the proliferative response of local lymphocytes.[82] Also, if the wound bed temperature is inferior to the core body temperature, it is observed a decrease in collagen deposition, slow epithelial repair and the reduction of local fibroblasts and inflammatory cells.[129] Lower wound bed temperature can locally occur due to impaired oxygenation and blood supply, and in some types of chronic wounds this wound type is usually 5 ºC bellow comparatively to the normal body temperature.[130] Despite a temperature value of 33 ºC was observed as the minimum viable value for neutrophil, fibroblast and epithelial cell activity,[82, 129] studies have shown that mitotic activity is higher for wound dressings that maintain the wound at the body temperature. For example, Kloth *et al.*[131, 132] demonstrated that pressure ulcers shown a faster surface reduction rate at 36-38 ºC, in comparison with wounds above or below the normal body temperature. More recently in a cohort study, Kanazawa *et al.*[133] founded that for pressure ulcers comprising a lower temperature at the wound edge than the wound bed and periwound skin, 72.7 % of these pressure ulcers had developed an undermining condition. Several strategies have been utilized to warm wounded tissues at temperatures ~ 37 ºC. Khan *et al.*[134] utilized topical radiant heating to improve the wound healing rate in split-thickness skin graft donor-site wounds, while Price *et al.*[135] reported a superior healing rate when radiant heat dressings were used in chronic wounds. In this way, a functional requirement of a wound dressing it will be its capacity to provide thermal insulation, supporting a wounded bed temperature as close as to the core body temperature for proper healing.

1.3 THESIS OULTLINE AND MAIN GOALS

1.3.1 Is there an ideal wound dressing?

As previously introduced, the concept of a unique "ideal" wound dressing is impossible to attend due to the fact that each wound pathophysiology represents a specific set of functional requirements. For instance, regarding the wound exudate production rate parameter, diabetic foot ulcers are commonly characterized by a poor exudate production, while in contrast third-degree burns exhibit severe exudate production. The hypothesis to develop a wound dressing that can simultaneously be adequate, for example, for diabetic foot ulcers and third-degree burns, is unrealistic from a clinical point of view. A high absorptive wound dressing can dry out a diabetic foot ulcer promoting tissue adherence, while in the other hand a poor absorptive wound dressing can cause the skin maceration due to locally and excessively accumulated exudate.

Wound dressings are frequently selected according to the following wound aspects: color, depth and exudate. A wound color varies from black (necrotic tissue), to yellow (sloughy), to red (granulation), to pink (epithelization). A wound depth varies from deep cavity, shallow or superficial, while exudation can be high, moderate, minimal or none. Other aspects with a strong influence in choosing a wound dressing are: type of the tissue that surrounds the wound, presence of infection, need to apply compression or current skin fragility. In this way, the conceptualization of a wound dressing to attend all the potential aspects of a wounded environment is unpractical. Nevertheless, upon the dynamic behavior of the healing environment, the dressing choice can also vary according to the healing stages. A wound healing therapy can be initiated by using a certain type of wound dressing that is the most appropriate at that time point, but accordingly to the healing process evolution a new type of dressing can be used in agreement with the now occurring wound characteristics at that time frame.

In summary, despite the absence of a unique and ideal wound dressing, two development strategies may be followed: (i) conceptualize and conceive a single-based wound dressing that targets a specific wound pathophysiology; and, (ii) conceptualize and conceive a common wound dressing substrate that can be readily tailored throughout common techniques according to the patient needs.

1.3.2 Chapter outline and thesis goals

This thesis embraces the opportunity to develop a wound dressing substrate that not only attends the previously enumerated functional requirements, but also avoids the need of secondary dressings. While the pursuit of an ideal wound dressing is technically unadvised, it was the intent of this PhD work plan to elaborate a substrate that could offer the required structural, mechanical and physicochemical characteristics (**Figure 1.5**). Upon the key pursued features, the author highlights the achievement of each feature throughout Chapter 2 and 3, while quantifying their contribution to the main goal of this thesis. From a potential technology transfer point of view, econometric parameters such as production cost, production time and suitability score for full-scale industrial processes, were also taken in consideration. In addition, the construct was intentionally produced in such manner that could favor its functional modification by common industrial practices, allowing to spin-off several wound dressing types from the proposed substrate. As a showcase of this two-step based process, after the production of the wound dressing substrate, such construct was properly modified to achieve high absorptive capacity and proper delivery of healing promoting compounds. It is further provided modeling suitability of promising pharmaceutical compounds with the proposed wound dressing substrate, being strongly encouraged the execution of these leads as a future guidance. This thesis is mainly characterized not only by the acquisition of extensive data sets from lab intensive activities, but also by the continuous provision of theoretical and semi-empirical models proposed by the author. The author looked to validate his models and equations either by the data reported in this document (properly referenced in each chapter), as well as by the data published by others that were not fully understood until this moment.

According to the multi-scientific domains of the present thesis, this document is divided in four chapters, and each chapter goals are now summarized:

CHAPTER 1 – WOUND PATHOPHYSIOLOGY AND WOUND DRESSING CONCEPTUALIZATION

Chapter 1 aims to introduce the reader into the pathophysiology of the wound healing phenomena, highlighting the complexity of the comprised biochemical events. It is also aimed to familiarize the reader with the current functional requirements of a wound dressing, while in parallel it is established the association of such requirements with the proper biochemical cues needed to attend. This chapter has also as a primary goal to report the wound dressing state of the art, completing such information with their advantages and disadvantages, while further information is provided according to the clinical use of secondary dressings.

CHAPTER 2 – FABRICATION OF THREE-DIMENSIONAL ELECTRO-SPUN CONSTRUCTS

Chapter 2 is dedicated to report the fabrication method of the wound dressing substrate. It is aimed to provide experimental information about the employed technique – *electrospining* – and

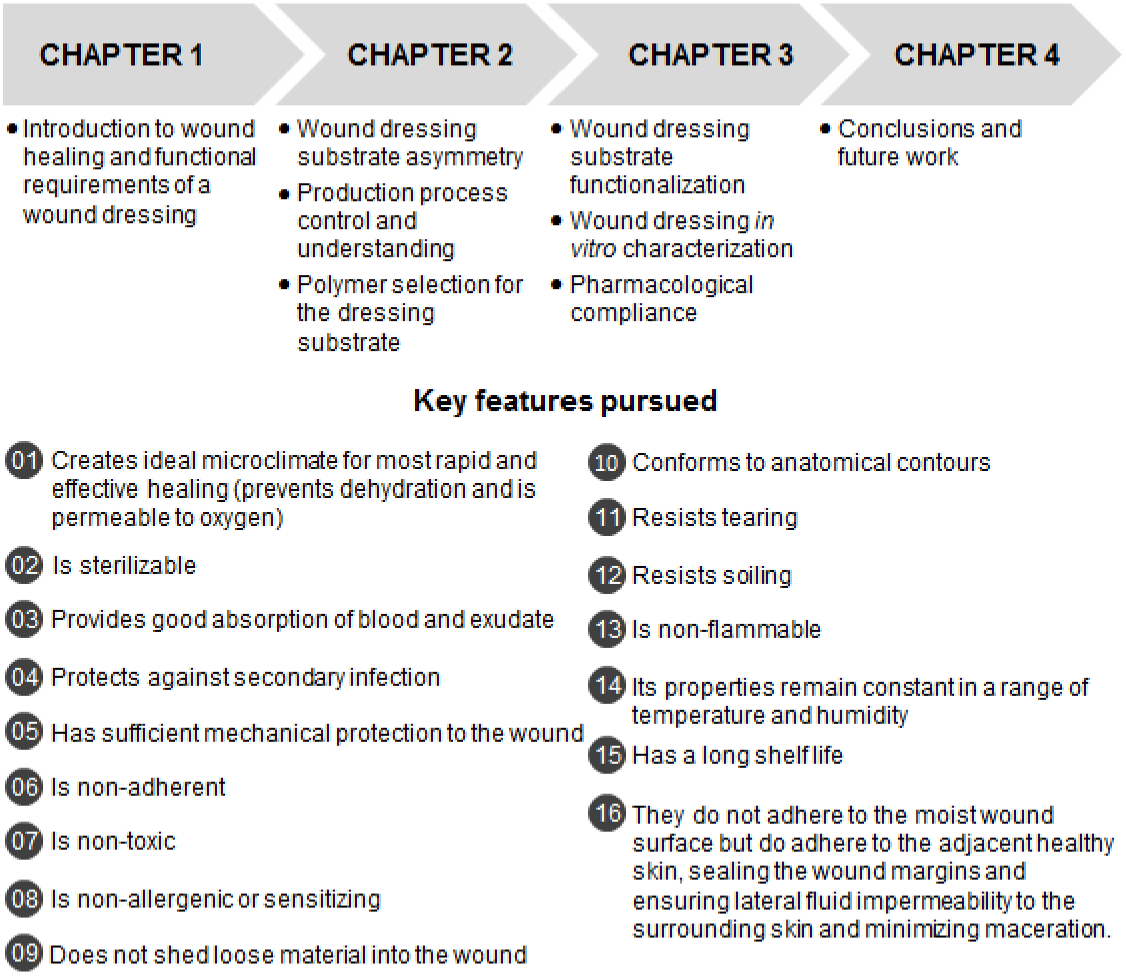

CHAPTER 1
- Introduction to wound healing and functional requirements of a wound dressing

CHAPTER 2
- Wound dressing substrate asymmetry
- Production process control and understanding
- Polymer selection for the dressing substrate

CHAPTER 3
- Wound dressing substrate functionalization
- Wound dressing *in vitro* characterization
- Pharmacological compliance

CHAPTER 4
- Conclusions and future work

Key features pursued

01 Creates ideal microclimate for most rapid and effective healing (prevents dehydration and is permeable to oxygen)
02 Is sterilizable
03 Provides good absorption of blood and exudate
04 Protects against secondary infection
05 Has sufficient mechanical protection to the wound
06 Is non-adherent
07 Is non-toxic
08 Is non-allergenic or sensitizing
09 Does not shed loose material into the wound
10 Conforms to anatomical contours
11 Resists tearing
12 Resists soiling
13 Is non-flammable
14 Its properties remain constant in a range of temperature and humidity
15 Has a long shelf life
16 They do not adhere to the moist wound surface but do adhere to the adjacent healthy skin, sealing the wound margins and ensuring lateral fluid impermeability to the surrounding skin and minimizing maceration.

Figure 1.5 Thesis schematics and wound dressing key features pursued.

how such technique was used to manufacture asymmetrical substrates according to an electrostatic driven self-assembly mechanism. Proper process control through the experimental parameters is disclosed. Moreover, this chapter also aims to provide a theoretical model that cannot only describe the self-assembly mechanism of the generated constructs, but can also describe the data published by other peers.

CHAPTER 3 – THREE-DIMENSIONAL MULTILAYERED FIBROUS CONSTRUCTS FOR WOUND HEALING APPLICATIONS

Chapter 3 follows the successful fabrication of asymmetrical wound dressing substrates by a novel electrostatic driven self-assembly mechanism. The generated fibrous-based materials with enhanced tissue interaction features, are now functionalized by the *layer-by-layer* method. This chapter is dedicated to explore the best polyelectrolytes regarding wound healing, while in parallel cellular adhesion to the dressing is avoided. By properly selecting the polyelectrolytes to be used, Chapter 3 also aims to report a set of pharmaceutical compounds to target MMP-9, where such compounds are compatible with the functionalized dressings accordingly to the intermolecular models employed herein. In addition, this chapter reports in deep detail the outcome data of key characterization techniques, demonstrating therefore the good performance of these wound dressings according to the functional requirements previously introduced.

CHAPTER 4 – CONCLUSION AND FUTURE WORK

Chapter 4 highlights the most important findings within the scope of the wound dressing substrate fabrication and according to its functionalization. Moreover, upon the current state of the art and achieved goals, it is further provided instructions for future work and guidance.

1.4 CHAPTER REFERENCES

[1] Saxena V. 3 - Biomechanics of skin. In: Orgill D, Blanco C, editors. Biomaterials for Treating Skin Loss: Woodhead Publishing; 2009. p. 18-24.

[2] Thomas DR. Prevention and treatment of pressure ulcers. Journal of the American Medical Directors Association 2006;7:46-59.

[3] Atiyeh BS, Ioannovich J, Al-Amm CA, El-Musa KA. Management of acute and chronic open wounds: the importance of moist environment in optimal wound healing. Current pharmaceutical biotechnology 2002;3:179-95.

[4] Braddock M, Campbell CJ, Zuder D. Current therapies for wound healing: electrical stimulation, biological therapeutics, and the potential for gene therapy. International journal of dermatology 1999;38:808-17.

[5] Harding KG, Morris HL, Patel GK. Science, medicine and the future: healing chronic wounds. Bmj 2002;324:160-3.

[6] Furtado A. Úlceras de perna: Tratamento baseado na evidência. Revista Nursing Portuguesa2003. p. 1-9.

[7] Sgonc R, Gruber J. Age-related aspects of cutaneous wound healing: a mini-review. Gerontology 2013;59:159-64.

[8] Eltorai IM, Montroy RE, Kobayashi M, Jakowatz J, Guttierez P. Marjolin's ulcer in patients with spinal cord injury. The journal of spinal cord medicine 2002;25:191-6.

[9] Raffetto JD. Dermal pathology, cellular biology, and inflammation in chronic venous disease. Thrombosis research 2009;123 Suppl 4:S66-71.

[10] Falanga V. Wound healing and its impairment in the diabetic foot. Lancet 2005;366:1736-43.

[11] Lazarus GS, Cooper DM, Knighton DR, Margolis DJ, Pecoraro RE, Rodeheaver G, et al. Definitions and guidelines for assessment of wounds and evaluation of healing. Archives of dermatology 1994;130:489-93.

[12] Hanlon MD. Wound Care: A Collaborative Practice Manual for Physical Therapists and Nurses. Nutrition in Clinical Practice 2001;16:371-.

[13] Heng MC. Wound healing in adult skin: aiming for perfect regeneration. International journal of dermatology 2011;50:1058-66.

[14] Menke NB, Ward KR, Witten TM, Bonchev DG, Diegelmann RF. Impaired wound healing. Clinics in dermatology 2007;25:19-25.

[15] Demidova-Rice TN, Hamblin MR, Herman IM. Acute and impaired wound healing: pathophysiology and current methods for drug delivery, part 1: normal and chronic wounds: biology, causes, and approaches to care. Advances in skin & wound care 2012;25:304-14.

[16] Diegelmann RF. Excessive neutrophils characterize chronic pressure ulcers. Wound repair and regeneration : official publication of the Wound Healing Society [and] the European Tissue Repair Society 2003;11:490-5.

[17] Caley MP, Martins VL, O'Toole EA. Metalloproteinases and Wound Healing. Advances in wound care 2015;4:225-34.

[18] Ren Y, Gu G, Yao M, Driver VR. Role of matrix metalloproteinases in chronic wound healing: diagnostic and therapeutic implications. Chinese medical journal 2014;127:1572-81.

[19] Martins VL, Caley M, O'Toole EA. Matrix metalloproteinases and epidermal wound repair. Cell and tissue research 2013;351:255-68.

[20] Filkor K, Nemeth T, Nagy I, Kondorosi E, Urban E, Kemeny L, et al. The expression of inflammatory cytokines, TAM tyrosine kinase receptors and their ligands is upregulated in venous leg ulcer patients: a novel insight into chronic wound immunity. International wound journal 2016;13:554-62

[21] Demidova-Rice TN, Hamblin MR, Herman IM. Acute and impaired wound healing: pathophysiology and current methods for drug delivery, part 2: role of growth factors in normal and pathological wound healing: therapeutic potential and methods of delivery. Advances in skin & wound care 2012;25:349-70.

[22] Brem H, Stojadinovic O, Diegelmann RF, Entero H, Lee B, Pastar I, et al. Molecular markers in patients with chronic wounds to guide surgical debridement. Molecular medicine 2007;13:30-9.

[23] Li J, Chen J, Kirsner R. Pathophysiology of acute wound healing. Clinics in dermatology 2007;25:9-18.

[24] Watkins SA, Zippin JH. When wound healing goes awry. A review of normal and abnormal wound healing, scar pathophysiology, and therapeutics. Journal of drugs in dermatology : JDD 2008;7:997-1005.

[25] Casini A, Duval C, Pan X, Tintillier V, Biron-Andreani C, Ariens RA. Fibrin clot structure in patients with congenital dysfibrinogenaemia. Thrombosis research 2016;137:189-95.

[26] Jun JI, Kim KH, Lau LF. The matricellular protein CCN1 mediates neutrophil efferocytosis in cutaneous wound healing. Nat Commun 2015;6:7386.

[27] Mirza RE, Fang MM, Weinheimer-Haus EM, Ennis WJ, Koh TJ. Sustained inflammasome activity in macrophages impairs wound healing in type 2 diabetic humans and mice. Diabetes 2014;63:1103-14.

[28] Rosowski EE, Huttenlocher A. Neutrophils, wounds, and cancer progression. Dev Cell 2015;34:134-6.

[29] Leoni G, Neumann PA, Sumagin R, Denning TL, Nusrat A. Wound repair: role of immune-epithelial interactions. Mucosal Immunol 2015;8:959-68.

[30] Singer AJ, Clark RA. Cutaneous wound healing. The New England journal of medicine 1999;341:738-46.

[31] Sabino F, Hermes O, Egli FE, Kockmann T, Schlage P, Croizat P, et al. In vivo assessment of protease dynamics in cutaneous wound healing by degradomics analysis of porcine wound exudates. Mol Cell Proteomics 2015;14:354-70.

[32] Raffetto JD. Pathophysiology of wound healing and alterations in venous leg ulcers-review. Phlebology / Venous Forum of the Royal Society of Medicine 2016;31:56-62.

[33] Penn JW, Grobbelaar AO, Rolfe KJ. The role of the TGF-beta family in wound healing, burns and scarring: a review. International journal of burns and trauma 2012;2:18-28.

[34] Faler BJ, Macsata RA, Plummer D, Mishra L, Sidawy AN. Transforming growth factor-beta and wound healing. Perspect Vasc Surg Endovasc Ther 2006;18:55-62.

[35] Gould LJ. Topical Collagen-Based Biomaterials for Chronic Wounds: Rationale and Clinical Application. Advances in wound care 2016;5:19-31.

[36] Li D, Ye Y, Li D, Li X, Mu C. Biological properties of dialdehyde carboxymethyl cellulose crosslinked gelatin-PEG composite hydrogel fibers for wound dressings. Carbohydr Polym 2016;137:508-14.

[37] Wiegand C, Springer S, Abel M, Ruth P, Hipler U-C. Differences in fluid distribution during negative pressure wound therapy (NPWT) in a large-pored PU-foam dressing, drainage film, and a specialized NPWT dressing system. Wound Medicine 2014;6:22-5.

[38] Zhao M. Electrical fields in wound healing—An overriding signal that directs cell migration. Seminars in Cell & Developmental Biology 2009;20:674-82.

[39] Gainza G, Villullas S, Pedraz JL, Hernandez RM, Igartua M. Advances in drug delivery systems (DDSs) to release growth factors for wound healing and skin regeneration. Nanomedicine 2015;11:1551-73.

[40] Icli B, Nabzdyk CS, Lujan-Hernandez J, Cahill M, Auster ME, Wara AKM, et al. Regulation of impaired angiogenesis in diabetic dermal wound healing by microRNA-26a. Journal of molecular and cellular cardiology 2016;91:151-9.

[41] Borena BM, Martens A, Broeckx SY, Meyer E, Chiers K, Duchateau L, et al. Regenerative Skin Wound Healing in Mammals: State-of-the-Art on Growth Factor and Stem Cell Based Treatments. Cell Physiol Biochem 2015;36:1-23.

[42] Li Z, Wang H, Yang B, Sun Y, Huo R. Three-dimensional graphene foams loaded with bone marrow derived mesenchymal stem cells promote skin wound healing with reduced scarring. Materials Science and Engineering: C 2015;57:181-8.

[43] Gurtner GC, Werner S, Barrandon Y, Longaker MT. Wound repair and regeneration. Nature 2008;453:314-21.

[44] Kim JT, Kim YH, Kim SW. Customized negative pressure wound therapy for intractable auricular defects using alginate dressings and feeding tubes. Journal of Plastic, Reconstructive & Aesthetic Surgery 2014;67:e284-e6.

[45] Shan Y-H, Peng L-H, Liu X, Chen X, Xiong J, Gao J-Q. Silk fibroin/gelatin electrospun nanofibrous dressing functionalized with astragaloside IV induces healing and anti-scar effects on burn wound. International Journal of Pharmaceutics 2015;479:291-301.

[46] Wen X, Zheng Y, Wu J, Yue L, Wang C, Luan J, et al. In vitro and in vivo investigation of bacterial cellulose dressing containing uniform silver sulfadiazine nanoparticles for burn wound healing. Progress in Natural Science: Materials International 2015;25:197-203.

[47] Falanga V, Iwamoto S, Chartier M, Yufit T, Butmarc J, Kouttab N, et al. Autologous bone marrow-derived cultured mesenchymal stem cells delivered in a fibrin spray accelerate healing in murine and human cutaneous wounds. Tissue Eng 2007;13:1299-312.

[48] Boateng J, Catanzano O. Advanced Therapeutic Dressings for Effective Wound Healing--A Review. Journal of pharmaceutical sciences 2015;104:3653-80.

[49] Jones KS. Assays on the influence of biomaterials on allogeneic rejection in tissue engineering. Tissue engineering Part B, Reviews 2008;14:407-17.

[50] Tang L, Eaton JW. Inflammatory responses to biomaterials. American journal of clinical pathology 1995;103:466-71.

[51] Chen H, Yuan L, Song W, Wu Z, Li D. Biocompatible polymer materials: Role of protein–surface interactions. Progress in Polymer Science 2008;33:1059-87.

[52] Smiley ST, King JA, Hancock WW. Fibrinogen Stimulates Macrophage Chemokine Secretion Through Toll-Like Receptor 4. The Journal of Immunology 2001;167:2887-94.

[53] Tang L, Eaton JW. Fibrin(ogen) mediates acute inflammatory responses to biomaterials. The Journal of experimental medicine 1993;178:2147-56.

[54] Zhou G, Niepel MS, Saretia S, Groth T. Reducing the inflammatory responses of biomaterials by surface modification with glycosaminoglycan multilayers. Journal of biomedical materials research Part A 2016;104:493-502.

[55] Sánchez O, Rodríguez-Sureda V, Domínguez C, Fernández-Figueras T, Vilches A, Llurba E, et al. Study of biomaterial-induced macrophage activation, cell-mediated immune response and molecular oxidative damage in patients with dermal bioimplants. Immunobiology 2012;217:44-53.

[56] Lau D, Baldus S. Myeloperoxidase and its contributory role in inflammatory vascular disease. Pharmacol Ther 2006;111:16-26.

[57] van Eijk M, van Roomen CP, Renkema GH, Bussink AP, Andrews L, Blommaart EF, et al. Characterization of human phagocyte-derived chitotriosidase, a component of innate immunity. International immunology 2005;17:1505-12.

[58] Rathcke CN, Vestergaard H. YKL-40--an emerging biomarker in cardiovascular disease and diabetes. Cardiovascular diabetology 2009;8:61.

[59] Orrenius S, Nicotera P, Zhivotovsky B. Cell Death Mechanisms and Their Implications in Toxicology. Toxicological Sciences 2011;119:3-19.

[60] Kemp M, Go YM, Jones DP. Nonequilibrium thermodynamics of thiol/disulfide redox systems: a perspective on redox systems biology. Free Radic Biol Med 2008;44:921-37.

[61] Nakagawa T, Zhu H, Morishima N, Li E, Xu J, Yankner BA, et al. Caspase-12 mediates endoplasmic-reticulum-specific apoptosis and cytotoxicity by amyloid-beta. Nature 2000;403:98-103.

[62] Gardner S. 'M' is for Moisture: friend or foe? How developing a better understanding of exudate can prevent moisture-related complications. Dermatological Nursing 2015;14:40-7.

[63] Day RM. 6 - Functional requirements of wound repair biomaterials A2 - Farrar, David. Advanced Wound Repair Therapies: Woodhead Publishing; 2011. p. 155-73.

[64] Moore Z, Strapp H. Managing the problem of excess exudate. British journal of nursing 2015;24:S12, S4-7.

[65] Vuolo J. Current options for managing the problem of excess wound exudate. Prof Nurse 2004;19:487-91.

[66] Rippon MG, Ousey K, Cutting KF. Wound healing and hyper-hydration: a counterintuitive model. Journal of wound care 2016;25:68-75.

[67] Kowluru RA. Role of matrix metalloproteinase-9 in the development of diabetic retinopathy and its regulation by H-Ras. Investigative ophthalmology & visual science 2010;51:4320-6.

[68] Li Z, Guo S, Yao F, Zhang Y, Li T. Increased ratio of serum matrix metalloproteinase-9 against TIMP-1 predicts poor wound healing in diabetic foot ulcers. Journal of diabetes and its complications 2013;27:380-2.

[69] Marola S, Ferrarese A, Solej M, Enrico S, Nano M, Martino V. Management of venous ulcers: State of the art. International journal of surgery 2016, *In Press*

[70] Tian M, Qing C, Niu Y, Dong J, Cao X, Song F, et al. The Relationship Between Inflammation and Impaired Wound Healing in a Diabetic Rat Burn Model. Journal of burn care & research : official publication of the American Burn Association 2016;37:e115-24.

[71] Sweeney IR, Miraftab M, Collyer G. A critical review of modern and emerging absorbent dressings used to treat exuding wounds. International wound journal 2012;9:601-12.

[72] Jin SG, Yousaf AM, Kim KS, Kim DW, Kim DS, Kim JK, et al. Influence of hydrophilic polymers on functional properties and wound healing efficacy of hydrocolloid based wound dressings. International Journal of Pharmaceutics 2016;501:160-6.

[73] Kim S, Park S-G, Kang S-W, Lee KJ. Nanofiber-Based Hydrocolloid from Colloid Electrospinning Toward Next Generation Wound Dressing. Macromolecular Materials and Engineering 2016: *in press*

[74] Agache PG, Agache P, Humbert P. Measuring the skin: Springer Science & Business Media; 2004.

[75] Stein B. Building technology: mechanical and electrical systems: John Wiley & Sons; 1997.

[76] Lamke LO, Nilsson GE, Reithner HL. The evaporative water loss from burns and the water-vapour permeability of grafts and artificial membranes used in the treatment of burns. Burns : journal of the International Society for Burn Injuries 1977, 3:159-65.

[77] Yan L, Si S, Chen Y, Yuan T, Fan H, Yao Y, et al. Electrospun in-situ hybrid polyurethane/nano-TiO2 as wound dressings. Fibers and Polymers 2011;12:207-13.

[78] Schneider LA, Korber A, Grabbe S, Dissemond J. Influence of pH on wound-healing: a new perspective for wound-therapy? Archives of dermatological research 2007;298:413-20.

[79] Percival SL, McCarty S, Hunt JA, Woods EJ. The effects of pH on wound healing, biofilms, and antimicrobial efficacy. Wound repair and regeneration : official publication of the Wound Healing Society [and] the European Tissue Repair Society 2014;22:174-86.

[80] Wilson IA, Henry M, Quill RD, Byrne PJ. The pH of varicose ulcer surfaces and its relationship to healing. Vasa 1979;8:339-42.

[81] Roberts G, Hammad L, Collins C, Shearman C, Mani R. Some effects of sustained compression on ulcerated tissues. Angiology 2002;53:451-6.

[82] Kruse CR, Nuutila K, Lee CC, Kiwanuka E, Singh M, Caterson EJ, et al. The external microenvironment of healing skin wounds. Wound repair and regeneration : official publication of the Wound Healing Society [and] the European Tissue Repair Society 2015;23:456-64.

[83] Gordillo GM, Sen CK. Revisiting the essential role of oxygen in wound healing. American journal of surgery 2003;186:259-63.

[84] Sen CK. Wound healing essentials: let there be oxygen. Wound repair and regeneration : official publication of the Wound Healing Society [and] the European Tissue Repair Society 2009;17:1-18.

[85] Schreml S, Szeimies RM, Prantl L, Karrer S, Landthaler M, Babilas P. Oxygen in acute and chronic wound healing. The British journal of dermatology 2010;163:257-68.

[86] Guo S, Dipietro LA. Factors affecting wound healing. J Dent Res 2010;89:219-29.

[87] Eisenbud DE. Oxygen in wound healing: nutrient, antibiotic, signaling molecule, and therapeutic agent. Clinics in plastic surgery 2012;39:293-310.

[88] Krock BL, Skuli N, Simon MC. Hypoxia-induced angiogenesis: good and evil. Genes Cancer 2011;2:1117-33.

[89] Spallotta F, Cencioni C, Straino S, Nanni S, Rosati J, Artuso S, et al. A nitric oxide-dependent cross-talk between class I and III histone deacetylases accelerates skin repair. J Biol Chem 2013;288:11004-12.

[90] Olson N, van der Vliet A. Interactions between nitric oxide and hypoxia-inducible factor signaling pathways in inflammatory disease. Nitric Oxide 2011;25:125-37.

[91] Zhang Q, Chang Q, Cox RA, Gong X, Gould LJ. Hyperbaric oxygen attenuates apoptosis and decreases inflammation in an ischemic wound model. The Journal of investigative dermatology 2008;128:2102-12.

[92] Zhang Q, Gould LJ. Hyperbaric oxygen reduces matrix metalloproteinases in ischemic wounds through a redox-dependent mechanism. The Journal of investigative dermatology 2014;134:237-46.

[93] Gordillo GM, Roy S, Khanna S, Schlanger R, Khandelwal S, Phillips G, et al. Topical oxygen therapy induces vascular endothelial growth factor expression and improves closure of clinically presented chronic wounds. Clin Exp Pharmacol Physiol 2008;35:957-64.

[94] Taylor CT, Cummins EP. Regulation of gene expression by carbon dioxide. J Physiol 2011;589:797-803.

[95] Tawfik Amin A, Shiraishi N, Ninomiya S, Tajima M, Inomata M, Kitano S. Activation of nuclear factor kappa B and induction of migration inhibitory factor in tumors by surgical stress of laparotomy versus carbon dioxide pneumoperitoneum: an animal experiment. Surg Endosc 2010;24:578-83.

[96] Tsuji T, Aoshiba K, Itoh M, Nakamura H, Yamaguchi K. Hypercapnia accelerates wound healing in endothelial cell monolayers exposed to hypoxia. Open Respir Med J 2013;7:6-12.

[97] Brandi C, Grimaldi L, Nisi G, Brafa A, Campa A, Calabro M, et al. The role of carbon dioxide therapy in the treatment of chronic wounds. In Vivo 2010;24:223-6.

[98] Scalise A, Bianchi A, Tartaglione C, Bolletta E, Pierangeli M, Torresetti M, et al. Microenvironment and microbiology of skin wounds: the role of bacterial biofilms and related factors. Seminars in Vascular Surgery 2016;28:151-9.

[99] Percival SL, McCarty SM, Lipsky B. Biofilms and Wounds: An Overview of the Evidence. Advances in wound care 2015;4:373-81.

[100] Payen VL, Brisson L, Dewhirst MW, Sonveaux P. Common responses of tumors and wounds to hypoxia. Cancer journal 2015;21:75-87.

[101] Eming SA, Krieg T, Davidson JM. Inflammation in Wound Repair: Molecular and Cellular Mechanisms. Journal of Investigative Dermatology;127:514-25.

[102] Kirker KR, Secor PR, James GA, Fleckman P, Olerud JE, Stewart PS. Loss of viability and induction of apoptosis in human keratinocytes exposed to Staphylococcus aureus biofilms in vitro. Wound Repair and Regeneration 2009;17:690-9.

[103] Zhao G, Usui ML, Underwood RA, Singh PK, James GA, Stewart PS, et al. Time course study of delayed wound healing in a biofilm-challenged diabetic mouse model. Wound Repair and Regeneration 2012;20:342-52.

[104] Boateng JS, Matthews KH, Stevens HNE, Eccleston GM. Wound healing dressings and drug delivery systems: A review. Journal of pharmaceutical sciences 2008;97:2892-923.

[105] Jain A, Duvvuri LS, Farah S, Beyth N, Domb AJ, Khan W. Antimicrobial polymers. Adv Healthc Mater 2014;3:1969-85.

[106] Mosti G, Magliaro A, Mattaliano V, Picerni P, Angelotti N. Comparative study of two antimicrobial dressings in infected leg ulcers: a pilot study. Journal of wound care 2015;24:121-2; 4-7.

[107] Moghadas B, Dashtimoghadam E, Mirzadeh H, Seidi F, Hasani-Sadrabadi MM. Novel chitosan-based nanobiohybrid membranes for wound dressing applications. RSC Advances 2016;6:7701-11.

[108] Connell S, Li J, Durkes A, Zaroura M, Shi R. Non-dermal Irritating Hyperosmotic Nanoemulsions Reduce Treatment Times in a Contamination Model of Wound Healing. Wound repair and regeneration : official publication of the Wound Healing Society [and] the European Tissue Repair Society 2016.

[109] Jones EM, Cochrane CA, Percival SL. The Effect of pH on the Extracellular Matrix and Biofilms. Advances in wound care 2015;4:431-9.

[110] Meng H, Li Y, Faust M, Konst S, Lee BP. Hydrogen peroxide generation and biocompatibility of hydrogel-bound mussel adhesive moiety. Acta biomaterialia 2015;17:160-9.

[111] Tamai N, Akase T, Minematsu T, Higashi K, Toida T, Igarashi K, et al. Association Between Components of Exudates and Periwound Moisture-Associated Dermatitis in Breast Cancer Patients With Malignant Fungating Wounds. Biological Research For Nursing 2016;18:199-206.

[112] Shirasu M, Nagai S, Hayashi R, Ochiai A, Touhara K. Dimethyl Trisulfide as a Characteristic Odor Associated with Fungating Cancer Wounds. Bioscience, Biotechnology, and Biochemistry 2009;73:2117-20.

[113] Samala RV, Davis MP. Comprehensive wound malodor management: Win the RACE. Cleveland Clinic journal of medicine 2015;82:535-43.

[114] Gethin G, Grocott P, Probst S, Clarke E. Current practice in the management of wound odour: An international survey. International journal of nursing studies 2014;51:865-74.

[115] Schreml S, Klein S, Babilas P, Karrer S. Wound dressings in chronic wound therapy. Phlebologie 2013;42:189-96.

[116] Narayanan G, Ormond BR, Gupta BS, Tonelli AE. Efficient wound odor removal by β-cyclodextrin functionalized poly (ε-caprolactone) nanofibers. Journal of Applied Polymer Science 2015;132:n/a-n/a.

[117] Upton D, Solowiej K, Hender C, Woodyatt KY. Stress and pain associated with dressing change in patients with chronic wounds. Journal of wound care 2012;21:53-4, 6,8 passim.

[118] Kim JY, Kim NK, Lee YJ. A descriptive study of Korean nurses' perception of pain and skin tearing at dressing change. International wound journal 2016;13:47-51.

[119] Hollinworth H, Collier M. Nurses' views about pain and trauma at dressing changes: results of a national survey. Journal of wound care 2000;9:369-73.

[120] Bacakova L, Filova E, Parizek M, Ruml T, Svorcik V. Modulation of cell adhesion, proliferation and differentiation on materials designed for body implants. Biotechnol Adv 2011;29:739-67.

[121] Leal-Egana A, Diaz-Cuenca A, Boccaccini AR. Tuning of cell-biomaterial anchorage for tissue regeneration. Adv Mater 2013;25:4049-57.

[122] Martins A, Pinho ED, Faria S, Pashkuleva I, Marques AP, Reis RL, et al. Surface modification of electrospun polycaprolactone nanofiber meshes by plasma treatment to enhance biological performance. Small 2009;5:1195-206.

[123] Koblinski JE, Wu M, Demeler B, Jacob K, Kleinman HK. Matrix cell adhesion activation by non-adhesion proteins. Journal of cell science 2005;118:2965-74.

[124] Wei Q, Becherer T, Angioletti-Uberti S, Dzubiella J, Wischke C, Neffe AT, et al. Protein interactions with polymer coatings and biomaterials. Angew Chem Int Ed Engl 2014;53:8004-31.

[125] Rechendorff K, Hovgaard MB, Foss M, Zhdanov VP, Besenbacher F. Enhancement of protein adsorption induced by surface roughness. Langmuir 2006;22:10885-8.

[126] Damanik FF, Rothuizen TC, van Blitterswijk C, Rotmans JI, Moroni L. Towards an in vitro model mimicking the foreign body response: tailoring the surface properties of biomaterials to modulate extracellular matrix. Sci Rep 2014;4:6325.

[127] Campbell N, Campbell D. Evaluation of a non-adherent, povidone-iodine dressing in a case series of chronic wounds. Journal of wound care 2013;22:401-2, 4-6.

[128] Sood A, Granick MS, Tomaselli NL. Wound Dressings and Comparative Effectiveness Data. Advances in wound care 2014;3:511-29.

[129] McGuiness W, Vella E, Harrison D. Influence of dressing changes on wound temperature. Journal of wound care 2004;13:383-5.

[130] Fierheller M, Sibbald RG. A Clinical Investigation into the Relationship between Increased Periwound Skin Temperature and Local Wound Infection in Patients with Chronic Leg Ulcers. Advances in skin & wound care 2010;23:369-79.

[131] Kloth LC, Berman JE, Dumit-Minkel S, Sutton CH, Papanek PE, Wurzel J. Effects of a normothermic dressing on pressure ulcer healing. Advances in skin & wound care 2000;13:69-74.

[132] Kloth LC, Berman JE, Nett M, Papanek PE, Dumit-Minkel S. A randomized controlled clinical trial to evaluate the effects of noncontact normothermic wound therapy on chronic full-thickness pressure ulcers. Advances in skin & wound care 2002;15:270-6.

[133] Kanazawa T, Kitamura A, Nakagami G, Goto T, Miyagaki T, Hayashi A, et al. Lower temperature at the wound edge detected by thermography predicts undermining development in pressure ulcers: a pilot study. International wound journal 2015:n/a-n/a.

[134] Khan AA, Banwell PE, Bakker MC, Gillespie PG, McGrouther DA, Roberts AH. Topical radiant heating in wound healing: an experimental study in a donor site wound model*. International wound journal 2004;1:233-40.

[135] Price P, Bale S, Crook H, Harding KG. The effect of a radiant heat dressing on pressure ulcers. Journal of wound care 2000;9:201-5.

2

Fabrication of Three-Dimensional Electrospun Constructs

SUMMARY[1]

The rational design of three-dimensional electrospun constructs (3DECs) can lead to striking topographies and tailored shapes of electrospun materials. This new generation of materials is suppressing some of the current limitations of the usual 2D non-woven electrospun fiber mats, such as small pore sizes or only flat shaped constructs. Herein, it is pursued an explanation for the self-assembly of 3DECs based on electrodynamic simulations and experimental validation. It is concluded that the self-assembly process is driven by the establishment of attractive electrostatic forces between the positively charged aerial fibers and the already collected ones, which tend to acquire a negatively charged network oriented towards the nozzle. The *in situ* polarization degree is strengthened by higher amounts of clustered fibers, and therefore the initial high density fibrous regions are the preliminary motifs for the self-assembly mechanism. As such regions increase their *in situ* polarization electrostatic repulsive forces will appear, favoring a competitive growth of these self-assembled fibrous clusters. Highly polarized regions will evidence higher distances between consecutive micro-assembled fibers (MAFs). Different processing parameters – deposition time, electric field intensity, concentration of polymer solution, environmental temperature and relative humidity – were evaluated in an attempt to control material's design.

---

[1] The content present in this Chapter was partially published (Tiago C. Reis et al., Nanoscale, 2013, 5, 7528)

2.1 CHAPTER INTRODUCTION AND THESIS ALIGNEMENT

2.1.1 Chapter Introduction

Nanofabrication, associated or not with self-assembly, has led to a diversity of processing techniques.[1-4] Among them, electrospinning is one of the few techniques that allow the continuous fabrication of nanoscale fibers, generating fibrous constructs with high surface areas.[4, 5] Moreover, electrospun materials are regularly obtained as 2D flat non-woven meshes, evidencing small pore sizes due to their dense fiber packing.[6] Regardless of the successful use of these constructs as nerve agent sensors,[7] supports for ion battery anodes,[8] degradable scaffolds[9] or catalysts,[10] some applications are hindered by the construct's restrictive inner morphology. For instance, 2D fibrous meshes have been recognized as superior scaffolds for tissue engineering due to their unique feature to mimic the extracellular milieu.[11] However, their small pore sizes tend to restrain cellular infiltration and therefore proper tissue regeneration does not occur.[12] In order to promote the presence of larger pores several approaches have been attempted such as incorporation of porogens,[13] co-electrospinning of sacrificial polymers[14] and polymer flow rate variations.[15] Still, the above described methods had led to non-uniform and mechanically brittle 2D non-woven fiber mats, hampering their use in applications where mechanical strength and structural integrity are mandatory.

Recently, a special focus has been given to the production of 3DECs rather than 2D non-woven fiber mats.[16-21] 3DECs represent a new generation of electrospun constructs that aim to offer: (i) novel topographical features, solving issues such as enhanced mass transfer performance, cellular infiltration or energy storage; and (ii) suitable 3D designs, which may be tailored to have a certain shape or volume necessary for case-dependent applications such as the production of implantable devices.[20] These materials are currently produced under two different strategies: post-modification or assembly mechanisms. In post-modification, after the electrospun constructs being manufactured, they are further modified by independent techniques such as modulated femtosecond laser pulses,[16] photopatterning[22] or stacking layered mats.[23] On the other hand, the use of assembly mechanisms relies on taking advantage of electrostatic forces to direct or selfassemble the continuously spun fibers. Direct-assembly mechanisms usually comprise a tailor made collector that distorts the electric field, and hence the fiber deposition only occurs in specific regions leading to 3D constructs that may be patterned[22, 24] or not.[25] Another direct-assembly mechanism is direct-writing, in which due to a short tip-to-collector distance and a fast motion of the collector, complex patterns are possible to be created through a precise fiber deposition.[26] In contrast, self-assembly mechanisms rely on the establishment of electrostatic forces between the already collected fibers and the aerial ones, which leads to a preferential fiber deposition despite the random whipping motion of the continuously processed jet.[18, 19, 27, 28]

While direct-assembled 3DECs are uniform across the construct's thickness, self-assembled 3DECs are dual, that is, the top and bottom topographical properties are different. This spurring advantage leads to the production of surfaces with different properties at the same construct. However, the published literature[19, 28] does not take into consideration such advantages, focusing only on the texturization of the membrane's top side. Moreover, the literature does not converge to a unifying explanation of the self-assembly phenomenon. Thandavamoorthy *et al.*[28] reported self-assembled honeycomb polyurethane nano-fibers, hypothesizing that such structural assembly was due to the electrostatic repulsion established between the collected fibers and the aerial ones. They argued that the *in situ* electrostatic repulsions oblige the incoming fibers to be deposited in nearby conducting regions for easier charge dissipation. Yan *et al.*[19] studied the self-assembly of polyvinyl alcohol (PVA), polyacrylonitrile (PAN) and polyethylene oxide (PEO) fibers. They described self-assembly as a phenomenon that occurs due to a balance between surface tension and repulsion. In contrast, Sun *et al.*[18] developed cone-like polystyrene fiber stacks. They hypothesized that the underlying electrostatic phenomenon that leads to self-assembly is not caused by repulsion, but it is due to electrostatic attraction. Bonino *et al.*[27] also produced cone-like fibrous stacks of alginate-polyethylene oxide, but they supported their conclusions in electrostatic repulsion phenomena. However, they reported that lower humidity hinders the self-assembly mechanism, which is in contrast to what was previously reported by Yan *et al.*.[19] In addition, Yan *et al.*[19] and Thandavamoorthy *et al.*[28] reported that the self-assembly mechanism was possible even when using insulating collectors such as cotton, glass sheets, plastic films and wooden boards. On the other hand, Sun *et al.*[18] reported that the fibers' self-assembly was impossible when using insulating collectors, a result that was validated either by using an insulating poly(methylmethacrylate) (PMMA) collector or by using an electrostatic generator that controlled the discharging process of fibers. In this way, and regarding the potential of these new constructs, the lack of consensus and contradictory scientific evidence, it was pursued a clarification of the self-assembly mechanism in order to master it.

With the purpose to clarify the underlying phenomena, it was exploited the self-assembly of poly(ε-caprolactone) (PCL) electrospun fibers into 3DECs. PCL was chosen as the polymer to be studied because it is a biodegradable and biocompatible polyester with a major interest for tissue engineering applications,[29] a field that can benefit greatly from the use of these microtexturized constructs. Also, PCL has been already successfully electrospun into 2D nonwoven fiber mats,[30-32] which offers a good comparison with the produced 3DECs. To the best of my knowledge, it was the first time that electrodynamic simulations were used to provide an explanation for the self-assembly phenomenon on the production of 3DECs. Special attention was given to the influence of key parameters such as: deposition time, electric field intensity, polymer solution concentration, environmental temperature and relative humidity. Moreover, the conclusions were experimentally validated and extended to other authors' published data.

2.1.2 Thesis Alignment

For the sake of this thesis, in this chapter it is intended to develop innovative highly structured electrospun materials that will be used as substrates for potential wound dressings. According to the advantages reported in Chapter 1, this chapter is dedicated to explore, understand and master the fabrication process of such constructs, allowing the rational design of their properties. Such understanding of the versatile design of these materials, it will allow to tailor their structural properties towards the needs for an ideal wound dressing in future chapters.

The content present in this Chapter was partially published (Tiago C. Reis *et al.*, *Nanoscale*, 2013, 5, 7528), where such article was mainly written to address the findings related to the self-assembly mechanism. Nevertheless, it was my intent to broaden the scope of results and discussion, in order to also include the findings related to the direct-assembly mechanism developed during the R&D activities of my PhD work plan.

2.2 MATERIALS AND METHODS

2.2.1 Preparation of electrospun materials

PCL with an average molecular weight of 65×10^3 g.mol^{-1} was used as received from Sigma-Aldrich. Acetic acid (99.8%, AA) and formic acid (≥ 98%, FA) were also used as received from Riedel-de Haën and Sigma-Aldrich, respectively. Predefined amounts of PCL were dissolved in predefined mixtures of AA and FA. The polymer solutions were magnetically stirred for 4 h at room temperature. The shear viscosities of the solutions were measured at 25 ºC, in a shear range of 1–10^3 s^{-1} using a Bohlin (Gemini HRnan) rotational rheometer equipped with 40 mm cone and plate fixtures. Prior to measuring the shear behavior, a pre-shear was applied to the samples in order to ensure a steady state (**Figure 2A.1**).

Each polymer solution was pumped through a metallic capillary (21 gauge) by the use of a syringe pump (Nexus 6000, Chemyx). The metallic capillary was positively charged by a DC power supplier (Alpha Series II, Brandenburg) and a 25×25 cm ground aluminum plate was vertically displaced. Both the capillary and collector were within a glass sealed box with a controlled surrounding temperature. The glass sealed box also comprised a ventilation system to control the humidity and solvent content in the working atmosphere (**Figure 2.1**). The electrospun patterned features were left to dry in air for 24 h.

2.2.2 Morphological characterization.

The architectural patterned features were analyzed by scanning electron microscopy (SEM). Each sample was displaced on an aluminum stub and sputter coated with gold. A Hitachi S-2400

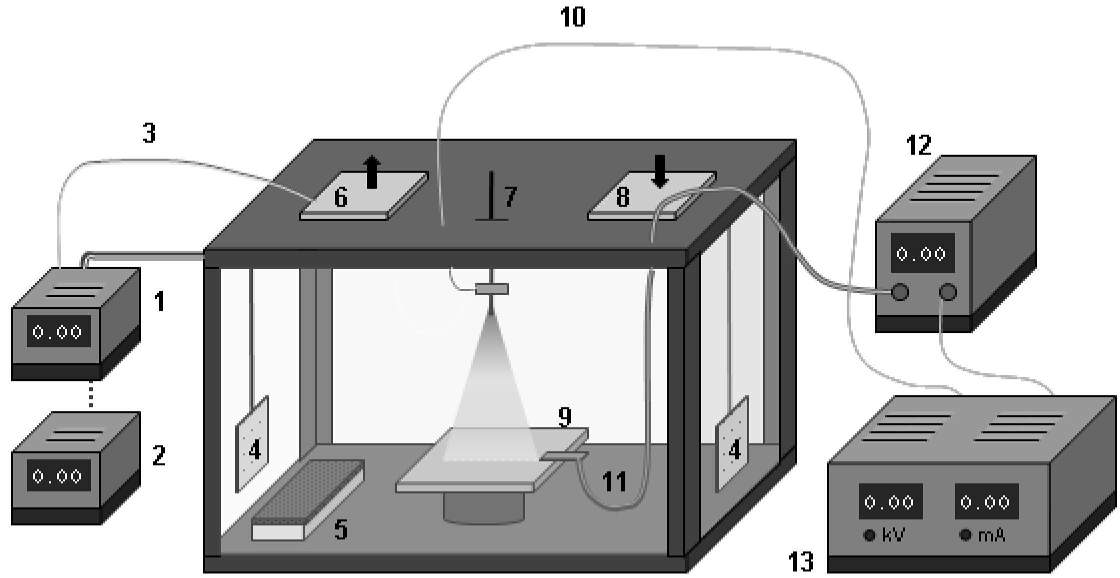

Figure 2.1 Electrospinning apparatus description. **1**, Temperature indicator. **2**, Temperature proportional-integral-derivative controller. **3**, Resistance thermometer Pt100. **4**, Flat heating elements. **5**, Relative humidity controlling agent container (the relative humidity controlling agent was chose accordingly with the experimental conditions and literature guidance). **6**, Outlet flow of the working atmosphere. **7**, Metallic capillary position to pump the polymeric solutions. **8**, Inlet air flow. **9**, Ground aluminum plate. **10**, Contacting tip to charge the metallic capillary. **11**, Contacting tip to ground the aluminum plate. **12**, Multimeter. **13**, DC power supply.

scanning electron microscope at an accelerating voltage set to 20 kV was used to analyze the produced materials. The collected SEM images were analyzed using ImageJ software. Using this software, shapes without a predefined geometry were fitted to each cell and their area, perimeter, major and minor axes were recorded. The major axis is the longest distance between any two points along the selection boundary, while the minor axis is the shorter one. These parameters are described in the literature as Feret's diameter components.[33] Using these parameters, a set of three shape descriptors was employed: circular equivalent diameter (CE Diameter), circularity and aspect ratio. CE Diameter is the diameter of an equivalent circle with the same area as the detected shape under analysis. Circularity gives how closely packed the shape is, while the Aspect Ratio gives a notion of elongation and symmetry about the shape. The equations that described the previous shape descriptors are:

$$\text{CE Diameter} = 2 \times \sqrt{\frac{\text{Area}}{\pi}} \qquad \text{(Equation 2A)}$$

$$\text{Circularity} = \frac{4\pi \times \text{Area}}{\text{Perimeter}^2} \qquad \text{(Equation 2B)}$$

$$\text{Aspect Ratio} = \frac{\text{Major axis}}{\text{Minor axis}} \qquad \text{(Equation 2C)}$$

Each parameter was defined by the cumulative distribution value for 50% (d_{50}) of the population and its span value.

2.2.3 Electrodynamic simulations

The random fiber model was developed in Matlab R2011b, generating six sets of possible fibers (total number of fibers of 600), in which the incremental number of fibers deposited (N) was taken into consideration as a time-driven parameter. Posteriorly, the output scenarios were then transferred into the COMSOL Multiphysics 4.0 and the electric field configuration and intensity were simulated. The considered geometry relies on a box full of air (length = 50 cm; depth = 50 cm; height = 26 cm), which contains a grounded aluminum collector (length = 25 cm; depth = 25 cm; height = 0.1 cm) and a steel tubular nozzle (external diameter = 0.1 cm; internal diameter = 0.07 cm; height = 4 cm). The nozzle-to-collector distance was set at 16 cm and the applied voltage in the nozzle was set at 24 kV, unless otherwise stated. Preference was given to the software material library: air (Air), aluminum (UNS A91050) and steel (UNS S31600). The electrodynamics mathematical simulation was based on the Maxwell's equations for general time-varying fields.

2.3 RESULTS AND DISCUSSION

2.3.1 3DEC morphology

The PCL 3DECs manufactured show a distinct topography compared to the 2D non-woven PCL fiber mats reported in the literature.[30-32] Their topographical difference relies on the presence of a diversity of cells at their top side (**Figure 2.2**). These cells were limited by thick boundary constructs, resulting from the self-assembly of thousands of nanofibers named as MAFs. The observed morphological differences between the top and bottom sides imply that the self-assembly process was not happening from the very first moment. Through macroscopic analysis it was possible to observe a rough surface topography, which resulted from the formation of these cells. However, it was noticed that this roughness tends to decrease in peripheral regions of the collected mat (**Figure 2.3**). Recognizing the importance of having different topographies in the same construct, the static contact angle for each side was determined (**Figure 2.4**). It was possible to verify a distinct glycerol permeation resistance depending on the construct's side, which therefore states the potential use of 3DECs for, as an example, unidirectional mass flux applications.

2.3.2 Electrodynamic simulations

To elucidate the physical phenomena behind the microtexturization development, it was simulated the electric field over the three-dimensional processing space before and during the fiber deposition.

Electric field simulation before the electrospinning process

In all the reported cases of self-assembled 3DECs[18, 19, 27, 28] a stationary collector has been used as also in our setup. To assess the initial influence of the resultant electric field, electrodynamic simulations were previously performed for fiber deposition (**Figure 2.5**). In this initial stage, it was possible to observe that the force lines are vertically displaced according to the collector. However, the electric field intensity is not constant across the collector x- and y-axes. It is 28% stronger in the middle and its intensity profile remains similar even at a height of 1 mm. The field magnitude is related to the inverse square of the distance (Coulomb's law). Therefore, by taking into account this law and since the shortest distance possible is between the center of the collector and the tip of the nozzle, inner regions will sense stronger fields. The high intensity in the collector's center obligates the fiber deposition to occur there initially. Moreover, due to the characteristic whipping and bending motion of electrospun jets,[34] the deposited fibers will form a circular flat mesh. During this process the 2D non-woven mesh spreads towards the peripheral regions. Such observation was also previously verified by Thandavamoorthy *et al.*[28] and Bonino *et al.[27]* A non-equal field intensity across the collector plane will lead to a non-uniform fiber deposition, and therefore to a broad pore size distribution, since the stretching and binding susceptibilities are space dependent (**Figure 2.6**). This observation underlines an important issue for those that are using static collectors, since a wide fiber distribution across the collector is expected to be obtained when these experimental conditions are used. Such a fact will always lead to non-uniform

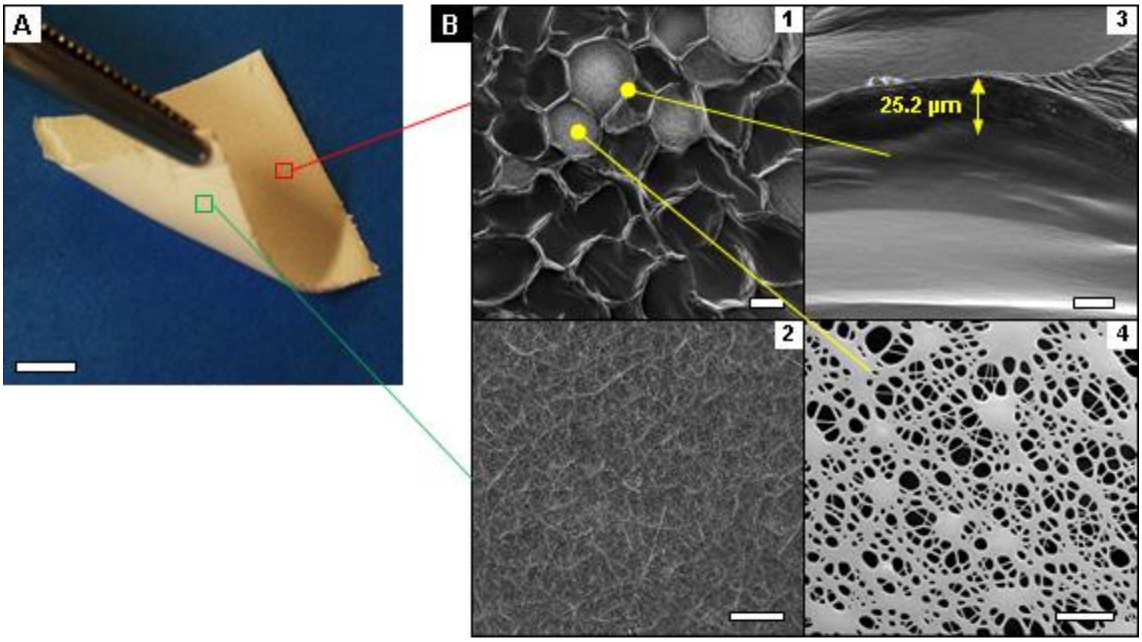

Figure 2.2 Micropatterned electrospun membrane. **A**, Macroscopic image (scale bar = 1 cm). **B**, SEM micrographs from the (B1, scale bar = 200 µm) top side, (B2, scale bar = 100 µm) bottom side, (B3, scale bar = 20 µm) micro-assembled fiber cluster and (B4, scale bar = 3 µm) cell floor. The experimental conditions were 35 wt. % PCL in 40 AA/60 FA (v/v) at 1.5 kV.cm^{-1} (potential difference = 24 kV and nozzle–collector distance = 16 cm) with a flow rate of 0.07 mL.h^{-1}. The surrounding environment was set at 20 ºC and a humidity level of 31 ± 1%.

materials, with a direct impact on the construct's properties (mean pore size: center, (3.5 ± 0.5)×10^2 nm; 3 cm from the center, (3.7 ± 0.6)×10^2 nm; 6 cm from the center, (3.8 ± 0.6)×10^2 nm; 9 cm from the center, (4.8 ± 1.2)×10^2 nm).

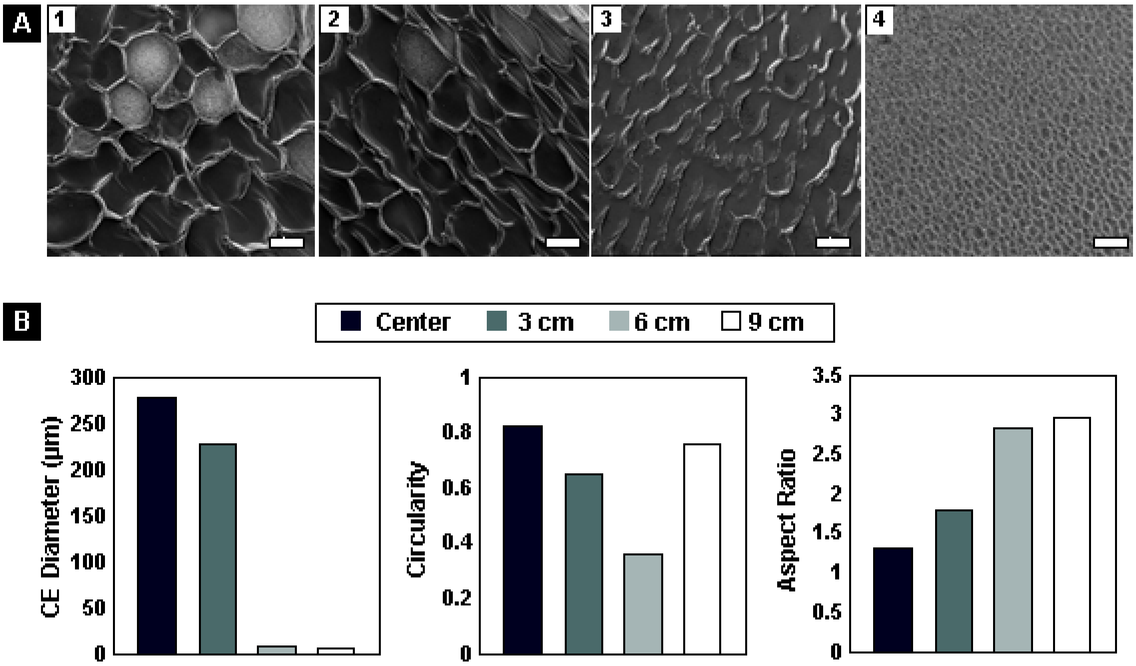

	Span
Center	0.77
3 cm	0.71
6 cm	0.87
9 cm	0.55

	Span
Center	0.35
3 cm	0.86
6 cm	1.08
9 cm	1.20

	Span
Center	1.18
3 cm	0.94
6 cm	1.14
9 cm	1.19

Figure 2.3 Surface roughness and morphology comparison of different localized portions of the same electrospun membrane (35 wt. % PCL in 40AA/60FA at 1.5 kV.cm^{-1} with a flow rate of 0.07 mL.h^{-1}). The surrounding environment was set for 20 ºC and a humidity level of 31 ± 1%. **A,** SEM micrographs (A1) center, (A2) distance from the center of 3 cm, (A3) distance from the center of 6 cm and (A4) distance from the center of 9 cm (scale bar = 200 µm). **B,** Shape analysis and comparison accordingly to CE Diameter, Circularity and Aspect Ratio, showing their span values tabled below each bar chart. The span values were determined as: $(d_{90\%} - d_{10\%})/d_{50\%}$, where $d_{X\%}$ is the cumulative distribution value for X % of the population.

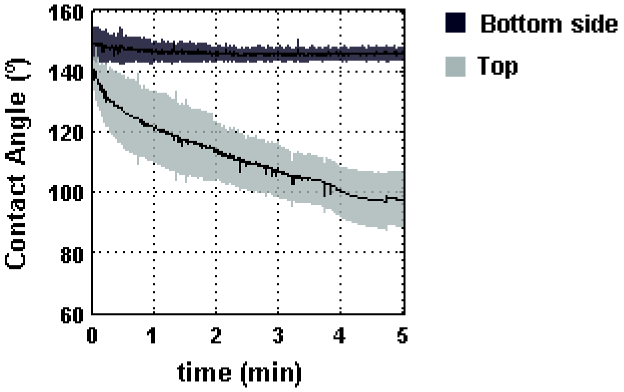

Figure 2.4 Static contact angles assessment. The static contact angles were measured at room temperature by a KSV Goniometer (model CAM 100) by applying the sessile drop method. The used liquid was glycerol (≥ 99.0%, Sigma-Aldrich) whereas each droplet had a volume of 100 µL, while the acquisition time was

extended up to 5 minutes with a frame interval of 300 ms. At least four measurements were carried out per sample and the shown data are averaged values.

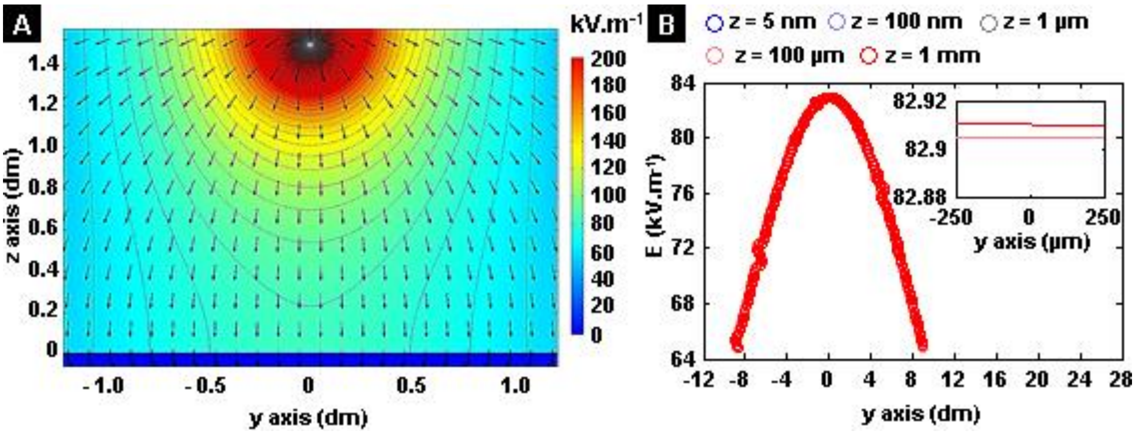

Figure 2.5 Electric field simulation before the fibers deposition. The electric field configuration and intensity was simulated in COMSOL Mutiphysics 4.0. The geometry relies in a box full of air (length = 50 cm; depth = 50 cm; height = 26 cm), whereas within was placed a grounded aluminum collector (length = 25 cm; depth = 25 cm; height = 0.1 cm) and a steel tubular nozzle (external diameter = 0.1 cm; internal diameter = 0.07 cm; height = 4 cm). The nozzle-to-collector distance was set at 15 cm and the applied voltage in the nozzle was set at 24 kV. Preference was given to the software material library: Air (Air), Aluminum (UNS A91050) and steel (UNS S31600). **A**, Electric field configuration and intensity coupled with isolines. **B**, Electric field intensity assessment across de collector x axis between - 9 to + 9 cm, where z states the distance from the collector's plan towards the tip of the nozzle.

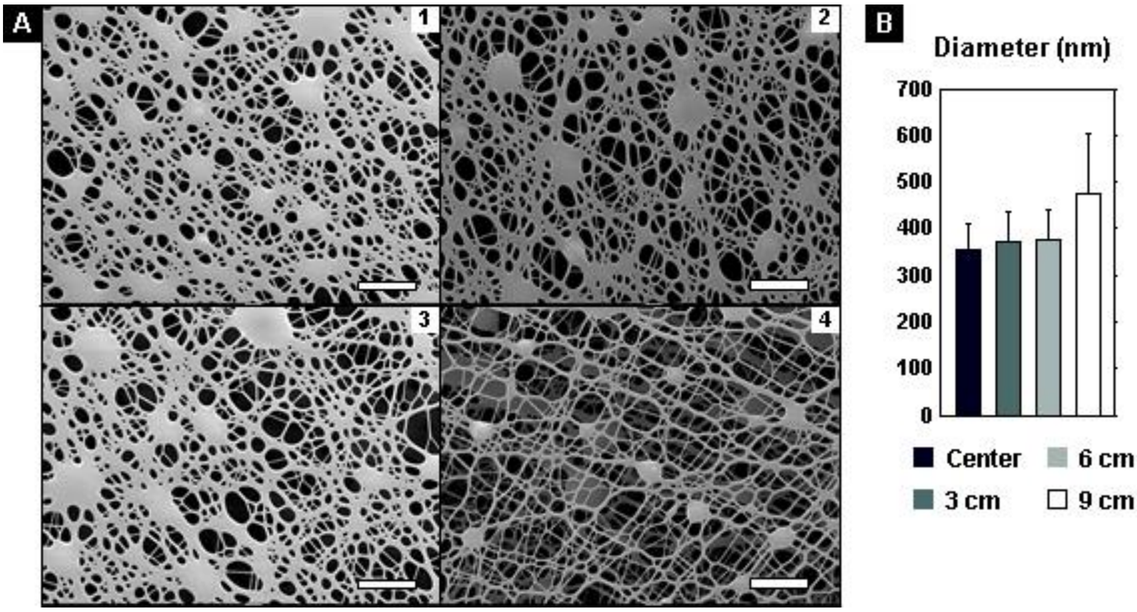

Figure 2.6 Pore size at different localized portions of the same electrospun membrane (35 wt. % PCL in 40AA/60FA at 1.5 kV.cm^{-1} with a flow rate of 0.07 mL.h^{-1}). The surrounding environment was set for 20 ºC and a humidity level of 31 ± 1%. **A**, SEM micrographs (A1) center, (A2) distance from the center of 3 cm, (A3) distance from the center of 6 cm and (A4) distance from the center of 9 cm (scale bar = 3 µm). **B**, Mean diameter comparison.

Initial fiber density, electric field and collector type influence on the collected fibers

Due to the initial random fiber deposition and accumulation, it is clear that the fiber density is not constant across the collector plane, thus leading to the formation of high density fibrous regions

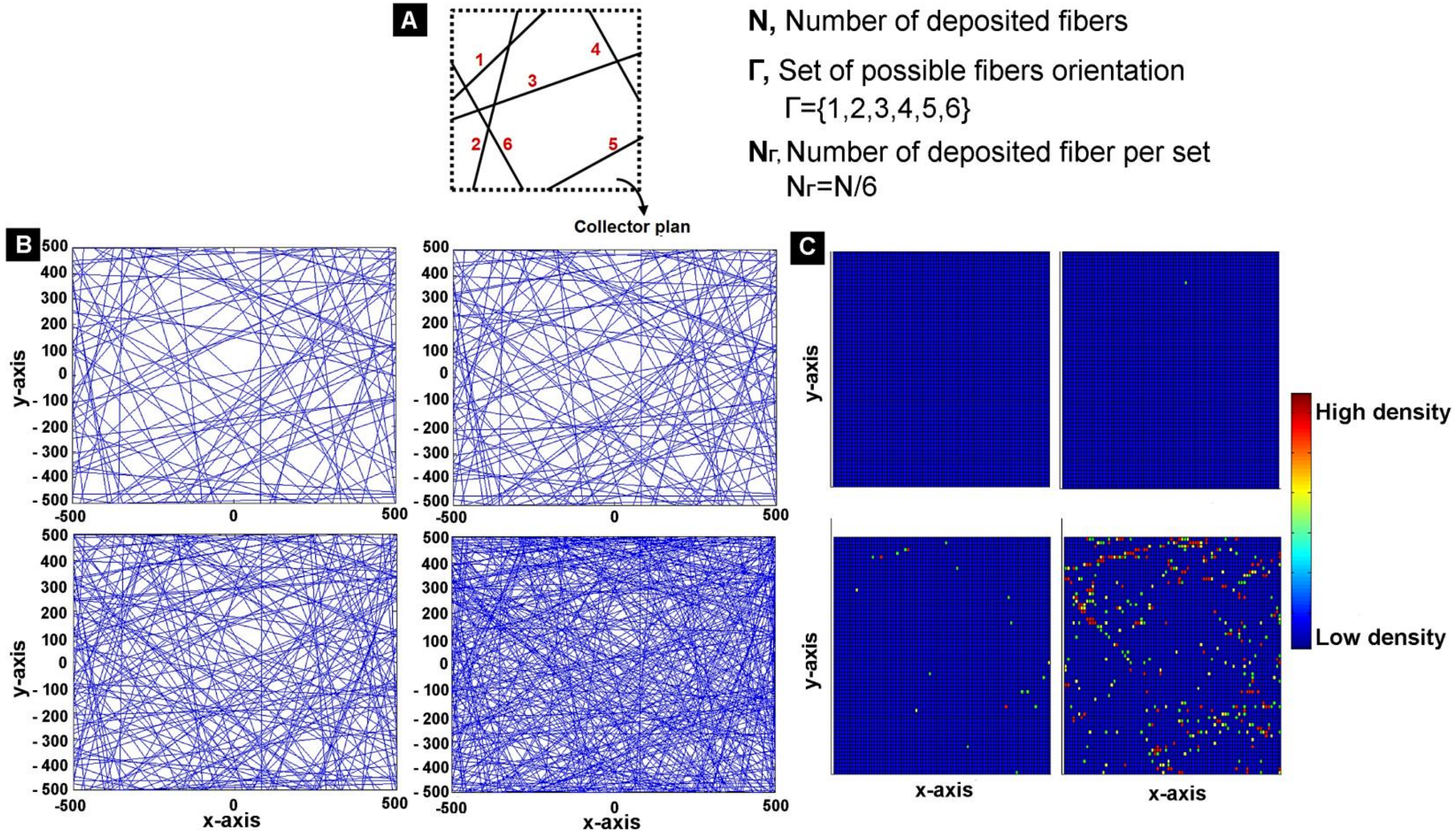

Figure 2.7 Arbitrary fiber deposition in the collector's center. **A**, The random fiber model was developed in Matlab R2011b, generating six sets of possible fibers (Total number of fibers, N=400). The output scenarios were then transferred into the COMSOL Mutiphysics simulation for further studies. **B**, Random fiber deposition, whereas the incremental number of fiber deposited (N) was taken in consideration as a time-driven parameter. **C**, Fiber density representation, whereas the incremental number of fiber deposited (N) was taken in consideration as a time-driven parameter.

(**Figure 2.7**). It was simulated such fiber deposition profile and evaluated its influence on the electric field distribution and intensity (**Figure 2.8**). The highly populated fiber zones were able to slightly distort the electric field, turning it more intense compared to the less dense fibrous zones (Figure 2.8[3]). So far, the published literature has only focused on understanding the electric field influence on the jet spinning process,[4, 5] underestimating the influence of the electric field on the already collected fibers. Thus, it was simulated the fiber–field interaction (**Figure 2.9**). From the simulation it was possible to verify a slight distortion of the electric force lines towards the fiber's surface. After reaching a grounded collector, the electrospun fiber becomes neutral and regarding the present electric field – which continues to be necessary to electrospin further fibers – the collected fiber is then polarized. Due to the polarization phenomenon, the fiber accumulates a negatively charged network towards the positively charged nozzle. Higher amounts of clustered fibers will result in a higher *in situ* polarization degree, and consequently an increased impact on positive aerial fibers will be placed preferentially on these regions driven by electrostatic attraction (Figure 2.8[4]).

Indeed, Theron *et al.*[35] reported that most electrospun fibers were attracted to the sharp edge of a rotating disk, due to a higher field strength compared to the other areas of the collector. Hence, for the self-assembly phenomenon under study, the randomly generated high density fibrous regions are the initial motifs for the self-assembly occurrence. Complementarily, the cumulative and preferential fiber deposition on these fibrous clusters increases continuously the *in situ* polarization degree, boosting the self-assembly mechanism. This phenomenon can be described as a snow ball effect. In agreement, Bonino *et al.*[27] studied the growth evolution of PEO-alginate 3DECs with time, where it is possible to observe the initial formation of small fibrous clusters that turn into complex peaks as time goes by. In agreement, as a side validation experiment, a polymer blend of 70/30 wt. % of PCL and gelatin (Sigma-Aldrich, 300 bloom) 40AA/60FA was electrospun, resulting also in fibrous clusters that turn into complex peaks as time goes by (**Figure 2.10**), a consequence of using polymers with high susceptibility to polarize (in this case, gelatin).

Another issue rose when cross-validating published data was the reported inconsistent scientific observations when using insulating collectors.[18, 19, 28] In our model, in order for the fibers to polarize, such fibers must initially acquire a neutral state when collected. Therefore, it would be expected that by using such a type of collector, the fiber's charge migration is hindered and consequently the self-assembly mechanism cannot happen, which is in contrast to some published reports.[19, 28] Sun *et al.*[18] proved that the discharge of fibers must happen for the self-assembly to occur, otherwise they could not observe the formation of cone-like polystyrene fiber stacks. Looking at the reported apparatus, the insulating collectors used by Yan *et al.*[19] were made of glass, plastic and wood, while the ones used by Thandavamoorthy *et al.*[28] were made of cotton and glass, and the PMMA plate used by Sun *et al.*[18] had a thickness of 5 mm. Despite the poor electric conducting properties of all the above mentioned materials, they are in fact dielectrics, which can be polarized when an intense electric field is applied. For instance, Zhao *et al.*[21] observed that

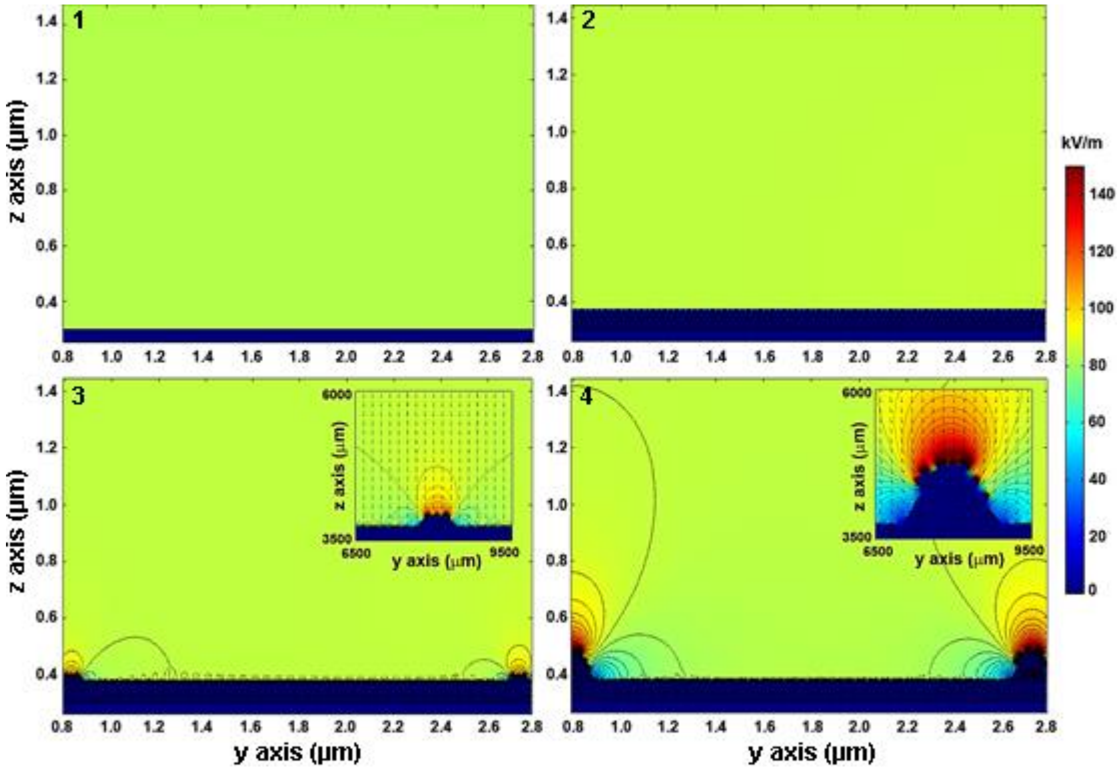

Figure 2.8 Electric field simulation during the electrospinning process. **1**, No fibers deposition. **2**, 2D non-woven fiber mats. Electric field distortion and intensity near: (**3**) a high dense fiber region and (**4**) a grown fibrous cluster. Simulating parameters are fully described in the experimental section.

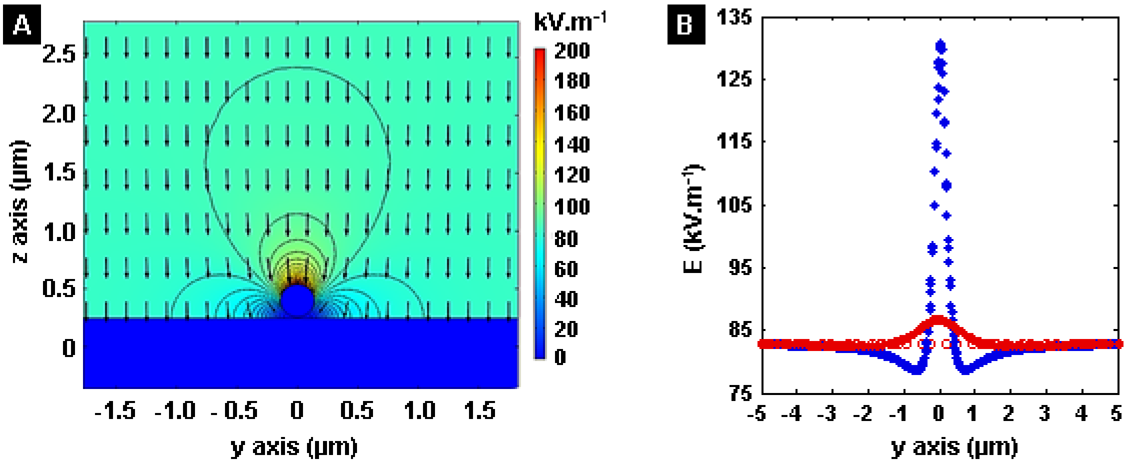

Figure 2.9 Electric field in the presence of one nanofiber. **A**, Orientation and contour lines. **B**, Field intensity in x = 0 plane (No fiber at z=150 nm, ○ blue; No fiber at z = 1 µm, ○ red; One fiber at z = 150 nm, ■ blue; One fiber at z = 150 nm, ■ red). It was simulated the polarization of one nanofiber under an intense electric field. It is possible to observe that a nanofiber can be polarized and can cause a slight distortion of the electric field due to the surface charge accumulation at its surface. Despite the electric field becomes stronger near to the fiber surface, one single fiber does not have a significant impact at higher heights.

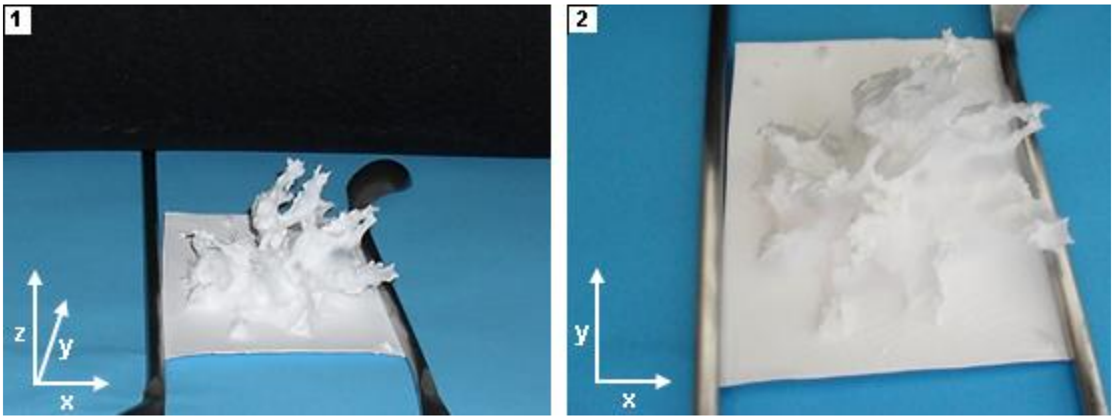

Figure 2.10 Photograph of a fibrous PCL-gelatin cluster that turn into complex peaks as time goes by (70 wt. % PCL /30 wt. % gelatin in 40AA/60FA at 1.5 kV.cm^{-1} with a flow rate of 1.0 mL.h^{-1}). The surrounding environment was set for 20 ºC and a humidity level of 31 ± 1%.

when a gauze was submitted to an intense electric field, negative charge was induced at the gauze's protrusions, favoring the attraction of the incoming positively charged aerial fibers.

The polarization of a dielectric material obliges its charges to segregate according to the electric field orientation, leading to the formation of a superficial negatively charged network at the beginning of the process. In this way, when the positively charged aerial fibers reach the insulating collector, they will become neutral due to the presence of a superficial negatively charged collector, a fundamental condition that fits in our model. It is important to note that the polarization occurs more easily as less work is required during the charge segregation process, which is proportional to the collector's dielectric constant and inverse to its thickness. Summing up, higher dielectric constants or thinner insulating collectors are more prone to be polarized at the same electric field intensity, favoring the formation of a superficial negatively charged network that will neutralize the incoming aerial fibers. Thus, that is why the use of cotton, glass sheets or plastic films does allow the self-assembly mechanism, in contrast to the use of a thick PMMA plate. For instance, despite PMMA and glass having close values for their dielectric constant – PMMA, 3.5;[36] and glass, 3.8;[37] – the used constructs had different thicknesses, and this particularity was crucial to hinder the self-assembly mechanism in the PMMA's case, which had a lower collector's surface polarization.

In this way, and after realizing that dielectric collectors can also guide the fibers deposition, it was envisioned to use already patterned collectors to tailor the random deposition of electrospun materials. Despite metal-based collectors with engraved patterns had also been used for the same end,[38] such substrates are usually rigid (e.g. stainless steel plates) and/or lack on reasonable elasticity (e.g. aluminum foil), an important property for their use on mechanical roller pieces for automated electrospun devices. Instead of having a non-patterned and conductive collector, where preliminary fiber deposition must occur in order to acquire a subsequent polarized fibrous layer, in this strategy, by providing an already patterned dielectric collector, the as soon electrospun fibers will be preferentially deposited directly on the polarized regions of the dielectric substrate used, leading therefore to the copy of the same patterns on the electrospun materials that were engraved on the paper-based collectors. After contacting the polarized collectors, those fibers already deposited will be therefore polarized and attract the positive aerial fibers in a similar fashion as observed previously in the self-assembly process. Since the work for polarization is proportional to the collector's dielectric constant and inverse to its thickness, thin sheets of patterned paper (mainly composed by cellulose, with a reported[39] dielectric constant of 7.6) where utilized as dielectric collectors (**Figure 2.11**) in order to demonstrate the possibility to micropattern electrospun non-woven meshes through direct-assembly.

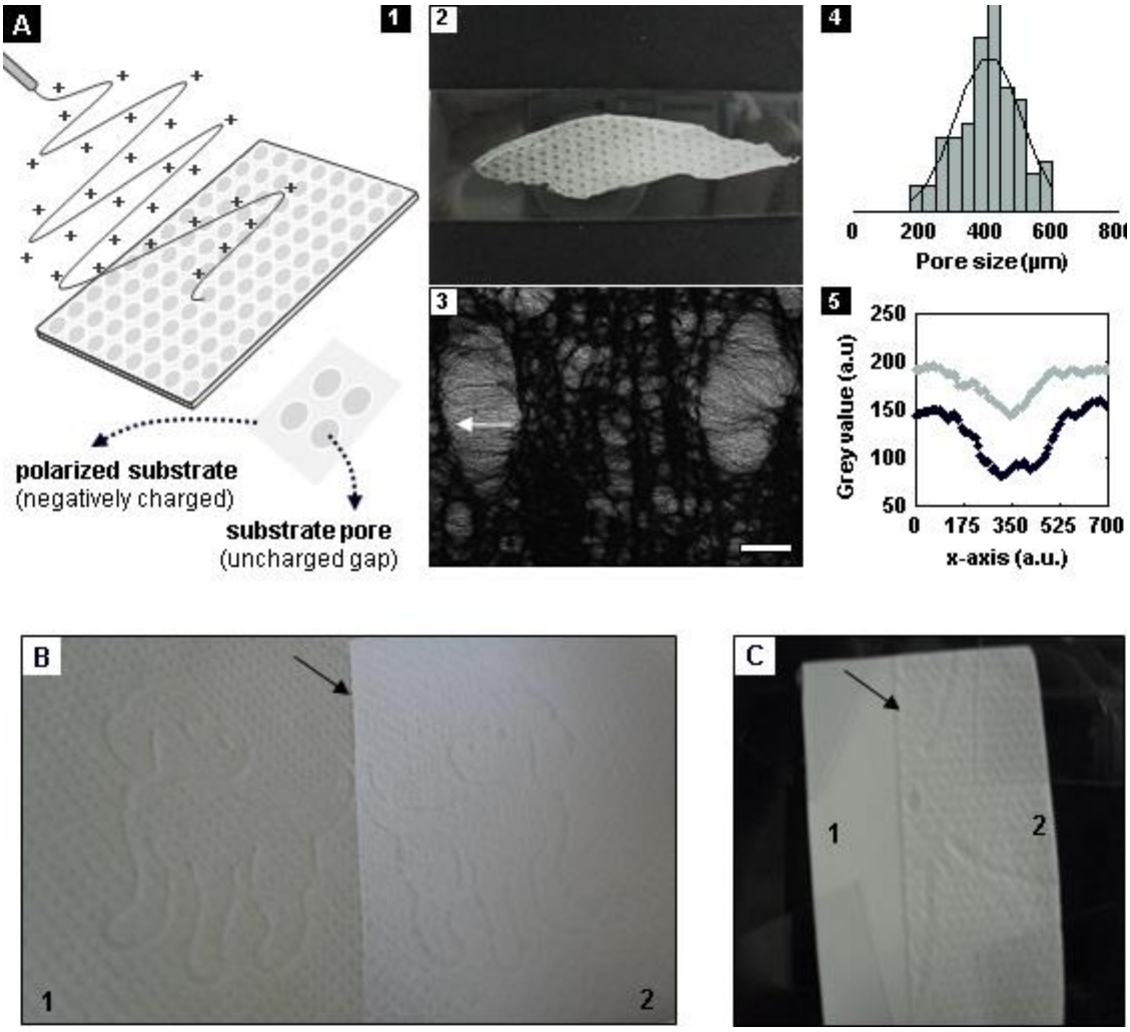

Figure 2.11 Direct-assembly mechanism tested on porous paper-based substrates. **A**, Direct-assembly mechanism using a paper-based substrate with a uniform gap distribution: 1, Scheme of the deposition of the aerial charged electrospun fibers, where the aerial fibers are preferentially deposited on the polarized

substrate due to attractive forces, while bridging the substrate regular gaps forming micropores; 2, Photo of a portion of an electrospun construct collected on the polarized substrate; 3, Micrograph of the previous sample (scale bar = 400 µm). The white arrow shows the main orientation of the electrospun fibers within the micropore established; 4, Micropore size distribution (mean pore size = (4.1 ± 1.0)×10^2 µm); 5, Grey scale intensity across a micropore according to a peripheral micropore (black) and a micropore in the center region of an electrospun mat (grey). Higher values of grey intensity represent denser fiber regions. **B**, Peeling off an electrospun scaffold from a patterned paper-based substrate (1), whereas the peeled off mesh still evidences the imprinted pattern (2). The black arrow denotes the contacting line between the two materials, as the electrospun construct is peeled off. **C**, Electrospun construct where half of the collecting region was covered with aluminum foil (1) and the other half with a patterned paper-based substrate. The black arrow denotes the limiting line between the two used collectors. All the examples correspond to the following experimental conditions: 17 wt. % PCL in 40AA/60FA at 1.5 $kV.cm^{-1}$ with a flow rate of 0.07 $mL.h^{-1}$.

2.3.3 Experimental validation

Influence of parameters: electric field and polymer concentration

In order to experimentally validate the concept of a transition state, from 2D low density fibrous mats up to 3DECs, PCL was electrospun under different periods of time. It was observed that the electrospun constructs have a maximum radius (R_{max}), which is a function of the electric field, polymer solution concentration and production time (**Figure 2.12**). Until the complete coverage of a deposition area with a radius R_{max}, a thin fibrous mesh is produced (**Figure 2.13[1]**). After reaching this threshold, the self-assembly of the incoming electrospun fibers occurs (**Figure 2.13[2,3]**). Progressively, MAFs became thicker which emphasizes the preferential fiber deposition on these paths, and such observation is in agreement with the electrodynamic simulations performed. It is important to notice that the polarization degree of a dielectric material within an electric field can be expressed by the following equation:

$$\mathrm{P} = \varepsilon_0 \times \chi_e \times \mathrm{E} \qquad \text{(Equation 2D)}$$

where P is the dielectric polarization density, ε_0 is the electric permittivity of the free space, χ_e is the electric susceptibility, and E is the electric field intensity.

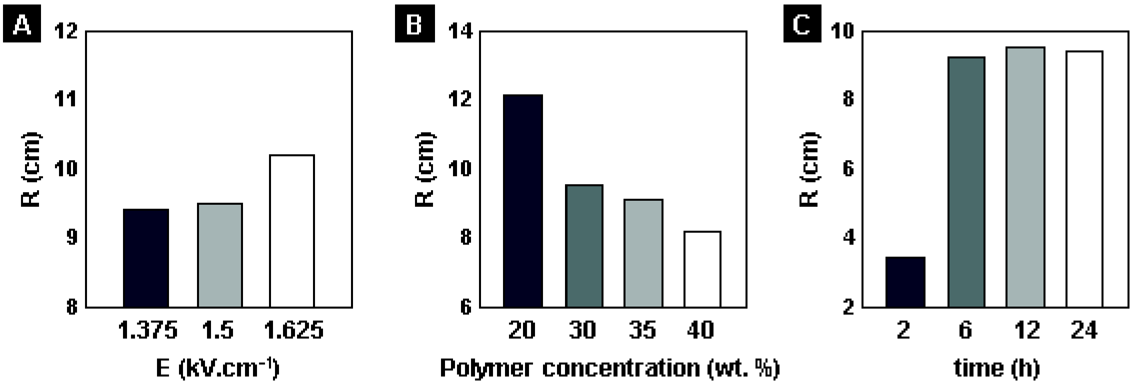

Figure 2.12 Variation of R_{max}: **A**, According to the electric field intensity (35 wt. % PCL in 40AA/60FA with a flow rate of 0.07 $mL.h^{-1}$ during 24 h, the surrounding environment was set for 21 ºC and a humidity level of 31 ± 1%); **B**, According to the polymer concentration (PCL in 40AA/60FA processed at 1.5 $kV.cm^{-1}$ with a flow rate of 0.07 $mL.h^{-1}$ during 24 h, the surrounding environment was set for 21 ºC and a humidity level of 32 ± 1%); **C**, According to the production time (35 wt. % PCL in 40AA/60FA at 1.5 $kV.cm^{-1}$ with a flow rate of 0.07 $mL.h^{-1}$, the surrounding environment was set for 20 ºC and a humidity level of 31 ± 1%).

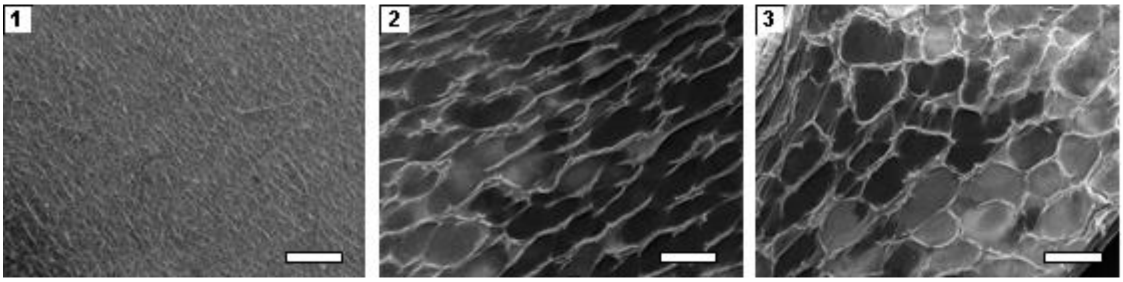

Figure 2.13 Transition state for self-assembly (**1**) 2 h (R_{max} = 3.4 cm), (**2**) 6 h (R_{max} = 9.2 cm) and (**3**) 24 h (R_{max} = 9.5 cm). The experimental conditions were 30 wt. % PCL in 40AA/60FA at 1.5 $kV.cm^{-1}$ (potential difference = 24 kV and nozzle-collector distance = 16 cm) with a flow rate of 0.07 $mL.h^{-1}$. The surrounding environment was set for 21 ºC and a humidity level of 31 ± 1%.

According to Equation 2D, the polarization degree of a material is proportional to the electric field intensity and so different field intensities were applied (**Figure 2.14**). It was possible to observe distinct topographic morphologies in each case, despite all of them presented self-assembled fibers. The electrospun material processed with the higher field intensity led to large (CE Diameter = 439.6 µm) and elongated non-circular cells (aspect ratio = 2.3 and circularity = 0.46). This observation relies on the fact that stronger polarization degrees inhibit the deposition of nearby MAFs due to repulsive electrostatic forces. In this way, despite our main findings being in line with what was observed by Sun *et al.*[18] – which suggests that the assembly mechanism relies on attractive forces – it was also validated the hypothesis wherein the self-assembly mechanism is explained through repulsive forces, proposed by other authors.[19, 27, 28] More accurately, our observations showed that the self-assembly phenomenon is driven by a balance between attractive (the black arrow in **Scheme 2.1**) and repulsive electrostatic forces (the white arrow in Scheme 2.1).

Attractive electrostatic forces are established by the aerial positively charged fibers and the negatively charged ones, which when collected tend to polarize regarding the present electric field. On the other hand, repulsive interactions are present between nearby MAF clusters due to the fact of their like charges (**Figure 2.15**). Since the clustered fibers are negatively charged, the existent repulsion forces will play a major role under short MAF distances. Despite the initial possibility of having nearby high density regions, as the process continues only a few of the initial clusters will prevail regarding the competitive repulsion phenomena. At the same time, the presence of such high polarization on the MAF surfaces does not allow them to bend, appearing as almost straightforward lines (Figure 2.13A3). Hence, these cells will hardly self-close and therefore exhibit higher extended surface areas. Thus, using a less intense electric field should lead to larger cell sizes, higher bending of the MAFs and small aspect ratio of cells as observed in Figure 2.13. In agreement, Yan *et al.*[19] verified that the PEO-made cells' pore size increases with increasing the electrospinning distance or decreasing the applied potential difference, *i.e.*, both strategies lead to less intense electric fields and the repulsion forces were minimized. When a less intense field was applied, the produced cells did not close as well as under more intense field

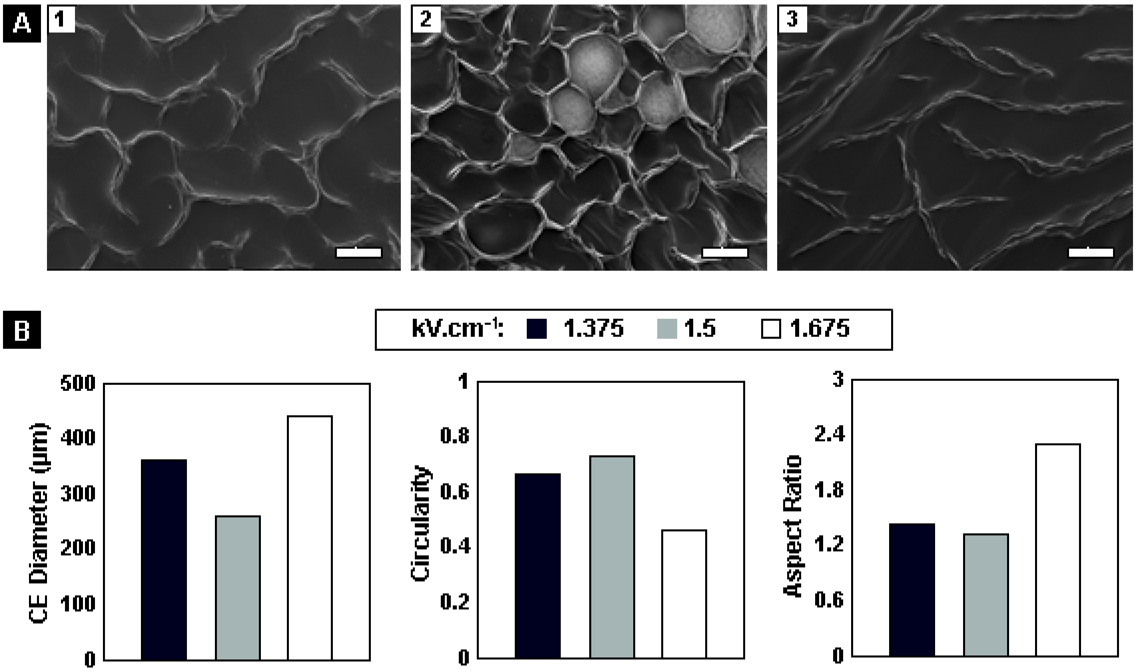

	Span
1.375	0.98
1.5	0.71
1.675	0.85

	Span
1.375	0.52
1.5	0.39
1.675	0.67

	Span
1.375	0.63
1.5	0.67
1.675	0.98

Figure 2.14 Topographic morphology comparison of equivalent electrospun membranes processed under different electric field intensities (35 wt. % PCL in 40AA/60FA with a flow rate of 0.07 mL.h^{-1} during 24 h, the surrounding environment was set for 20 ºC and a humidity level of 31 ± 1%). **A**, SEM micrographs (A1) 1.375 kV.cm^{-1}, (A2) 1.5 kV.cm^{-1} and (A3) 1.625 kV.cm^{-1} (scale bar = 300 µm). **B,** Shape analysis and comparison accordingly to CE Diameter, Circularity and Aspect Ratio, showing their span values tabled below each bar chart. The span values were determined as: $(d_{90\%} - d_{10\%})/d_{50\%}$, where $d_{X\%}$ is the cumulative distribution value for X % of the population.

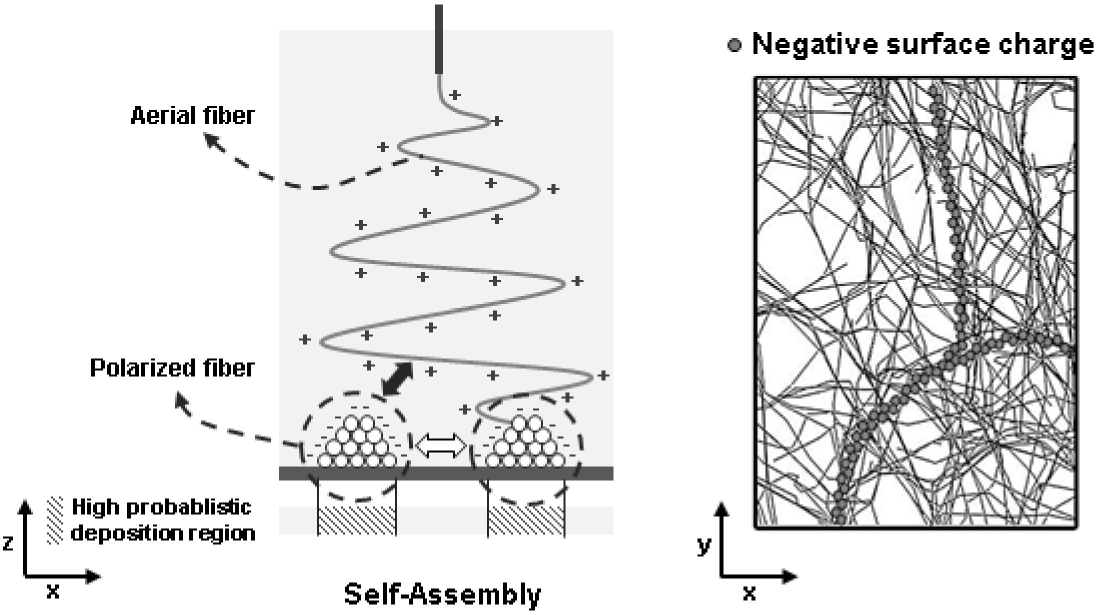

Scheme 2.1 Balance between attractive electrostatic forces (black arrow) and repulsive electrostatic forces (white arrow).

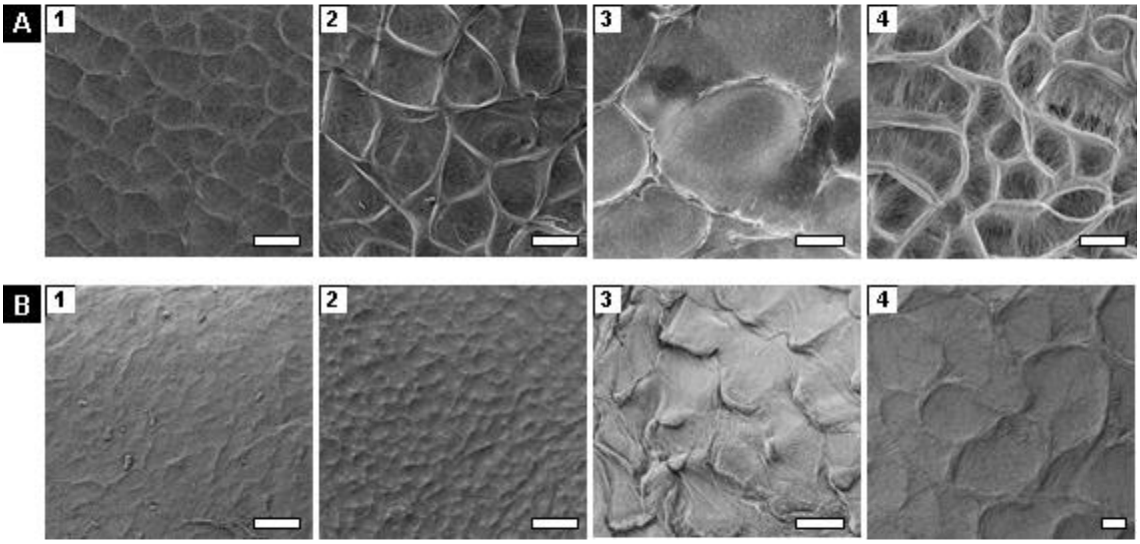

Figure 2.15 Topographic morphology comparison of equivalent electrospun membranes processed under different temperature and humidity levels. **A,B**, SEM micrographs: 20 wt. % PCL in 40AA/60FA at 1.5 kV.cm^{-1} with a flow rate of 0.07 mL.h^{-1} during 24 h and humidity level of 32 ± 1% (A1) T=21 ºC and (A2) T=29 ºC; 30 wt. % PCL in 40AA/60FA at 1.5 kV.cm^{-1} with a flow rate of 0.07 mL.h^{-1} during 24 h and humidity level of 31 ± 1% (A3) T=21 ºC and (A4) T=29 ºC; 30 wt. % PCL in 40AA/60FA with a flow rate of 0.07 mL.h^{-1} during 12 h with a surrounding temperature of 21 ºC and a humidity level of (B1) 42 ± 1%; (B2) 37± 1%; (B3) 34 ± 1%, and (B4) 31 ± 1% (scale bar = 100 µm).

conditions. In this case, the field intensity was not enough to polarize properly the electrospun fibers. Despite the provided higher MAFs' ability to bend under lower polarization degree (aspect ratio = 1.4 and circularity = 0.66), MAFs still show an inability to self-close and consequently present higher surface areas when compared to the 1.5 kV.cm^{-1} case. The 1.375 kV.cm^{-1} case represents the importance of the deposition time in order to obtain self-closed cells (**Figure 2.16**). Since the polarization degree is low, more time is expected to be needed for the assembly of a microtexturized structure. Accumulative deposition times will allow increasing the amount of electrospun fibers. This strategy will favor stronger polarization phenomena even under weak fields, due to a greater amount of processed polymer. Looking at the 1.5 kV.cm^{-1} case, this construct resembles circular cells (aspect ratio = 1.3 and circularity = 0.73). The low span values confirm uniformity in cell morphology of the obtained population.

Further experiments were performed in order to explore the importance of polarization (**Figure 2.17**). One of the followed strategies was to increase the concentration of the polymer solution. Higher concentrations meant higher amounts of polymer to be polarized and consequently enhanced capability to achieve greater polarization degrees. The most concentrated polymer solution (40 wt. %) led to elongated non-circular cells, due to the establishment of strong repulsive electrostatic forces between the self-assembled MAFs. In this case, the MAFs were thicker, a finding that is in line with our hypothesis that higher polarization degrees catalyze the self-assembly process. In contrast, the most diluted solution (20 wt. %) showed a higher bending of the MAFs that favored the production of resembling circular shapes. Since smaller concentrations lead to smaller polymer amounts that were polarized, the surface charge accumulation on the

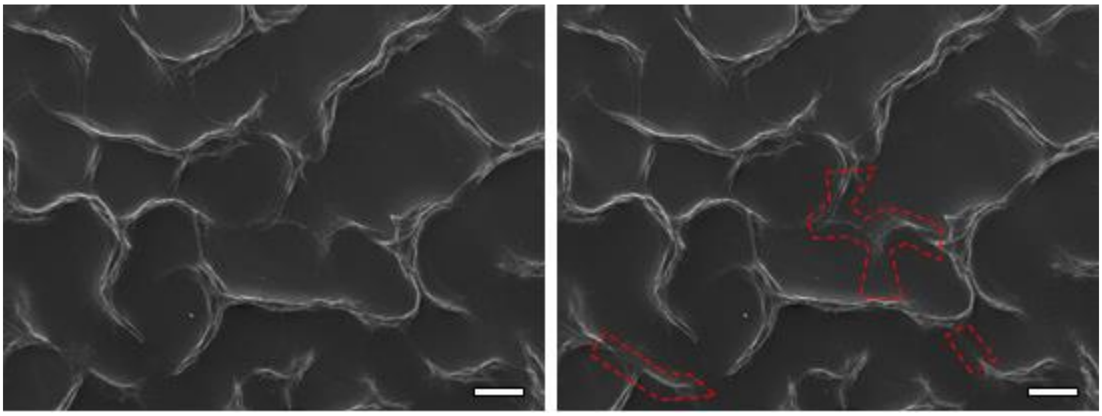

Figure 2.16 Evidence of the need to extend the production time of the electrospun material (35 wt.% PCL in 40AA/60FA processed at 1.375 kV.cm^{-1} with a flow rate of 0.07 mL.h^{-1} during 24 h, the surrounding environment was set for 20 ºC and a humidity level of 31 ± 1%) for the sake of obtaining closed cells. On the right it is highlighted the smooth appearance of new MAFs.

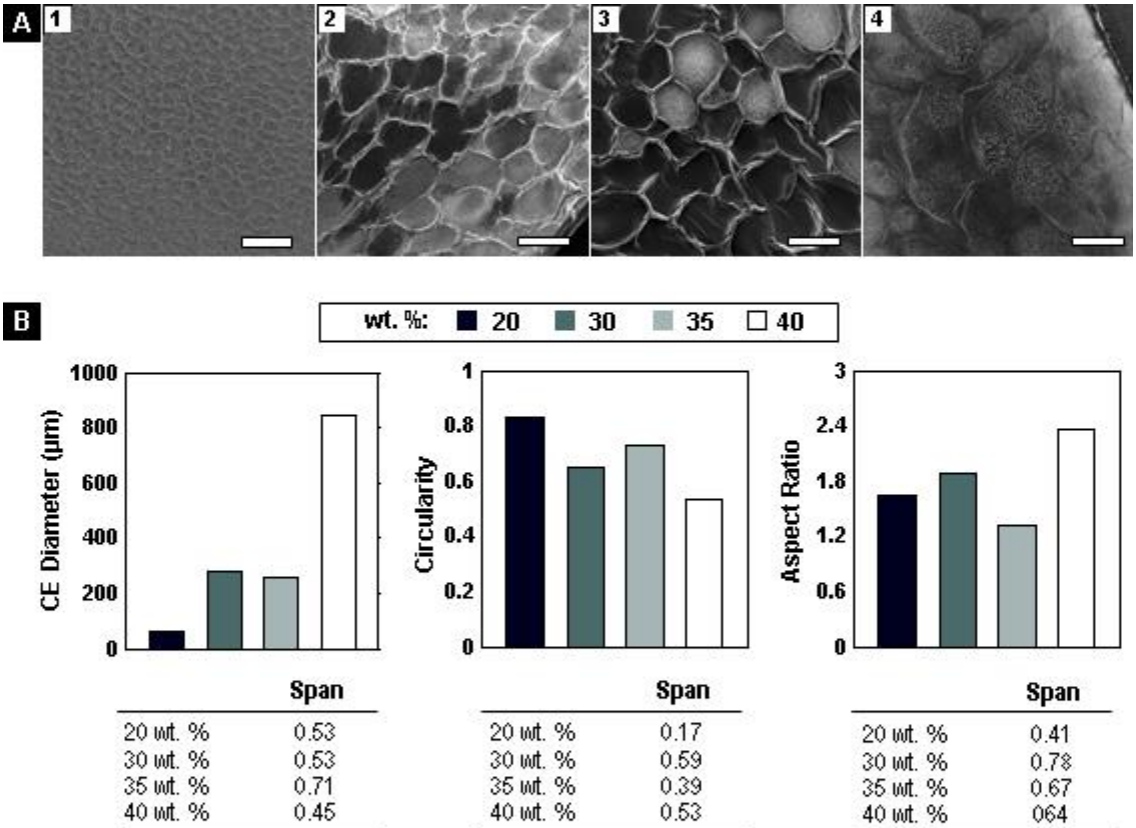

	Span
20 wt. %	0.53
30 wt. %	0.53
35 wt. %	0.71
40 wt. %	0.45

	Span
20 wt. %	0.17
30 wt. %	0.59
35 wt. %	0.39
40 wt. %	0.53

	Span
20 wt. %	0.41
30 wt. %	0.78
35 wt. %	0.67
40 wt. %	064

Figure 2.17 Morphology comparison of electrospun membranes processed from parental polymer solutions with different concentration under the same processing conditions (PCL in 40AA/60FA at 1.5 kV.cm^{-1} during 24 h with a flow rate of 0.07 mL.h^{-1}, the surrounding environment was set for 21 ºC and a humidity level of 32 ± 1%). **A**, SEM micrographs (A1) 20 wt. %, (A2) 30 wt. %, (A3) 35 wt. % and (A4) 40 wt. % (scale bar = 300 µm). **B,** Shape analysis and comparison accordingly to CE Diameter, Circularity and Aspect Ratio, showing their span values tabled below each bar chart. The span values were determined as: ($d_{90\%}$ – $d_{10\%}$)/$d_{50\%}$, where $d_{X\%}$ is the cumulative distribution value for X % of the population.

MAF surfaces is reduced, contributing to the cell self-closing process. Therefore small diameters and less elongated shapes are obtained.

A general overview of the present results will summarize some conclusions. The effect of having a high intensity electric field or a high polymer concentration is similar, since both ways will increase the polarization degree. Hence, it is expected that cells do not self-close and present elongated shapes, showing higher distances between consecutive MAFs. On the other hand, less intense electric fields or diluted polymer solutions will favor the bending of the MAFs and their self-closing process, since lower polarization degrees are achieved.

Influence of parameters: temperature and relative humidity.

It was also studied the influence of the environmental temperature and humidity on the process (Figure 2.15). From the literature, the importance of the environmental temperature during the electrospinning process is known. Higher temperatures are responsible for enhancing the evaporation of the solvent during the jet whipping process. A diminished solvent content will reduce the surface tension of the processed polymer jet, and therefore leads to the production of smooth fibers.[4, 5] As the temperature increases, it was could verify that the electrospun fibers still self-assembled into MAFs providing a fibrous-like cell floor. Such observation contradicts the assumption of the need for having fibres on a wet state in order to promote their self-assembly, whereas, supposedly, the surface tension is mandatory for fiber merging and preferential deposition.20 This fact strengthens our findings in which the preferential fiber deposition is driven by attractive forces only.

Moisture has been associated with the creation of fiber porous surfaces,[40, 41] and with the creation or absence of bead defects.[42] Additionally, the charge amount dissipated by corona discharge increases with increasing humidity, leading to a lower charge density on the fibers.[43, 44] It is also known that moisture increases the conductivity of permeable insulators.[45] Therefore, higher moisture contents are expected to hinder the polarization phenomena, hampering the necessary negative charge network accumulation on the collected fiber surface. Such limited charge accumulation leads to a poor electrostatic driven self-assembly mechanism. it was found out that the control of the humidity content is a key variable to control the maximum surface charge accumulation, and consequently different topographic structures might be achieved.

As the relative humidity (RH) decreases, the electrospun constructs change from 2D flat-meshes to microtexturized 3DECs. This happens since the ease of achieving higher *in situ* polarization degrees is inversely proportional to the moisture content, due to lower charge dissipation into the surrounding medium. Yan *et al.*[19] also studied the influence of the relative humidity on the self-assembly mechanism of PAN, PVA and PEO, where the threshold relative humidity levels for a successful assembly were < 60%, < 45% and < 40% respectively. In addition, Bonino *et al.*[27] verified that the relative humidity threshold for the self-assembly of PEO-alginate fibers was < 60%, whereas alginate was preferentially deposited on the fiber surface. In our case, PCL could self-assemble for a relative humidity lower than 31 ± 1%. Knowing the importance of different moisture levels, it was correlated these observations with our previous conclusions.

As previously simulated, fiber polarization favors the formation of a negatively charged network toward the nozzle. Hence, despite the potential difference used, if a material is more prone to be polarized, the *in situ* polarization is easier to be achieved and a higher impact on field's configuration is then expected. Consequently, due to an easier polarization, the limiting relative humidity threshold for a successful self-assembly can be higher. Permanent dipole–permanent dipole interactions are inherently intermolecular interactions, which contribute to the polymer's polar cohesive energy.[46] When a polymer is polarized, dipolar intermolecular forces are important since they may hinder or facilitate the charge segregation process. Regarding the polymers' Hansen solubility polar parameter (δp) (**Table 2.1**), it is possible to verify that lower δp values demand a lower relative humidity threshold (the polarization phenomenon is harder to achieve and charge dissipation into the surrounding environment must be hindered). On the other hand, higher δp values allow the self-assembly to occur under a broader moisture range. In this way, it was strengthen the idea that self-assembly relies on the collected fibers polarization, extending the conclusion to the findings of the cited authors.[18, 19, 27, 28]

Table 2.1 Hansen solubility polar parameters.

Polymer	Dipolar forces parameter, δ_P (MPa$^{0.5}$)	Reference	RH threshold (%)
PCL	6.2		31
PVA	9.0	44	45
PEO	10.9	44	40
PAN	14.1	44	60
PEO-aliginate [a]	17.9	–	60

[a] Alginate's Hansen solubility polar parameter was estimated from the Hoy's group contribution method.[47]

So as to validate the correlation between δp and the RH threshold, a side validation experiment was conducted where dextran (DEX, Mw ~ 70×10^3 g.mol^{-1}, Sigma-Aldrich) was electrospun under the following experimental conditions: 50 wt. % DEX in Distilled Water at 1.667 kV.cm^{-1} with a flow rate of 0.2 mL.h^{-1}, where the surrounding environment was set for 40 ºC and a humidity level of 24 ± 1%. (**Figure 2.18**). Besides its great importance in many related biopharmaceutical applications,[48] dextran was chosen due to its reported[49] δp value of 24.3 MPa$^{0.5}$, which is above than any of the examples present in Table 2.1. Accordingly to the present rational, such polymer in order to self-assemble would required an RH threshold higher than 60 %. Among all the efforts to optimize the electrospinning process of this polymer, it was not possible to generate the dextran-based fibrous scaffolds for RH thresholds above 45 ± 1%, a fact justified by its great hygroscopic nature (expressed also in its high δp value). Moreover, no evidence of self-assembly was observed for these materials. This finding highlights that high polar polymers are not suitable to self-assemble accordingly with the method herein reported, since the required high RH threshold leads to their solubilization in the collector. Nevertheless, self-assembly of such polymers can still be pursued when they are properly blended with less polar polymers, as reported by Bonino *et al.*[27] and demonstrated in Figure 2.10.

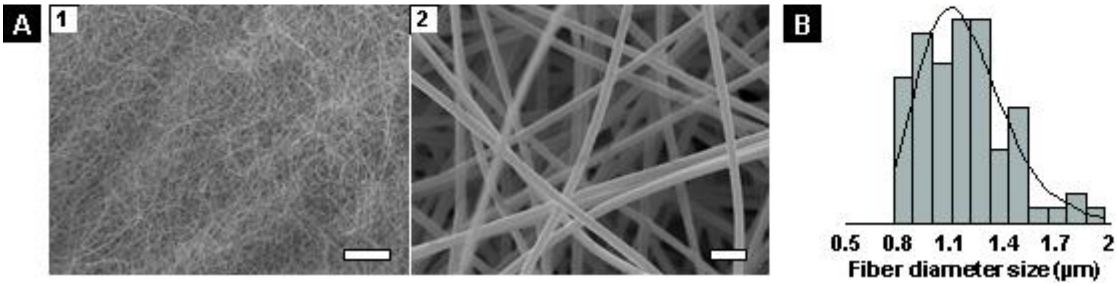

Figure 2.18 Example of a dextran electrospun mesh, where the experimental conditions where defined as follow: 50 wt. % DEX in Distilled Water at 1.667 kV.cm^{-1} with a flow rate of 0.2 mL.h^{-1}, in a surrounding environment set for 40 ºC and a humidity level of 24 ± 1%. **A**, SEM micrographs (1, scale bar = 200 µm; 2, scale bar = 3 µm). **B**, Diameter fiber distribution (mean fiber diameter = 1.17 ± 0.25 µm, the distribution fitter is an Inverse Gaussian distribution / Bayesian Information Criteria = 6.80).

2.4 CONCLUDING REMARKS

3DECs represent a new generation of electrospun materials. Their enhanced topographies, as well as their tailored shapes and volumes, open new avenues for the design of novel materials in fields such as tissue engineering and unidirectional mass flux applications. Among the ways of producing 3DECs, the self-assembly strategy allows us to obtain dual constructs whereas the construct's top and bottom sides are topographically different.

Regarding the literature, there is a lack of consensus on explaining how the self-assembly process occurs. Therefore, it was pursued an explanation for this phenomenon. By coupling the information retained through simulations and experimental data, it was concluded that the self-assembly mechanism relies on a balance between attractive and repulsive electrostatic forces. Initially, the electrospun fibers form a flat mesh while high density fiber regions are favored due to a random fiber deposition. From the moment that the fibers reach the grounded collector, their charges are conducted away turning these electrospun elements neutral. However, the necessary electric field to continuously electrospin new fibers will polarize the already collected ones. Such fibers acquire a negatively charged network oriented toward the nozzle, which will attract the positive incoming aerial and disordered fibers towards their position. This *in situ* polarization degree is strengthened by higher amounts of clustered fibers, and therefore the initial high density fibrous regions are the preliminary motifs for the self-assembly mechanism. As such regions increase their *in situ* polarization electrostatic repulsive forces will appear, favoring a competitive growth of these self-assembled fibrous clusters. Highly polarized regions will evidence higher distances between consecutive MAFs.

It was also verified that very intense fields or high concentrated solutions favor strong polarization degrees and the MAFs cannot self-close, appearing as almost straightforward lines. On the other hand, weak fields or diluted polymer solutions allow a higher bending of the MAFs that contributes to the production of resembling circular-like cells. By tuning the *in situ* polarization, by controlling the electric field intensity, time of production, polymer solution concentration, environmental temperature and relative humidity, it is possible to microtexturize electrospun mats that may allow the rational design of novel energy storage/guidance constructs, implantable devices and tailored filters.

2.5 CHAPTER REFERENCES

[1] Leong TG, Zarafshar AM, Gracias DH. Three-Dimensional Fabrication at Small Size Scales. Small 2010;6:792-806.

[2] Liu TB, Burger C, Chu B. Nanofabrication in polymer matrices. Prog Polym Sci 2003;28:5-26.

[3] Rogers JA. Slice and dice, peel and stick: Emerging methods for nanostructure fabrication. Acs Nano 2007;1:151-3.

[4] Greiner A, Wendorff JH. Electrospinning: A Fascinating Method for the Preparation of Ultrathin Fibers. Angewandte Chemie International Edition 2007;46:5670-703.

[5] Bhardwaj N, Kundu SC. Electrospinning: A fascinating fiber fabrication technique. Biotechnol Adv 2010;28:325-47.

[6] Soliman S, Sant S, Nichol JW, Khabiry M, Traversa E, Khademhosseini A. Controlling the porosity of fibrous scaffolds by modulating the fiber diameter and packing density. J Biomed Mater Res A 2011;96A:566-74.

[7] Kwon OS, Park SJ, Lee JS, Park E, Kim T, Park HW, et al. Multidimensional Conducting Polymer Nanotubes for Ultrasensitive Chemical Nerve Agent Sensing. Nano Lett 2012;12:2797-802.

[8] Hwang TH, Lee YM, Kong BS, Seo JS, Choi JW. Electrospun core-shell fibers for robust silicon nanoparticle-based lithium ion battery anodes. Nano Lett 2012;12:802-7.

[9] Grafahrend D, Heffels KH, Beer MV, Gasteier P, Moller M, Boehm G, et al. Degradable polyester scaffolds with controlled surface chemistry combining minimal protein adsorption with specific bioactivation. Nature materials 2011;10:67-73.

[10] Krogman KC, Lowery JL, Zacharia NS, Rutledge GC, Hammond PT. Spraying asymmetry into functional membranes layer-by-layer. Nature materials 2009;8:512-8.

[11] Vaquette C, Cooper-White JJ. Increasing electrospun scaffold pore size with tailored collectors for improved cell penetration. Acta Biomater 2011;7:2544-57.

[12] Zhang LJ, Webster TJ. Nanotechnology and nanomaterials: Promises for improved tissue regeneration. Nano Today 2009;4:66-80.

[13] Wright LD, Andric T, Freeman JW. Utilizing NaCl to increase the porosity of electrospun materials. Mat Sci Eng C-Mater 2011;31:30-6.

[14] Baker BM, Gee AO, Metter RB, Nathan AS, Marklein RA, Burdick JA, et al. The potential to improve cell infiltration in composite fiber-aligned electrospun scaffolds by the selective removal of sacrificial fibers. Biomaterials 2008;29:2348-58.

[15] Rnjak-Kovacina J, Wise SG, Li Z, Maitz PKM, Young CJ, Wang YW, et al. Tailoring the porosity and pore size of electrospun synthetic human elastin scaffolds for dermal tissue engineering. Biomaterials 2011;32:6729-36.

[16] Jenness NJ, Wu YQ, Clark RL. Fabrication of three-dimensional electrospun microstructures using phase modulated femtosecond laser pulses. Mater Lett 2012;66:360-3.

[17] Ng R, Zang R, Yang KK, Liu N, Yang ST. Three-dimensional fibrous scaffolds with microstructures and nanotextures for tissue engineering. Rsc Adv 2012;2:10110-24.

[18] Sun B, Long YZ, Yu F, Li MM, Zhang HD, Li WJ, et al. Self-assembly of a three-dimensional fibrous polymer sponge by electrospinning. Nanoscale 2012;4:2134-7.

[19] Yan GD, Yu J, Qiu YJ, Yi XH, Lu J, Zhou XS, et al. Self-Assembly of Electrospun Polymer Nanofibers: A General Phenomenon Generating Honeycomb-Patterned Nanofibrous Structures. Langmuir 2011;27:4285-9.

[20] Zhang DM, Chang J. Electrospinning of Three-Dimensional Nanofibrous Tubes with Controllable Architectures. Nano Lett 2008;8:3283-7.

[21] Zhao S, Zhou Q, Long YZ, Sun GH, Zhang Y. Nanofibrous patterns by direct electrospinning of nanofibers onto topographically structured non-conductive substrates. Nanoscale 2013;5:4993-5000.

[22] Sundararaghavan HG, Metter RB, Burdick JA. Electrospun Fibrous Scaffolds with Multiscale and Photopatterned Porosity. Macromol Biosci 2010;10:265-70.

[23] Srouji S, Kizhner T, Suss-Tobi E, Livne E, Zussman E. 3-D Nanofibrous electrospun multilayered construct is an alternative ECM mimicking scaffold. J Mater Sci-Mater M 2008;19:1249-55.

[24] Lavielle N, Hebraud A, Mendoza-Palomares C, Ferrand A, Benkirane-Jessel N, Schlatter G. Structuring and Molding of Electrospun Nanofibers: Effect of Electrical and Topographical Local Properties of Micro-Patterned Collectors. Macromol Mater Eng 2012;297:958-68.

[25] Blakeney BA, Tambralli A, Anderson JM, Andukuri A, Lim DJ, Dean DR, et al. Cell infiltration and growth in a low density, uncompressed three-dimensional electrospun nanofibrous scaffold. Biomaterials 2011;32:1583-90.

[26] Lee J, Lee SY, Jang J, Jeong YH, Cho DW. Fabrication of Patterned Nanofibrous; Mats Using Direct-Write Electrospinning. Langmuir 2012;28:7267-75.

[27] Bonino CA, Efimenko K, Jeong SI, Krebs MD, Alsberg E, Khan SA. Three-Dimensional Electrospun Alginate Nanofiber Mats via Tailored Charge Repulsions. Small 2012;8:1928-36.

[28] Thandavamoorthy S, Gopinath N, Ramkumar SS. Self-assembled honeycomb polyurethane nanofibers. J Appl Polym Sci 2006;101:3121-4.

[29] Woodruff MA, Hutmacher DW. The return of a forgotten polymer-Polycaprolactone in the 21st century. Prog Polym Sci 2010;35:1217-56.

[30] Martins A, Pinho ED, Faria S, Pashkuleva I, Marques AP, Reis RL, et al. Surface Modification of Electrospun Polycaprolactone Nanofiber Meshes by Plasma Treatment to Enhance Biological Performance. Small 2009;5:1195-206.

[31] Moghe AK, Hufenus R, Hudson SM, Gupta BS. Effect of the addition of a fugitive salt on electrospinnability of poly(epsilon-caprolactone). Polymer 2009;50:3311-8.

[32] Van der Schueren L, De Schoenmaker B, Kalaoglu OI, De Clerck K. An alternative solvent system for the steady state electrospinning of polycaprolactone. Eur Polym J 2011;47:1256-63.

[33] Merkus HG. Particle Size Measurements Fundamentals, Practice, Quality Introduction: Springer; 2009.

[34] Sun YF, Zeng YC, Wang XH. Three-Dimensional Model of Whipping Motion in the Processing of Microfibers. Ind Eng Chem Res 2011;50:1099-109.

[35] Theron A, Zussman E, Yarin AL. Electrostatic field-assisted alignment of electrospun nanofibres. Nanotechnology 2001;12:384-90.

[36] Dusek K, Joanny JF, Berret JF. Polymer Characterization: Rheology, Laser Interferometry, Electrooptics: Springer; 2010.

[37] Minges ML, Committee AIH. Electronic Materials Handbook: Packaging: Asm International; 1989.

[38] Zander N. Hierarchically Structured Electrospun Fibers. Polymers 2013;5:19.

[39] Stoops WN. The Dielectric Properties of Cellulose. Journal of the American Chemical Society 1934;56:1480-3.

[40] Casper CL, Stephens JS, Tassi NG, Chase DB, Rabolt JF. Controlling surface morphology of electrospun polystyrene fibers: Effect of humidity and molecular weight in the electrospinning process. Macromolecules 2004;37:573-8.

[41] Pai CL, Boyce MC, Rutledge GC. Morphology of porous and wrinkled fibers of polystyrene electrospun from dimethylformamide. Macromolecules 2009;42:2102-14.

[42] Tripatanasuwan S, Zhong ZX, Reneker DH. Effect of evaporation and solidification of the charged jet in electrospinning of poly(ethylene oxide) aqueous solution. Polymer 2007;48:5742-6.

[43] Kalayci VE, Patra PK, Kim YK, Ugbolue SC, Warner SB. Charge consequences in electrospun polyacrylonitrile (PAN) nanofibers. Polymer 2005;46:7191-200.

[44] Li D, Ouyang G, McCann JT, Xia YN. Collecting electrospun nanofibers with patterned electrodes. Nano Lett 2005;5:913-6.

[45] Bailey AG. The charging of insulator surfaces. J Electrostat 2001;51:82-90.

[46] Hansen CM. Hansen Solubility Parameters: A User's Handbook: CRC Press; 1999.

[47] Vay K, Scheler S, Friess W. Application of Hansen solubility parameters for understanding and prediction of drug distribution in microspheres. Int J Pharmaceut 2011;416:202-9.

[48] Puppi D, Chiellini F, Piras AM, Chiellini E. Polymeric materials for bone and cartilage repair. Prog Polym Sci 2010;35:403-40.

[49] Antoniou E, Alexandridis P. Polymer conformation in mixed aqueous-polar organic solvents. Eur Polym J 2010;46:324-35.

3

Three-Dimensional Multilayered Fibrous Constructs for Wound Healing Applications

SUMMARY[1]

Electrospun materials are promising scaffolds due to their light-weight, high surface-area and low-cost fabrication, however, such scaffolds are commonly obtained as ultrathin two-dimensional non-woven meshes, lacking on topographical specificity and surface side-dependent properties. Herein, it is reported the production of bioinspired three-dimensional fibrous materials with an asymmetrical inner structure and engineered surfaces. The manufactured constructs evidence fibrous-based microsized conical protrusions [length: $(9.5 \pm 2.9)\times10^2$ µm; width: $(3.8 \pm 0.8)\times10^2$ µm] at their top side, with a median peak density of 73 peaks.cm^{-2}, while their bottom side resembles to a non-woven mesh commonly observed in the fabrication of two-dimensional electrospun materials. Regarding their thickness (3.7 ± 0.1 mm) and asymmetric fibrous inner architecture, such materials avoid external liquid absorption while promoting internal liquid uptake. Nevertheless, such constructs also observed the high porosity (89.9%) and surface area (1.44 m^2.g^{-1}) characteristic of traditional electrospun mats. Spray layer-by-layer assembly is used to effectively coat the structurally complex materials, allowing to complementary tailor features such water vapor transmission, swelling ratio and bioactive agent release. Tested as wound dressings, the novel constructs are capable of withstanding $(11.0 \pm 0.3)\times10^4$ kg.m^{-2} even after 14 days of hydration, while actively promote wound healing (90 ± 0.5 % of wound closure within 48 hours) although avoiding cell adhesion on the dressings for a painless removal.

---

[1] The content present in this chapter was partially published (Tiago C. Reis et al., Biomater. Sci., 2016, 4, 319-330)

3.1 CHAPTER INTRODUCTION AND THESIS ALIGNEMENT

3.1.1 Chapter Introduction

The importance of construct topography in applications ranging from anisotropic wetting[1] and antireflection[2] to stem cell differentiation[3, 4] and tissue engineering,[5] has driven multidisciplinary teams to develop a number of novel scaffolds fabrication methods.[6-9] Electrospinning is a versatile means of producing nano- and micro-sized fibers to assemble materials with controlled orientation and fiber density,[10-12] being currently developed towards new methods to enhance yield and the rate of fabrication.[13] However, even the current electrospinning-based approaches have only been used to create two-dimensional electrospun constructs (2DECs). The promising combination of controlled three-dimensional topography, with the existing benefits of electrospun scaffolds, offers new opportunities for the production of fibrous materials with superior structural and surface properties. Three-dimensional electrospun constructs (3DECs) with tailored topographies can be obtained by either post-construction modification or assembly-based mechanisms. The former consists in the use of independent techniques to alter the as-spun materials, such as modulated femtosecond laser pulses[14] or photopatterning.[15] Such methods rely on surface ablation or sacrificial removal of construct material, a strategy that is undesirable when spinning high-value and perishable materials. Controlling topography via process-based assembly mechanisms, in contrast, harnesses the electrostatic forces used to guide the fiber deposition, by either using tailored grounded collectors or by inducing the self-organization of fibers.[16] Self-organization also has the unique feature of allowing for z-axis asymmetric fiber deposition, wherein the bottom and top sides of the same scaffold can show different structural features (e.g. fiber alignment, pore size, etc.). The bottom side of the construct is commonly composed of randomly distributed fibers, similar to the case of many 2D non-woven electrospun meshes, and the materials top side can be tuned into fibrous macro-assembled structures such as stacks,[17, 18] honey-comb patterns[19, 20] or yarns.[21] It has been previously described the mechanism underlying this microstructuring process as a result of the in situ polarization of collected fibers due to the strong electric field applied, favoring the continuous electrostatic attraction of incoming fibers to specific regions.[22] The use of strong electric fields for electrospinning polymer blends or doped solutions however, causes charged species within the material to separate due to electrophoretic phenomena,[21, 23] driving the anionic elements to the outer surface of the fiber. This process causes poor intermolecular blending, which affects mechanical strength,[24] electrical conductivity[25] and drug release profiles.[26] Thus, the process conditions used to induce the assembly of structures constrain the potential of 3DECs in several applications, especially in cases where incorporation of charged elements is desired.

Layer-by-layer (LbL) assembly technique is a simple and robust method for the incorporation of material into ultra-thin polymer coatings which has been used for applications ranging from surface modification to drug delivery,[27, 28] being an aqueous process that relies on the alternating adsorption of material species through complementary interactions.[29] This method has been used to coat a wide range of materials with complex geometries including bone implants and scaffolds,[30] bandages[31] and microneedles,[32, 33] made of a diverse array of materials such as stainless steel, titanium or polystyrene. The LbL technique allows for high material incorporation (10-40 wt.%) of sensitive therapeutic compounds (e.g. cytokines, RNA, or DNA) with nanoscale precision, a striking advantage in comparison with other strategies such as polymer blending,[34] often used to produce functional electrospun fibers.

In the context of soft tissue wound care, the proposed approach offers the potential for a number of unique benefits by combining these methods. Taking a cue from how nature facilitates interaction with soft tissues, namely using prominent protrusions (e.g. spiny-backed orb-weavers, Gasteracantha cancriformis), it is created for the first time electrospun constructs with enhanced 3D microprotrusions (**Figure 1**). Such structures are beneficial for wound care, since they are characterized by having higher friction factors and Nusselt numbers,[35] which improve mechanical interlocking with soft tissues, heat dissipation and increased contact with the wound. Moreover, the unique reported manufacturing process allows to generate dressings that are impermeable to external liquid-form sources of infection (e.g. sweat), while keeping an inner structure suitable to wound exudate uptake and balanced moisture retention. The generated scaffolds are still characterized by the traditional high porosity and tortuosity of two-dimensional electrospun constructs, a key aspect to allow the required gaseous exchange during the wound healing process. Functionalizing these biologically inspired 3DECs with LbL films provides a means to modulate surface-tissue interaction, avoiding cellular adhesion on the dressings and therefore contributing for the dressing's painless removal, while continuously releasing active agents for the wounded tissue regeneration, as well as it allows to alter the transport and physical characteristics of the electrospun scaffolds. In this work, it is described the combination of cutting-edge electrospinning techniques and LbL functionalization to generate biologically inspired three-dimensional multilayered electrospun constructs, a methodology that can be used to enhance potential two-dimensional fibrous materials[36-38] or current production methodologies[39-43] with no further complexity.

3.1.2 Thesis Alignment

In this chapter, it is aimed to develop a potential wound dressing consisting in a three-dimensional electrospun material, which has asymmetric structural and physicochemical properties specially designed for the wound healing cause. In addition to their increased contact area with the wounded tissue, the scaffolds are functionalized with the best LbL formulation of the previous chapter. *In vitro* assessment of the potential impact in the wounded environment, as well as in the final dressing properties is further explored. The content present in this chapter was partially published (Tiago C. Reis *et al.*, *Biomater. Sci.*, 2016, 4, 319-330).

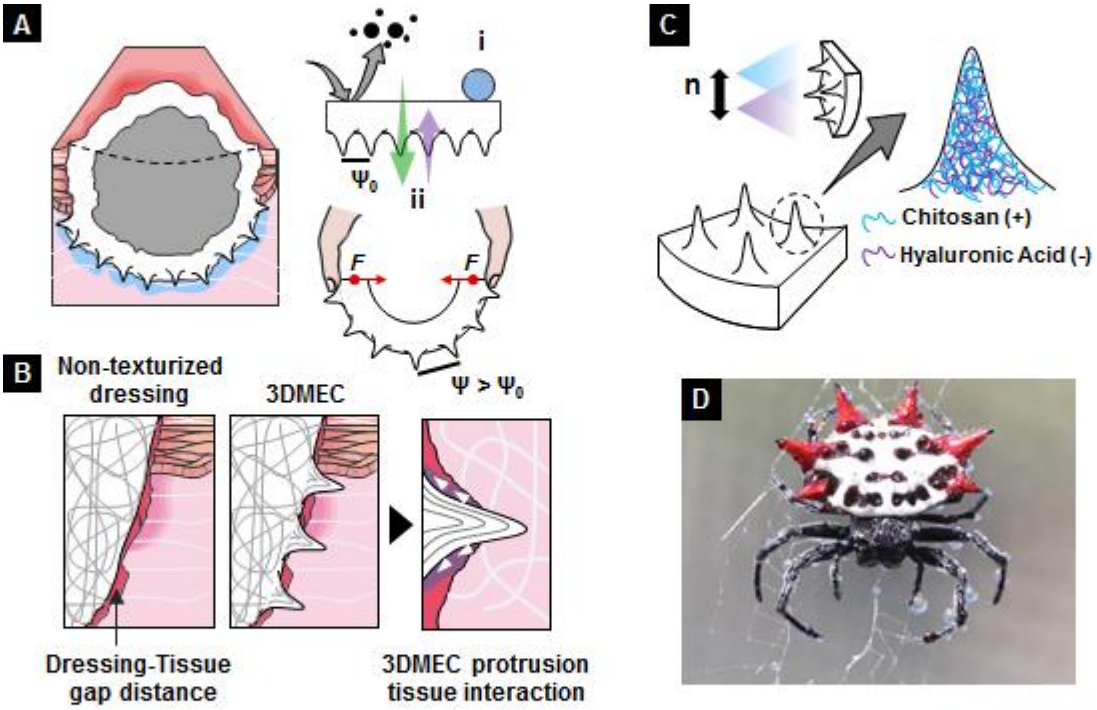

Figure 3.1 Conceptualization of three-dimensional multilayered electrospun constructs (3DMECs). **A**, Concept application as a wound dressing displaying the ideal dressing properties: *i*, impermeability to external infectious microorganisms and liquids; *ii*, gas exchanges across bandage (Ψ, interprotrusion distance). **B**, 3DMEC-tissue interaction in irregular wound bed sites in comparison with traditional dressings. **C**, Chitosan and hyaluronic acid incorporation through spray-LbL. **D**, Photograph of a spiny-backed orb weaver (*s.p. Gasteracantha cancriformis*) showing prominent protrusions in its abdomen.

3.2 MATERIALS AND METHODS

3.2.1 Fabrication of three-dimensional multilayered electrospun constructs

Poly(ε-caprolactone) (PCL, Mw ~ 65.0×10^3 g.mol^{-1}, Sigma-Aldrich) was dissolved in a 40/60 (% v/v) solution of acetic (99.8%, Riedel-de Haën) and formic acid (≥ 98%, Sigma-Aldrich) at a desired concentration of 35 wt. %. The polymer solution was magnetically stirred for 4 h at room temperature and, posteriorly its shear viscosity was measured at 25 ºC in a shear range of 1-10^3 s^{-1} by using a rotational rheometer (Gemini HR nano). The PCL polymer solution was pumped through a metallic capillary (21 gauge) by using a syringe pump (Nexus 6000, Chemyx) with a flow rate of 1.0 mL.h^{-1} during 4 hours. The metallic capillary was positively charged by a DC power supplier (Alpha Series II, Brandenburg) at 28 kV, and a 25×25 cm^2 ground aluminum foil was vertically displaced at a tip-to-collector distance of 16 cm. Both the capillary and collector were within a glass sealed box with a controlled surrounding temperature (31.0 ± 0.1 ºC). The glass sealed box also comprised a ventilation system to control the relative humidity level (30.0 ± 1.0 %) and solvent content in the working atmosphere. For plasma modification, the scaffolds were placed on a nonporous metallic plate, holding their edges with a glass frame and placed inside a

2 dm^3 radio frequency tubular reactor (Plasma System Fento v5.0, Diener). After chamber evacuation, argon was supplied into the working environment during 5 minutes prior to the treatment. The pressure within the chamber was kept at 0.4 mbar and a power intensity of 80 W was applied during 5 and 10 minutes (**Figure 3A.1**). Other attempts to modify the surface of the wound dressing substrates were performed, and those can be consult in **Annex 3C**. Posteriorly, the electrospun constructs were exposed to air. In order to produce three-dimensional multilayered electrospun constructs (3DMECs), samples were plasma cleaned for 30 seconds and soaked in a 10 mM linear polyethyleneimine (LPEI, Mw ~ 25.0×10^3 $g.mol^{-1}$, Polyscience Inc.) solution for 30 minutes. Excessive media was posteriorly removed by vacuum filtration before spray-LbL. The electrospun materials were fixed in a metallic grid displaying their top side towards the nozzles. Films were prepared using a programmable spray LbL apparatus (Svaya Nanotechnologies), in a similar fashion as reported in literature.[44, 45] Briefly, polyelectrolytes were alternately sprayed during 20 seconds with an intermediary wash step of 5 seconds. Chitosan (CHI, Mw ~ 15.0×10^3 $g.mol^{-1}$, Polyscience Inc.) with a reported[46] was used as polycation, while hyaluronic acid (HA, Mw ~ 2.0×10^6 g.mol-1, Lifecore Biomedical) with a reported[47] pKa ~ 2.9 was used as polyanion. Prior to bilayer deposition, LPEI and dextran sulfate (DS, Mw > 500.0×10^3 $g.mol^{-1}$, Sigma-Aldrich) were initially sprayed in order to promote the formation of a $(LPEI/DS)_{10}$ baselayer.

3.2.2 Constructs morphology characterization

3DECs and 3DMECs were coated with a 10 nm layer of Au/Pd and observed by Scanning Electron Microscopy (JSM-6010LA, JEOL). The observed topographical features were computationally segmented by using ImageJ (NIH). As-spun 3DECs porosity and pore size distribution was determined by mercury porosimetry (Autopore IV porosimeter, Micromeritrics) as described in the literature.[48] The mercury surface tension and its intrinsic contact angle with the electrospun constructs was considered to be γ_{Hg}=480 $mN.m^{-1}$ and θ=140º. In order to cross-validate the porosity value obtained through the mercury porosimetry data, equation 4A was used:

$$\text{Porosity (\%)} = 100 \times \left(1 - \frac{m_{3DEC}}{V_{3DEC}} * \frac{1}{\rho_{PCL}}\right), \text{with } \rho_{PCL} = 1.145\ g.cm^{-3} \quad \text{(Equation 4A)}$$

3.2.3 Constructs chemical characterization

10 mg of untreated and treated 3DECs were solubilized in $CDCl_3$ (99.8%, Cambridge Isotope Laboratories). ^{1}H-NMR spectra of each construct was obtained recording 96 scans per sample (ARX 400 MHz, Bruker). In parallel, portions from the top and bottom sides were delaminated and separately milled in KBr (1:200 w/w) being posteriorly pressed to form a disk. For each sample, a FTIR spectrum was recorded at a resolution of 1 cm^{-1} with a total of 128 scans (Spectrum 1000, Perkin Elmer). The constructs surface chemical composition was studied by X-ray Photoelectron Spectroscopy (XPS) and static contact angles. For the XPS analysis, as-spun and plasma treated electrospun constructs were cut in square sections (1×1 cm^2) and fixed to a holder by a metallic

spring. Unmonochromatic Al Kα radiation (hν = 1486.6 eV), from a spectrometer XSAM800 (Kratos Analytical) operated in a fixed analyzer transmission mode, was used. The operation parameters and data treatment methodology was followed as described elsewhere.[49] Charge accumulation was not compensated by a flood gun. The charge shift of the untreated and treated 3DECs was corrected setting the binding energy of the C 1s photoelectrons ejected from carbon in C-C and C-H bonds to 285.0 eV.[50] The following sensitivity factors were considered for quantification purposes: 0.25 (C 1s) and 0.66 (O 1s). Static contact angles (N=4) were measured at room temperature by applying the sessile drop method (CAM 100, KSV Goniometer). A 10 µL glycerol (≥ 99.0%, Sigma-Aldrich) drop was placed on the 3DECs surfaces (top and bottom). The acquisition time was extended up to 5 minutes with a frame interval of 300 ms. Each frame was retrieved to MatLab R2012b (MathWorks) and the drop height and base diameter were measured.

3.2.4 *In vitro* swelling ratio

Rectangular samples (2×1 cm^2) of each type of the three-dimensional dressing were initially weighted (W_0) and then incubated in Acetate Buffer Solution (ABS, pH=5.0 0.1 M), Phosphate Buffer Solution (PBS, pH=7.4 0.1 M) and TRIS Buffer Solution (TBS, pH=8.0 0.1 M) at room temperature during 30 days (N=4). Each beaker contained 10 mL of medium. Periodically, the samples were removed from the swelling medium and wiped to remove the excess of buffered medium. After weighting the swelled dressings (W_t), each sample returned to the original beaker. The swelling ratio (SR) was determined by the following equation:

$$\mathrm{SR} = \frac{\mathrm{W_t}}{\mathrm{W_0}} \quad \text{(Equation 4B)}$$

3.2.5 *In vitro* degradation and mechanical properties

Circular shape specimens (diameter=1cm) of untreated and plasma treated electrospun constructs were incubated in ABS, PBS and TBS media at room temperature during 30 days after being initially weighted (W_{m0}). Each beaker contained 1 mL of medium. Periodically, samples were removed from the medium, gently washed with distilled water for five times, lyophilized during 24 hours and then once more weighted (W_{mt}), while in parallel the erosion media were stored at –18.0 °C. The degradation process was assessed by the percentage of weight loss (N=4) and UV spectroscopy. The percentage of weight loss (WL) was determined by the following equation:

$$\mathbf{WL}(\%) = \frac{\mathbf{W_{mt}}}{\mathbf{W_{m0}}} \quad (\textbf{Equation 4C})$$

The UV absorbance at 250 nm was measured for each erosion media (Lambda 25, Perkin Elmer), since such wavenumber is attributed to the n→π* transition of the ester carbonyl in a PCL polymeric component.[51, 52] The mechanical properties of the electrospun dressings were tested with a tensile testing machine (MINIMAT firm-ware v.3.1) at room temperature. The samples were cut into 2×1 cm^2 strips and immersed in PBS, ABS and TBS medium during 30 days. Periodically, the specimens were removed and their tensile properties were assessed until rupture (N=4). In addition, the mechanical properties of as-spun constructs were also analyzed. The initial length between the clamps was set at 1 cm with a testing speed of 0.2 mm.min^{-1}.

3.2.6 Water Vapor Transmission Rate

Specimens (N=4) were initially conditioned for 24 hours in a desiccator (room temperature, 30% relative humidity) to achieve moisture content equilibrium. A glass tube with a 1 cm^2 opening area (A) was filled with 2 mL of distilled water and covered with a circular sample. The glass tube was then placed in a tube flask with a saturated solution of K_2CO_3 in a temperature controlled storage unit (25.0 ± 1.0 ºC), re-weighting daily the assembly glass tube + construct (m). WVTR was calculated by the following equation:

$$\mathrm{WVTR(g.cm^{-2}.day^{-1})} = \frac{\Delta \mathrm{m}}{\mathrm{A \times time}} \quad \text{(Equation 4D)}$$

3.2.7 Thermal Insulation

3DECs and 3DMECs were initially conditioned for 24 hours at room temperature. 3×3 cm^2 samples were place in a 2×2 cm^2 polystyrene frame with a thickness of 5 cm, covering a 5×5×10 cm^3 heating chamber with a temperature controlled heating plate. The heating environment was set at an equilibrium temperature of 37 ºC with a relative humidity of 30-35 %. The chamber temperature was continuously measured by a local thermocouple. The samples were placed in such way that the side with the multiple protrusions was in contact with the heated environment, while the smooth side was facing the external environment (room temperature). A second thermocouple was placed in close contact with this side, allowing the recording of any superficial temperature variation. The experiment was run during 3 hours (N=3).

3.2.8 Film thickness and surface characterization

Glass and silicon substrates were sprayed in a similar fashion as described earlier, being afterwards dried under a gentle nitrogen flow. Prior to film construction, the substrates were sequentially cleaned with methanol, ethanol, 2-propanol and milli–q water. Spray-coated glass slides (N=3) were scored by a razor blade and the step height difference, between untouched film regions and the score's bottom was tracked at nine different locations by profilometry (Dektak 150, Veeco). In addition, a (CHI/HA)10 30×30 µm^2 film area was examined by Atomic Force Microscopy (Dimension 3100 AFM, Veeco Metrology) in tapping mode.

3.2.9 Hyaluronic acid release studies

HA fluorescence dye was synthesized for confocal microscopy use and release studies. 120 mg of HA were mixed with 50 mg of N–(3–dimethylaminopropyl)–N'–ethylcarbodiimide hydrochloride (EDC, ≥ 98 %, Sigma-Aldrich) and 30 mg of N–hydroxysulfosuccinimide sodium salt (NHSS, ≥ 98

%, Sigma-Aldrich) in sodium acetate buffer (pH=5.0, 0.1 M) for 45 minutes. 60 mg of hexamethylenediamine (98 %, Sigma-Aldrich) were posteriorly added and allowed to react during 4 hours, followed by three precipitation cycles in isopropanol to remove unreacted diamine. The hyaluronic acid amine derivative was then mixed with 0.5 mg of fluorescein isothiocyanate isomer I (FITC, ≥ 90%, Sigma-Aldrich) in a sodium bicarbonate solution (pH=8.5) during 8 hours in the dark. FITC-HA was then recovery by precipitation cycles in ethanol and two precipitation cycles in a mixture of ethanol/water. The absorbance of the supernatant was compared with a fresh mixture of ethanol/water, in order to conclude that non-reacted FITC was completely removed.

The HA release profile of the produced 3DMECs at 37 ºC was determined in two different media: PBS (pH=7.4 0.1 M) and cell conditioned media. Cell conditioned media was prepared from NIH-3T3 cells grown to confluence. An initial cell concentration of 50×10^3 was seeded into a 24-well plate and cultured in Advanced-MEM (Invitrogen) media containing 5% FBS, 1% antibiotic-antimitotic and 2mM L-glutamine. After 72 hours, media was removed and filtered with a 0.2 µm syringe filter in order to remove cellular debris. Posteriorly, circular specimens (diameter=1cm) were incubated in 1.5 mL of each media (N=3). At a given interval, 250 µL of medium was replaced. A standard curve of the FITC-HA was used to interpret the concentration of HA in the release media (excitation peak=492 nm).

3.2.10 Wound scratch assay

The wound scratch assay, an *in vitro* technique consisting on the formation of an artificial scratch in a confluent cell monolayer,[53-55] is used to evaluate the rate of wound closure promoted by the generated LbL coated fibrous materials. Briefly, NIH-3T3 (GFP+) cells, with an initial concentration of 20×10^3, were seeded into a 24-well plate and grown to a sub-confluent (80–90 %) monolayer. The resultant monolayer was then wounded with a sterile 200 µL pipette tip. The wound consisted in a straight line scratch across each well, being posteriorly washed with PBS (pH=7.4 0.1 M) in order to remove cellular debris and culture further with media containing degraded polymer material. Uncoated (A-type 3DECs) and coated 3DEMCs ($A+(CHI/HA)_{10}$ and $A10+(CHI/HA)_{10}$) were incubated at 37 ºC in PBS (pH=7.4 0.1 M) during 7 days. At the end of the incubation period, the media with soluble degraded polymer products was filtered with a 0.2 µm syringe filter and diluted (50 % v/v) in fresh Advanced-MEM (Invitrogen) media containing 5 % FBS, 1 % antibiotic-antimitotic and 2mM L-glutamine. Each final formulation was applied to the wounded cell monolayer (N=4). Wound closure was followed during a 48 h period (Axiovert 200, Zeiss), in which the wound size was determined by the gap from opposing wound edges, while considering four measurements per field of view. The wound closure was then expressed as a percentage of the initial wound gap.

3.3 RESULTS AND DISCUSSION

3.3.1 Production and morphological characterization of three-dimensional electrospun constructs (3DECs)

Poly(ε-caprolactone), a biocompatible aliphatic polyester, was used to manufacture 3DECs for wound healing applications. In addition to its long-term degradation in physiological media,[56] PCL presents several advantages over other polymers that meet the specifications for an ideal wound dressing (**Table 3.1**). It has been demonstrated that PCL could be polarized under intense electric fields by controlling the surrounding relative humidity, favoring the formation of 3DECs.22 Nevertheless, thus far PCL had been assembled only into microfibrous constructs that generate honeycomb patterns,[22, 57] a type of topography with limited applications. In this work, it is generated 3DECs with multiple protrusions on the top surface, while maintaining a flat bottom surface (**Figure 3.2A, B, C**).

Table 3.1 Ideal specifications of a wound dressing[58, 59] and advantages in the use of poly(ε-caprolactone). Chapter 1 key features achieved: 2 (Sterilizable), 7 (Non-toxic), 8 (Non-allergenic or sensitizing), 13 (Non-flammable) and 15 (Long shelf life).

Characteristics	**Poly(ε-caprolactone)**
● Non-toxic and non-allergenic	● Biocompatibility[56]
● Can be removed without causing trauma to the wound	● Hydrophobic polymer (Reduces cell adherence). When placed onto the wound site, a layer of water molecules adheres to the biomaterial surface preceding the rapid attachment of proteins. Cell adherence is then promoted in biointegrative manner, leading to tissue adhesion. By reducing the initial protein adsorption, wound dressings cause less trauma when removed.[60]
● Impermeable to external microorganisms and fluids	● Hydrophobic polymer (Protective external barrier)
● Thermally insulating (+) Allows gaseous exchanges	● Easily processed through different technologies allowing a deep control of the dressings' inner structure (e.g. particulate leaching, thermally induced phase separation, electrospinning, 3D printing, stereolitography, etc.)
● Reduced number of changes	● Mechanical and Physicochemical stability in physiological medium[61]
● Cost-effective	● Low cost
● Long shelf-life	● Mechanical and Physicochemical stability[56]

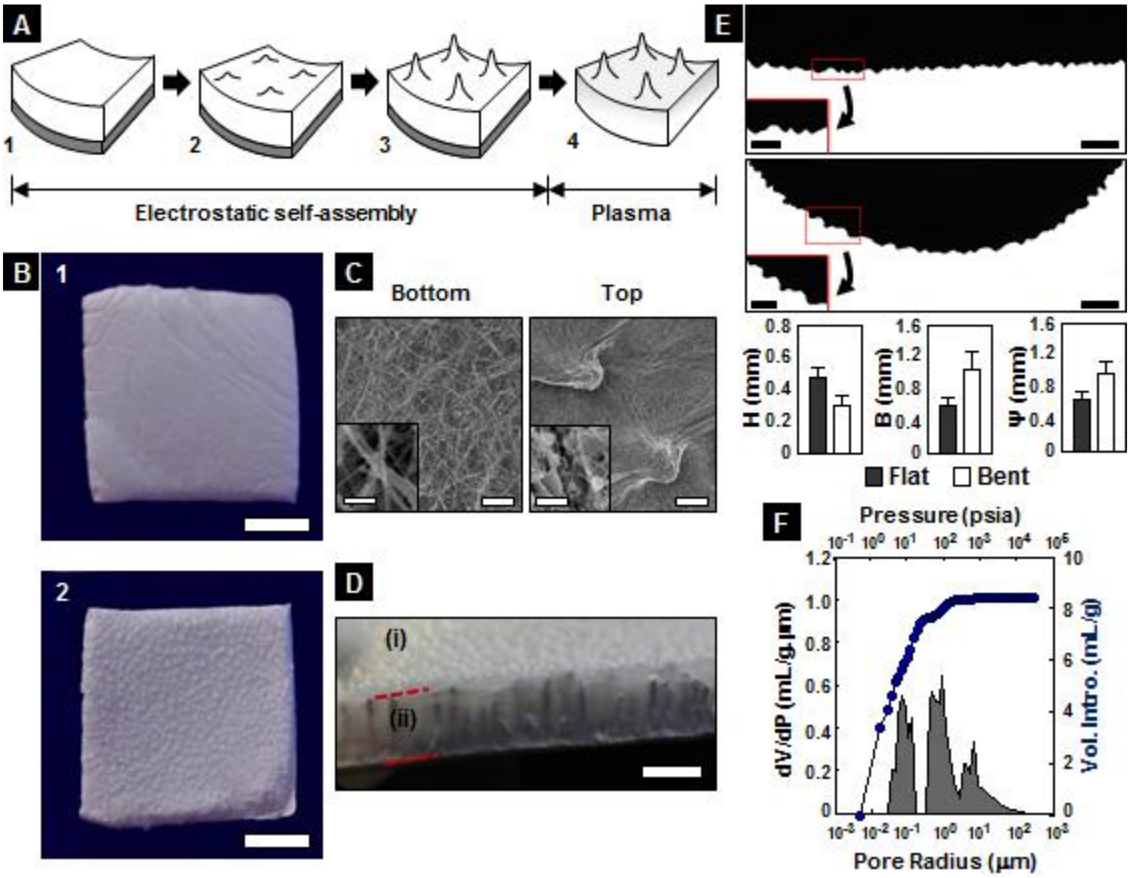

Figure 3.2 Bioinspired production of 3DMECs. **A**, Scheme of the electrical-driven self-organized 3DECs fabrication process and bottom plasma treatment to improve surface hydrophilicity. **B**, Photograph of the (1) bottom and (2) top side of a 3DEC (scale bar=1 cm). The top side presents multiple protrusions along the surface with a median protrusion density of 73 peaks.cm^{-2}. **C**, SEM images from bottom and top sides having a scale bar=100 μm with an inset scale bar=5 μm. **D**, Photograph of a 3DEC evidencing multiple protrusions at the top side (i) and their z-axis formation in the cross section (ii). Scale-bar=3 mm. **E**, Micrographs in flat and bent conformations (scale bar=3 mm, inset scale bar=1.5 mm) and parametric shape comparison (H, protrusion height; B, equivalent base; Ψ, interprotrusion distance). Data evidence p-value < 0.01. **F**, Mercury porosimetry data after buckling correction for the electrospun materials.[45] Chapter 1 key features achieved: 1 (Permeable to ocygen) and 10 (Conforms to anatomical countours),

The bottom side, which corresponds to the side in contact with the grounded collector, is characterized by a random fiber deposition, commonly observed as well in 2DECs.[44, 62, 63] On this side, the scaffolds exhibited a bimodal fiber diameter distribution: Population 1, fiber diameter= (21 ± 9)×10 nm; Population 2, fiber diameter=(15 ± 4)×10^2 nm (**Figure 3A.2**). It was hypothesized that the bimodal distribution is related to the instability of the electrospun polymer jet due to the intense electric field, a phenomenon also reported in the production of 2DECs.[64] The top side of the construct shows multiple conical protrusions, resulting from the preferential deposition of fibers in specific regions driven by local in situ polarization of high dense fiber regions in the plane of the collector.[22] The electrostatic attraction between these regions and the depositing fibers promotes the localized preferred deposition of fibers and the generation of sub-millimeter features over time (**Figure 3.3**). The generated 3DECs demonstrated a median protrusion density of 73 peaks.cm^{-2}

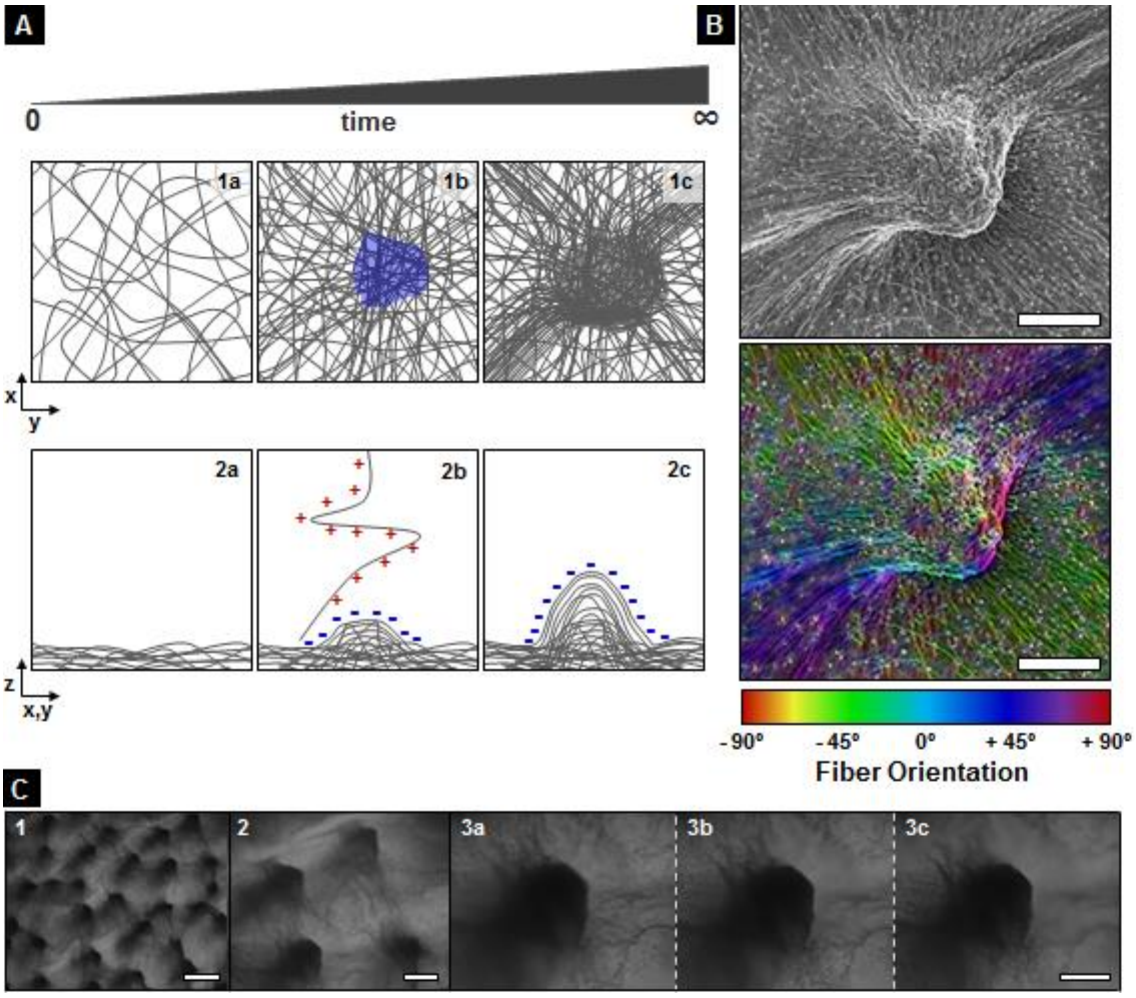

Figure 3.3 Fibers self-assembly induced by their *in situ* polarization leads to the generation of protrusions. **A**, Scheme of the protrusions formation due to the fibers in situ polarization. As time passes by, the electrospun fibers acquire a negative superficial charge that drives the incoming aerial positive fibers to be collected on top of them. The electrostatic forces of attraction generate a densely packed fibrous network, shaping tightly the self-assembled construct into protrusions. **B**, SEM micrographs and fiber colored orientation analysis (scale bar=100 µm). **C**, DIC microscopy images from the top side evidencing multiple protrusions with a conical shape. (Image 1, scale bar=500 µm; image 2, scale bar=200 µm; image 3a-3c, scale bar=50 µm). Images 3a-3c were taken at different z-planes.

while the median inter-protrusion distance was 528 µm (**Figure 3.4**). As a consequence of the fibers' preferential deposition, each protrusion shows a z-axis densely packed fibrous core (Figure 3.2D, **Figure 3.5**). As determined by mercury porosimetry, the fibrous materials have a multimodal pore size distribution (Figure 3.2F), with an overall porosity of 89.9% (92.7% when considering Equation 4A) and a surface area of 1.44 m^2.g^{-1}, values in the range of what is expected for electrospun materials.[65]

The protrusion geometric characterization was evaluated at two dressing configurations: (i) flat (conformation corresponding to a superficial wound), or (ii) curved (conformation corresponding to a full thickness wound) (Figure 3.2E). After being bent (bend angle=110º), the protrusions are effectively reduced in height by 37.6%, while the inter-protrusion distance is increased by 50.7%.

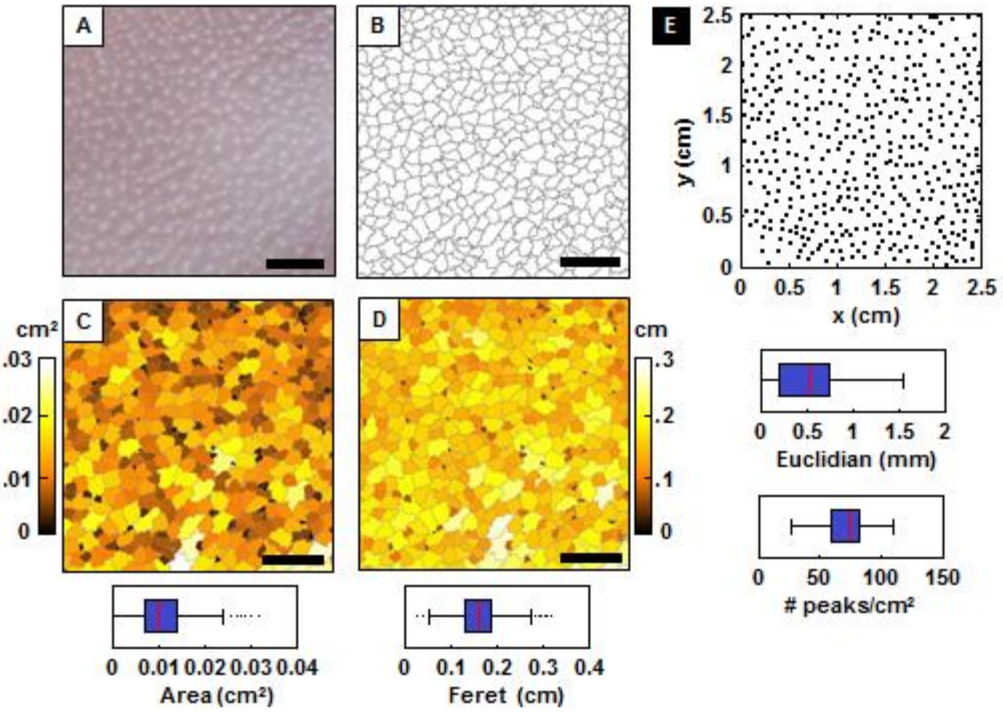

Figure 3.4 3DEC topographic characterization. **A**, 3DEC top side photograph evidencing protrusions. **B**, Image optimal segmentation by cell elements. **C**, Cell area distribution. **D**, Cell Feret diameter distribution (A-D images, scale bar=500 mm). **E**, Scattered protrusions centroids with determination of the interprotrusion Euclidian distance and protrusion density.

3DECs can thus offer topographical features that support the dressing fixation at the wound bed in a broad range of wounds,[66] a feature lacking in traditionally used wound dressings. An ideal property for wound dressings is the capability to be impermeable to external liquids so as to avoid sources of infection, while allowing the uptake of wound exudate. For our bandage to achieve this property, it is proposed to treat differentially each side of the construct in order to create a hydrophilic gradient across the bandage, in association with the already generated z-axis construct asymmetry. Therefore, to reduce the PCL-based 3DECs hydrophobicity, the materials were plasma treated in argon and then exposed to atmospheric air. It has been chosen to use an inert gas to avoid the 3DECs surface ablation or etching, otherwise observed with reactive gases such as oxygen.[67] To determine the effect of this treatment, three groups of 3DECs were investigated: A, 3DECs without plasma treatment; A5, 3DECs plasma treated for 5 min, and A10, 3DECs plasma treated for 10 min. After solubilizing as-spun 3DECs in $CDCl_3$, ^{1}H-NMR spectra were acquired (**Figure 3.6**), indicating the complete absence of the acetic and formic acid initially used to prepare the PCL. Contact angle measurements of both top and bottom sides of each construct validated our approach, as the bottom untreated side was unchanged from the control, while the plasma treated groups exhibited a significantly lower contact angle on their top surface than the untreated control (**Figure 3.7A**). The plasma treatment creates a hydrophilic gradient across the materials, in which their top sides are the most hydrophilic regions of the dressings. 3DECs were delaminated and portions from the top and bottom of the construct were analyzed by FTIR and

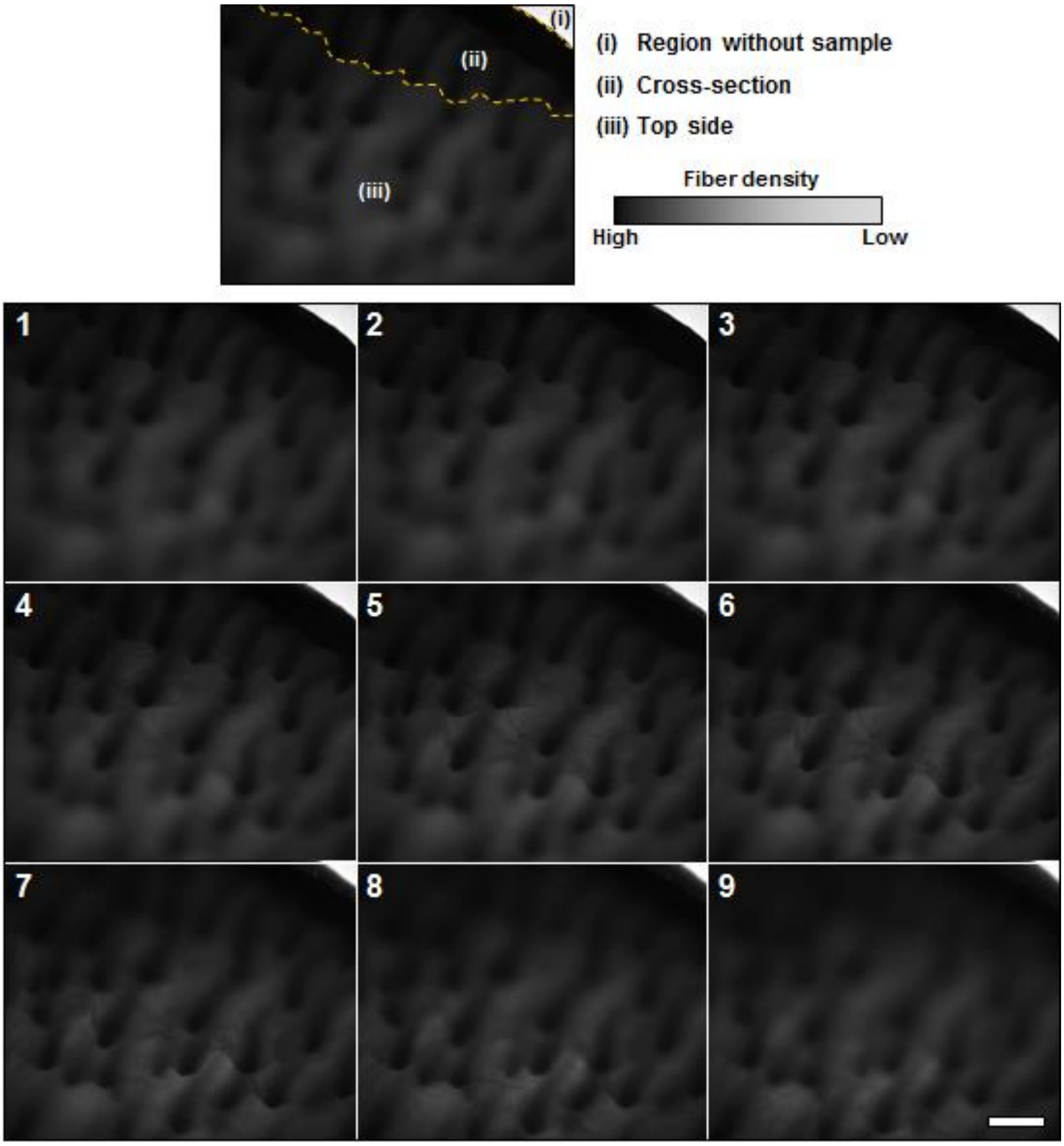

Figure 3.5 Phase contrast microscopy images from a 3DEC, including the cross-section and top side at different z-planes, evidencing, simultaneously, multiple protrusions and z-axis built in core characterized by dense fiber regions (scale bar=500 µm).

XPS (**Figure 3.7B-D**), showing stronger v(OH), v(C=O) and v(C–O) signals in comparison with the non-treated ones.

Moreover, it was possible to observe on the plasma treated constructs, a noticeable difference of these signals between their top and bottom sides. In addition, XPS characterization demonstrated a higher O/C ratio in the plasma treated samples, supporting the preferential development of oxygenated hydrophilic groups (-OH, -COOH) near the top surface of the constructs.

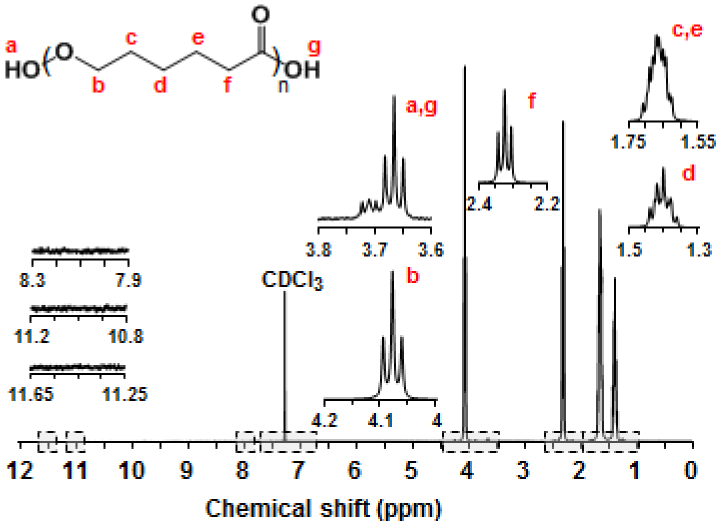

Figure 3.6 Solvent contamination assessment by ^{1}H-NMR of as-spun 3DECs in $CDCl_3$. In case of contamination shifts at 2.10 and 11.40 ppm (acetic acid) and/or 2.10 and 8.27 ppm (formic acid) should be noticed.[68]

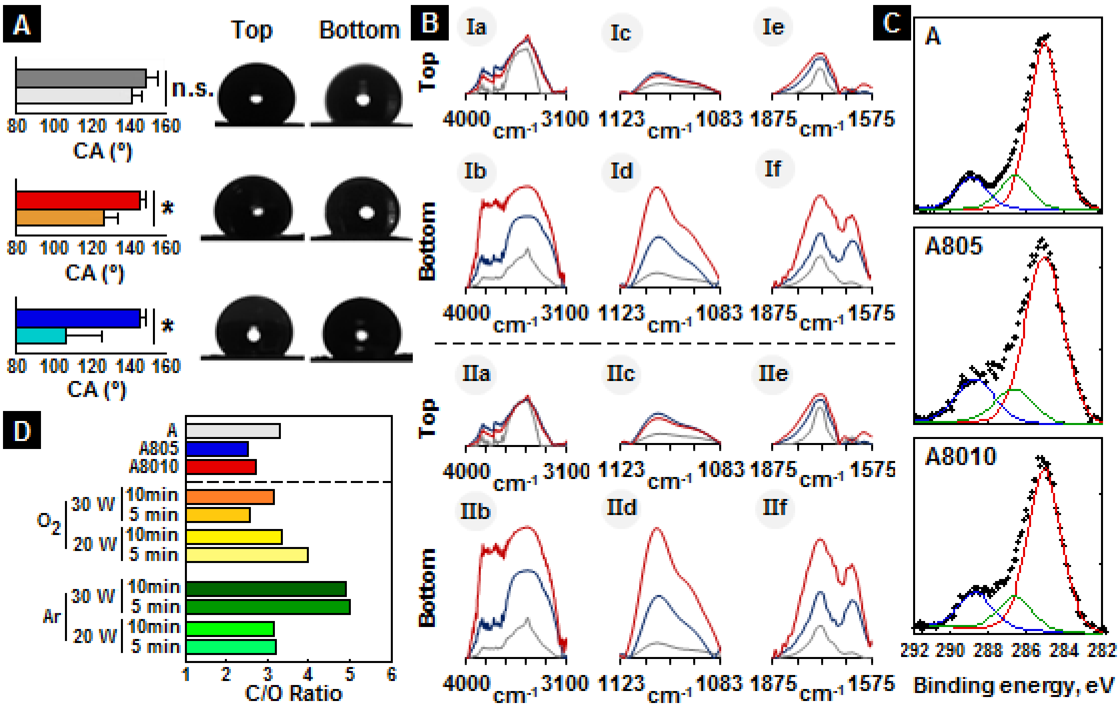

Figure 3.7 3DECs chemical characterization after plasma treatment. **A**, Static contact angle determination (n.s., not significant; *, p-value < 0.01). **B**, FTIR spectra at different sides (A, grey; A5, blue; A10, red) normalized by $\nu_{S(CH2)}$ (Ia-f) and $\nu_{AS(CH2)}$ (IIa-f) in the following characteristic bands: $\nu_{(OH)}$, 3000-4000 cm^{-1}; $\nu_{(C=O)}$, 1729 cm^{-1}; $\nu_{(C-O)}$, 1108 cm^{-1}. **C**, XPS spectra of high resolution C 1s core level signal (Blue, Ester functional groups, O–C=O, and/or carboxylate functional groups, O-C=O-; Green, Carbon singly bound to oxygen –C–OH or –C–O–; Red, Aliphatic carbon in bonds –C–C– or –C–H). **D**, Carbon/Oxygen ratio determination from elemental surface composition (A, C 1s: 76.6 & O 1s: 23.4; A5, C 1s: 71.3 & O 1s: 28.7; A10, C 1s: 72.9 &

O 1s: 27.1). Data comparison with similar reported plasma treatment strategies of 2D non-woven PCL meshes.[69]

3.3.2 Fluid uptake directionality and long-term mechanical stability

Prior to studying the fluid uptake directionality, the 3DECs mechanical properties were determined, showing no significant change after using plasma treatment to modify the materials top side (**Figure 3.8A**). 3DECs evidenced an initial non-linear stress-strain response (toe region), followed by a stiff linear region characteristic of an elastic domain, which it was hypothesized is due to the alignment of the randomly oriented fibers as often observed in 2DECs.[70]

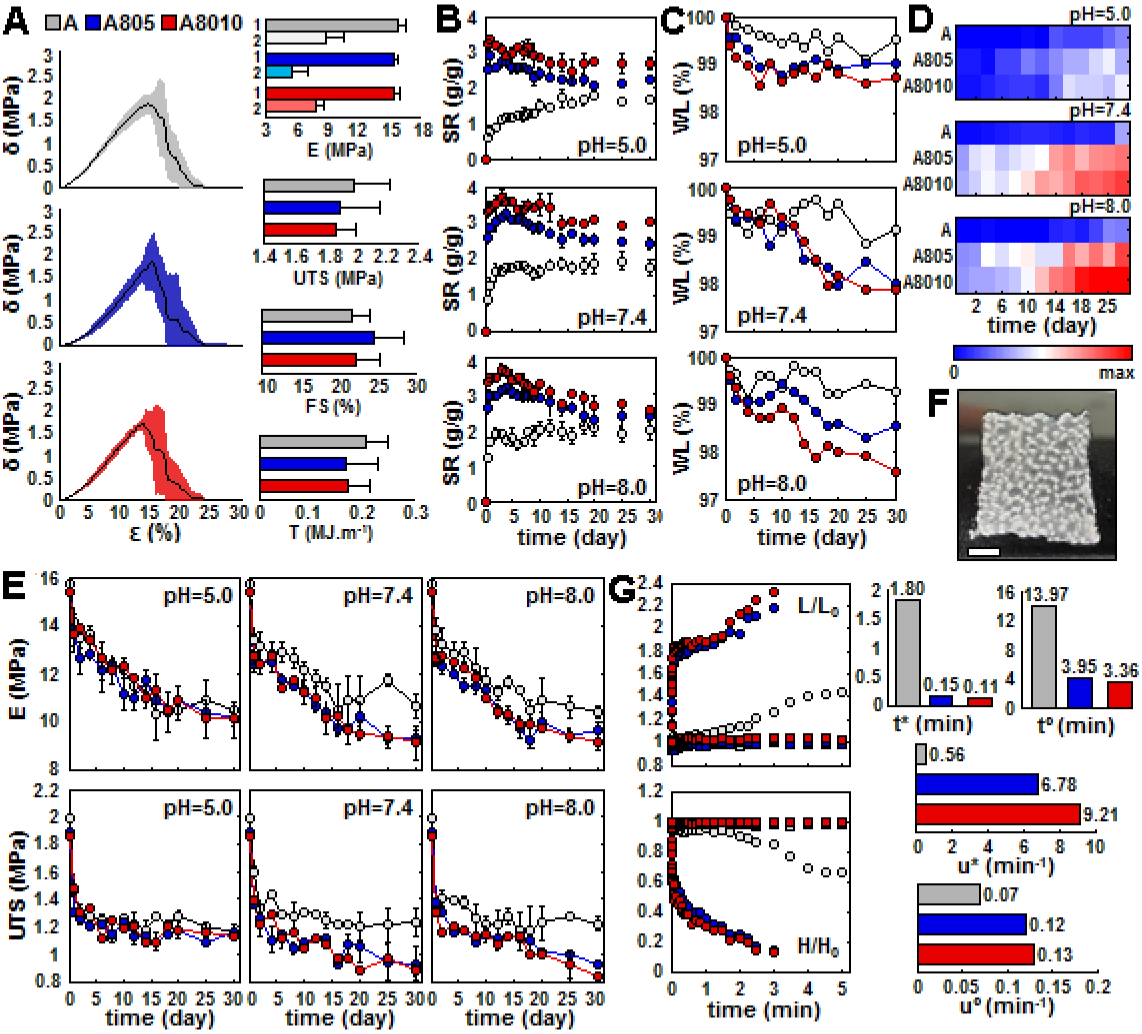

Figure 3.8 Physicochemical characterization of 3DECs. **A**, Stress(δ)-strain(ε) curves and mechanical properties determined after plasma treatment (E, Young's Modulus – 1, toe region, 2, elastic domain; UTS, Ultimate Tensile Strength; FS, Fracture Strain; T, Toughness). Time dependent swelling (**B**) and *in vitro* weight loss (**C**) as a function of pH. **D**, Cross-validation of weight loss by the qualitative PCL release profile, determined by UV absorbance measurements at 250 nm. **E**, Time dependent mechanical properties as a function of pH. **F**, Photograph of a swelled delaminated top side 3DEC while showing the presence of protrusions (scale bar=25mm). **G**, Spreading and absorption dynamics (L/L₀, normalized droplet base; H/H₀, normalized droplet height; □, ○, bottom and top sides respectively; t*, u*, spreading time and velocity; t°, u°, imbibition

time and velocity). Chapter 1 key features achieved: 5 (Good mechanical protection to the wound), 9 (Does not shed loose material) and 11 (Resists tearing).

These self-assembled materials are highly elastic compared with recently produced PCL-based 2DECs (E, Elastic modulus: E2DECs=19 ± 2 MPa), while maintaining a relatively high ultimate tensile strength (UTS) despite having a lower value (UTS2DECs=2.5 ± 0.1 MPa).[71] However, it is important to notice that even the lowest UTS value observed (UTSA10=1.9 ± 0.1 MPa) corresponds to apply $(19 \pm 1)\times10^4$ kg in 1 m^2 of the dressing area, an unlikely situation to occur when a patient is using a wound dressing. Despite the elastic modulus of human skin ranging between 3.5 to 8 kPa,[72] it has been demonstrated that the proliferation rate of human dermal fibroblasts is directly proportional to the stiffness of their tested substrates (E=0.5–120 MPa).[73] In this way, it is expected that 3DECs are capable to enhance cellular proliferation while being mechanically suitable to fit non-uniform wound sites. Another ideal characteristic of a wound dressing is the reduction of the necessary dressing changes,[74, 75] which is usually limited by the dressing physicochemical properties and mechanical stability. To evaluate whether 3DECs could be easily replaced, it is investigated the dressing properties in three different simulated wound exudate pH conditions for up to 30 days. Plasma treated 3DECs showed an increased weight loss compared with the untreated controls, however the overall degradation was less than 3 wt. % (**Figure 3.8C**). These findings were cross-validated with UV absorbance measurements at 250 nm, corresponding to the $n\rightarrow\pi^*$ transition of the ester carbonyl in PCL (**Figure 3.8D**). The swelling ratio of the surface modified and unmodified constructs was also assessed over the 30-day study period. The plasma treated 3DECs also demonstrated a higher swelling ratio compared to untreated materials, improving their capability to absorb wound exudate (**Figure 3.8B**). In comparison with the chemically unmodified scaffolds, and regardless of the medium pH, A5 and A10 exhibited a continuous swelling decay after day 3. Since it was previously confirmed a degradation lower than 3 wt. % for these materials, it was hypothesized that this decay results exclusively from the progressive re-organization of the bottom fibrous network after the maximum swelling ratio has been reached. The absorption process consists in a fluid entering in a scaffold by diffusion and being drawn by capillary force into the porous regions.[76] The continuous water uptake leads to the adherence of a water layer on the fiber surface, which reduces the fiber-fiber drag force under stress. In this way, at the maximum swelling ratio, the generated inner pressure promotes fibrous network re-orientation due to fiber-fiber sliding, resulting in a smaller average pore size and consequent expelling of fluid. Fiber hydration is likely responsible for the reduction of the 3DEC elastic modulus and UTS (**Figure 3.8E**), which is a common phenomenon found in the traditional 2DECs when wetted.[77, 78] Nonetheless, at day 14 and a pH=7.4, A, A5 and A10 constructs still have the ability to absorb $(12.7 \pm 0.6)\times10^4$ kg, $(11.3 \pm 0.2)\times10^4$ kg and $(11.0 \pm 0.3)\times10^4$ kg of water per m^2 of dressing area respectively, where the typical dressing thickness is 3.7 ± 0.1 mm, while demonstrating the mechanical properties needed for dressing changes when necessary.

Characterization of uptake and directionality of a liquid, according to each side of the 3DECs, was done by investigating both liquid spreading on the dressing surface and imbibition into the dressing inner structure. As shown in Figure 3.2, the induced z-axis asymmetric fiber deposition in 3DECs favors the formation of a protective fibrous bottom layer due to a higher fiber density in this side. Therefore, the produced 3DECs have a pore size and hydrophobic gradient across the scaffolds' thickness that favors fluid handling properties. Analogous to Martins et al.,[69] it has been chosen to use glycerol for the contact angle measurements due to the similarity of its surface tension ($\gamma_{25°C}$=62.4 mN.m^{-1}) with water surface tension ($\gamma_{25°C}$=72.0 mN.m^{-1}) and its viscosity, which is comparable to that of wound exudate. Time-lapse contact angle measurements showed similar droplet behavior on the bottom side of all 3DECs, where droplet spreading and imbibition did not take place (**Figure 3.9**).

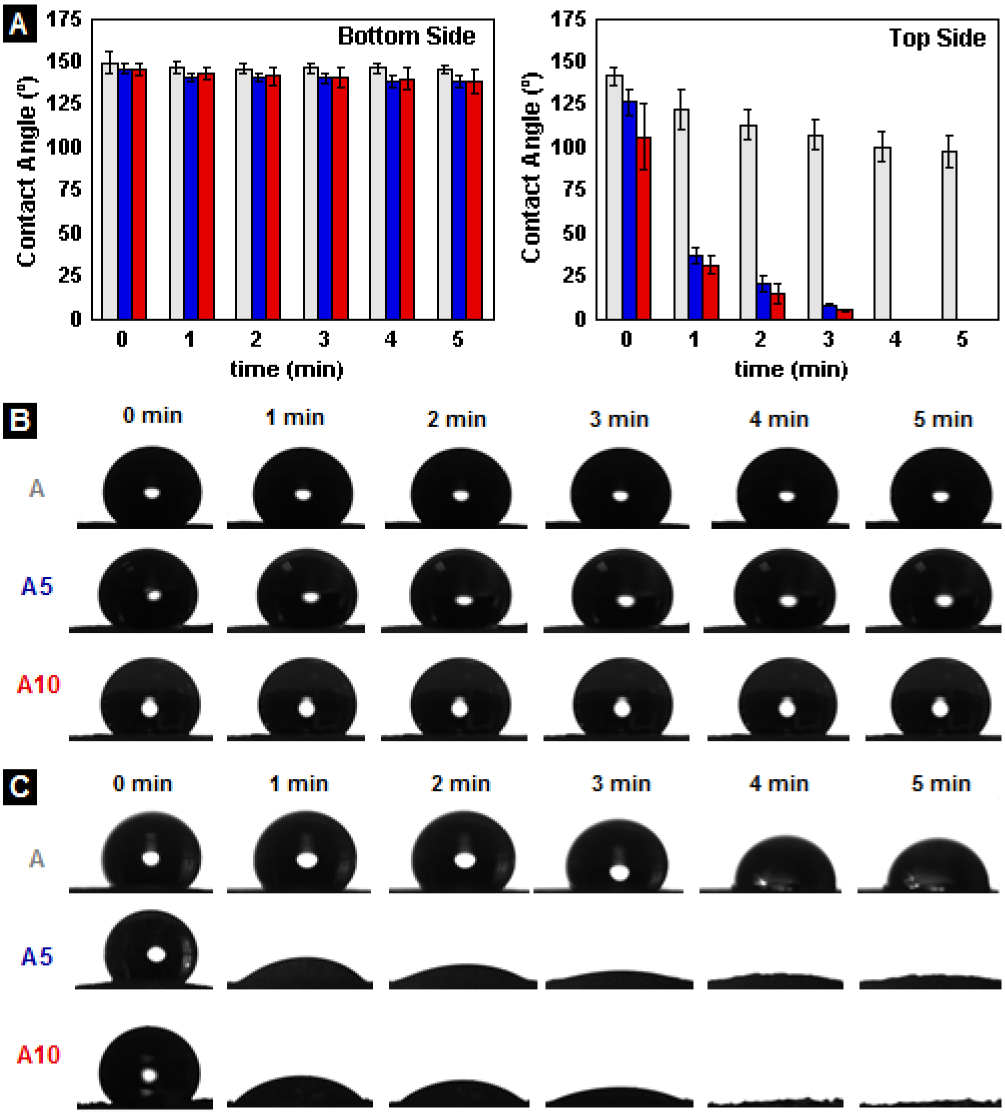

Figure 3.9 Spreading and imbibition dynamics. Extended contact angle measurements (**A**) and corresponding images from the bottom (**B**) and top (**C**). Chapter 1 key features achieved: 4 (Protection against secondary infection) and 12 (Resists soiling).

The first stage of a drop motion in contact with a dressing is the spreading, meaning the motion of the three-phase contact line through the dressing surface (see **Annex A4**). In the case of the 3DECs bottom side, the differences in the polarity of the non-functionalized PCL fibers and glycerol hindered wetting, which in turn inhibits liquid imbibition. Due to the z-axis asymmetric fiber deposition, the 3DECs topography at the top side is microtexturized. This, in combination with the higher hydrophilic functionalization, offers a distinct environment for liquid spreading and imbibition. The surface functionalization of the dressings A5 and A10, in comparison with the A type constructs, significantly accelerated spreading by an order of magnitude as well as reduced the total liquid imbibition time to approximately 3 minutes, compared to an approximated 14 minutes in the A type dressings (**Figure 3.8G**). While the bottom side of the 3DECs is structurally and chemically similar, their top sides are only morphologically similar, leading to different spreading and imbibition dynamics. Conversely, comparing the top and bottom sides of the A type wound dressings, which have the same chemical composition, it is possible to observe a distinct drop in spreading and imbibition at the top side. This suggests that the topography of the 3DECs is also important. It is likely due to the increased porosity and subsequent increase in permeability of the construct on its top side, caused by the reduction of resistance of the porous medium to flow. Thus, the observed pore size gradient across the membrane thickness also favors the wound exudate transport from the top side to the bottom side, while simultaneously hindering the imbibition of external contaminated liquids in the opposite direction.

3.3.3 LbL coating and *in vitro* assessment of the modified multilayered electrospuns constructs

With the successful fabrication of 3DECs, possessing desirable mechanical and structural properties for wound dressings, it is aimed to incorporate increased functionality to the surface of the bandage through the use of LbL coatings. An ideal bandage surface would both promote wound healing as well as impair tissue integration into the construct.[74] These properties would reduce the time that the bandage would need to be in contact with the wound and reduce the pain associated with bandage changes (consult **Annex 3B** for deep understanding of the polyelectrolyte selection process). Based on their widely reported benefits in wound healing applications it has been chosen to incorporate the combination of chitosan (CHI) and hyaluronic acid (HA).[79, 80] Chitosan is a poly-cationic species and has been used extensively in wound dressings as an antimicrobial and pro-clotting agent.[81] Hyaluronic acid is also widely used in bandages and resorbable matrices due to its high biocompatibility and role in the natural extracellular matrix.[82] To reduce tissue integration into the dressing it was aimed to achieve a coating that both bridges the pores of the top of the construct, providing a physical barrier to penetration, and has a low elastic modulus to reduce cell adherence.[83] Films were deposited on the plasma treated surface of the 3DECs by the spray-LbL method which was not observed to significantly alter the structure of the 3DECs (**Figure 3.10-3.11**). The film architecture of $(CHI/HA)_x$, where x is the number of bilayer repeats, was first studied by assembling films on oxygen plasma treated glass substrates. Thickness and roughness properties of the film were determined by profilometry (**Figure 3.12A**).

The film was observed to deposit in a near-linear fashion with an average growth rate of 25 ± 4 nm per bilayer (R^2=0.98), reaching a thickness of (26 ± 4)×10 nm after 10 bilayers. Coating of 3DECs was performed similarly, generating three-dimensional multilayered electrospun constructs (3DMECs). To evaluate the uniformity of the coating, fluorescently labeled HA was used

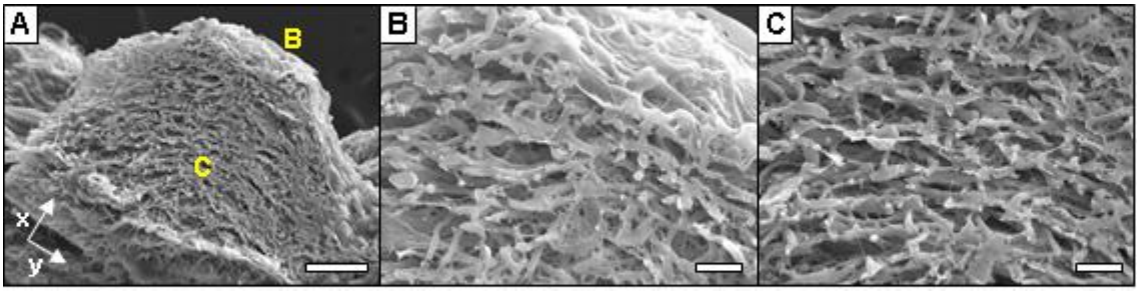

Figure 3.10 SEM cross-section images of a coated protrusion evidencing the electrospun fibers self-assembly. The fiber based network evidences a high tortuosity. (**A**, scale bar=50 µm; **B/C**, scale bar=10 µm).

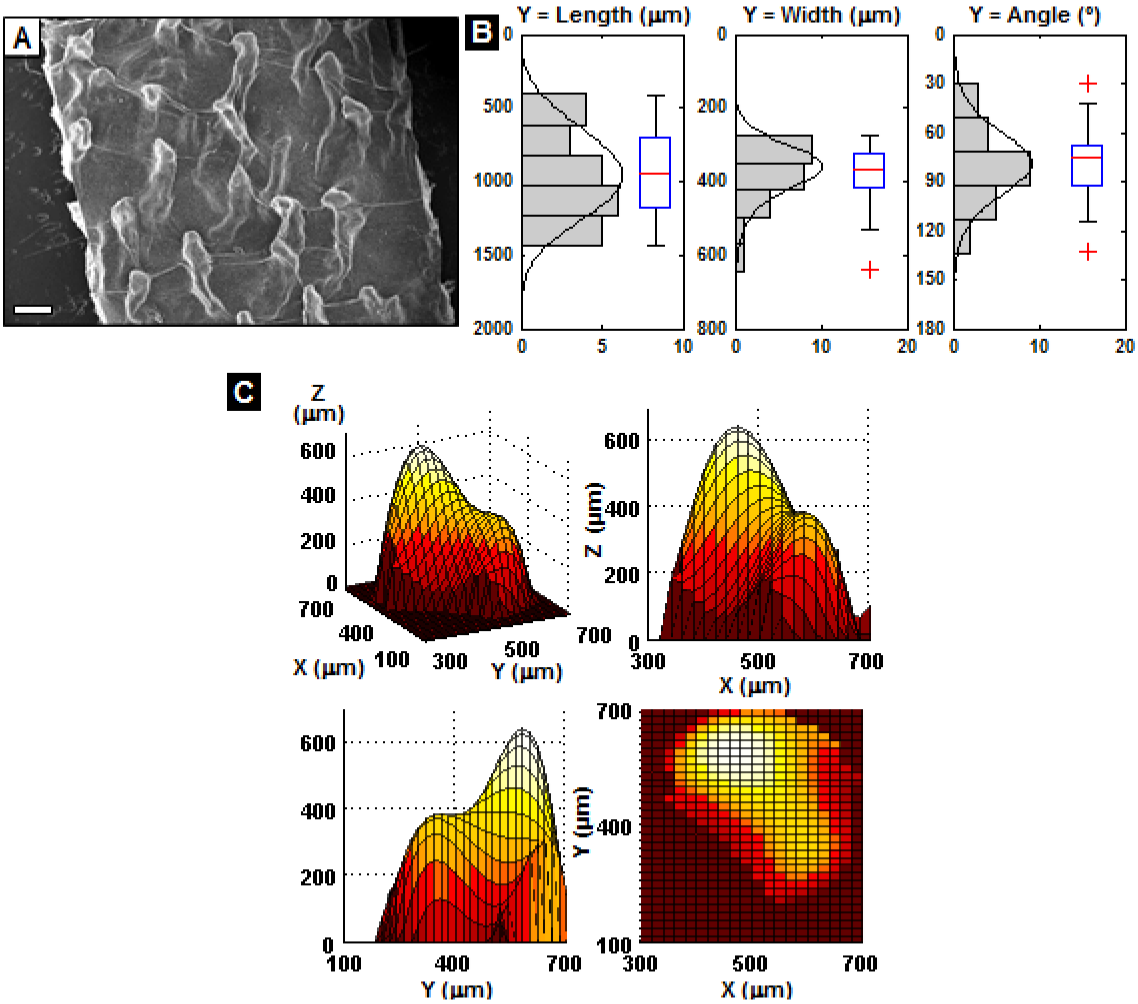

Figure 3.11 LbL coated protrusions characterization. **A**, SEM image from a 3DMEC top side (scale bar=500 µm). **B**, Shape descriptors distributions. **C**, Three-dimensional reconstruction of a coated protrusion.

in film assembly and coated substrates were imaged via fluorescent imaging (**Figure 3.12B**). The 3DMECs were successfully coated by the LbL film while preserving their unique topography. Moreover, by comparing the top and bottom sides of 3DMECs, the materials showed significantly increased material adsorption to their top surface side (**Figure 3.13**), which is expected due to the direction of film deposition and the constructs' unidirectional permeability.

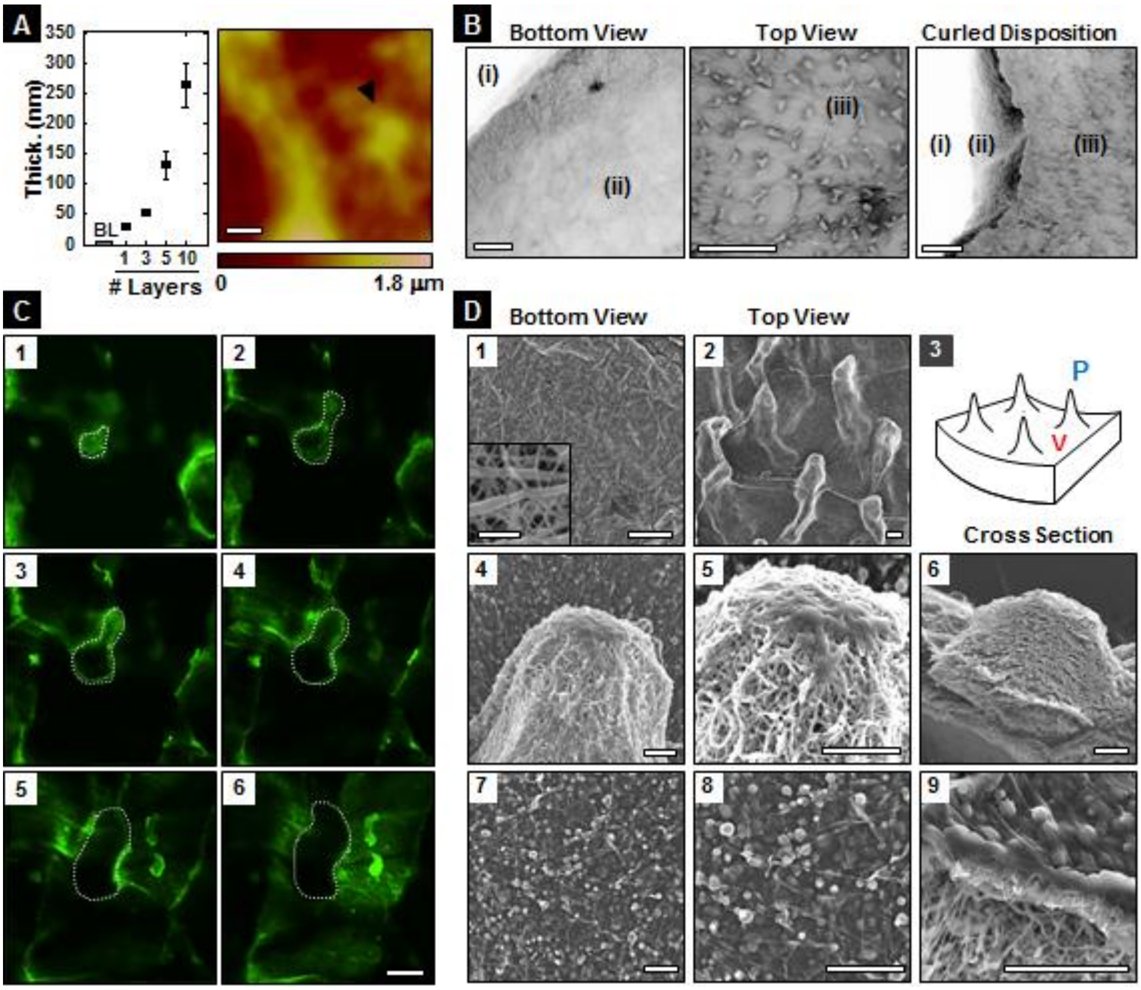

Figure 3.12 Chitosan and hyaluronic acid incorporation through spray-LbL. **A**, Film thickness growth as opposed to the number of repeated film architectures after spraying $(LPEI/DS)_{10}$ as a base layer (BL). Atomic force micrograph at 10 repeated bilayers of CHI/HA (scale bar=5 µm). **B**, Flat-bed imaging of different 3DMECs perspectives (*i*, region scanned without sample; *ii*, bottom surface; *iii*, top surface; scale bar=2 mm). **C**, Representative confocal images from a set of 33 figures with a height step of 7.17 µm, evidencing a conformal coating across the protrusion (scale bar=2 mm). **D**, SEM images from (1) bottom, (2) top and (6,9) cross section perspectives. Images 4-6 are representative of a protrusion (P), images 7-9 are representative of an interprotrusion space (valley, V). Images 1 and 2 have a scale bar=200 µm, where the inset scale bar in 1=5 µm. Images 4-9 have a scale bar=50 µm.

Confocal microscopy (**Figure 3.12C**) and scanning electron microscopy (**Figure 3.12D**), were also used to assess the LbL coating on the 3DMECs. Both techniques showed a uniform coating of the protrusions and their interspaces. SEM imaging also suggested little to no coating on the bottom side of the scaffolds, with the electrospun fibers appearing similar to uncoated substrates.

Despite the film adherence and uniformity of the coating on the construct, there is very little penetration of the film into the porous fibrous network within the material (**Figure 3.14**). The process of spraying also yielded a unique morphology to develop on the surface of the 3DMECs, on generating particles with an average diameter of 6 ± 4 µm on the construct surface, primarily in the interspaces between protrusions (**Figure 3.15**). It was hypothesized that the poor film interpenetration as well as the particle generation were related to both the pressure gradient across the

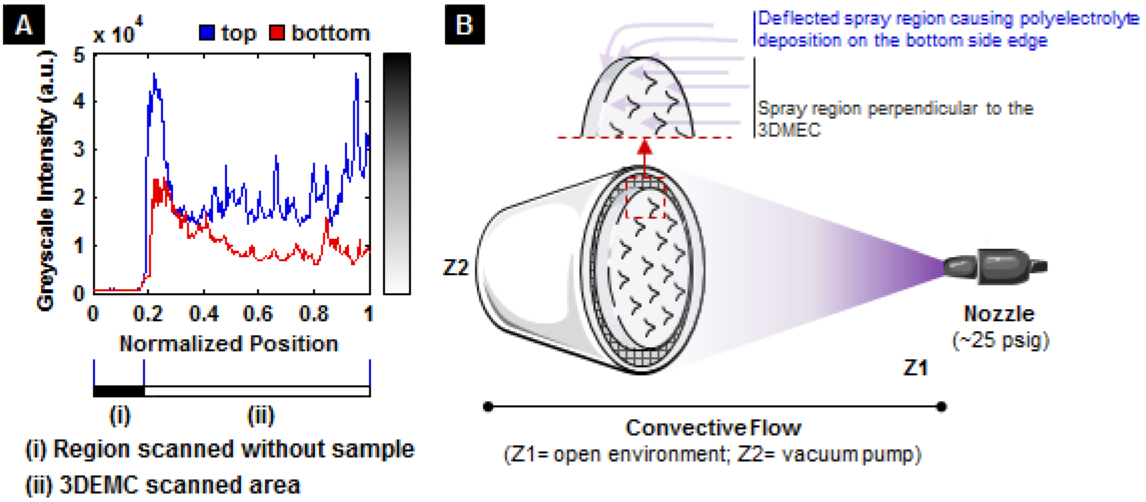

Figure 3.13 LbL coated protrusions characterization. **A**, SEM image from a 3DMEC top side (scale bar=500 µm). **B**, Shape descriptors distributions. **C**, Three-dimensional reconstruction of a coated protrusion.

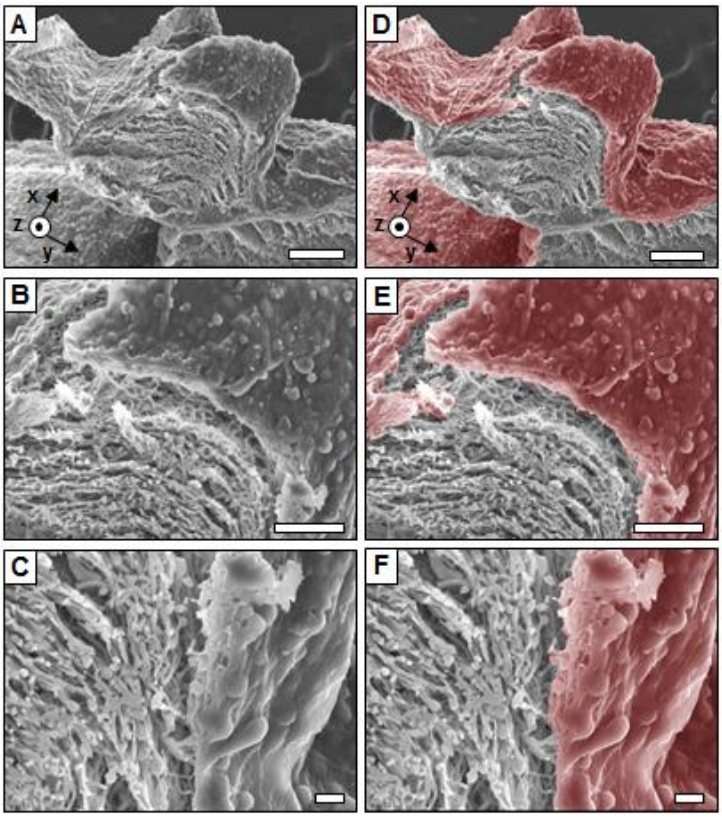

Figure 3.14 SEM images (**A**, **B** and **C**) and pseudo-colored SEM (**D**, **E** and **G**) of a pulled out coated protrusion. (A/D, scale bar=100 µm; B/E, scale bar=50 µm; C/F, scale bar=1 µm).

materials and the HA solution viscosity. Due to the hygroscopic nature of chitosan and hyaluronic acid, water uptake contributes to the generation of a rubbery film layer,[84] with poor rigidity and consequent reduced cellular adhesion on the top of the scaffold (**Figure 3.16**). In contrast, when NIH-3T3 cells were purposely seeded in the 3DMECs lacking the LbL film coating, there was significant cellular adhesion (**Figure 3.17**).

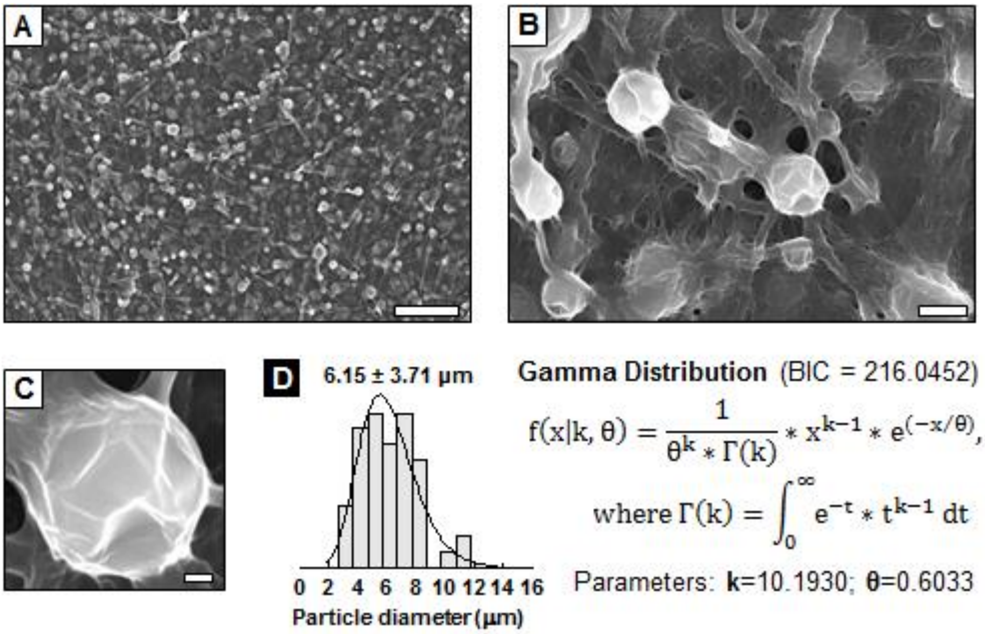

Figure 3.15 Morphological characterization at the interprotrusion space. SEM images at different magnifications (**A**, scale bar=50 μm; **B**, scale bar=5 μm; **C**, scale bar=1 μm). **D**, Microparticle distribution (N=50; BIC, Bayesian Information Criteria).

To determine the effect of the film coating on important wound dressing properties, it was evaluated the changes in swelling ratio, water vapor transmission, and thermal insulation for coated and uncoated constructs. The LbL film coatings led to significant increases in the swelling of the dressings (**Figure 3.18A**), achieving a 1.6-fold increase in the A10 type constructs over its uncoated control. The combination of the plasma treatment and LbL functionalization, allows the generation of a range of wound dressings with different absorption capabilities, a versatile feature for physicians selecting the proper wound dressing for a patient.[85]

As important as the ability to promote the uptake of wound exudate, the water vapor transmission rate (WVTR) is critical when selecting a wound dressing. Ideal dressings must favor the presence of a moist wound environment to avoid dehydration and dressing adherence, while avoiding maceration of the healthy surrounding tissue.[86] Non-plasma treated three-dimensiona wound dressings consistently demonstrated increased WVTR compared to commercially available dressings (**Figure 3.18B**), which is primarily due to the 3DECs porosity and thickness. Incorporation of LbL in 3DECs caused a significant drop in WVTR, which it was hypothesized is due to increased water retention within the $(CHI/HA)_{10}$ film due to swelling and the film's role as a barrier to diffusion. The thermal insulation of a recovering wound has also been highlighted as an

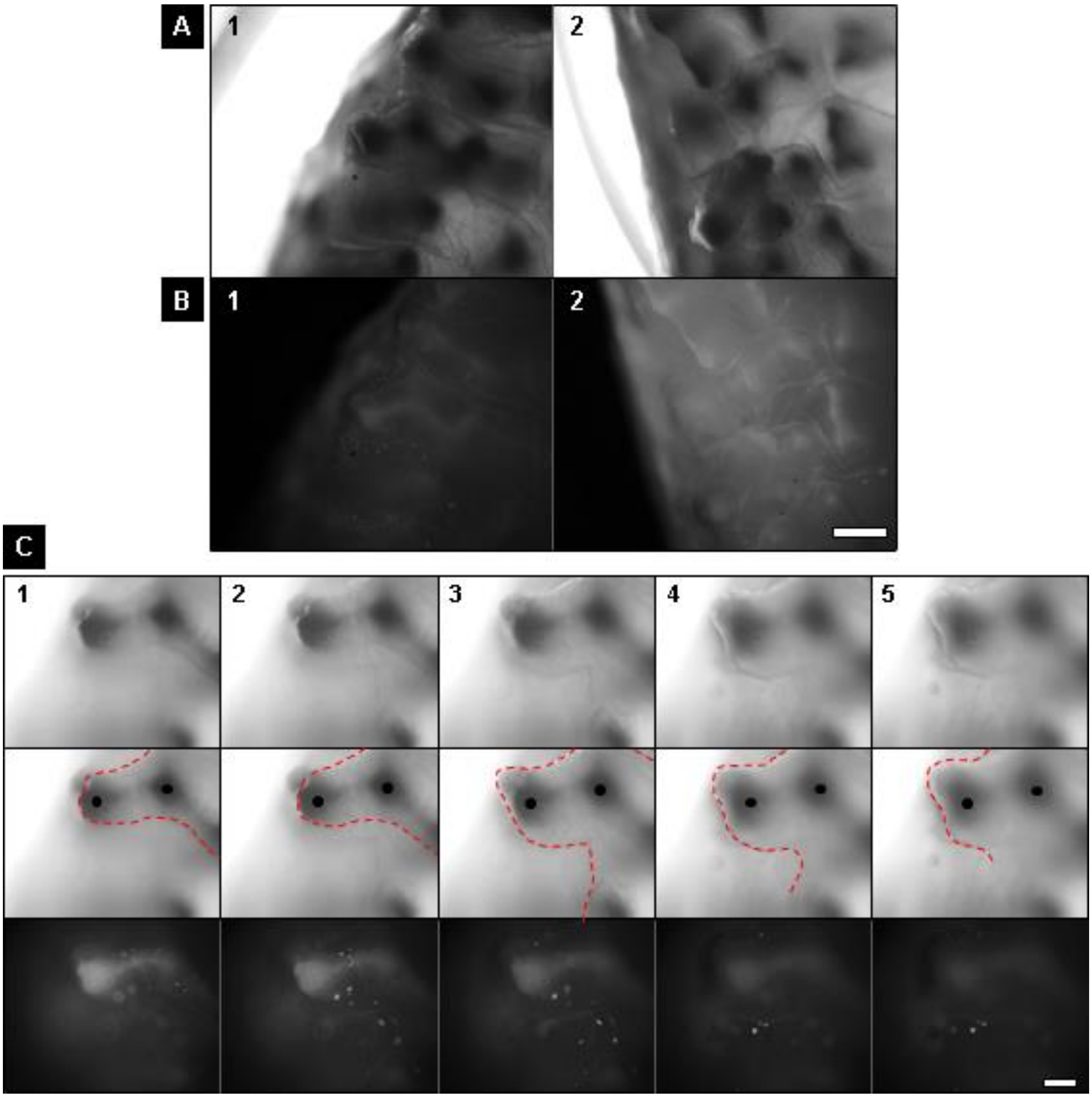

Figure 3.16 Phase contrast and fluorescent microscopy images of cell seeded 3DMECs top side evidencing the LbL film swelling (**A,B** scale bar=500 μm; **C**, scale bar=200 μm). Dark dots were placed at the protrusions center.

important feature in the design of wound dressings which can significantly impact wound healing.[87-89] When wound-tissue temperature falls below 33 ºC neutrophil, fibroblast and epithelial cell activity decreases,[90] leading to a poor healing. In our assessment (**Figure 3.18C**), both 3DECs and 3DMECs have shown the ability to thermally insulate a wound bed environment.

After demonstrating that the $(CHI/HA)_{10}$ film coating can significantly reduce cell adhesion to the coated bandage while maintaining its desired properties as a wound dressing, we set out to determine if the incorporated materials, in particular HA, had an *in vitro* healing benefit. Hyaluronic acid has been reported to interact with cell surface receptors as CD44, RHAMM and ICAM-1, favoring cellular proliferation and migration.[82] The release of fluorescent labeled HA from hydrated bandages was evaluated in PBS and in cell conditioned media at 37 ºC for 7 days (**Figure 3.19A**).

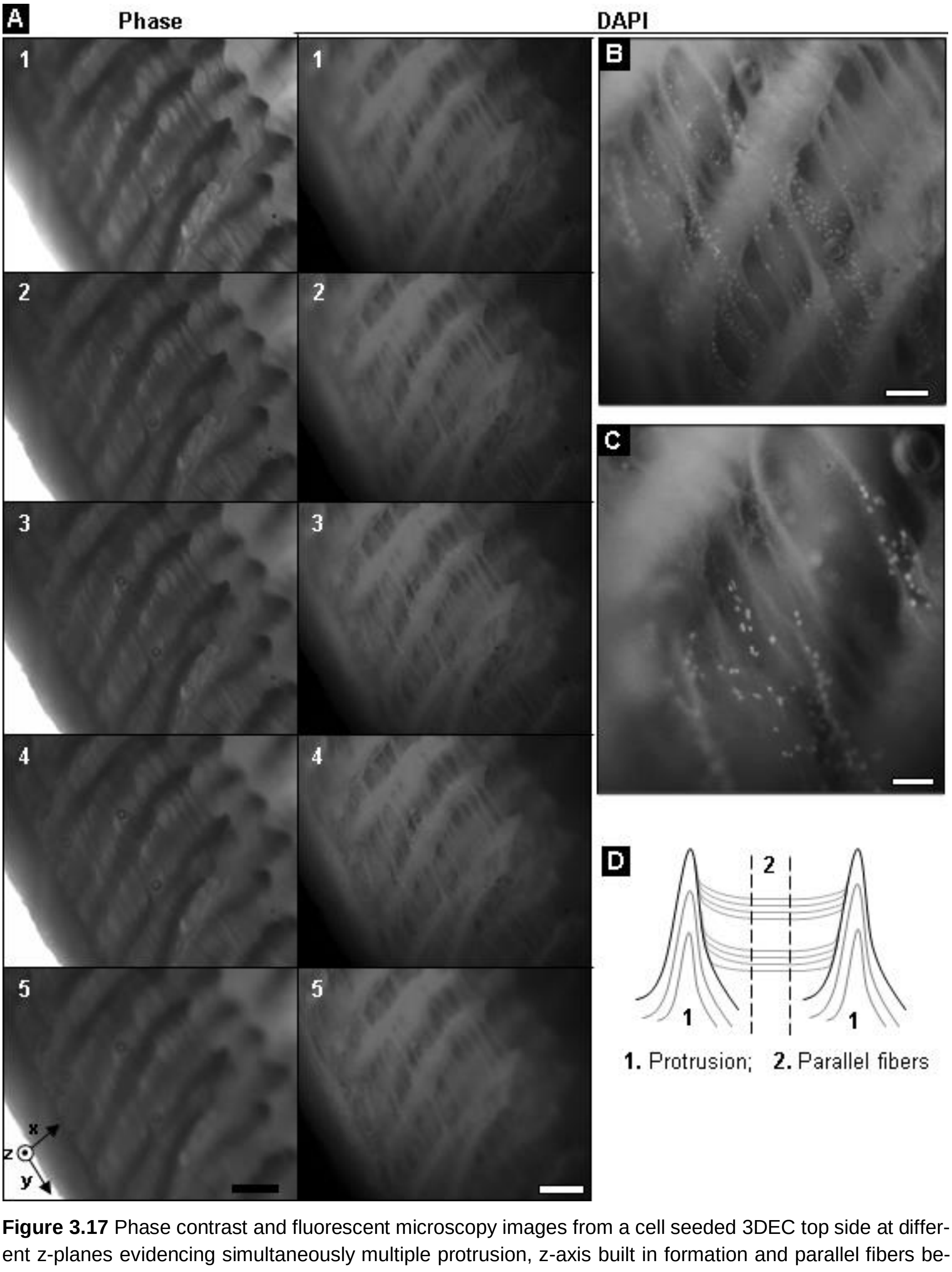

Figure 3.17 Phase contrast and fluorescent microscopy images from a cell seeded 3DEC top side at different z-planes evidencing simultaneously multiple protrusion, z-axis built in formation and parallel fibers between protrusions (**A**, scale bar=500 μm; **B**, scale bar=200 μm; **C**, scale bar=100 μm). **D**, Scheme regarding the presence of parallel fibers between protrusions.

Release of HA from 3DMECs was sustained for the seven day period with a linear profile regardless of the type of construct or release media. A-type 3DECs were observed to release more HA during the study period in both environments, releasing nearly all of the coated HA in cell conditioned media (**Figure 3.19B**). A10-type dressings showed the slowest and most sustained HA

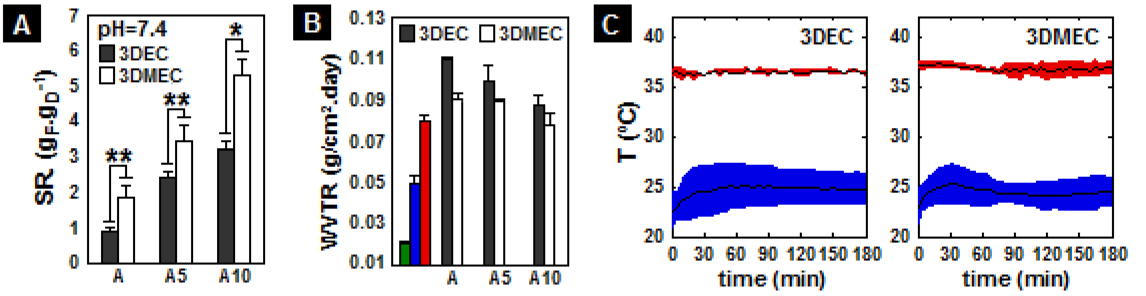

Figure 3.18 LbL-film incorporation influence in dressing properties. **A**, Swelling ratio (*, p-value < 0.01; **, p-value < 0.025). **B**, Water vapor transmission rate (Green, Normal skin; Blue, Tegaderm®; Red, OpSite®). **C**, Thermal insulation of A-type three-dimensional construct in which red stands as the wound bed temperature, and blue stands as the temperature at the constructs top side. Chapter 1 key features achieved: 1 (Prevents dehydration), 3 (Provides absorption) and 14 (Unchanged proprieties according to temperature and humidity)

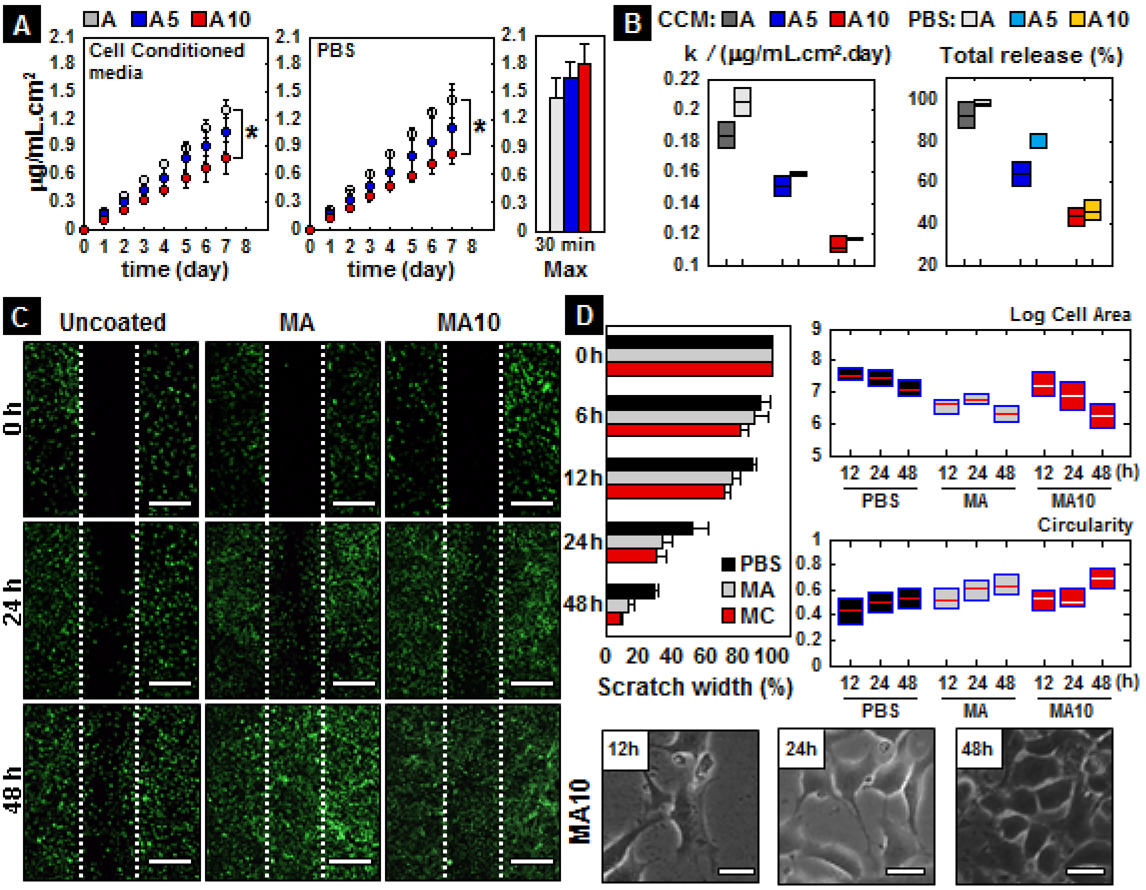

Figure 3.19 Hyaluronic acid release assessment. **A**, Hyaluronic acid release in cell conditioned media (CCM), in PBS (*, p-value < 0.025) and after sonicating samples during 30 min. **B**, Release kinetic constants (k) and total percentage of release at day 7 estimation with 95% confidence bounds. **C**, Wound scratch assay of uncoated, A-type and A10-type 3DMECs. **D**, Gap closure dynamics and cell shape analysis at the scratch. Chapter 1 key features achieved: 6 (Non-adherent) and 16 (Wound sealing, lateral fluid impermeability with maceration minimization),

release comparatively to the other specimens. Due to their distinct HA incorporation and release profiles, uncoated, A-type, and A10-type three dimensional scaffolds were used for *in vitro* wound scratch assays.

In general, groups treated with release media from 3DECs coated with $(CHI/HA)_{10}$ were observed to close the scratch faster than uncoated control bandage treated groups (**Figure 3.19C,D**). After 48 hours, A-type and A10-type 3DMECs reached 87 ± 4 % and 90 ± 0.5 % of wound closure respectively, in contrast to 70 ± 2 % observed in groups treated with the uncoated 3DECs. Cell shape was assessed within the scratch region to help determine the cellular behavior and proliferation within the defect. Groups treated with 3DMECs showed significantly reduced cell areas and increased cell circularity compared to uncoated controls after only 12 hours and was sustained for the two day test period. This supports the hypothesis that the released material promotes cell proliferation, suggesting that confluence is reached sooner when using these LbL coated constructs.

3.4 CONCLUDING REMARKS

In this chapter it was produced for the first time bioinspired three-dimensional multilayered electrospun constructs. The generated scaffolds are characterized by a flat bottom side and a top side populated with fibrous-based microsized protrusions, which have a median inter-protusion distance of 528 µm and a median peak density of 73 peaks per cm^2. These constructs can be readily produced by taking advantage of the self-organization phenomena when electrospinning PCL nanofibers. As prepared these materials are capable of withstanding $(11.0 \pm 0.3)\times10^4$ kg per m^2 after 14 days of hydration. Their unique asymmetry promotes unidirectional liquid uptake (from the top side towards the inner structure of the materials), while being impermeable to potential external liquid-forms of infection at its bottom side. Nevertheless, such constructs also observed the high porosity (89.9%) and high surface area ($1.44\ m^2.g^{-1}$) characteristic of traditional electrospun mats. To incorporate broader functionality into these dressings it was used spray-LbL assembly to create an ultrathin coating on the top surface of the scaffolds consisting in chitosan and hyaluronic acid, two biocompatible polymers widely used in the field of wound care. This coating reduced cellular adhesion on the constructs throughout the generation of a rubbery film layer, which would also provide a means to tailor water vapor transmission and swelling ratio for different wound environments specifications (e.g. ischemic wounds, I/II/III-degree burns, etc.). Moreover, the three-dimensional fibrous constructs treated with LbL were able to achieve 90 ± 0.5 % of wound closure within 48 hours, comparatively to 70 ± 2 % verified for uncoated dressings. This work provides an important first step in producing electrospun wound dressings that can better meet the needs of medical practitioners and improve patient care, while taking advantages of already, but limited, two-dimensional fibrous bandages and fabrication methods.

3.5 CHAPTER REFERENCES

[1] Wu SZ, Wu D, Yao J, Chen QD, Wang JN, Niu LG, et al. One-step preparation of regular micropearl arrays for two-direction controllable anisotropic wetting. Langmuir 2010;26:12012-6.

[2] Li Y, Zhang J, Yang B. Antireflective surfaces based on biomimetic nanopillared arrays. Nano Today 2010;5:117-27.

[3] Downing TL, Soto J, Morez C, Houssin T, Fritz A, Yuan F, et al. Biophysical regulation of epigenetic state and cell reprogramming. Nat Mater 2013;12:1154-62.

[4] Viswanathan P, Ondeck MG, Chirasatitsin S, Ngamkham K, Reilly GC, Engler AJ, et al. 3D surface topology guides stem cell adhesion and differentiation. Biomaterials 2015;52:140-7.

[5] Yin Z, Chen X, Song HX, Hu JJ, Tang QM, Zhu T, et al. Electrospun scaffolds for multiple tissues regeneration in vivo through topography dependent induction of lineage specific differentiation. Biomaterials 2015;44:173-85.

[6] Morgado PI, Aguiar-Ricardo A, Correia IJ. Asymmetric membranes as ideal wound dressings: An overview on production methods, structure, properties and performance relationship. Journal of Membrane Science 2015;490:139-51.

[7] Morgado PI, Lisboa PF, Ribeiro MP, Miguel SP, Simões PC, Correia IJ, et al. Poly(vinyl alcohol)/chitosan asymmetrical membranes: Highly controlled morphology toward the ideal wound dressing. Journal of Membrane Science 2014;469:262-71.

[8] Wegst UG, Bai H, Saiz E, Tomsia AP, Ritchie RO. Bioinspired structural materials. Nat Mater 2015;14:23-36.

[9] Rees A, Powell LC, Chinga-Carrasco G, Gethin DT, Syverud K, Hill KE, et al. 3D Bioprinting of Carboxymethylated-Periodate Oxidized Nanocellulose Constructs for Wound Dressing Applications. Biomed Res Int 2015;2015:925757.

[10] Bhardwaj N, Kundu SC. Electrospinning: A fascinating fiber fabrication technique. Biotechnology Advances 2010;28:325-47.

[11] Agarwal S, Greiner A, Wendorff JH. Functional materials by electrospinning of polymers. Progress in Polymer Science 2013;38:963-91.

[12] Zhou X, Dai Z, Liu S, Bao J, Guo Y-G. Ultra-Uniform SnOx/Carbon Nanohybrids toward Advanced Lithium-Ion Battery Anodes. Advanced Materials 2014;26:3943-9.

[13] Persano L, Camposeo A, Tekmen C, Pisignano D. Industrial Upscaling of Electrospinning and Applications of Polymer Nanofibers: A Review. Macromolecular Materials and Engineering 2013;298:504-20.

[14] Lee BL-P, Jeon H, Wang A, Yan Z, Yu J, Grigoropoulos C, et al. Femtosecond laser ablation enhances cell infiltration into three-dimensional electrospun scaffolds. Acta Biomaterialia 2012;8:2648-58.

[15] Jenness NJ, Wu Y, Clark RL. Fabrication of three-dimensional electrospun microstructures using phase modulated femtosecond laser pulses. Materials Letters 2012;66:360-3.

[16] Sun B, Long YZ, Zhang HD, Li MM, Duvail JL, Jiang XY, et al. Advances in three-dimensional nanofibrous macrostructures via electrospinning. Progress in Polymer Science 2014;39:862-90.

[17] Bonino CA, Efimenko K, Jeong SI, Krebs MD, Alsberg E, Khan SA. Three-Dimensional Electrospun Alginate Nanofiber Mats via Tailored Charge Repulsions. Small 2012;8:1928-36.

[18] Sun B, Long Y-Z, Yu F, Li M-M, Zhang H-D, Li W-J, et al. Self-assembly of a three-dimensional fibrous polymer sponge by electrospinning. Nanoscale 2012;4:2134-7.

[19] Liang T, Mahalingam S, Edirisinghe M. Creating “hotels” for cells by electrospinning honeycomb-like polymeric structures. Materials Science and Engineering: C 2013;33:4384-91.

[20] Nedjari S, Schlatter G, Hébraud A. Thick electrospun honeycomb scaffolds with controlled pore size. Materials Letters 2015;142:180-3.

[21] Okuzaki H, Takahashi T, Miyajima N, Suzuki Y, Kuwabara T. Spontaneous Formation of Poly(p-phenylenevinylene) Nanofiber Yarns through Electrospinning of a Precursor. Macromolecules 2006;39:4276-8.

[22] Reis TC, Correia IJ, Aguiar-Ricardo A. Electrodynamic tailoring of self-assembled three-dimensional electrospun constructs. Nanoscale 2013;5:7528-36.

[23] Sun XY, Shankar R, Börner HG, Ghosh TK, Spontak RJ. Field-Driven Biofunctionalization of Polymer Fiber Surfaces during Electrospinning. Advanced Materials 2007;19:87-91.

[24] Sionkowska A. Current research on the blends of natural and synthetic polymers as new biomaterials: Review. Progress in Polymer Science 2011;36:1254-76.

[25] Huang J-C. Carbon black filled conducting polymers and polymer blends. Advances in Polymer Technology 2002;21:299-313.

[26] Sill TJ, von Recum HA. Electrospinning: Applications in drug delivery and tissue engineering. Biomaterials 2008;29:1989-2006.

[27] Richardson JJ, Björnmalm M, Caruso F. Technology-driven layer-by-layer assembly of nanofilms. Science 2015;348.

[28] Hammond PT. Layer-by-layer approaches to staging medicine from surfaces. AIChE Journal 2015;61:1106-17.

[29] Borges J, Mano JF. Molecular Interactions Driving the Layer-by-Layer Assembly of Multilayers. Chemical Reviews 2014;114:8883-942.

[30] Shah NJ, Hyder MN, Moskowitz JS, Quadir MA, Morton SW, Seeherman HJ, et al. Surface-mediated bone tissue morphogenesis from tunable nanolayered implant coatings. Sci Transl Med 2013;5:191ra83.

[31] Castleberry S, Wang M, Hammond PT. Nanolayered siRNA Dressing for Sustained Localized Knockdown. ACS Nano 2013;7:5251-61.

[32] DeMuth PC, Min Y, Huang B, Kramer JA, Miller AD, Barouch DH, et al. Polymer multilayer tattooing for enhanced DNA vaccination. Nat Mater 2013;12:367-76.

[33] DeMuth PC, Su X, Samuel RE, Hammond PT, Irvine DJ. Nano-Layered Microneedles for Transcutaneous Delivery of Polymer Nanoparticles and Plasmid DNA. Advanced Materials 2010;22:4851-6.

[34] Hammond PT. Building biomedical materials layer-by-layer. Materials Today 2012;15:196-206.

[35] Chen Y, Chew YT, Khoo BC. Heat transfer and flow structure in turbulent channel flow over protrusions. International Journal of Heat and Mass Transfer 2013;66:177-91.

[36] Sofokleous P, Stride E, Edirisinghe M. Preparation, characterization, and release of amoxicillin from electrospun fibrous wound dressing patches. Pharm Res 2013;30:1926-38.

[37] Lowe A, Bills J, Verma R, Lavery L, Davis K, Balkus KJ, Jr. Electrospun nitric oxide releasing bandage with enhanced wound healing. Acta biomaterialia 2015;13:121-30.

[38] Huang R, Li W, Lv X, Lei Z, Bian Y, Deng H, et al. Biomimetic LBL structured nanofibrous matrices assembled by chitosan/collagen for promoting wound healing. Biomaterials 2015;53:58-75.

[39] Sofokleous P, Stride E, Bonfield W, Edirisinghe M. Design, construction and performance of a portable handheld electrohydrodynamic multi-needle spray gun for biomedical applications. Mater Sci Eng C Mater Biol Appl 2013;33:213-23.

[40] Wade RJ, Burdick JA. Advances in nanofibrous scaffolds for biomedical applications: From electrospinning to self-assembly. Nano Today 2014;9:722-42.

[41] Wang X, Ding B, Sun G, Wang M, Yu J. Electro-spinning/netting: A strategy for the fabrication of three-dimensional polymer nano-fiber/nets. Progress in Materials Science 2013;58:1173-243.

[42] Zhang S, Karaca BT, VanOosten SK, Yuca E, Mahalingam S, Edirisinghe M, et al. Coupling Infusion and Gyration for the Nanoscale Assembly of Functional Polymer Nanofibers Integrated with Genetically Engineered Proteins. Macromolecular Rapid Communications 2015;36:1322-8.

[43] Mahalingam S, Edirisinghe M. Forming of Polymer Nanofibers by a Pressurised Gyration Process. Macromolecular Rapid Communications 2013;34:1134-9.

[44] Krogman KC, Lowery JL, Zacharia NS, Rutledge GC, Hammond PT. Spraying asymmetry into functional membranes layer-by-layer. Nat Mater 2009;8:512-8.

[45] Shukla A, Fang JC, Puranam S, Jensen FR, Hammond PT. Hemostatic Multilayer Coatings. Advanced Materials 2012;24:492-6.

[46] Liu W, Sun S, Cao Z, Zhang X, Yao K, Lu WW, et al. An investigation on the physicochemical properties of chitosan/DNA polyelectrolyte complexes. Biomaterials 2005;26:2705-11.

[47] Lapčík L, Lapčík L, De Smedt S, Demeester J, Chabreček P. Hyaluronan: Preparation, Structure, Properties, and Applications. Chemical Reviews 1998;98:2663-84.

[48] Lowery JL, Datta N, Rutledge GC. Effect of fiber diameter, pore size and seeding method on growth of human dermal fibroblasts in electrospun poly(ε-caprolactone) fibrous mats. Biomaterials 2010;31:491-504.

[49] Nunes de Carvalho C, Lavareda G, Parreira P, Valente J, Amaral A, Botelho do Rego AM. Influence of oxygen partial pressure on the properties of undoped InOx films deposited at room temperature by rf-PERTE. Journal of Non-Crystalline Solids 2008;354:1643-7.

[50] Hantsche H. High resolution XPS of organic polymers, the scienta ESCA300 database. By G. Beamson and D. Briggs, Wiley, Chichester 1992, 295 pp., hardcover, £ 65.00, ISBN 0-471-93592-1. Advanced Materials 1993;5:778-.

[51] Muñoz-Bonilla A, Cerrada M, Fernández-García M, Kubacka A, Ferrer M, Fernández-García M. Biodegradable Polycaprolactone-Titania Nanocomposites: Preparation, Characterization and Antimicrobial Properties. International Journal of Molecular Sciences 2013;14:9249-66.

[52] Christensen PA, Egerton TA, Martins-Franchetti SM, Jin C, White JR. Photodegradation of polycaprolactone/poly(vinyl chloride) blend. Polymer Degradation and Stability 2008;93:305-9.

[53] Kulkarni M, O'Loughlin A, Vazquez R, Mashayekhi K, Rooney P, Greiser U, et al. Use of a fibrin-based system for enhancing angiogenesis and modulating inflammation in the treatment of hyperglycemic wounds. Biomaterials 2014;35:2001-10.

[54] Kramer N, Walzl A, Unger C, Rosner M, Krupitza G, Hengstschläger M, et al. In vitro cell migration and invasion assays. Mutation Research/Reviews in Mutation Research 2013;752:10-24.

[55] Liang CC, Park AY, Guan JL. In vitro scratch assay: a convenient and inexpensive method for analysis of cell migration in vitro. Nat Protoc 2007;2:329-33.

[56] Woodruff MA, Hutmacher DW. The return of a forgotten polymer—Polycaprolactone in the 21st century. Progress in Polymer Science 2010;35:1217-56.

[57] Ahirwal D, Hebraud A, Kadar R, Wilhelm M, Schlatter G. From self-assembly of electrospun nanofibers to 3D cm thick hierarchical foams. Soft Matter 2013;9:3164-72.

[58] Abdelrahman T, Newton H. Wound dressings: principles and practice. Surgery (Oxford) 2011;29:491-5.

[59] Jones V, Grey JE, Harding KG. Wound dressings2006.

[60] Farrar D, Stephens P, Thomas J, Motlagh H, Percival S, Thomas J, et al. Contributor contact details. In: Farrar D, editor. Advanced Wound Repair Therapies: Woodhead Publishing; 2011. p. xiii-xvii.

[61] Lam CXF, Hutmacher DW, Schantz J-T, Woodruff MA, Teoh SH. Evaluation of polycaprolactone scaffold degradation for 6 months in vitro and in vivo. Journal of Biomedical Materials Research Part A 2009;90A:906-19.

[62] Grafahrend D, Heffels K-H, Beer MV, Gasteier P, Möller M, Boehm G, et al. Degradable polyester scaffolds with controlled surface chemistry combining minimal protein adsorption with specific bioactivation. Nat Mater 2011;10:67-73.

[63] Grey CP, Newton ST, Bowlin GL, Haas TW, Simpson DG. Gradient fiber electrospinning of layered scaffolds using controlled transitions in fiber diameter. Biomaterials 2013;34:4993-5006.

[64] Hohman MM, Shin M, Rutledge G, Brenner MP. Electrospinning and electrically forced jets. II. Applications. Physics of Fluids (1994-present) 2001;13:2221-36.

[65] Greiner A, Wendorff JH. Electrospinning: A Fascinating Method for the Preparation of Ultrathin Fibers. Angewandte Chemie International Edition 2007;46:5670-703.

[66] Yang SY, O'Cearbhaill ED, Sisk GC, Park KM, Cho WK, Villiger M, et al. A bio-inspired swellable microneedle adhesive for mechanical interlocking with tissue. Nat Commun 2013;4:1702.

[67] France RM, Short RD. Plasma Treatment of Polymers: The Effects of Energy Transfer from an Argon Plasma on the Surface Chemistry of Polystyrene, and Polypropylene. A High-Energy Resolution X-ray Photoelectron Spectroscopy Study. Langmuir 1998;14:4827-35.

[68] Haynes WM, Lide DR. CRC handbook of chemistry and physics : a ready-reference book of chemical and physical data. Boca Raton, Fla.: CRC Press; 2011.

[69] Martins A, Pinho ED, Faria S, Pashkuleva I, Marques AP, Reis RL, et al. Surface modification of electrospun polycaprolactone nanofiber meshes by plasma treatment to enhance biological performance. Small 2009;5:1195-206.

[70] Neel EAA, Cheema U, Knowles JC, Brown RA, Nazhat SN. Use of multiple unconfined compression for control of collagen gel scaffold density and mechanical properties. Soft Matter 2006;2:986-92.

[71] Jin G, Prabhakaran MP, Kai D, Annamalai SK, Arunachalam KD, Ramakrishna S. Tissue engineered plant extracts as nanofibrous wound dressing. Biomaterials 2013;34:724-34.

[72] Pailler-Mattei C, Bec S, Zahouani H. In vivo measurements of the elastic mechanical properties of human skin by indentation tests. Med Eng Phys 2008;30:599-606.

[73] Hopp I, Michelmore A, Smith LE, Robinson DE, Bachhuka A, Mierczynska A, et al. The influence of substrate stiffness gradients on primary human dermal fibroblasts. Biomaterials 2013;34:5070-7.

[74] Ovington LG. Advances in wound dressings. Clinics in Dermatology 2007;25:33-8.

[75] Rieger KA, Birch NP, Schiffman JD. Designing electrospun nanofiber mats to promote wound healing - a review. Journal of Materials Chemistry B 2013;1:4531-41.

[76] Markicevic B, Hoff K, Li H, Zand AR, Navaz HK. Capillary force driven primary and secondary unidirectional flow of wetting liquid into porous medium. International Journal of Multiphase Flow 2012;39:193-204.

[77] Kharaziha M, Nikkhah M, Shin S-R, Annabi N, Masoumi N, Gaharwar AK, et al. PGS:Gelatin nanofibrous scaffolds with tunable mechanical and structural properties for engineering cardiac tissues. Biomaterials 2013;34:6355-66.

[78] McManus MC, Boland ED, Koo HP, Barnes CP, Pawlowski KJ, Wnek GE, et al. Mechanical properties of electrospun fibrinogen structures. Acta Biomaterialia 2006;2:19-28.

[79] Price RD, Myers S, Leigh IM, Navsaria HA. The role of hyaluronic acid in wound healing: assessment of clinical evidence. Am J Clin Dermatol 2005;6:393-402.

[80] Ueno H, Mori T, Fujinaga T. Topical formulations and wound healing applications of chitosan. Advanced Drug Delivery Reviews 2001;52:105-15.

[81] Anitha A, Sowmya S, Kumar PTS, Deepthi S, Chennazhi KP, Ehrlich H, et al. Chitin and chitosan in selected biomedical applications. Progress in Polymer Science 2014;39:1644-67.

[82] Collins MN, Birkinshaw C. Hyaluronic acid based scaffolds for tissue engineering—A review. Carbohydrate Polymers 2013;92:1262-79.

[83] Zeng X, Li S. Multiscale modeling and simulation of soft adhesion and contact of stem cells. Journal of the Mechanical Behavior of Biomedical Materials 2011;4:180-9.

[84] Miller-Chou BA, Koenig JL. A review of polymer dissolution. Progress in Polymer Science 2003;28:1223-70.

[85] Sussman C. Wound care: a collaborative practice manual for physical therapists and nurses. USA: Lippincott Williams & Wilkins; 2007.

[86] Wu P, Fisher AC, Foo PP, Queen D, Gaylor JDS. In vitro assessment of water vapour transmission of synthetic wound dressings. Biomaterials 1995;16:171-5.

[87] Kloth LC, Berman JE, Dumit-Minkel S, Sutton CH, Papanek PE, Wurzel J. Effects of a normothermic dressing on pressure ulcer healing. Advances in skin & wound care 2000;13:69-74.

[88] McCulloch J, Knight CA. Noncontact normothermic wound therapy and offloading in the treatment of neuropathic foot ulcers in patients with diabetes. Ostomy Wound Manage 2002;48:38-44.

[89] Whitney JD, Salvadalena G, Higa L, Mich M. Treatment of pressure ulcers with noncontact normothermic wound therapy: healing and warming effects. Journal of wound, ostomy, and continence nursing : official publication of The Wound, Ostomy and Continence Nurses Society / WOCN 2001;28:244-52.

[90] McGuiness W, Vella E, Harrison D. Influence of dressing changes on wound temperature. Journal of wound care 2004;13:383-5.

4

Concluding Remarks

SUMMARY

This chapter summarizes the principal findings of this thesis. It is reviewed the electrostatic self-assembled fabrication process of the generated wound dressings, while it is provided a clear understanding of the process. Optimization and further guidance for the production of future constructs are provided as well. Herein it is also highlighted the surface functionalization of the wound dressing substrates through the *layer-by-layer* technique, preceded by the characterization of the final product as a wound dressing. Nevertheless, and regarding the interest of those that aim to continue the work here reported, further guidance is also provided regarding key aspects for an ideal wound dressing.

4.1 CONCLUDING REMARKS

Upon the clear demonstration in Chapter 1 that there is no such thing as an “ideal” wound dressing, the strategy followed in this thesis was the conceptualization and fabrication of a common wound dressing substrate that can be readily tailored throughout common techniques according to the wound to be treated. It was reviewed in Chapter 1 the most important functional requirements for a wound dressing, while such requirements were properly framed according to the biochemical pathways of the regeneration process. From the very beginning of the work plan under the scope of this thesis, sixteen key features were defined (**Figure 1.5**), and they will be now contextualized.

Chapter 2 was dedicated to report the fabrication method of the wound dressing substrate. The writer envisioned a process based on electrostatic driven self-assembly to generate asymmetrical wound dressing substrates, where two distinct morphologies could be obtained in the same substrate. At the top side of the dressing, it was planned to conceive a smooth and hydrophobic surface that would hinder particulate contamination and the imbibition of external fluids. On the other hand, at the bottom side of the dressing, the writer envisioned a structure that could enhance the interaction between the wound injured surface and the proposed dressing. By coupling the information within in Chapter 2 retained through simulations and experimental data, it was understood that the self-assembly mechanism relies on a balance between attractive and repulsive electrostatic forces. Initially, the electrospun fibers form a flat mesh while high density fiber regions are favored due to a random fiber deposition. From the moment that the fibers reach the grounded collector, their charges are conducted away turning these electrospun elements neutral. However, the necessary electric field to continuously electrospin new fibers will polarize the already collected ones. Such fibers acquire a negatively charged network oriented toward the nozzle, which will attract the positive incoming aerial and disordered fibers towards their position. This *in situ* polarization degree is strengthened by higher amounts of clustered fibers, and therefore the initial high density fibrous regions are the preliminary motifs for the self-assembly mechanism. As such regions increase their *in situ* polarization electrostatic repulsive forces will appear, favoring a competitive growth of these self-assembled fibrous clusters. It was also verified that very intense fields or high concentrated solutions favor strong polarization degrees and the locally assembled fibrous-based constructs cannot self-close, appearing as almost straightforward lines. On the other hand, weak fields or diluted polymer solutions allow a higher bending of the locally assembled fibrous-based constructs, contributing to the production of resembling circular-like cells. By tuning the *in situ* polarization, through controlling the electric field intensity, time of production, polymer solution concentration, environmental temperature and relative humidity, it is possible to microtexturize electrospun mats that will be used as wound dressing substrates. The author suggests those that want to continue his work to take in consideration the previously highlighted importance of the dipolar moment when self-assembling novel electrospun substrates (**Table 4.1**).

In Chapter 3 the fabricated scaffolds characterized by a flat bottom side and a top side populated with fibrous-based microsized protrusions, which have a median inter-protusion distance of 528 µm and a median peak density of 73 peaks per cm^2, are functionalized through the *layer-by-layer* technique. The use of PCL allows the fabrication of wound dressings substrates able to be sterilize (*key feature 2),* offering as a starting point a FDA approved material that is non-toxic (*key feature 7*), non-allergenic (*key feature 8*) and non-flammable (*key feature 13*), while in addition also offers a long shelf life (*key feature 15*). As prepared these materials are capable of withstanding (11.0 ± 0.3)×10^4 kg per m^2 after 14 days of hydration (*key feature 5: Good mechanical protection; key feature 11: Resists tearing*). Their unique asymmetry promotes unidirectional liquid uptake (from the top side towards the inner structure of the materials), while being impermeable to potential external liquid-forms of infection at its bottom side (*key feature 4; key feature 12*). Nevertheless, such constructs also observed the high porosity (89.9%) (*key feature 1: Permeable to oxygen*) and high surface area (1.44 m^2.g^{-1}) characteristic of traditional electrospun mats. Moreover, the generated constructs could maintain their topography regardless their conformation (flat or bent), demonstrating their suitably to conform different anatomical contours (*key feature 10*). Up to 30 days, the proposed wound dressings evidence reduced degradation and debris formation (*key feature 9*). The reported constructs have shown a desired thermal insulation, as well as a stable behavior in aqueous environments (*key feature 14*). To incorporate broader functionality into these dressings it was used spray-LbL assembly to create an ultrathin coating on the top surface of the scaffolds. Several combinations of polyelectrolytes (chitosan, gelatin, alginate, hyaluronic acid, poly-1, linear polyethyleneimine and dextran sulphate) and layer numbers (n = 1, 3, 5 or 10) are tested regarding the physicochemical properties of the generated multi-layered films. A chitosan/hyaluronic acid reduced cellular adhesion on the constructs throughout the generation of a rubbery film layer (*key feature 6; key feature 16*), which would also provide a means to tailor water vapor transmission (*key feature 1*) and swelling ratio (*key feature 3*) for different wound environments specifications (e.g. ischemic wounds, I/II/III-degree burns, etc.). Moreover, the three-dimensional fibrous constructs treated with LbL were able to achieve 90 ± 0.5 % of wound closure within 48 hours, comparatively to 70 ± 2 % verified for uncoated dressings, while avoiding cellular adhesion.

In summary, from the design of a novel technique to produce asymmetrical substrates, towards the selection of polyelectrolytes to functionalize the wound dressings and their *in vitro* assessment, this thesis has achieved all the sixteen key features proposed. Nevertheless, and contributing to the continuation of this project, the author suggest a set of research directions towards

Table 4.1 Hansen solubility polar parameters database for future work.

Polymer	**Dispersion forces parameter,** δ_D (MPa$^{0.5}$)	**Dipolar forces parameter,** δ_P (MPa$^{0.5}$)	**Hydrogen forces parameter,** δ_H (MPa$^{0.5}$)	**Reference**
Polyisobuthylene	16,0	2,0	7,2	A
Polyisoprene	17,4	3,1	3,1	A
Polyamide 6	17,0	3,4	10,6	A
Poly(d,l-lactic acid)	15,7	3,5	11,1	B
Poly(d,l-lactide(50)-co-glycolide(50))	16,4	3,6	8,7	B
Poly(d,l-lactide(85)-co-glycolide(15))	15,8	3,7	9,5	B
Poly(a-allyl-valerolactone)	17,4	4,0	7,5	C
Polystyrene	18,5	4,5	2,9	D
Poly(b-methyl-d-valerolactone)	17,2	5,0	8,4	C
Polybutadiene	18,0	5,1	2,5	A
Polycarbonate	18,1	5,9	6,9	A
Poly(d-valerolactone)	17,8	5,9	9,2	C
Poly(b-benzyl-l-glutamate)	21,6	6,4	9,1	C
Poly(5-benzyloxy-trimethylenecarbonate)	20,1	6,5	9,5	C
Cellulose Acetate	14,9	7,1	11,1	A
Poly(b-benzyl-l-aspartate)	22,2	7,2	9,6	C
Poly(b-butyrolactone)	17,4	7,4	10,3	C
Poly[(3S)-sec-butylmorpholine-2,5-dione]	19,1	7,5	9,9	C
Poly(propyleneoxide)	16,6	7,6	7,6	C
Polycaprolactone	17,0	6,2	8,3	H
Polysulfone	19,7	8,3	8,3	A
Polyvinyl pyrrolidone	17,4	8,8	14,9	A
Poly(trimethylenecarbonate)	18,5	9,0	11,9	C
Poly(d,l-lactide(75)-co-glycolide(25))	15,8	9,1	8,7	B
Poly(vinylchloride)	19,2	9,2	7,2	A
Poly(b-propiolactone)	18,5	9,8	11,8	C
Poly(vinylacetate)	19,0	10,2	8,2	A
Poly(methylmethacrylate)	18,8	10,2	8,6	A

Poly(ethylmethacrylate)	18,8	10,8	4,3	A
Poly(ethyleneoxide)	22,2	11,2	13,2	A
Poly(N-isopropylacrylamide)	18,6	11,3	16,8	E
Poly(L-lactide)	16,3	11,7	11,5	E
Poly(vinylidenefluoride)	17,0	12,1	10,2	A
Poly(vinylidenefluoride)	17,2	12,5	9,2	F
Polyvinyl Alcohol	17,2	13,6	15,4	A
Polyacrylonitrile	21,7	14,1	9,1	A
Poly(glycolide)	19,4	14,4	14,3	C
Poly(acrylic acid)	19,1	14,7	12,4	E
Chitin	21,2	19,1	27,3	E
Dextran	24,3	19,9	22,5	G
Chitosan – 50% deacetylation degree	20,8	19,9	28,5	E
Chitosan – 60% deacetylation degree	20,7	20,1	28,7	E
Chitosan – 70% deacetylation degree	20,6	20,2	29,0	E
Chitosan – 80% deacetylation degree	20,5	20,4	29,2	E
Chitosan – 90% deacetylation degree	20,4	20,5	29,5	E
Chitosan	20,3	20,7	29,7	E
Hyaluronic Acid	25,7	21,9	27,8	E
Alginate	21,3	22,4	28,0	E

[A] Hansen CM., Hansen Solubility Parameters: A User's Handbook: CRC Press (1999); [B] Schenderlein *et al.*, International Journal of Pharmaceutics 286 (2004) 19-26; [C] Liu *et al.*, Journal of Pharmaceutical Sciences, 93 (2004) 132-143; [D] Bernardo *et al.*, European Polymer Journal 43 (2007) 938–948; [E] Mean values from the Hoy's system and Van-Krevelen-Hoftyzer calculation methods employed by the thesis' author; [F] Bottino *et al.*, Journal of Polymer Science: Part B: Polymer Physics, 26 (1988) 785-794; [G] Antoniou *et al.*, European Polymer Journal 46 (2010) 324-335 the further development of these materials. Due to the different domains embraced in this thesis, the author has divided his suggestion according to the following categories: (i) apparatus and technique improvement; (ii) new polymeric constructs and applications, and (iii) novel coatings and potential biotargets.

(i) Apparatus and technique improvement:

- Exploring inline and continuous eletrospinning platform based on rollers;
- Automation of the air inlet for better environment control.

(ii) New polymeric constructs and applications:

- Doping polymers characterized by high δ_P values with negatively charged polymeric beads, which can be further washed out;
- Exploring such electrostatic driven constructs for heat dissipation and unidirectional fluid separations.

(iii) Novel coatings and potential biotargets:

- Exploring the following tetralayers $(Cht/HA/X/Cht)_n$ or $(Cht/HA/Cht/Y)_n$, where X and Y are pharmaceutically relevant compounds for wound healing (e.g.; X = chondroitin-6-sulfate; Y = pirfenidone);
- Exploring the specific incorporation of gallic acid in the final construct for diabetic foot ulcers, which targets MMP-9.

2A

Annex I: Annex A Relative to Chapter 2

SUMMARY

This annex comprises the graphical representation of the flow curves of PCL polymer solutions in 40AA/60FA at different concentrations. In addition, SEM micrographs of as-spun poly(ε-caprolactone) and chitosan blends.

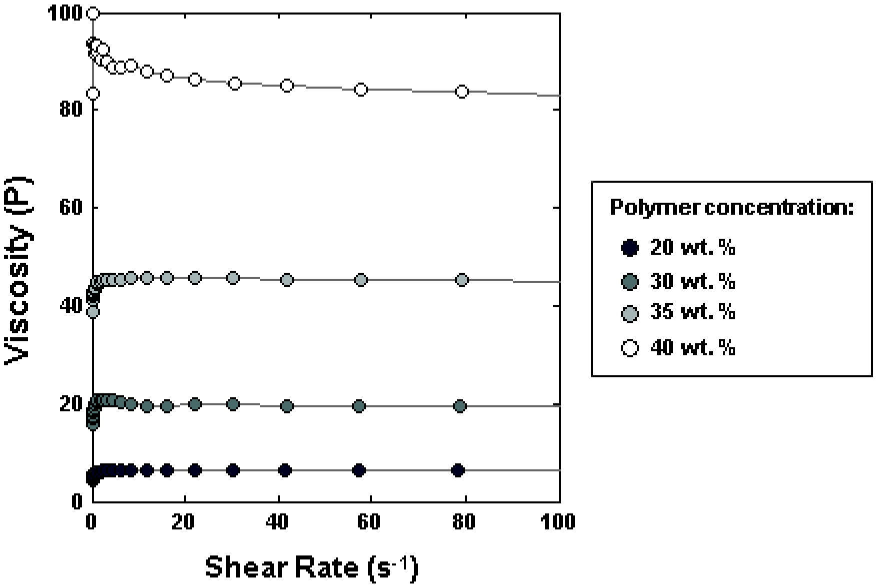

Figure 2A.1 Flow curves of PCL polymer solutions in 40AA/60FA at different concentrations.

In order to properly explore the novel electrostatic driven self-assembly mechanism, two experiments were conducted. Initially, a polymer blend of poly(ε-caprolactone) and chitosan was electrospun. Chitosan was chosen due to its reported benefit in wound dressing applications,[1-3] while it acts also as a polycation in an AA/FA media. In comparison with the reported electrospun constructs in Chapter 2, it was not observed any evidence of self-assembly at the minimum feasible electrospinning conditions, due to the charge neutralization promoted by chitosan.

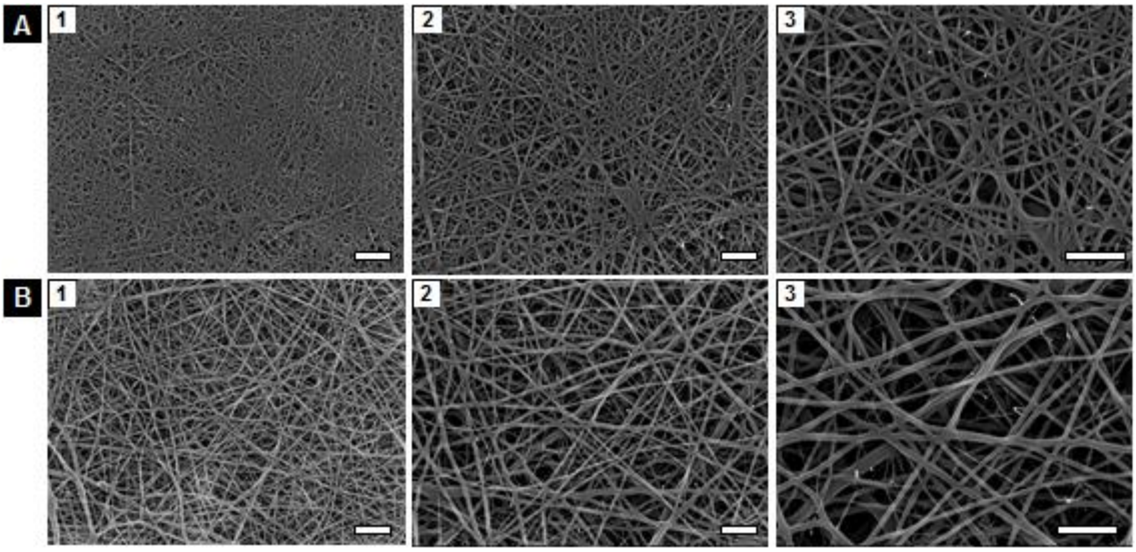

Figure 2A.2 SEM micrographs of poly(ε-caprolactone) and chitosan 95/5 % wt. polymeric blend (1, scale bar = 2 µm; 2, scale bar = 1 µm; 3, scale bar = 1 µm). **A,** The experimental conditions were 14 wt. % total polymer content in 40 AA/60 FA (v/v) at 4.2 kV.cm^{-1} (potential difference = 25 kV and nozzle–collector distance = 6 cm) with a flow rate of 0.10 mL.h^{-1}. The surrounding environment was set at 20 ºC and a humidity level of 50 ± 1%. **B,** The experimental conditions were 20 wt. % total polymer content in 40 AA/60 FA (v/v) at 4.2 kV.cm^{-1} (potential difference = 25 kV and nozzle–collector distance = 6 cm) with a flow rate of 0.10 mL.h^{-1}. The surrounding environment was set at 20 ºC and a humidity level of 50 ± 1%.

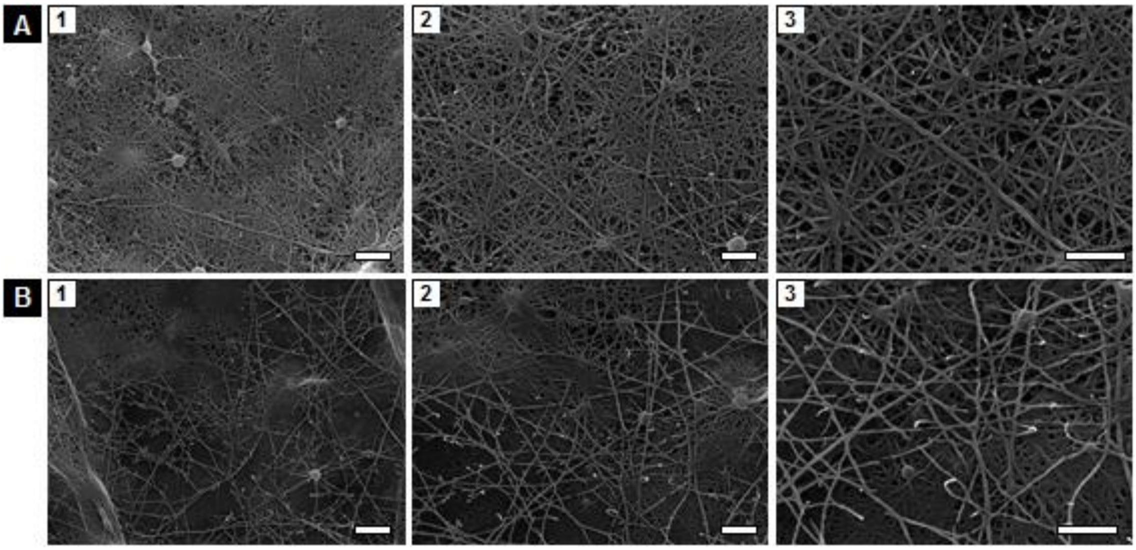

Figure 2A.3 SEM micrographs of poly(ε-caprolactone) and chitosan 90/10 % wt. polymeric blend (1, scale bar = 2 µm; 2, scale bar = 1 µm; 3, scale bar = 1 µm). **A,** The experimental conditions were 10 wt. % total polymer content in 40 AA/60 FA (v/v) at 7.0 kV.cm^{-1} (potential difference = 28 kV and nozzle–collector distance = 4 cm) with a flow rate of 0.10 mL.h^{-1}. The surrounding environment was set at 20 ºC and a humidity level of 50 ± 1%. **B,** The experimental conditions were 14 wt. % total polymer content in 40 AA/60 FA (v/v) at 7.0 kV.cm^{-1} (potential difference = 28 kV and nozzle–collector distance = 4 cm) with a flow rate of 0.10 mL.h^{-1}. The surrounding environment was set at 20 ºC and a humidity level of 50 ± 1%.

ANNEX REFERENCES

[1] Patrulea V, Ostafe V, Borchard G, Jordan O. Chitosan as a starting material for wound healing applications. European Journal of Pharmaceutics and Biopharmaceutics. 2015;97, Part B:417-26.

[2] Francesko A, Tzanov T. Chitin, Chitosan and Derivatives for Wound Healing and Tissue Engineering. In: Nyanhongo SG, Steiner W, Gübitz G, editors. Biofunctionalization of Polymers and their Applications. Berlin, Heidelberg: Springer Berlin Heidelberg; 2011. p. 1-27.

[3] Azad AK, Sermsintham N, Chandrkrachang S, Stevens WF. Chitosan membrane as a wound-healing dressing: Characterization and clinical application. Journal of Biomedical Materials Research Part B: Applied Biomaterials. 2004;69B:216-22.

3A

Annex II: Annex A Relative to Chapter 3

SUMMARY

This annex comprises the fiber distribution of the generated wound dressing substrates. Moreover, full disclosure of the reasoning behind the study of spreading and imbibition study is also provided.

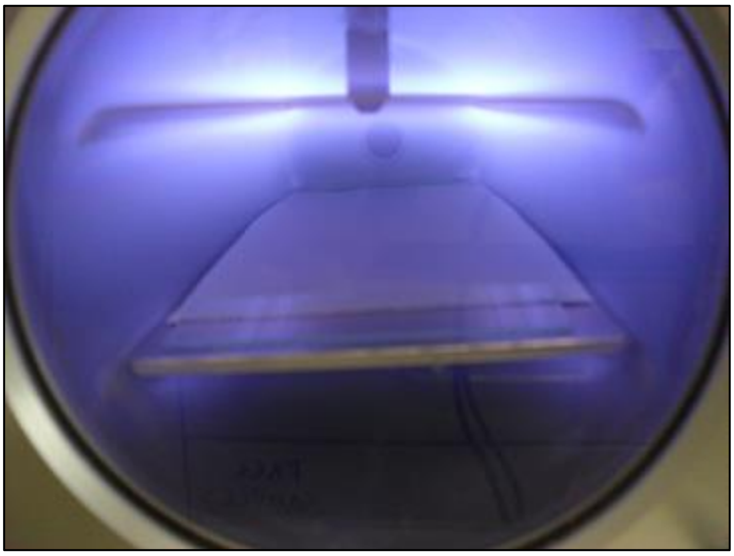

Figure 3A.1 Example of a three-dimensional electrospun constructs within the radio frequency tubular reactor for plasma treatment, placed on a non-porous metallic plate.

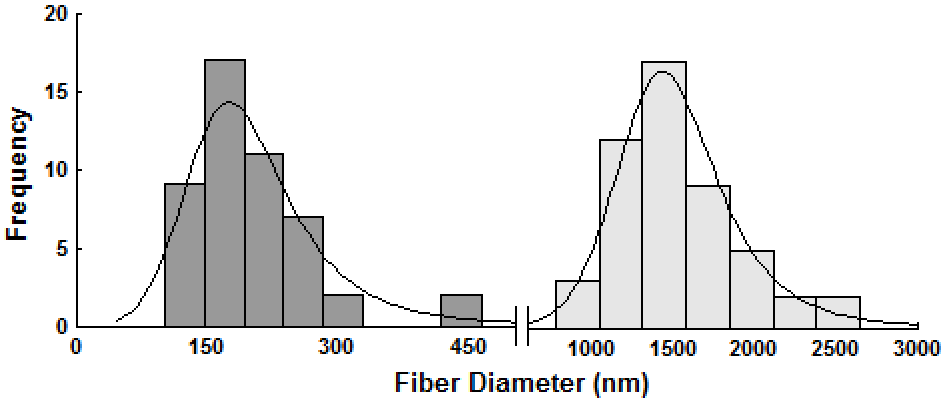

Figure 3A.2 3DECs fiber diameter distribution in the bottom side. The constructs shown a bimodal fiber distribution characterized by two independent log-logistic distribution (Population 1, BIC=742.075; Population 2, BIC=583.582).

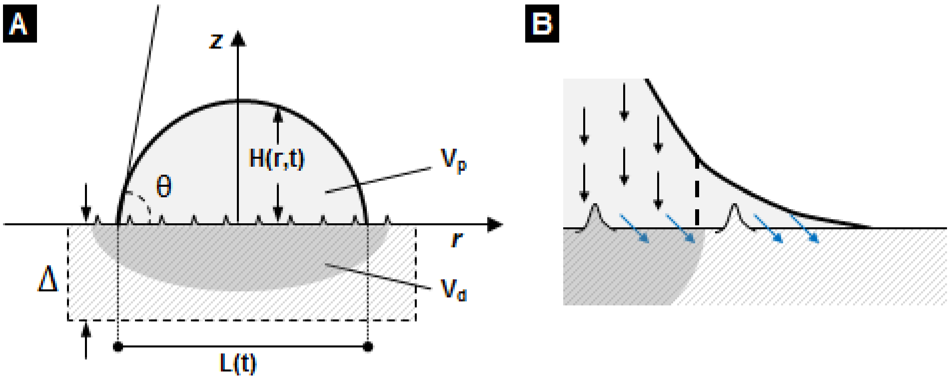

Scheme 3A.1 Resting droplet assay in a 3DEC construct. **A**, Spreading and imbibition study variables: Δ, construct thickness; θ, contact angle; H, drop height; L, drop base diameter; V_p, droplet volume; V_d, imbibed droplet volume; **B**, Oblique liquid absorption as a combination of the spreading and imbibition stages (blue arrows).

As previously highlighted, an ideal dressing is described as a construct which is impermeable to external liquids (avoiding sources of infection), while still allows the wound exudate uptake at the dressing-tissue boundary. The kinetics of wound exudate absorption over a porous wound dressing results of an interplay of two processes: i) the exudate spreading on the dressing interface, and ii) the exudate imbibition into the dressing inner structure. The superposition of the spreading and imbibition stages can be described as:

$$\frac{\mathrm{dH}}{\mathrm{dt}} = \mathrm{u}^{*} + \mathrm{u}^{0} \qquad \text{(Equation 3A. 1)}$$

where H is the height of a resting test drop in the material surface, u^* and u^0 are the velocities of the spreading and imbibition stages. It is important to note that the free energy (Φ) of a fluid drop with a volume V, in contact with a 3DEC surface, can be described as:

$$\phi = \gamma \mathrm{S} + \mathrm{P_e V} + \pi \left(\frac{\mathrm{L}}{2}\right)^2 (\gamma_{\mathrm{SL}} - \gamma_{\mathrm{SV}}) \qquad \text{(Equation 3A. 2)}$$

where γ is the liquid surface tension, S is the liquid-air interface area, P_e is the excess pressure inside the droplet, γ_{SL} and γ_{SV} are the solid-liquid and solid-vapor interfacial tension respectively. According to the previous equation, the free energy of a liquid drop is proportional to the dressing-liquid interfacial tension and it is also proportional to the square of the drop base diameter (L). As shown in **Figure 3.2**, the induced z-axis asymmetric fiber deposition in 3DECs favors the formation of a protective fibrous bottom layer due to a higher fiber density in this side. Therefore, the produced 3DECs have a pore size and hydrophobic gradient across the constructs' thickness, favoring the presence of side dependent fluid handling properties in the same material. Analogous to Martins et al.,[1] the contact angle measurements relied on the use of glycerol due to the similarity of its surface tension ($\gamma_{25^\circ C}$=62.4 mN.m^{-1}) with the water surface tension ($\gamma_{25^\circ C}$=72.0 mN.m^{-1}) and the viscous-like behavior comparatively to wound exudate. From **Figure 3.9**, one can observe that the contact angle at the 3DECs bottom side does not change regardless the time or type of construct. This observation is aligned with our earlier findings. Previously we showed that despite the use of plasma to chemically modify 3DECs, the use of a metallic plate hindered the functionalization in this region, contributing to a chemically unmodified bottom side. Therefore, A5 and A10 evidence a similar chemical composition comparatively to A at this region, leading to similar γ_{SL} and γ_{SV} values in this construct's side. In addition, it was also possible to observe earlier that the bottom side fibrous network is structurally similar in A, A5 and A10, which contributes to comparable solid-liquid interfaces. Hence, according to equation 3A.2, and since the characterization approach was the same for all the specimens, $\Phi_A \sim \Phi_{A5} \sim \Phi_{A10}$ in this region of the dressings, justifying the similar contact angles observed at this constructs side. Moreover, at this 3DECs side, the drop spreading and imbibition do not take place, leading to an unperturbed droplet base radius and profile. As stated above, the first stage of a drop motion in contact with a dressing is the spreading, meaning the motion of the three-phase contact line through the dressing surface (**Scheme 3A.1**). Such motion results from the *in situ* distortion of the droplet spherical shape caused by its capillary pressure (P_{cap}), generating a new incremental contact region where the disjoining pressure (Π) comes into play.[2] If $\Pi < P_{cap}$, the liquid in contact with the wound dressings spreads, otherwise if $\Pi > P_{cap}$ the spreading does not occur which is observed in the constructs top side. According to the DLVO theory, the total disjoining pressure is a sum of two main components: molecular (Π_m) and electrostatic (Π_e), where $\Pi(H) \sim \Pi_m(H) + \Pi_e(H)$. The molecular component of the disjoining pressure results from the van der Waals forces acting at the interfacial region,[3] while the electrostatic component results from the electrostatic interaction between the surface and contacting liquid. Moreover, the total disjoining pressure is proportional to the Gibbs free energy per unit of the interlayer area,[4] meaning that favorable dispersive and electrostatic forces, between the dressing and the contacting liquid, promote the droplet initial spreading (lower values of Π). In the case of the 3DECs bottom side, the differences in the polarity of the non-functionalized PCL fibers and glycerol hindered their intermolecular interactions, contributing for a higher disjoining pressure in comparison to the droplet capillary pressure, which inhibits the liquid spreading and imbibition at the 3DECs bottom side. Due to the z-axis asymmetric fiber deposition, the 3DECs topography at their top side is microtexturized. The observed higher hydrophilic functionalization, offer a distinct environment for liquid spreading and imbibition. According to **Figure 3.9**, it is possible to observe the contact angle decay in all the tested specimens, where the A type constructs evidence the highest contact angle measurements. Furthermore, it is also possible to verify a distinct drop profile and dynamic base diameter in all the analyzed constructs comparatively to the 3DECs top side. As stated above, the first stage in a droplet motion is the droplet's spreading. If this stage is hindered, the imbibition of the contacting liquid is compromised. In this way, in order to enhance the wound exudate uptake process, the wound dressing must initially favor the condition $\Pi < P_{cap}$, by tuning the chemical nature of the dressing while aiming to enhance the intermolecular interaction with the wound exudate. The top surface functionalization of the dressings A5 and A10, in comparison with the A type constructs, enhances the spreading stage where u^* is 1 order of magnitude faster. In addition, these plasma treated 3DECs showed a total liquid imbibition at t ~ 3 minutes, while the A type dressings present an extrapolated time value of ~ 14 minutes for total imbibition as well. While the bottom side of the produced 3DECs is structurally and chemically similar, their top sides only resemble in their structure, leading to different spreading and imbibition dynamics. Despite the chemical surface modification, the topography of the 3DECs top side reveals to be also important. When comparing the top and bottom sides of the A type wound dressings, which have the same chemical composition, it is possible to observe a distinct drop spreading and imbibition at the top side. According to Darcy's equation, the liquid imbibition over a saturated dressing can be described as:

$$\frac{\mathrm{dH}}{\mathrm{dt}} \sim \frac{\mathrm{K_p}}{\eta} * \frac{\mathrm{P_{cap}}}{\mathrm{z}} \qquad \text{(Equation 3A. 3)}$$

where $-\Delta<z<0$ and K_p is the permeability of the porous dressing. Several authors[5] have successfully correlated K_p with the porosity of fibrous materials. Generally, it is observed that as the materials’ porosity increases the construct becomes more permeable, since the resistance of the porous medium to flow decreases. Thus, the observed pore size gradient across the membranes thickness favors the wound exudate transport at the top side towards the construct bottom side, while simultaneously hinders the imbibition of external contaminated liquids on the opposite direction.

ANNEX REFERENCES

[1] Martins A, Pinho ED, Faria S, Pashkuleva I, Marques AP, Reis RL, et al. Surface Modification of Electrospun Polycaprolactone Nanofiber Meshes by Plasma Treatment to Enhance Biological Performance. Small 2009;5:1195-206.

[2] Boinovich L, Emelyanenko A. The prediction of wettability of curved surfaces on the basis of the isotherms of the disjoining pressure. Colloids and Surfaces A: Physicochemical and Engineering Aspects 2011;383:10-6.

[3] Li L, Köpf MH, Gurevich SV, Friedrich R, Chi L. Structure Formation by Dynamic Self-Assembly. Small 2012;8:488-503.

[4] Boinovich L. DLVO forces in thin liquid films beyond the conventional DLVO theory. Current Opinion in Colloid & Interface Science 2010;15:297-302.

[5] Dullien FAL. 4 - Selected Operations Involving Transport of a Single Fluid Phase through a Porous Medium. Porous Media (Second Edition). San Diego: Academic Press; 1992. p. 319-32.

3B

Annex III: Annex B Relative to Chapter 3

SUMMARY

With the secondary title “*Functional Materials According to Non-specific Cell-Material Mediating Mechanisms*”, this annex explores different polyelectrolytes and their combinations in order to select the most suitable pair for the generated wound dressing substrate in Chapter 3. The selection is primarily made by evaluating the polyelectrolytes performance in avoiding cellular adhesion on such coatings in the extended period of 10 days. Additional, molecular docking studies are performed in order to find suitable MMP-9 inhibitors, which are also compatible with the selected polyelectrolyte pair. Ten inhibitors are selected from a public database of FDA approved pharmaceutical compounds (ZINC[12], University of California, San Francisco). The selection process is based on the ligand efficiency to MPP-9 and computed Hanse parameters.

The overall performance of functional biomaterials, either responding to biomolecules or organisms, either dynamically adapting to physicochemical modifications in the surrounding environment, is governed by the established environment-material interface.[1] As the local surrounding milieu modification is often complex to achieve, scientists and engineers have relied on the use of material coating technologies as a mean to tailor the surface of constructs, redesigning their interface properties to specifically address the systems complexity. Prevalently, layer-by-layer (LbL) assembly has been used as a technique for coating constructs with ultra-thin functional films, generating novel materials suitable for drug delivery, scaffolds and biosensors.[2] Upon on LbL's simplicity and versatility, this technique comprises the alternating adsorption of material species through complementary molecular interactions such electrostatic, covalent, host-guest or hydrogen bonding, in which polymers, proteins, lipids or nucleic acids can be used as film constituents.[3-5] The sequential exposure of a construct to the species that compose the multi-layered films, has proven to generate an uniform coating independently the substrate's nature: planar, porous, or particulate;[6] even when using different LbL assembly approaches such spraying, spin-casting, dipping, microfluidics or others.[7]

LbL's modularity and adaptability of design, in addition of being an aqueous process, empower researchers with a broad set of strategies to reengineer the interface properties of biomaterials, especially when aiming to tailor cellular adhesion. For example, by changing the polyelectrolyte at the final layer, Picollet-D'hahan et al.[8] observed that poly(allylamine hydrochloride)-terminated films prevented long-term adhesion of epithelial cancerous prostatic cells, comparatively to fibronectin or poly(sodium 4-styrenesulphonate)-terminated surfaces. Alternatively, Blacklock et al.[9] while studying reducible hyperbranched poly(amide amine) and DNA multi-layered films, concluded that significant differences in cell attachment, growth and transfection activity are possible to achieve when modifying the rigidity of such bilayered architectures. The cellular adhesion phenomena has a strong impact on other biological processes including cell spreading, migration, polarization and differentiation,[10] being therefore an important feature to consider when developing biomaterials.

With the exception of artificial materials for epithelial regeneration (e.g. wound dressings for wound healing), or blood contacting materials, constructs designed for tissue engineering should be cell adhesive.[11, 12] The cellular adhesion phenomena is ruled by specific and non-specific mechanisms, mediated through the presence of cellular focal adhesions,[11, 13, 14] protein clusters composed by dimeric transmembrane integrins (α and β subtypes) and extracellular ECM binding motifs. Accordingly to the type of interaction between the focal adhesions and the scaffold, such interactions can be sorted into three main categories: (i) specific molecular recognition interactions; (ii) non-specific protein-scaffold interactions; and, (iii) non-specific morphological cell-material interactions. The first category is related to the specific biding between the non-covalently associated α and β subunits with cell adhesive peptide domains,[14] such as GEFYFDLRLKGDK (from collagen IV), YIGSR (from laminin) or the ubiquitous RGD, sequences that can be used to decorate a biomaterial’s surface. In the lack of specific peptide domains, cellular adhesion can be trigger via non-specific protein adsorption onto a scaffold,[15] a mechanism dependent on the construct’s physicochemical surface properties (e.g.: charge density, wettability, surface energy and chemical groups). As the last category, cell-material anchorage can be tailored through non-specific events of cellular interaction accordingly to the surface roughness and topology of the construct.[16] In addition to be involved in the cell-material anchorage, focal adhesions also exert the responsibility for sensing the mechanical properties of the potentially adhesive substrate. β integrins interact with the actin cytoskeleton via Talin and Vinculin, unravelling the traction forces generated by the actin cytoskeleton, which enables to sense the mechanical properties of a substrate’s interface (e.g. stiffness) upon contact.[17] Therefore, the long-term cellular adhesion on a biomaterial (and consequent biological processes, for example, cellular spreading and proliferation), depends not only on the type of cell-material anchorage, but also, on the spatiotemporal mechanical properties of the scaffold’s interface[18] upon phenomena such as the surface degradation or hydration.

Thus, in order to reengineer the surface of a scaffold for controlling the level of cellular adhesion, one must balance the contribution of specific and non-specific mechanisms that promote cell-material anchorage, with the proper stability of the interfacial mechanical properties for the scaffold in use. The satisfaction of just one criteria might be not enough to promote (or avoid) the cells adherence. Upon the unclear non-specific cellular adhesion mechanisms and on how they are intercorrelated, developing a biomaterial is often pursed on a trial-and-error basis, a time consuming and expensive approach,[19] that can lead to different results even when using the same type of construct. For instance, Liu et al.[20] reported an anti-adhesion cellular effect on poly-ʟ-lactic acid (PLLA) electrospun membranes, while conversely Corey et al.[21] observed cellular adherence on the same PLLA constructs when properly fiber-oriented. Despite scientists and engineers relying on published observations, the generation of novel scaffolds often shows a new paradigm which is initially unpredictable, since it converges to a new combination of cell-material anchorage and adhesion mechanisms to be used in a novel set of physiological conditions.

In this work, several combinations of polyelectrolytes and layer numbers are tested regarding the physicochemical properties of the generated multi-layered films, as well as the cellular adhesion on these constructs. It is intended to formulate, test and control, the underlying phenomena that avoids the cellular adhesion and proliferation on the future wound dressings. Therefore, and in compliance with the requirements for an ideal wound dressing as described in Chapter 1, *layer-by-layer* films are designed and studied towards the exploration of non-specific cell-material mediating mechanisms (**Figure 3B.1**). The main findings of the present content will allow to set the best polyelectrolyte multilayer coating.

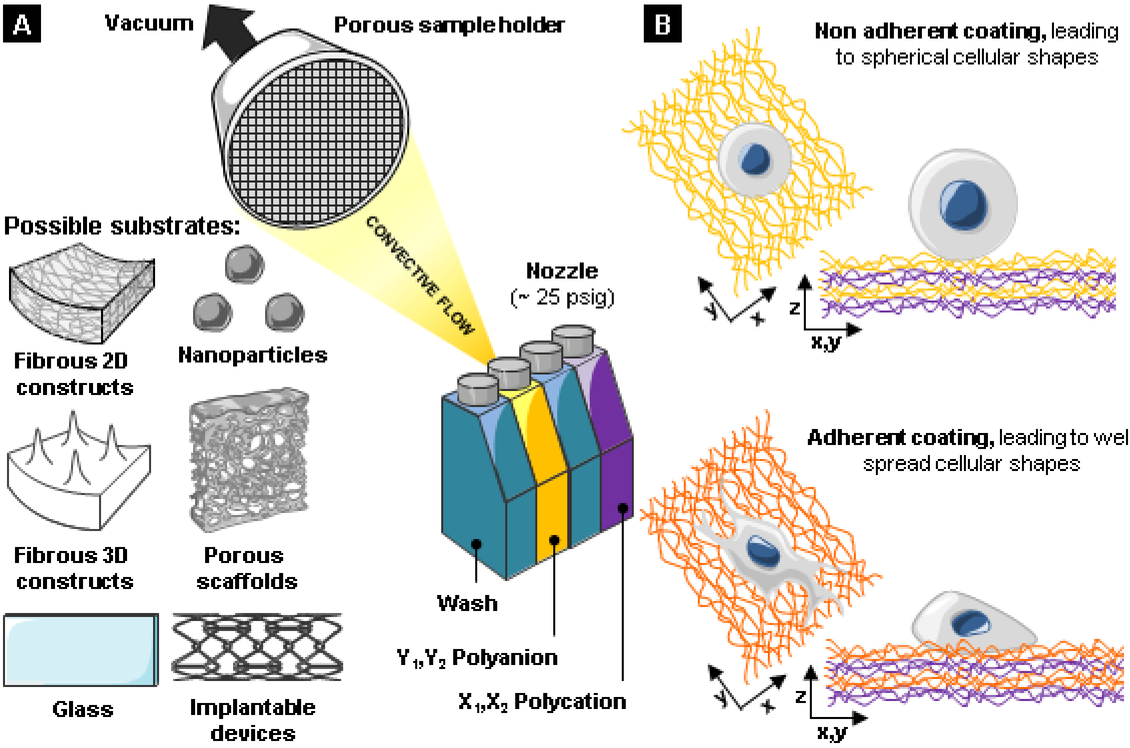

Figure 3B.1 Spray Layer-by-Layer (spray LbL) for surface coating of biomedical relevant scaffolds. **A**, Schematics of the spray LbL process where polyelectrolytes can be orderly and repeatedly (n) sprayed, in order to form surface coatings comprising bilayered $(X1/Y2)_n$ or tetralayered architectures $(X1/Y1/X2/Y2)_n$ on biomedical relevant materials through convective flow. **B**, Impact on the cellular shape according to the LbL coating suitability for cell adhesion, whereas non-adherent cells will evidence spherical forms (circularity ~ 1) and adherent cells will demonstrate elongated forms (circularity ~ 0) .

MATERIALS AND METHODS

Preparation of multi-layered coated constructs

The fabrication of LbL coated constructs was followed as reported in literature.[22, 23] Briefly, glass slides were initially cleaned with methanol, ethanol, 2-propanol and mili-q water, and gently dried under a nitrogen flow. The multi-layered films were built on the glass slides by using a programmable spray LbL apparatus (Svaya Nanotechnologies). Polyelectrolytes were alternately sprayed during 20 seconds with a wash step of 5 seconds, while combinatorially generating different types of polycation/polyanion bilayers and/or number of bilayers. Chitosan (Mw~15.0×10^3 g.mol^{-1}, Polyscience Inc.) and Gelatin (Mw~20.0-25.0×10^3 g.mol^{-1}, Sigma-Aldrich) were used as polycations, whereas Alginate (Mw~20.0×10^3 g.mol^{-1}, Sigma-Aldrich), Hyaluronic Acid (Mw~2.0×10^6 g.mol^{-1}, Lifecore Biomedical) and Poly-1 (Mw~15.0×10^3 g.mol^{-1}, synthesized as previously described[24]), were utilized as polyanions. Prior to bilayer deposition, linear polyethyleneimine (LPEI, Mw~25.0×10^3 g.mol^{-1}, Polyscience Inc.) and dextran sulphate (DS, Mw>500.0×10^3 g.mol^{-1}, Sigma-Aldrich) were initially sprayed to promote the formation of a

$(LPEI/DS)_{10}$ baselayer. For the complementary case-studies, two-dimensional and three-dimensional poly-ε-caprolactone based (Mw~25.0×10^3 $g.mol^{-1}$, Sigma-Aldrich) electrospun constructs were also sprayed-coated through the same protocol.

Film thickness and physic chemical surface characterization

After a gentle drying process with a nitrogen flow, spray-coated glass slides (N=3) were scored with a razor blade and the step height difference, between untouched film regions and the score's bottom, was tracked at nine different locations through profilometry (Dektak 150, Veeco). In addition, the films wettability was studied by extending the time of contact angle measuring. Static contact angles (N=4) were measured at room temperature by applying the sessile drop method (CAM 100, KSV Goniometer). A 10 µL glycerol (≥99.0%, Sigma-Aldrich) drop was placed on the multi-layered surfaces (top and bottom). The acquisition time was extended up to 5 minutes with a frame interval of 300 ms. Each frame was retrieved to MatLab R2012b (MathWorks) and the drop height and base diameter were measured, allowing to assess the spreading and imbibition dynamics.

In vitro cellular adhesion monitoring and characterization

$1x10^5$ NIH-3T3 cells were suspended in 1 mL of Advanced–MEM (Invitrogen) media containing 5% FBS, 1% antibiotic-antimitotic solution and 2 mM L–glutamine. 20 µL of concentrated cell solution were gently dropped on the bottom of spray-coated glass slides (N=4), while being posteriorly incubated for 30 minutes to allow cells to settle (37.0 ºC, 5.0% CO2). Afterwards, 3 mL of additional media were added from top to bottom, in order to remove unsettled cells from the substrates' surface. Media replacement occurred every 48 h. Phase-contrast images were acquired from the middle region of the substrates during 10 days (n=4 $images.(sample.day)^{-1}$). Area coverage was measured by implementing a watershed algorithm[25] in MatLab R2012b. Cell density was determined by counting the number of cells per image, while in parallel shape description was performed for 100–125 $cells.(sample.day)^{-1}$ in ImageJ, extracting as parameters the cells circularity and area.

Fabrication of three-dimensional electrospun constructs.

The electrospun fibrous scaffolds were fabricated as reported in the literature. Briefly, Poly(ε-caprolactone) (PCL, Mw ~ 65.0×10^3 $g.mol^{-1}$, Sigma-Aldrich) was dissolved in a 40/60 (v/v) solution of acetic (99.8%, Riedel-de Haën) and formic acid (≥98%, Sigma-Aldrich) at a desired concentration of 35 wt.%. The polymer solution was magnetically stirred for 4 h at room temperature and, posteriorly its shear viscosity was measured at 25 ºC in a shear range of $1\text{-}10^3$ s^{-1} by using a rotational rheometer (Gemini HR nano). The PCL polymer solution was pumped through a metallic capillary (21 gauge) by using a syringe pump (Nexus 6000, Chemyx) with a flow rate of 1.0

mL.h^{-1} during 4 hours. The metallic capillary was positively charged by a DC power supplier (Alpha Series II, Brandenburg) at 28 kV, and a 25×25 cm ground aluminum foil was vertically displaced at a tip-to-collector distance of 16 cm. Both the capillary and collector were within a glass sealed box with a controlled surrounding temperature (31.0 ± 0.1 ºC). The glass sealed box also comprised a ventilation system to control the relative humidity level (30.0 ± 1.0 %) and solvent content in the working atmosphere.

RESULTS

Multi-layered film coating and surface properties

To initially study the cellular adhesion on multi-layered functional materials, (polycation/polyanion)$_n$ bilayers were fabricated on top of glass slides, where *n* is the repeated number of layers. Gelatine (Gel), poly(β-amino-ester) (Poly-1) and Chitosan (Cht) were used as polycations. Such polyelectrolytes were alternately adsorbed with Alginate (Alg) or Hyaluronic Acid (HA), both used as complementary polyanionic species (**Figure 3B.2**).

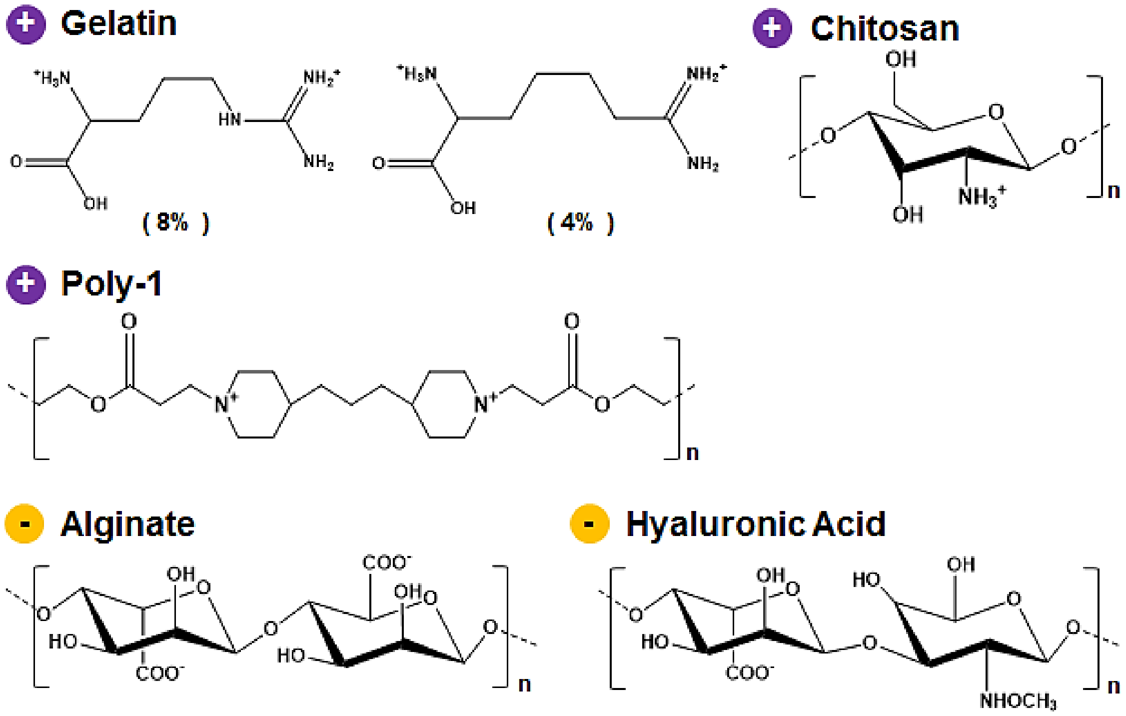

Figure 3B.2 Chemical structures of the used polycations (+) and polyanions (-).

In order to assess the impact of the number of layers in cellular adhesion, each combinatorial bilayer was generated with 1, 3, 5 and 10 repeating architectures. Despite all the bilayers were observed to deposit in a near-linear fashion up to n=10 (**Figure 3B.3 A, Table 3B.1**), the multi-layered films containing HA showed a growth rate (GR) 4.9-6.8 fold higher comparatively with

Alg-containing bilayers, leading to significant thickness differences as the number of layers was increased. It is possible to observe from the data that as *n* increases, the film thickness also

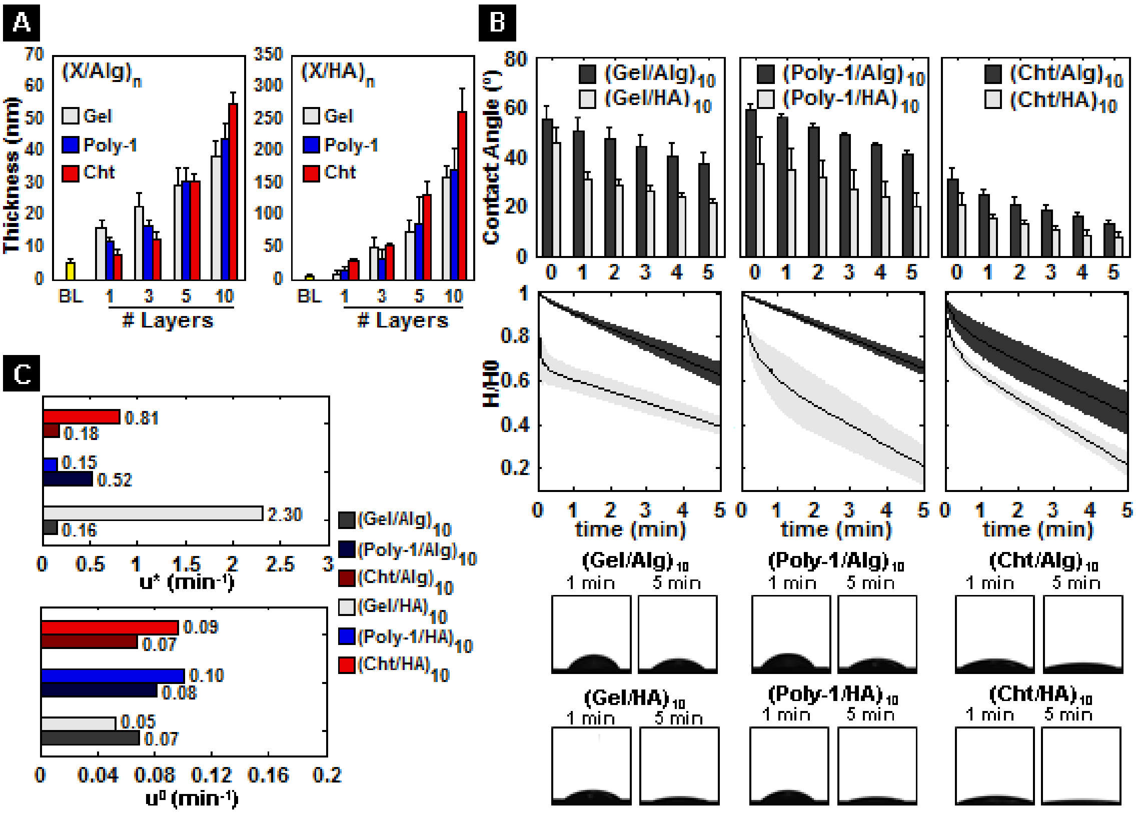

Figure 3B.3 LbL film characterization. **A,** Growth curves of spray LbL assembled films. **B,** Physicochemical charac-terization of the assembled LbL films accordingly to their contact angle measurements, normalized droplet height (H/H0) and droplet micrographs. **C,** Droplet spreading (u*) and imbibition (u0) dynamics on the assembled LbL films determined as reported on the literature.[26]

increases for the same polyelectrolyte architecture, since more material is deposited under experimental conditions that drive the self-assembly phenomena. Therefore, the manipulation of this variable it will allow to compare the cellular spreading and adhesion on substrates coated with the same polyelectrolyte architecture, while differing only in their dehydrated original thickness. Independently on the polyanion used, Gel-based films experienced the slowest growth rates: $(Gel/Alg)_n$= 2.5±0.2 nm.layer^{-1} and $(Gel/HA)_n$= (1.7±0.2)×10 nm.layer^{-1}; while Cht-based films demonstrated the highest growth rates values: $(Cht/Alg)_n$= 5.5±0.1 nm.layer^{-1} and $(Cht/HA)_n$= (2.7±0.4)×10 nm.layer^{-1}. Also, by replacing alginate with hyaluronic acid, such substitution had more impact on the final thickness of the HA-containing multi-layered films ($GR_{(Gel/HA)n}/GR_{(Gel/Alg)n}$=6.8), comparatively to the Poly-1 and Cht case studies ($GR_{(Poly-1/HA)n}/GR_{(Poly-1/Alg)n}$=5.3; $GR_{(Cht/HA)n}/GR_{(Cht/Alg)n}$=4.9). The shown data suggests that HA-containing films converge to higher thickness values comparatively to Alg-containing films, an observation mainly due to the reported effect of the polyanion molecular weight on the LbL film overall thickness (HA: Mw~2.0×10^{6} g.mol^{-1} vs. Alg: Mw~2.0-2.5×10^{4} g.mol^{-1}). The usage of weak up to moderately weak polyelectrolyte pairs, as those above mentioned, it is associated with the diffusion of at least one polyelectrolyte of the LbL architecture throughout the entire film, while coexisting an energetic barrier that prevents the complete coating dissociation of the polyelectrolyte chains. Despite several models have been developed to predict the LbL film thickness growth curves, since LbL are in a dehydrated state prior their utilization in physiological milieus, it was further investigated the influence of the film thickness and polymer architecture in the liquid spreading and imbibition upon contact (**Figure 3B.3 B-C, Figure 3B.4** and **Table 3B.2**).

Table 3B.1 Inter and intra-comparison of growth rate values for the generated LbL multilayered coatings.

X, Polycation	**Growth rate** (nm.layer^{-1})				**Growth rate comparison ratio** $\left(\frac{\text{Growth rate of }(\text{X/HA})_{\text{n}}}{\text{Growth rate of }(\text{X/Alg})_{\text{n}}}\right)$
	$(\text{X/Alg})_n$	R^2	$(\text{X/HA})_n$	R^2	
Gel	2.5 ± 0.23	0.972	17.0 ± 1.55	0.990	6.8
Poly-1	3.7 ± 0.36	0.961	18.9 ± 4.18	0.982	5.3
Cht	5.5 ± 0.13	0.978	27.0 ± 3.91	0.984	4.9

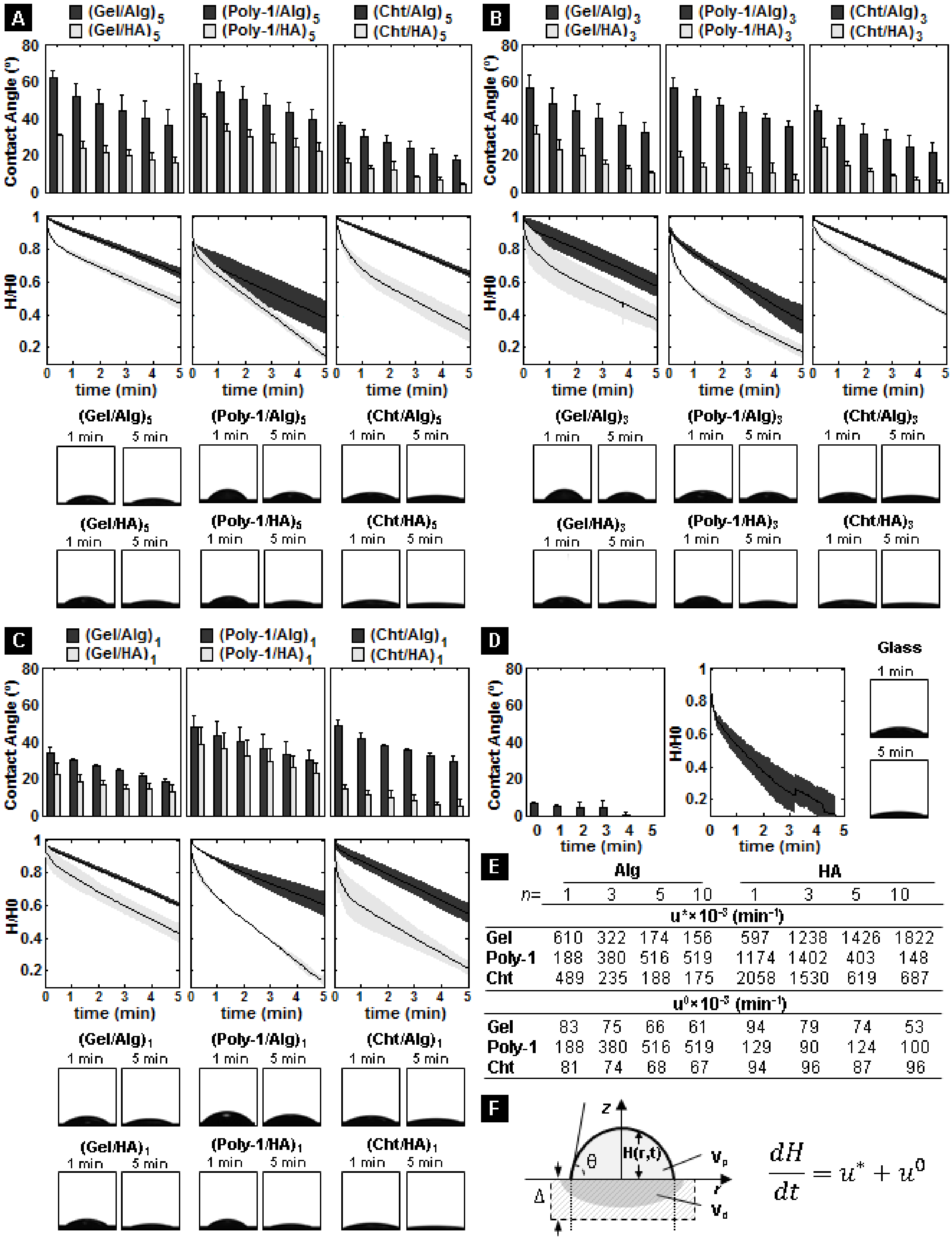

	Alg				HA			
n=	1	3	5	10	1	3	5	10
	$u^{*}\times10^{-3}$ (min^{-1})							
Gel	610	322	174	156	597	1238	1426	1822
Poly-1	188	380	516	519	1174	1402	403	148
Cht	489	235	188	175	2058	1530	619	687
	$u^{0}\times10^{-3}$ (min^{-1})							
Gel	83	75	66	61	94	79	74	53
Poly-1	188	380	516	519	129	90	124	100
Cht	81	74	68	67	94	96	87	96

$$\frac{dH}{dt} = u^{*} + u^{0}$$

Figure 3B.4 LbL film physicochemical characterization for the (X/Y)n architectures where, X is Gelatin, Poly-1 or Chitosan, Y is Alginate or Hyaluronic Acid, and n is 5, 3 or 1 layers. Spreading and absorption dynamics assessment for (X/Y)n architectures where n=5 (**A**), 3 (**B**) or 1 layers (**C**), as the overall evaluation of extended contact angle measurements, normalized droplet height (H/H0) and corresponding micrographs at 1 and 5 minutes. **D,** Spreading and absorption dynamics assessment on plasma cleaned glass substrates (PO), as the overall evaluation of extended contact angle measurements, normalized droplet height (H/H0) and corresponding micrographs at 1 and 5 minutes. **E,** Spreading and imbibition velocities (u* and u0, respectively) for the tested (X/Y)$_n$ architectures. **F,** Schematics describing the evaluated system variables (Δ, construct thickness; θ, contact angle; H, drop height; Vp, droplet volume; Vd, imbibed droplet volume) and main equation of the employed method, which is described in detail in the literature.[26]

Table 3B.2 Kinetic parameters t* and t^0 for the spreading and imbibition stages on the LbL multilayered coatings tested.

	Alg				HA			
n=	1	3	5	10	1	3	5	10
					t* (min)			
Gel	1.65	3.12	5.77	6.45	1.64	0.81	0.71	0.24
	R^2=0.979	R^2=0.991	R^2=0.995	R^2=0.993	R^2=0.769	R^2=0.943	R^2=0.973	R^2=0.977
Poly-1	5.31	2.54	2.10	1.91	0.86	0.71	0.55	0.54
	R^2=0.986	R^2=0.996	R^2=0.861	R^2=0.940	R^2=0.950	R^2=0.959	R^2=0.898	R^2=0.917
Cht	2.06	4.26	5.32	5.74	0.49	0.66	1.60	1.38
	R^2=0.996	R^2=0.953	R^2=1.000	R^2=0.995	R^2=0.926	R^2=0.914	R^2=0.961	R^2=0.915
					t^0 (min)			
Gel	11.56	12.77	15.03	15.95	9.22	9.69	11.37	12.49
	R^2=0.999	R^2=0.995	R^2=0.995	R^2=0.998	R^2=0.998	R^2=0.999	R^2=0.988	R^2=1.000
Poly-1	8.17	8.50	10.02	10.49	5.94	6.83	6.20	7.18
	R^2=0.999	R^2=0.991	R^2=0.999	R^2=0.999	R^2=1.000	R^2=0.997	R^2=0.999	R^2=0.999
Cht	11.86	13.35	14.54	14.80	9.45	9.18	8.55	7.15
	R^2=0.998	R^2=0.988	R^2=0.998	R^2=0.999	R^2=0.999	R^2=0.999	R^2=0.999	R^2=0.997

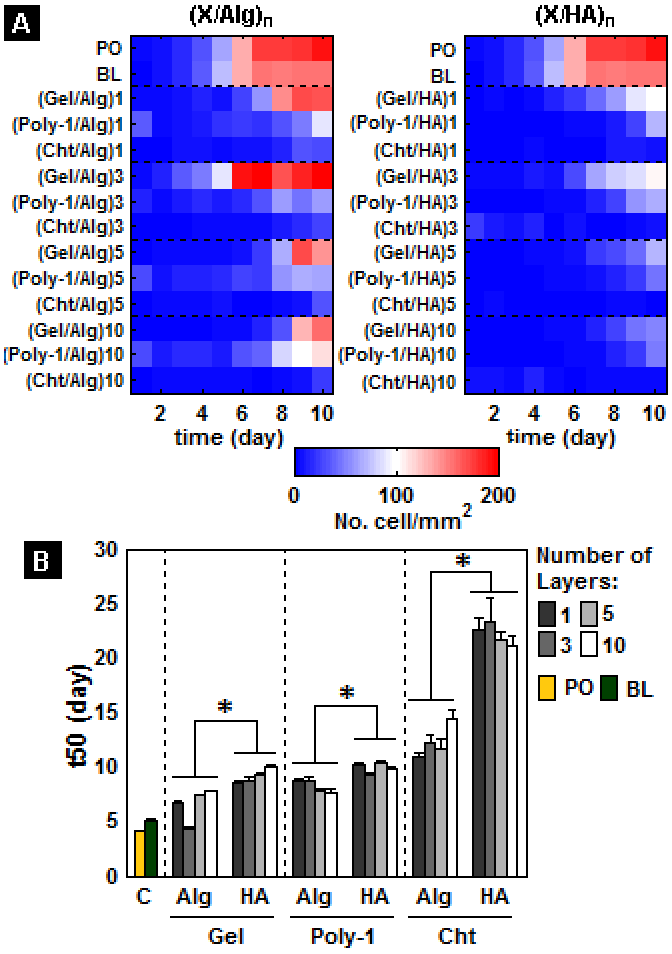

Figure 3B.5 Cellular proliferation and covering dynamics on the assembled LbL films. A, Cellular density up to 10 days. B, Kinetic parameter t50 corresponding to 50% area coverage of the sprayed LbL films (p-value < 0.025).

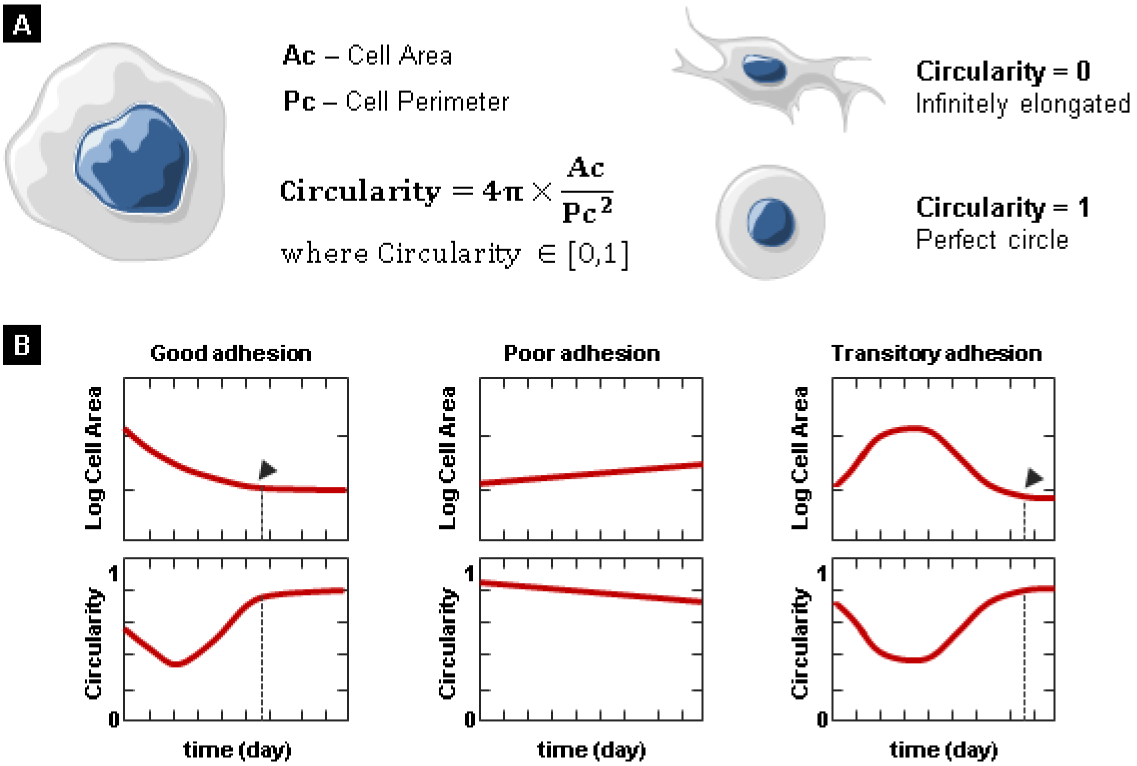

Figure 3B.6 A, Schematics illustrating the cell circularity determination and on how to interpret the calculated values accordingly with cell shape. **B,** Schematics about log cell area and circularity kinetic curves for a good cell adhesive substrate, a poor cell adhesive substrate and an initially poor cell adhesive substrate that posteriorly allows cellular adhesion (transitory) after a given period. (▼) Time period of cellular confluence, where the first derivative of the log cell area and the first derivative of circularity approach 0.

On a good cell adhesive substrate, seeded cells, that were initially suspended in a post-harvesting media (usually in a sphere-like conformation), upon the contact with a suitable surface for cellular adhesion will adhere and expand their initial area value for the highest expected cell area value throughout the experiment period. From early time points, cells will demonstrate the formation of lamellipodia that contributes to less circular shapes, while in parallel, proliferation occurs and leads to lower values of the average logarithm cell area. Since the substrate is populated with more cells, space restriction will inhibit elongated cellular shapes, converging to highly packed cells as reaching cell confluence, characterized by lower cell area values and not-elongated cellular shapes that perpetuate through time. On the case of poor cell adhesive substrates, the initially seed cells will not adhere to the material’s surface and minor rate changes on the cell area and circularity are expected, as cells slightly increase their cell area through expansion and converting themselves to more slightly elongated shapes. Nevertheless, the cellular proliferation rate on these materials is lower comparatively to the case of good cell adhesive surfaces. On the transitory cell adhesive substrates, the seeded cells will initially struggle to adhere to the substrate. However, as the surface properties of the coating materials are altered through time (e.g., stiffness variation due to surface erosion), cells will experience a delay to be properly attached.

As soon as cell attachment occurs, the log cell area and circularity kinetics curves will morphologically resembling to the case of good cell adhesive substrates, evidencing the same behavioral cell area and shape transformation. Therefore, confluent cells are obtained at later time periods comparatively to the observed time period for good cell adhesive substrates.

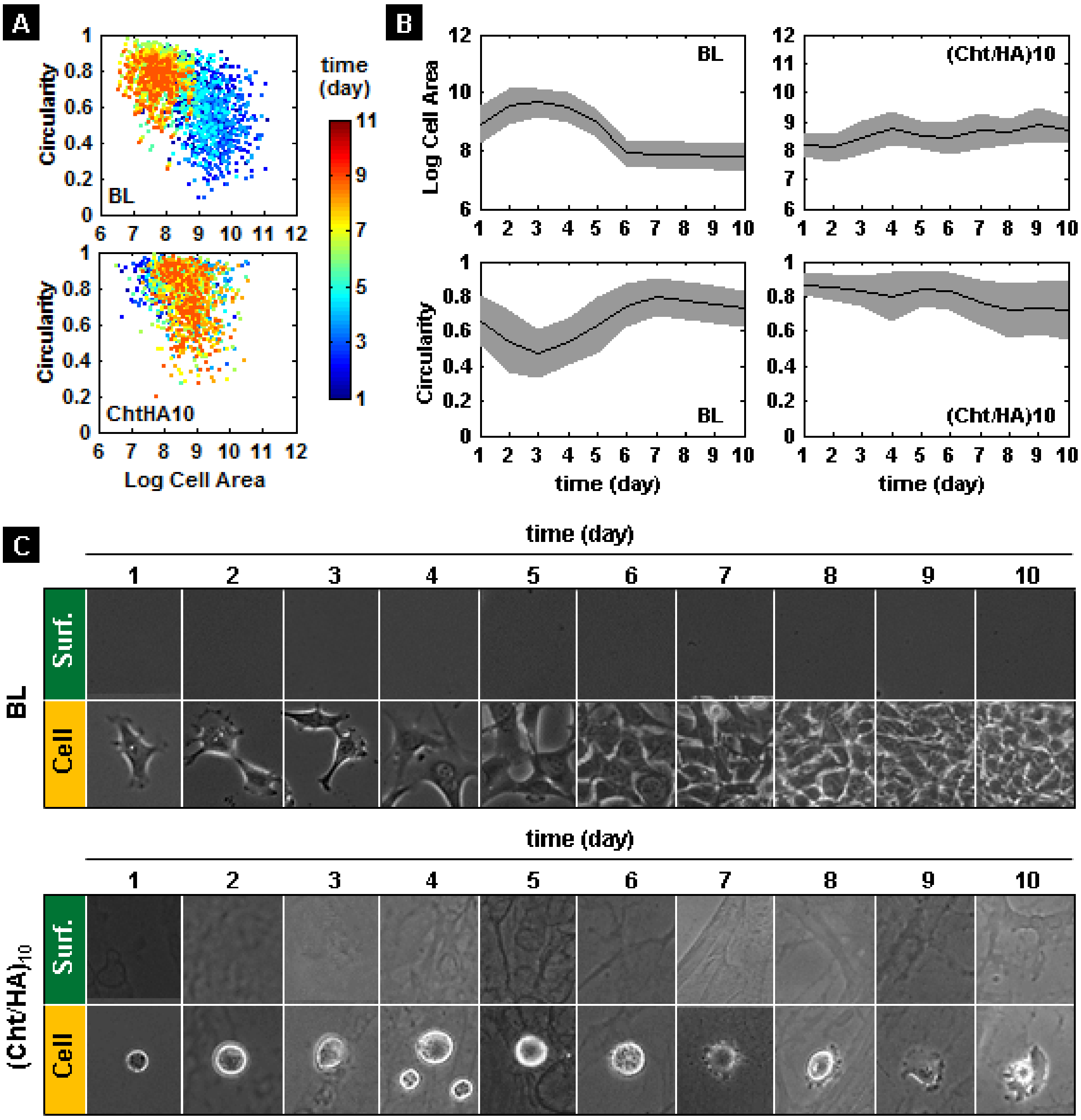

Figure 3B.7 Cellular shape assessment and LbL films degradation behavior for the baselayer [(LPEI/DS)$_{10}$] and (Cht/HA)$_{10}$ LbL coatings. Cellular shape scatter plots (**A**, mutlidimensional analysis) and time-based profiles (**B**, segregated bidimensional analysis) showcasing the shape parameters evolution throughout time. **C**, Phase contrast micrographs of film erosion and cultured cells on the sprayed LbL films up to day 10.

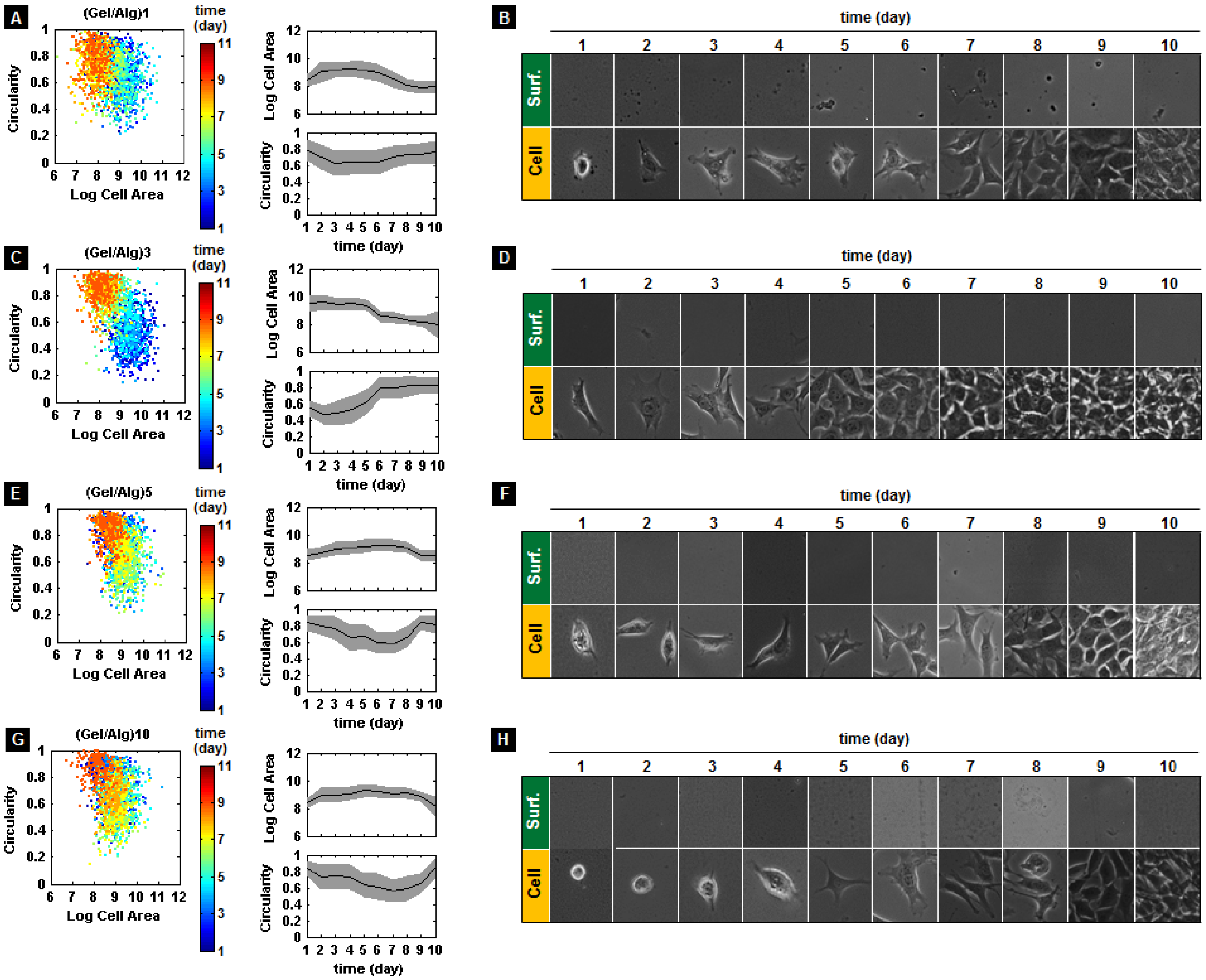

Figure 3B.8 Cellular shape assessment and LbL films degradation behavior for the (Gel/Alg)$_n$ LbL coatings (**A,B** n=1; **C,D** n=3; **E,F** n=5; **G,H** n=10), throughout the same analysis protocol of Figure 3B.7.

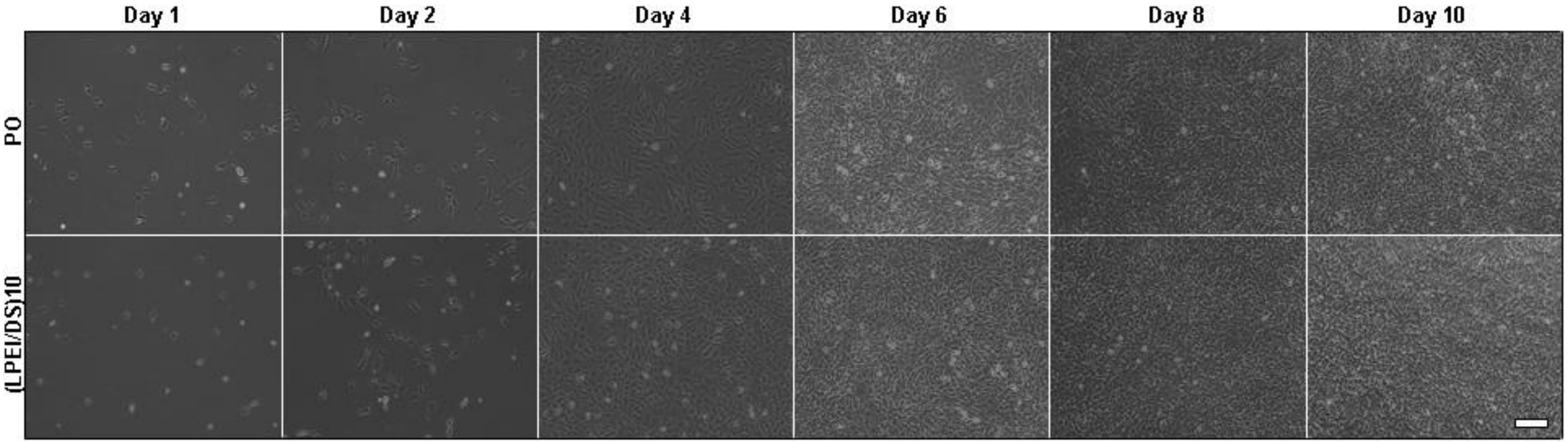

Figure 3B.9 Phase contrast micrographs of cultured cells on PO substrates (plasma cleaned glass slides) and $(LPEI/DS)_{10}$ multilayered coatings up to 10 days (scale-bar = 500 µm).

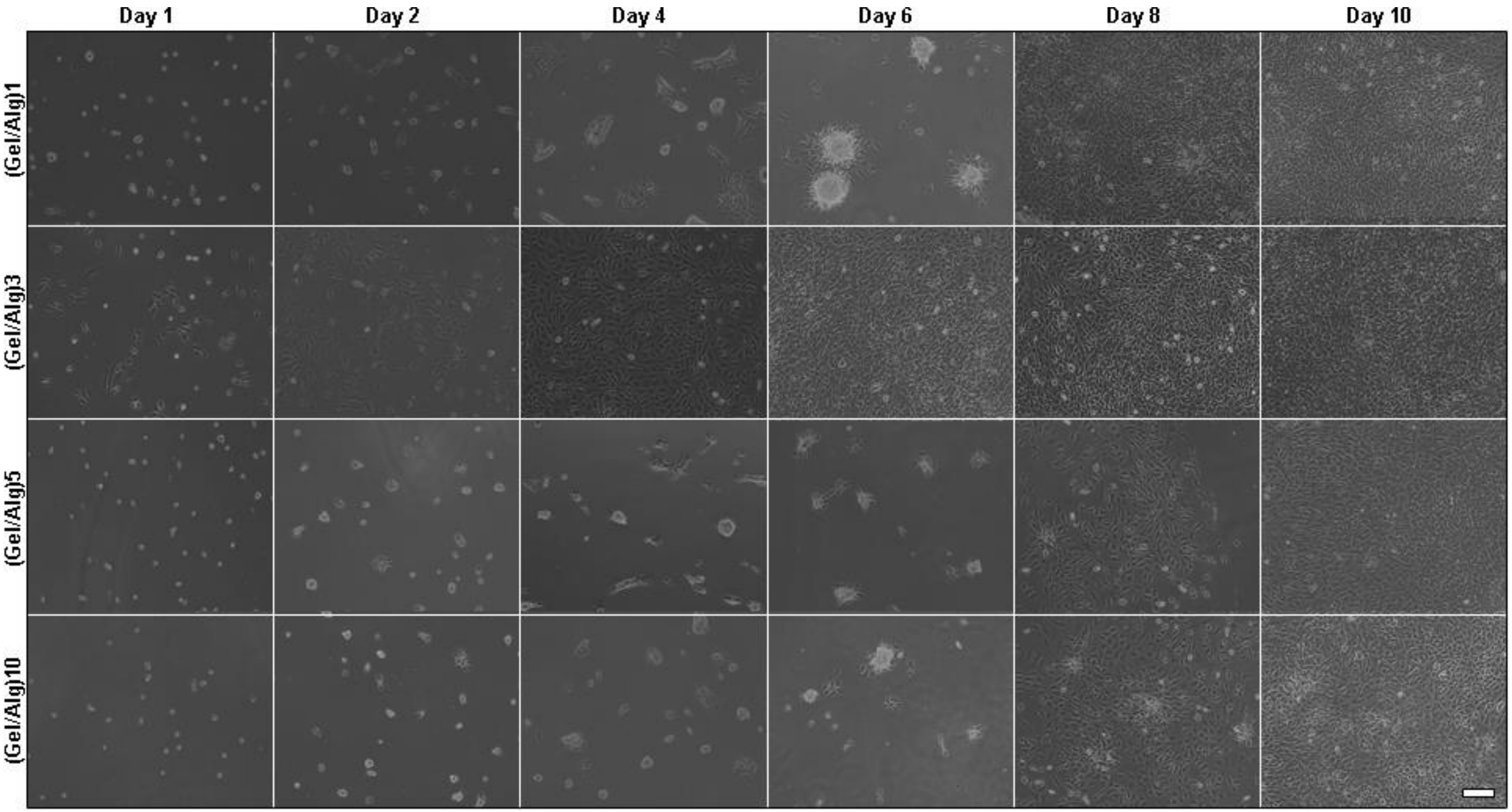

Figure 3B.10 Phase contrast micrographs of cultured cells on $(Gel/Alg)_n$ multilayered coatings up to 10 days, where *n* is 1, 3, 5 and 10 layers (scale-bar = 500 µm).

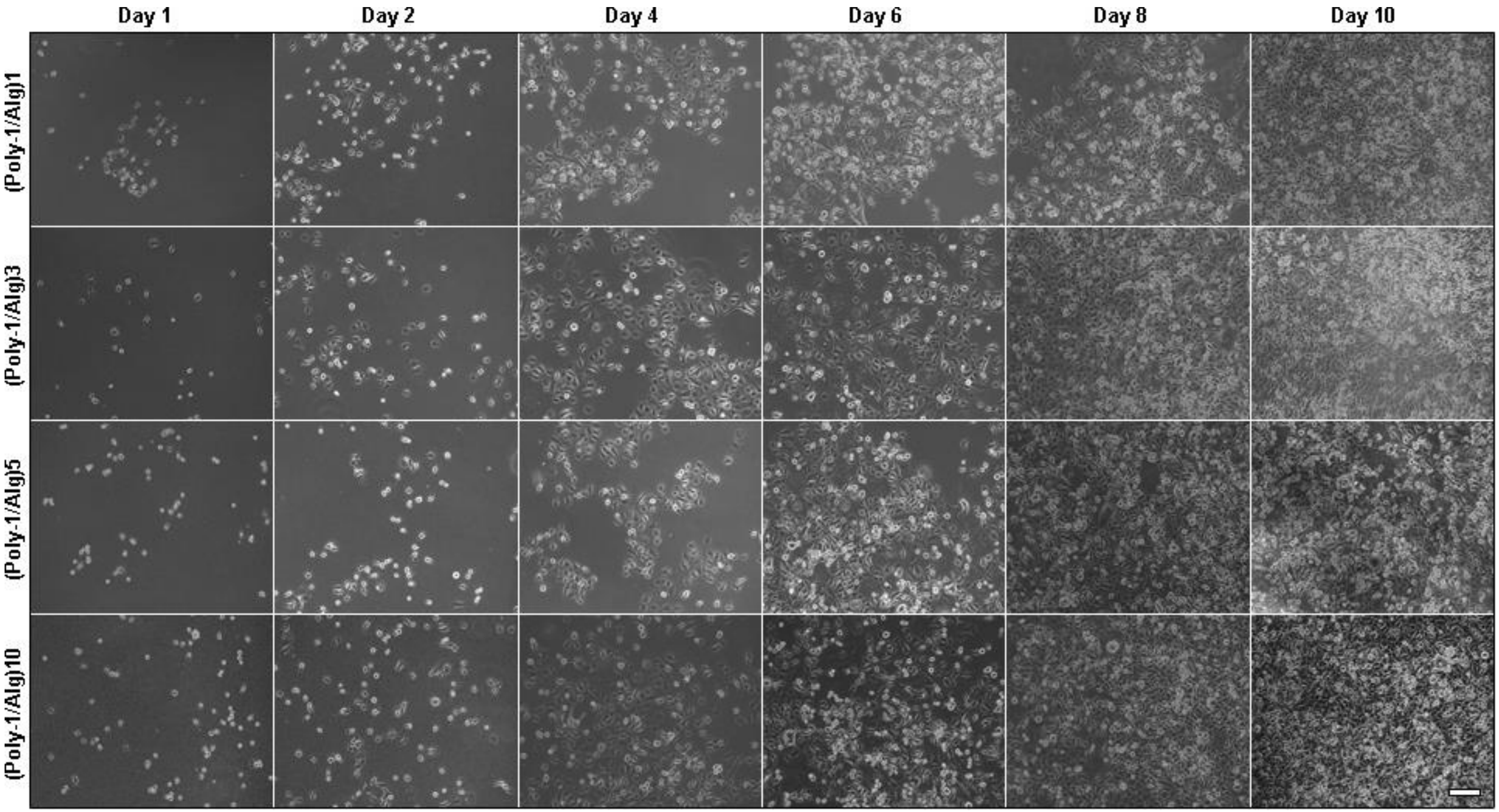

Figure 3B.11 Phase contrast micrographs of cultured cells on (Poly-1/Alg)$_n$ multilayered coatings up to 10 days, where *n* is 1, 3, 5 and 10 layers (scale-bar = 500 µm).

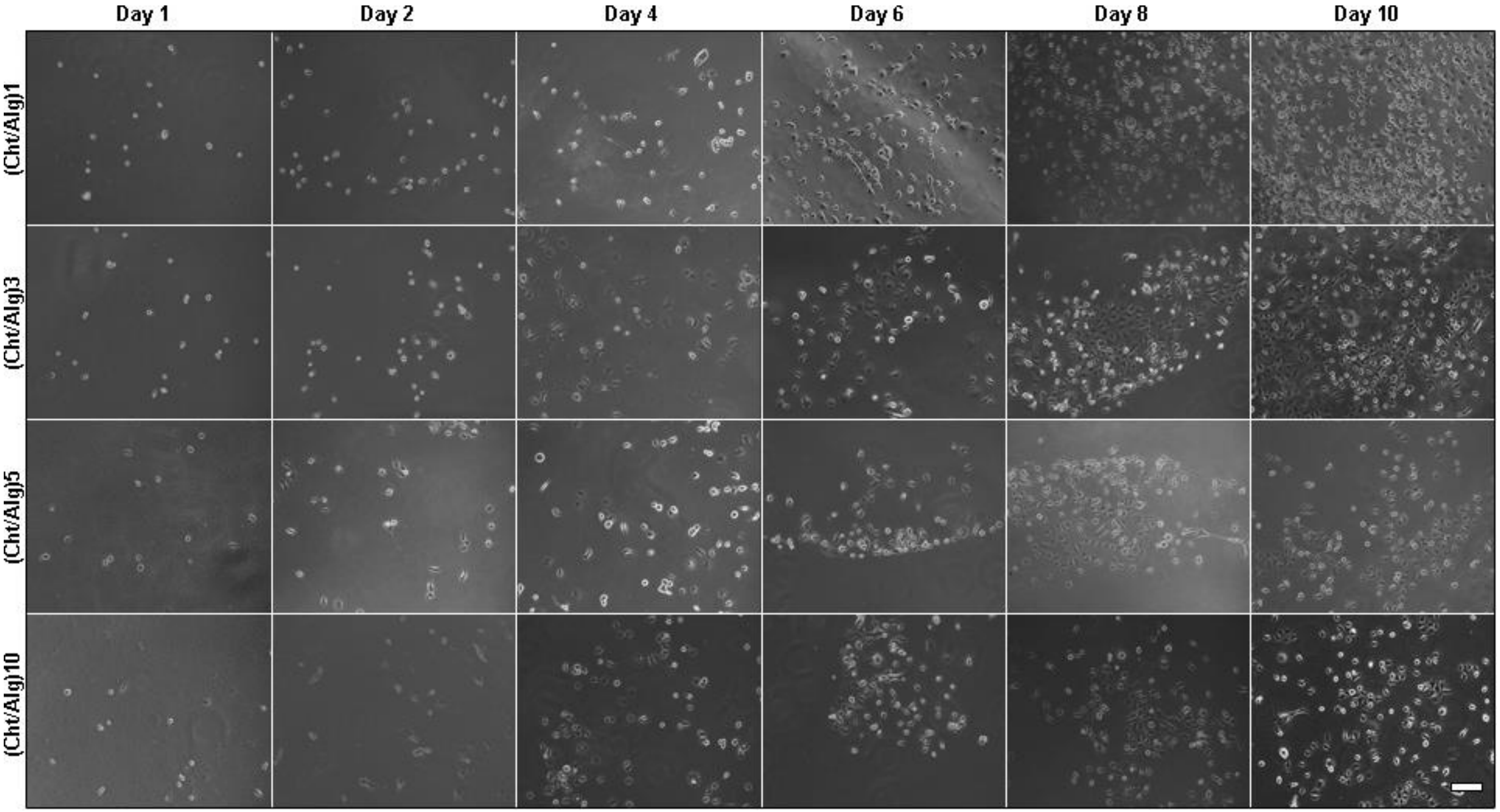

Figure 3B.12 Phase contrast micrographs of cultured cells on (Cht/Alg)$_n$ multilayered coatings up to 10 days, where *n* is 1, 3, 5 and 10 layers (scale-bar = 500 µm).

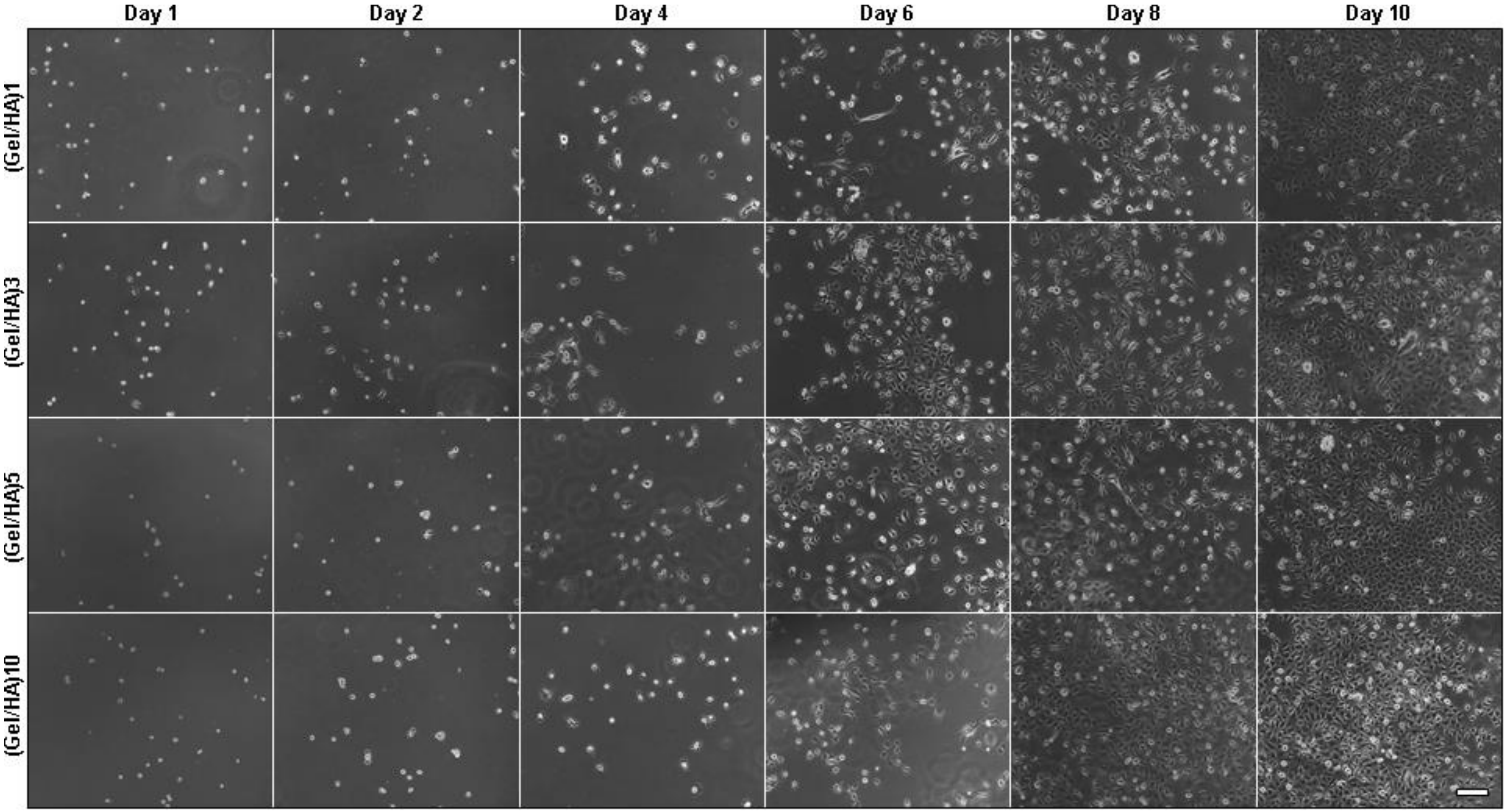

Figure 3B.13 Phase contrast micrographs of cultured cells on (Gel/HA)$_n$ multilayered coatings up to 10 days, where *n* is 1, 3, 5 and 10 layers (scale-bar = 500 µm).

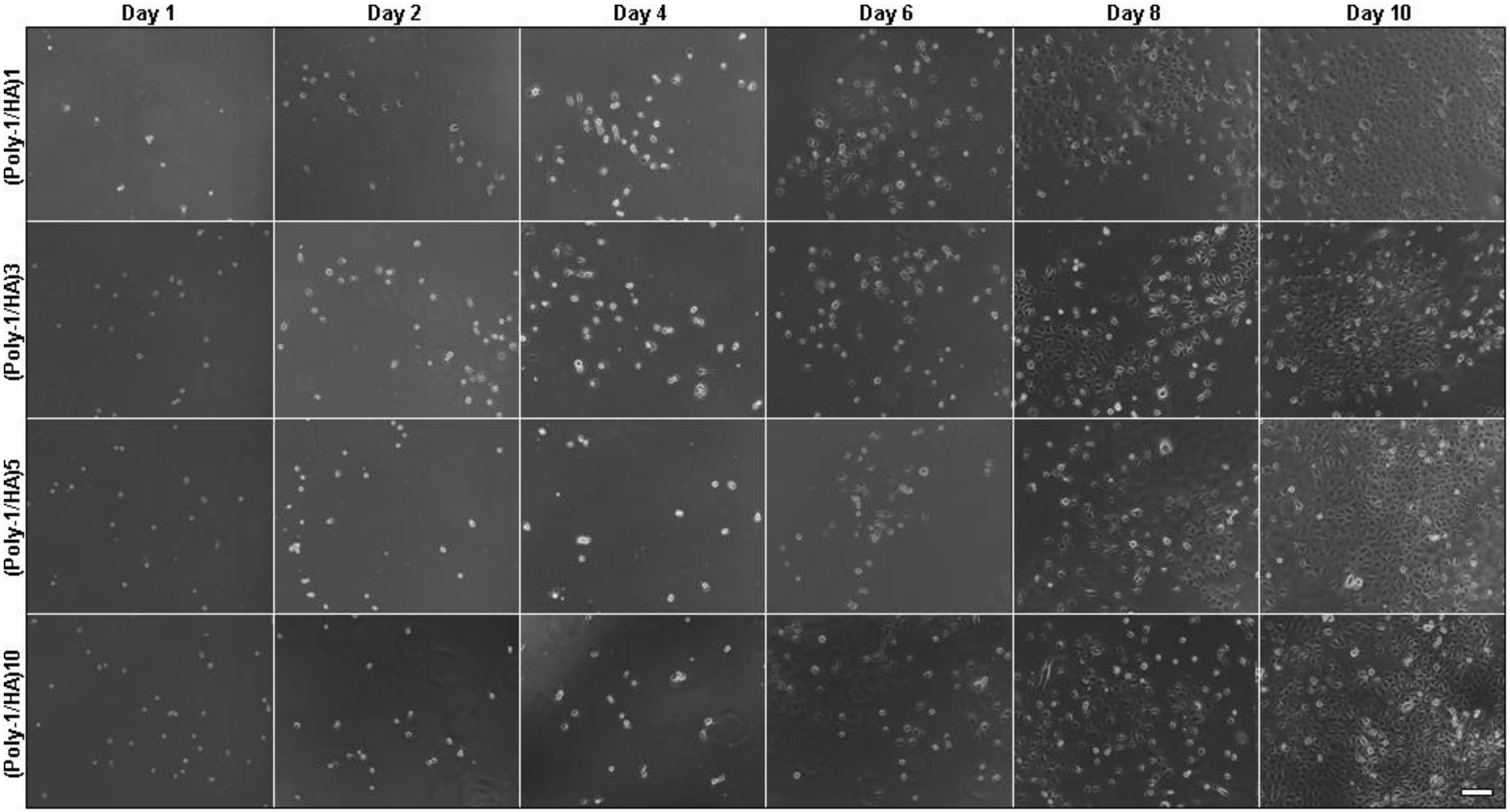

Figure 3B.14 Phase contrast micrographs of cultured cells on (Poly-1/HA)$_n$ multilayered coatings up to 10 days, where *n* is 1, 3, 5 and 10 layers (scale-bar = 500 µm).

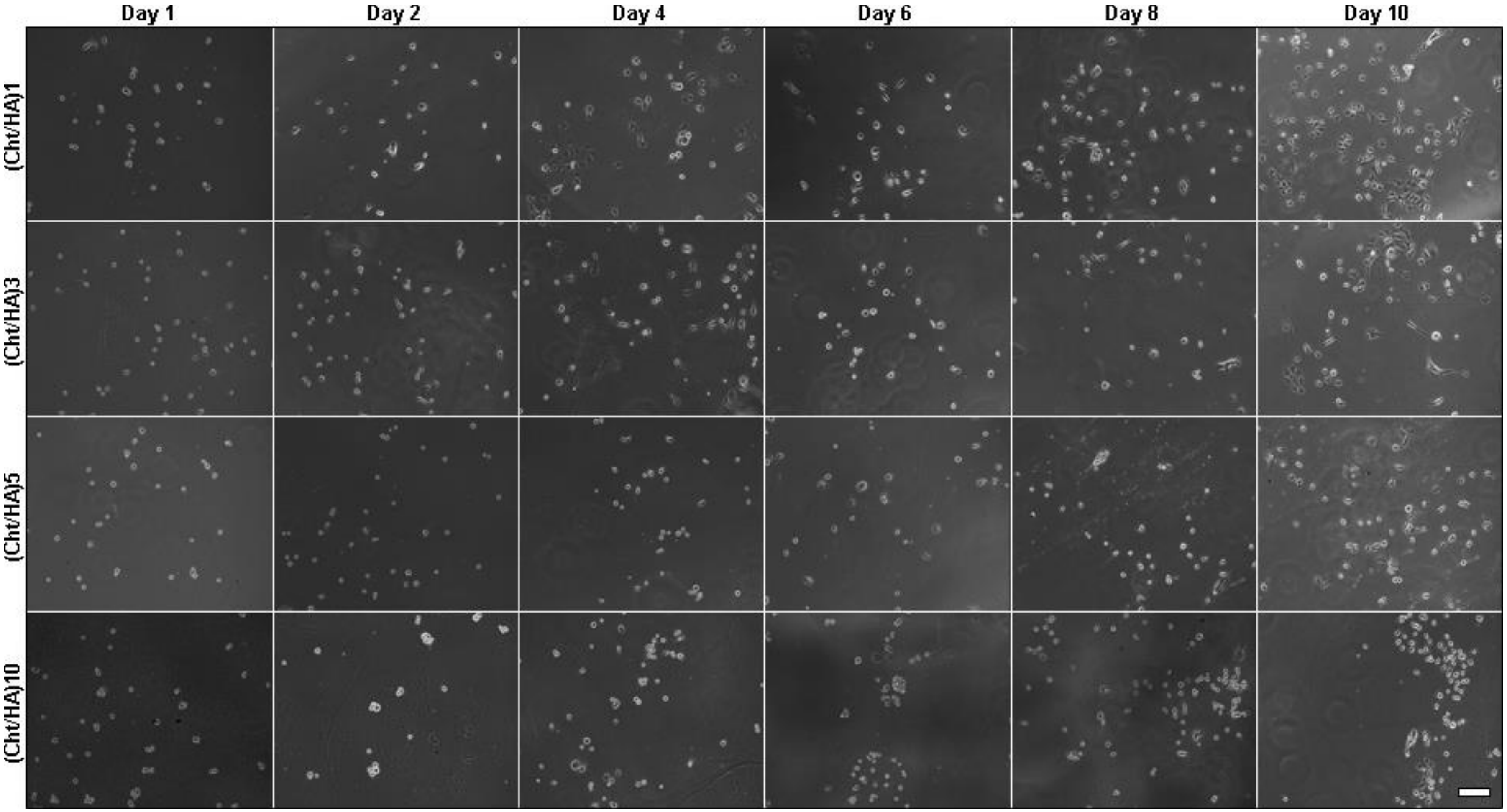

Figure 3B.15 Phase contrast micrographs of cultured cells on (Cht/HA)$_n$ multilayered coatings up to 10 days, where *n* is 1, 3, 5 and 10 layers (scale-bar = 500 µm).

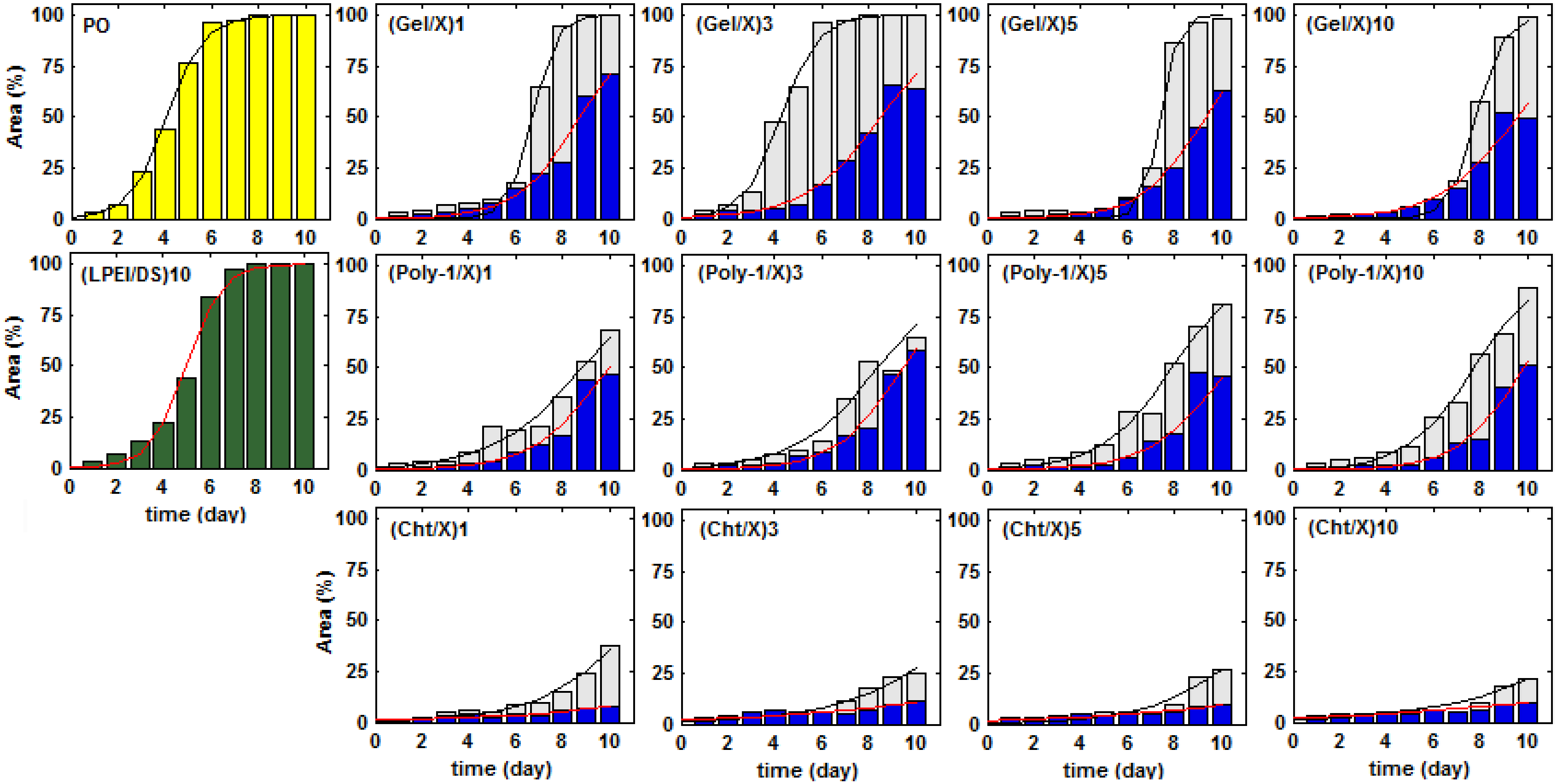

Figure 3B.16 Dynamic substrate area coverage up to 10 days, represented as the area percentage according to the initial substrate area, for all the *in vitro* tested samples: plasma cleaned glass slides (PO), used LbL baselayer $(LPEI/DS)_{10}$ and $(X/Y)_n$ LbL coatings, with the corresponding profile curves.

Table 3B.3 Sigmoid function parameters estimation of the dynamic substrate area coverage behavior for the determination of the kinetic parameter t_{50}.

LbL Film	**Sigmoid function* parameters estimation** (with 95% confidence bounds)		**R^2**
	a	*b*	
PO	1.29 (1.37,1.43)	4.08 (3.97,4.18)	0.998
BL – (LPEI/DS)$_{10}$	1.34 (1.02,1.65)	4.99 (4.79,5.19)	0.992
(Gel/Alg)$_1$	1.97 (1.39,2.54)	6.70 (6.53,6.87)	0.991
(Gel/HA)$_1$	0.74 (0.58,0.90)	8.76 (8.47,9.04)	0.977
(Gel/Alg)$_3$	1.26 (0.99,1.54)	4.25 (4.05,4.45)	0.993
(Gel/HA)$_3$	0.61 (0.48,0.73)	8.52 (8.20,8.84)	0.977
(Gel/Alg)$_5$	2.65 (1.90,3.40)	7.37 (7.23,7.51)	0.992
(Gel/HA)$_5$	0.73 (0.68,0.78)	9.33 (9.23,9.42)	0.997
(Gel/Alg)$_{10}$	1.72 (1.50,1.94)	7.82 (7.74,7.90)	0.998
(Gel/HA)$_{10}$	0.59 (0.43,0.76)	9.57 (9.11,10.04)	0.954
(Poly-1/Alg)$_1$	0.51 (0.40,0.63)	8.84 (8.43,9,25)	0.968
(Poly-1/HA)$_1$	0.63 (0.46,0.81)	9.96 (9.51,10.40)	0.956
(Poly-1/Alg)$_3$	0.52 (0.38,0.66)	8.62 (8.14,9.10)	0.957
(Poly-1/HA)$_3$	0.70 (0.57,0.82)	9.47 (9.22,9.72)	0.982
(Poly-1/Alg)$_5$	0.66 (0.54,0.78)	7.88 (7.60,8.15)	0.984
(Poly-1/HA)$_5$	0.64 (0.41,0.86)	9.90 (9.35,10.45)	0.934
(Poly-1/Alg)$_{10}$	0.70 (0.58,0.82)	7.74 (7.49,7.99)	0.987
(Poly-1/HA)$_{10}$	0.73 (0.58,0.88)	9.84 (9.56,10.11)	0.978
(Cht/Alg)$_1$	0.48 (0.38,0.57)	11.27 (10.72,11.82)	0.971
(Cht/HA)$_1$	0.17 (0.10,0.24)	24.83 (18.03,31.63)	0.835
(Cht/Alg)$_3$	0.37 (0.29,0.44)	12.69 (11.78,13.6)	0.965
(Cht/HA)$_3$	0.14 (0.07,0.21)	26.15 (16.33,35.97)	0.730
(Cht/Alg)$_5$	0.45 (0.30,0.60)	12.22 (11.01,13.42)	0.914
(Cht/HA)$_5$	0.16 (0.10,0.21)	24.61 (18.23,31.00)	0.847
(Cht/Alg)$_{10}$	0.34 (0.23,0.45)	13.93 (12.15,15.71)	0.908
(Cht/HA)$_{10}$	0.15 (0.08,0.23)	26.24 (16.86,35.62)	0.779

$$* \text{ Covered Area } (\%) = \frac{100}{1+\mathrm{e}^{-\mathrm{a(time-b)}}} \text{ where } a, b \in \mathbb{R}$$

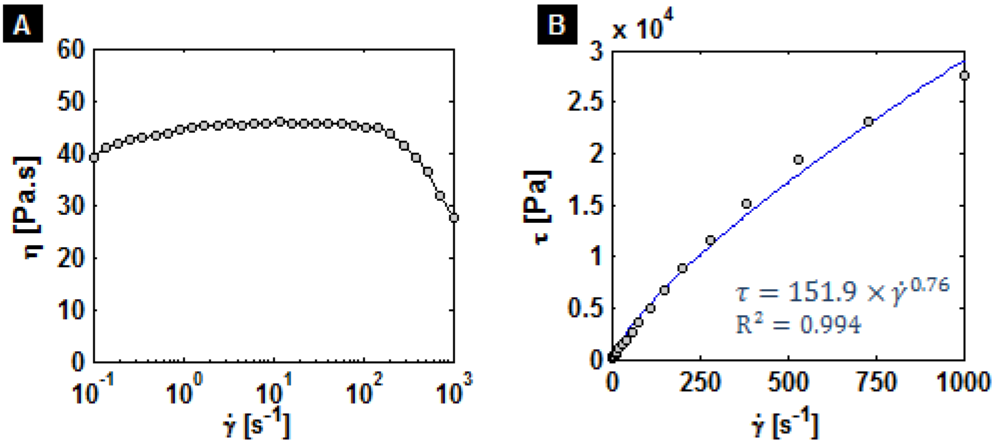

Figure 3B.17 Flow curves of PCL dissolved in a 40/60 (v/v) solution of acetic and formic acid at a desired concentration of 35 wt.% displaying (**A**) complex viscosity and (**B**) shear stress.

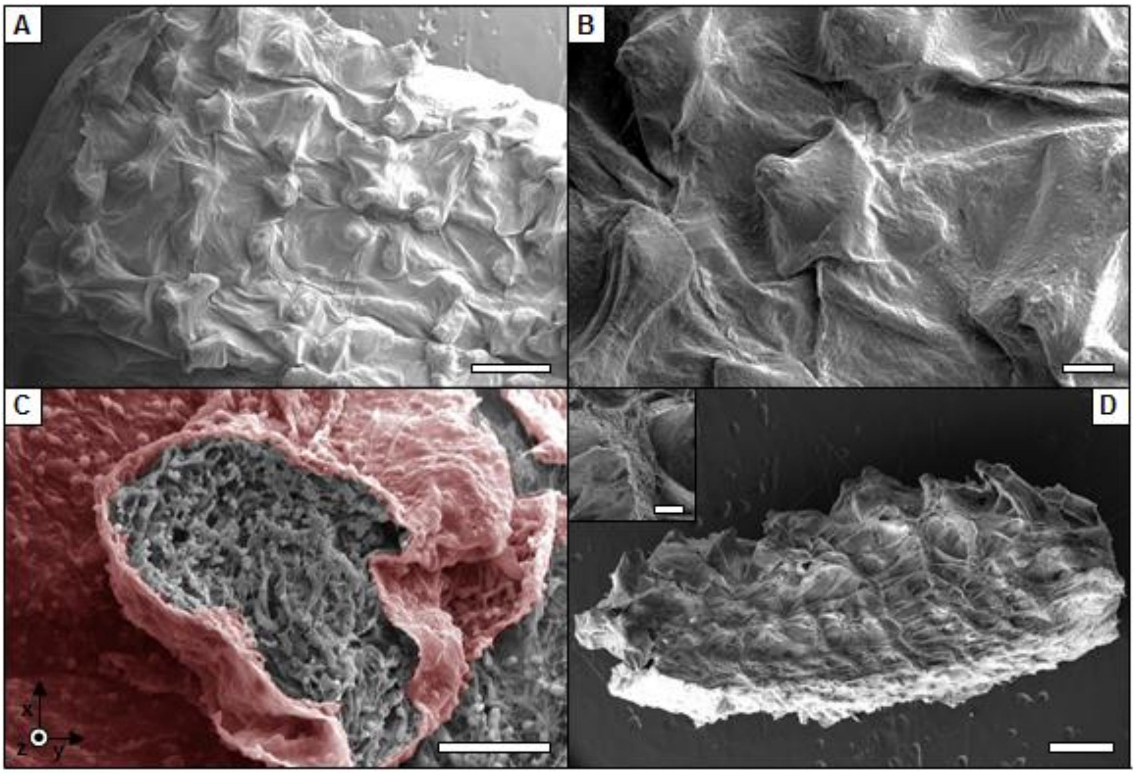

Figure 3B.18 SEM images of three-dimensional (Cht/HA)$_{10}$ multilayered electrospun construct (Top view: **A**, scale bar = 500 μm; **B**, scale bar = 100 μm; **C**, pseudo-colored SEM of a horizontally slashed multiprotrusion showing the LbL coating in red, scale bar = 50 μm; Cross section: **D**, scale bar = 500 μm and inset scale bar = 100 μm).

A

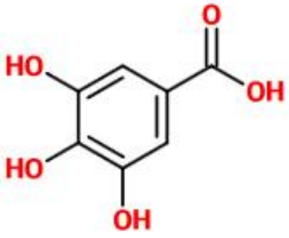

Gallic Acid

mode	affinity (kcal/mol)	Dist from rmsd l.b.	Beste mode rmsd l.b.
1	-6.5	0.000	0.000
2	-6.3	2.182	4.932
3	-6.2	6.201	8.056
4	-6.2	27.392	29.040
5	-6.2	28.974	30.648
6	-6.2	3.616	6.293
7	-6.2	29.630	31.209
8	-6.1	29.637	31.201
9	-6.1	5.568	8.20

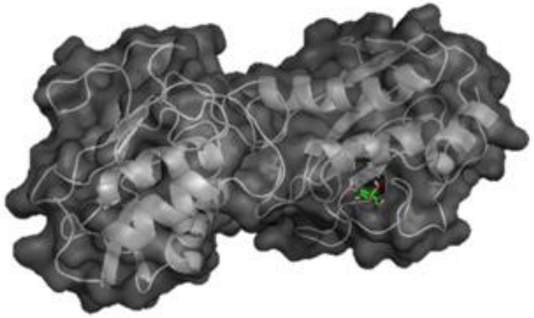

B

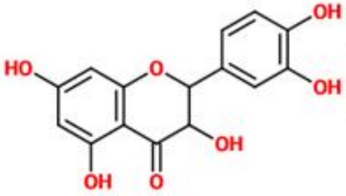

Quercetin

mode	affinity (kcal/mol)	Dist from rmsd l.b.	Beste mode rmsd l.b.
1	-6.4	0.000	0.000
2	-6.4	0.038	2.393
3	-6.0	1.306	3.461
4	-5.4	1.256	4.392
5	-5.3	26.685	28.458
6	-5.2	44.244	44.747
7	-5.2	27.004	28.761
8	-5.1	38.479	39.470
9	-5.1	38.478	39.514

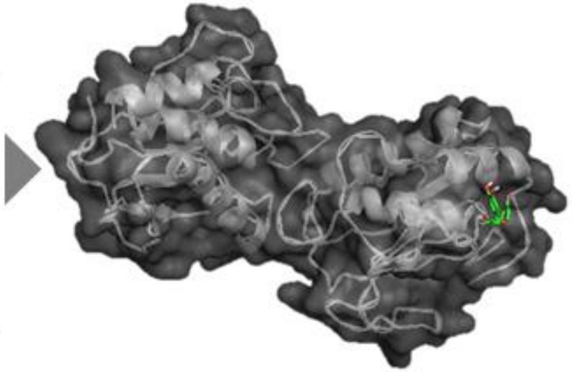

C

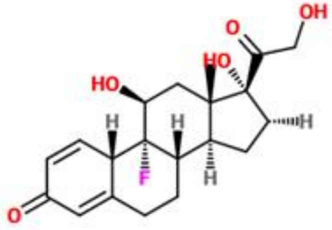

Ellagic Acid

mode	affinity (kcal/mol)	Dist from rmsd l.b.	Beste mode rmsd l.b.
1	-7.9	0.000	0.000
2	-7.4	32.577	34.364
3	-7.4	11.095	13.837
4	-7.4	11.107	13.873
5	-7.4	32.620	34.451
6	-6.9	34.096	36.017
7	-6.8	35.096	36.912
8	-6.5	13.064	14.487
9	-6.4	12.237	15.370

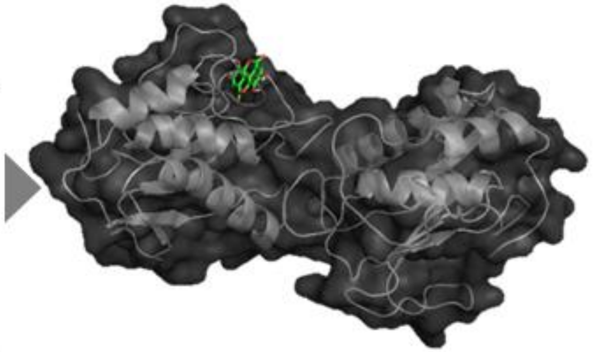

D

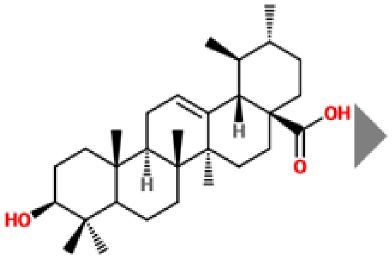

Ursolic Acid

mode	affinity (kcal/mol)	Dist from rmsd l.b.	Beste mode rmsd l.b.
1	-8.2	0.000	0.000
2	-7.3	26.767	29.707
3	-7.3	1.715	3.789
4	-7.2	32.967	36.265
5	-7.1	16.829	18.930
6	-6.9	22.166	24.469
7	-6.9	16.915	18.810
8	-6.9	26.102	28.713
9	-6.9	26.855	29.921

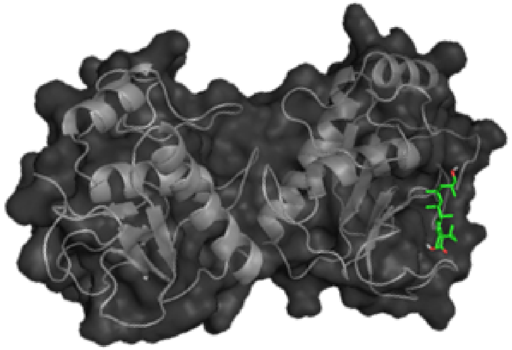

E

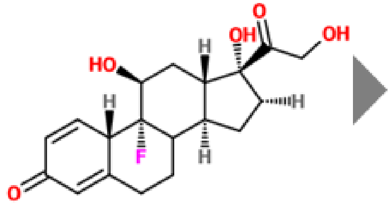

Dexamethasone

mode	affinity (kcal/mol)	Dist from rmsd l.b.	Beste mode rmsd l.b.
1	-6.8	0.000	0.000
2	-6.5	53.897	56.829
3	-6.4	37.841	41.616
4	-6.3	52.078	56.152
5	-6.3	16.364	17.922
6	-6.2	33.118	34.721
7	-6.2	25.904	27.174
8	-6.2	13.569	15.401
9	-6.1	23.501	25.603

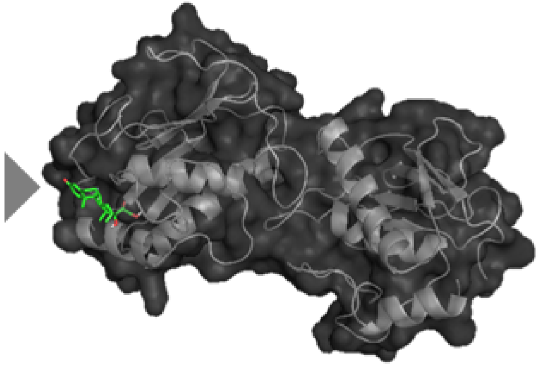

F

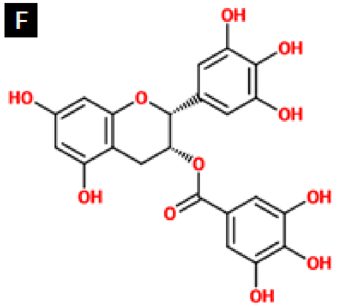

Epigallocatechin 3-gallate

mode	affinity (kcal/mol)	Dist from rmsd l.b.	Beste mode rmsd l.b.
1	-8.1	0.000	0.000
2	-8.1	0.029	2.041
3	-7.7	21.101	23.410
4	-7.6	21.100	23.446
5	-7.5	51.338	54.185
6	-7.5	51.348	54.207
7	-7.4	61.574	65.373
8	-7.4	26.208	29.667
9	-7.4	26.221	29.712

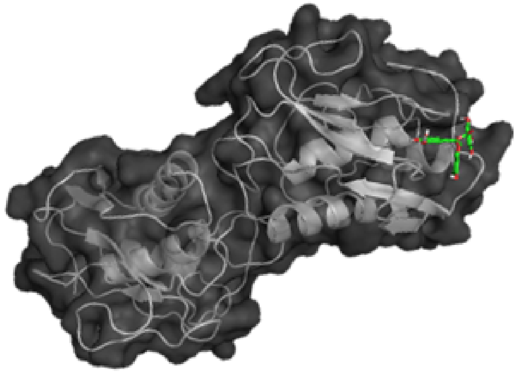

G

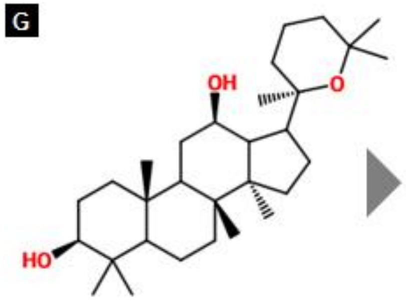

Panaxadiol

mode	affinity (kcal/mol)	Dist from rmsd l.b.	Beste mode rmsd l.b.
1	-7.6	0.000	0.000
2	-7.6	20.923	23.646
3	-7.4	9.974	16.358
4	-7.2	23.315	26.424
5	-7.1	27.847	30.608
6	-7.0	34.507	38.389
7	-6.9	26.213	28.265
8	-6.9	2.377	5.001
9	-6.8	35.525	38.265

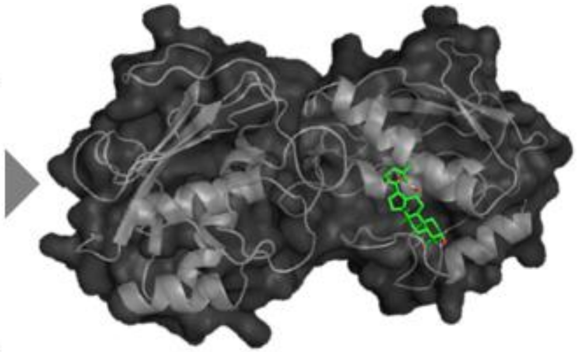

H

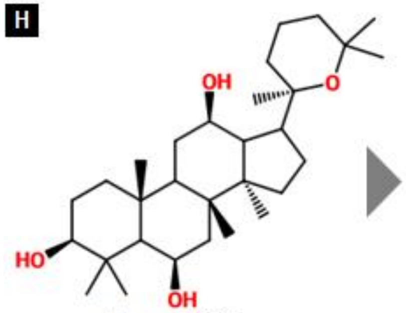

Panaxatriol

mode	affinity (kcal/mol)	Dist from rmsd l.b.	Beste mode rmsd l.b.
1	-7.5	0.000	0.000
2	-7.2	21.862	24.842
3	-7.1	21.667	24.545
4	-7.0	7.784	11.364
5	-6.8	2.235	5.027
6	-6.8	26.739	29.326
7	-6.6	33.027	36.082
8	-6.6	23.813	26.031
9	-6.5	20.369	22.916

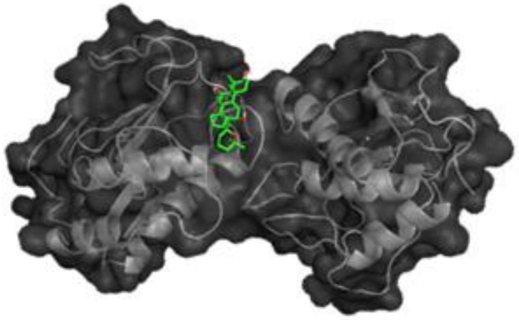

I

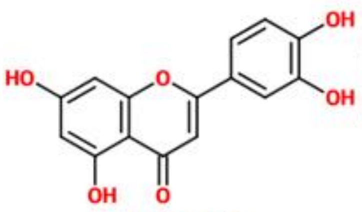

Luteolin

mode	affinity (kcal/mol)	Dist from rmsd l.b.	Beste mode rmsd l.b.
1	-9.8	0.000	0.000
2	-9.3	29.039	31.819
3	-9.3	1.758	7.182
4	-9.3	2.158	7.426
5	-8.9	30.661	33.297
6	-8.9	2.552	7.800
7	-8.6	1.607	3.292
8	-8.6	3.306	8.055
9	-8.4	32.969	35.495

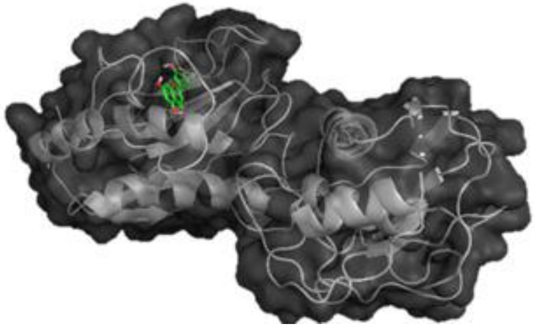

J

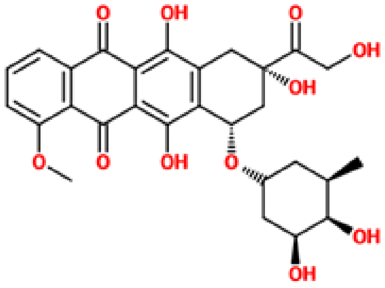

Doxorubicin

mode	affinity (kcal/mol)	Dist from rmsd l.b.	Beste mode rmsd l.b.
1	-8.3	0.000	0.000
2	-8.0	2.690	5.233
3	-7.6	39.684	44.526
4	-7.2	19.288	21.391
5	-7.1	41.216	45.786
6	-6.9	24.616	28.347
7	-6.8	3.563	7.268
8	-6.7	24.686	28.369
9	-6.7	15.441	18.603

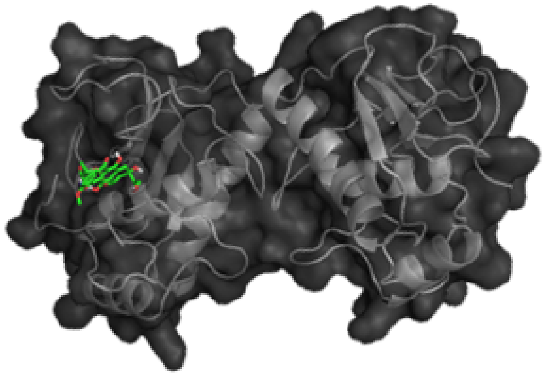

Figure 3B.19 MMP-9 inhibitors compatible with $(Cht/HA)_{10}$. MMP-9 structure has been downloaded from Protein Data Bank (PDB) and has been analyzed and handled with Chimera 1.5 (92 kDa Type IV Collagenase; EC# 3.4.24.35; Fragment: Catalytic domain residues 107-215,391-443; Gene Names: MMP9 CLG4B). The structure of compounds **A-J** has been prepared using MarvinSketch 5.5 software, while their lowest energy conformations were determined at pH 7.4 with OpenBabel 2.1 software. All docking studies have been performed with AutoDock 4.2 software, employing AutoDock Tools (ADT) 1.5.4 graphical interface. The ADT outcome data suggest 9 modes of interaction reporting the predicted binding affinity in kcal/mol (affinity, kcal/mol) and RMSD lower bound. The proposed 10 compounds represent the best ligand efficiency from the database regarding MMP-9.

ANNEX REFERENCES

[1] Oliveira SM, Reis RL, Mano JF. Towards the Design of 3D Multiscale Instructive Tissue Engineering Constructs: Current approaches and trends. Biotechnology advances.

[2] Tang Z, Wang Y, Podsiadlo P, Kotov NA. Biomedical Applications of Layer-by-Layer Assembly: From Biomimetics to Tissue Engineering. Advanced materials 2006;18:3203-24.

[3] Decher G. Fuzzy Nanoassemblies: Toward Layered Polymeric Multicomposites. Science 1997;277:1232-7.

[4] Hammond PT. Form and Function in Multilayer Assembly: New Applications at the Nanoscale. Advanced materials 2004;16:1271-93.

[5] Li Y, Wang X, Sun J. Layer-by-layer assembly for rapid fabrication of thick polymeric films. Chemical Society reviews 2012;41:5998-6009.

[6] Hammond PT. Layer-by-layer approaches to staging medicine from surfaces. AIChE Journal 2015;61:1106-17.

[7] Richardson JJ, Bjornmalm M, Caruso F. Multilayer assembly. Technology-driven layer-by-layer assembly of nanofilms. Science 2015;348:aaa2491.

[8] Picollet-D'hahan N, Gerbaud S, Kermarrec F, Alcaraz JP, Obeid P, Bhajun R, et al. The modulation of attachment, growth and morphology of cancerous prostate cells by polyelectrolyte nanofilms. Biomaterials 2013;34:10099-108.

[9] Blacklock J, Vetter A, Lankenau A, Oupicky D, Mohwald H. Tuning the mechanical properties of bioreducible multilayer films for improved cell adhesion and transfection activity. Biomaterials 2010;31:7167-74.

[10] Hanein D, Horwitz AR. The structure of cell-matrix adhesions: the new frontier. Current opinion in cell biology 2012;24:134-40.

[11] Leal-Egana A, Diaz-Cuenca A, Boccaccini AR. Tuning of cell-biomaterial anchorage for tissue regeneration. Adv Mater 2013;25:4049-57.

[12] Lih E, Oh SH, Joung YK, Lee JH, Han DK. Polymers for cell/tissue anti-adhesion. Progress in Polymer Science 2015;44:28-61.

[13] DuFort CC, Paszek MJ, Weaver VM. Balancing forces: architectural control of mechanotransduction. Nature reviews Molecular cell biology 2011;12:308-19.

[14] Parsons JT, Horwitz AR, Schwartz MA. Cell adhesion: integrating cytoskeletal dynamics and cellular tension. Nature reviews Molecular cell biology 2010;11:633-43.

[15] Bacakova L, Filova E, Parizek M, Ruml T, Svorcik V. Modulation of cell adhesion, proliferation and differentiation on materials designed for body implants. Biotechnol Adv 2011;29:739-67.

[16] Yao X, Peng R, Ding J. Cell-material interactions revealed via material techniques of surface patterning. Advanced materials 2013;25:5257-86.

[17] Hoffman BD, Grashoff C, Schwartz MA. Dynamic molecular processes mediate cellular mechanotransduction. Nature 2011;475:316-23.

[18] Guillame-Gentil O, Semenov O, Roca AS, Groth T, Zahn R, Voros J, et al. Engineering the extracellular environment: Strategies for building 2D and 3D cellular structures. Advanced materials 2010;22:5443-62.

[19] Simon CG, Jr., Lin-Gibson S. Combinatorial and high-throughput screening of biomaterials. Advanced materials 2011;23:369-87.

[20] Liu S, Qin M, Hu C, Wu F, Cui W, Jin T, et al. Tendon healing and anti-adhesion properties of electrospun fibrous membranes containing bFGF loaded nanoparticles. Biomaterials 2013;34:4690-701.

[21] Corey JM, Gertz CC, Wang BS, Birrell LK, Johnson SL, Martin DC, et al. The design of electrospun PLLA nanofiber scaffolds compatible with serum-free growth of primary motor and sensory neurons. Acta biomaterialia 2008;4:863-75.

[22] Krogman KC, Lowery JL, Zacharia NS, Rutledge GC, Hammond PT. Spraying asymmetry into functional membranes layer-by-layer. Nat Mater 2009;8:512-8.

[23] Shukla A, Fang JC, Puranam S, Jensen FR, Hammond PT. Hemostatic multilayer coatings. Advanced materials 2012;24:492-6.

[24] Lynn DM, Langer R. Degradable Poly(β-amino esters): Synthesis, Characterization, and Self-Assembly with Plasmid DNA. Journal of the American Chemical Society 2000;122:10761-8.

[25] Kim JH, Serra-Picamal X, Tambe DT, Zhou EH, Park CY, Sadati M, et al. Propulsion and navigation within the advancing monolayer sheet. Nat Mater 2013;12:856-63.

[26] Reis TC, Castleberry S, Rego AMB, Aguiar-Ricardo A, Hammond PT. Three-dimensional multilayered fibrous constructs for wound healing applications. Biomaterials Science 2016;4:319-30.

3C

Annex IV: Annex C Relative to Chapter 3

SUMMARY

This annex aims to report the strategy to tailor the porosity and hydrophilicity of the as-spun wound dressing substrates. Initially, the self-assembled electrospun materials were treated with NaOH and therefore properly studied. Further experiments were executed by plasma treating the wound dressing substrates, in order to simply the hydrophilicity enhancing step in this thesis framework.

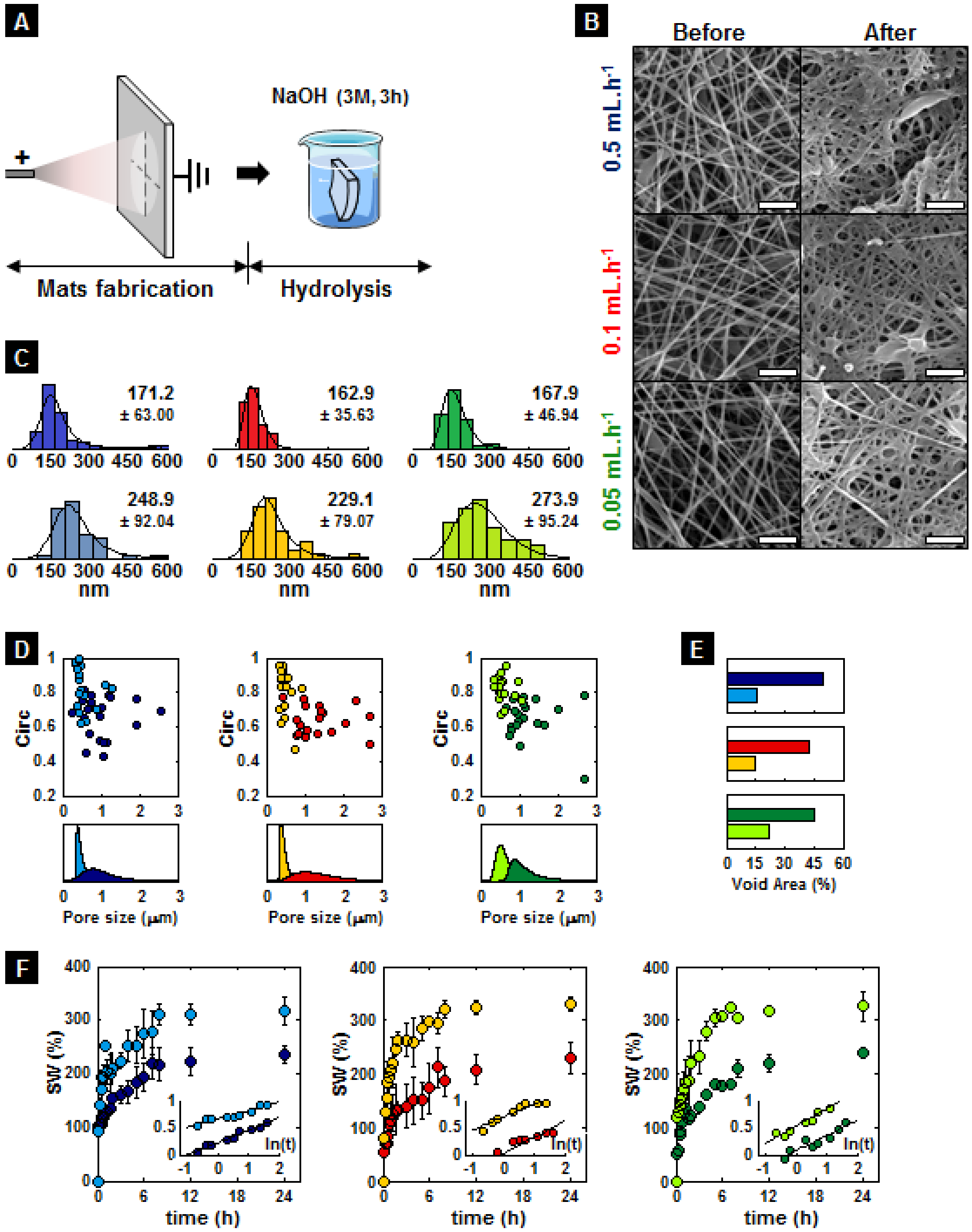

Figure 3C.1 **A**, Fabrication process of PCL based electrospun mats treated with NaOH. **B**, Scanning electron micrographs before and after NaOH treatment (scale bar = 2 µm) produced accordingly to different flow rates. **C**, Fiber diameter distribution before (top row) and after (bottom row) NaOH treatment. **D**, Pore circularity and size assessment before (darker colors) and after (lighter colors) NaOH treatment. **E**, Void area assessment before (darker colors) and after (lighter colors) NaOH treatment. **F**, Swelling ratio dynamics (0.5 mL.h^{-1}, R^2=0.9745; 0.5 mL.h^{-1}+NaOH, R^2=0.9204; 0.1 mL.h^{-1}, R^2=0.8564; 0.1 mL.h^{-1}+NaOH, R2=0.8945; 0.05 mL.h^{-1}, R^2=0.9046; 0.05 mL.h^{-1}+NaOH, R^2=0.9528). (G) Contact angle assessment.

Table 3C.1 Fiber distribution fitting (N=50; BIC, Bayesian Information Criteria).

Data set	Distribution fitted	Distribution Parameters	Mean ± Std (nm)
0.5 $mL.h^{-1}$	Log-logistic (BIC: 556.474)	a= 5.0840 ; b= 0.1881	171.2 ± 63.00
0.5 $mL.h^{-1}$ After NaOH treatment	Log-logistic (BIC: 591.318)	a= 5.4575 ; b= 0.1890	248.9 ± 92.04
0.1 $mL.h^{-1}$	Inverse Gaussian (BIC: 503.526)	μ= 162.8800 ; λ= 3403.6	162.9± 35.63
0.1 $mL.h^{-1}$ After NaOH treatment	Log-logistic (BIC: 574.629)	a= 5.3813 ; b= 0.1780	229.1 ± 79.07
0.05 $mL.h^{-1}$	Inverse Gaussian (BIC: 528.742)	μ= 167.2000 ; λ= 2121.3	167.2 ± 46.94
0.05 $mL.h^{-1}$ After NaOH treatment	Gamma (BIC: 541.273)	k= 8.2379; θ= 33.1232	273.86 ± 95.24

Table 3C.2 Pore size distribution fitting (N=75; BIC, Bayesian Information Criteria).

Data set	Distribution fitted	Distribution Parameters	Mean ± Std (nm)
0.5 $mL.h^{-1}$	Log-logistic (BIC: 307.733)	a= 6.8078 ; b= 0.2807	1033.8 ± 634.67
0.5 $mL.h^{-1}$ After NaOH treatment	Generalized Extreme Value (BIC: 262.1865)	k= 0.5293; a= 85.2684 b= 412.6778	554.68 ± 271.05
0.1 $mL.h^{-1}$	Birnbaum-Saunders (BIC: 315.426)	a= 1227.8 ; b= 0.4627	1359.2± 639.62
0.1 $mL.h^{-1}$ After NaOH treatment	Generalized Extreme Value (BIC: 250.719)	k= 0.4150 ; a= 68.8000 b= 405.2840	492.26 ± 293.19
0.05 $mL.h^{-1}$	Generalized Extreme Value (BIC: 305.407)	k= 0.4397 ; a= 265.6594 b= 947.2969	1302.4 ± 247.47
0.05 $mL.h^{-1}$ After NaOH treatment	Inverse Gaussian (BIC: 267.904)	μ= 570.5000 ; λ= 5999.9	570.50 ± 182.09

The equations used in distribution fitting where the following:

Log-logistic Distribution

$$\mathrm{f(x|a,b)} = \frac{1}{\mathrm{b}} * \frac{1}{\mathrm{x}} * \frac{e^z}{(1+e^z)^2}, \quad \text{for } \mathrm{x} \geq 0 \quad \text{and} \quad \text{where } \mathrm{z} = \frac{\log(\mathrm{x}) - a}{\mathrm{b}} \quad (\text{Equation 3C. 1})$$

Inverse Gaussian Distribution

$$\mathrm{f(x|\mu,\lambda)} = \sqrt{\frac{\lambda}{2\pi \mathrm{x}^3}} * \exp\left[-\frac{\lambda(x-\mu)^2}{2\mu^2 x}\right], \quad \text{for } \mathrm{x} \geq 0 \quad (\text{Equation 3C. 2})$$

Gamma Distribution

$$f(x|k,\theta) = \frac{1}{\theta^{k} * \Gamma(k)} * x^{k-1} * \exp\left[-\frac{x}{\theta}\right],$$

$$\text{where } \Gamma(k) = \int_{0}^{\infty} \exp(-y) * y^{k-1}\, dy \qquad \text{(Equation 3C.3)}$$

Generalized Extreme Value Distribution

$$f(x|k,a,b) = \frac{1}{b} * \exp\left(-\left(1 + k * \frac{(x-a)^{-\frac{1}{k}}}{b}\right)\right) * \left(1 + k\frac{(x-a)^{-\left(1-\frac{1}{k}\right)}}{b}\right),$$

$$x \geq 0, \text{for } 1 + k\frac{(x-a)}{b} > 0 \quad \text{(Equation 3C.4)}$$

Birnbaum-Saunders Distribution

$$f(x|k,\theta) = \frac{1}{\sqrt{2\pi}} * \exp\left[-\frac{\left(\sqrt{x/a} - \sqrt{a/x}\right)^{2}}{2b^{2}}\right] * \left[\frac{\left(\sqrt{x/a} + \sqrt{a/x}\right)}{2bx}\right],$$

$$\text{for } x \geq 0 \qquad \text{(Equation 3C.5)}$$

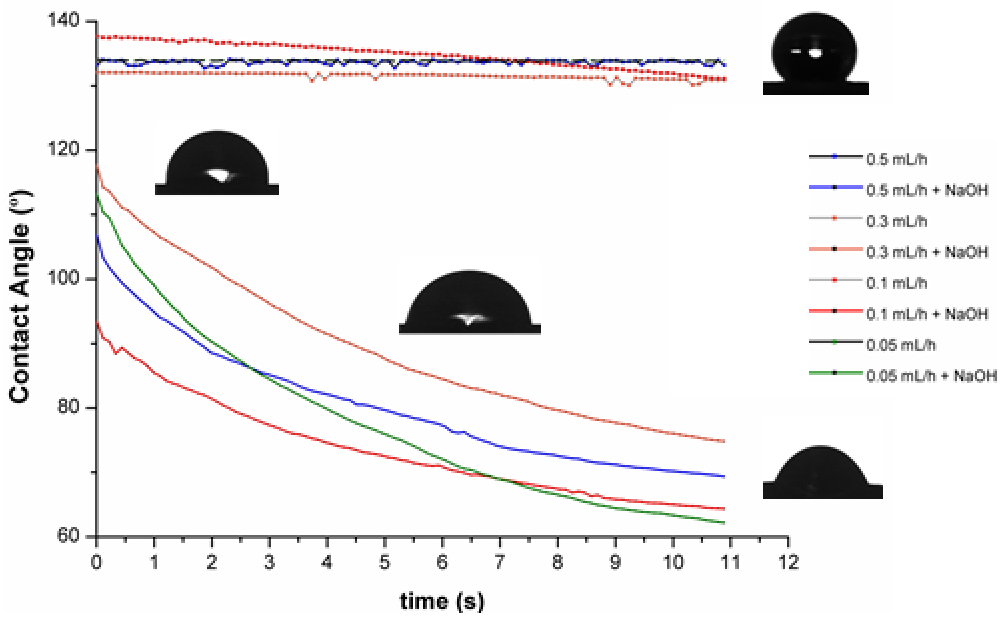

Figure 3C.2 Contact angles of untreated and NaOH treated wound dressing substrates. Static contact angles (N=4) were measured at room temperature by applying the sessile drop method (CAM 100, KSV Goniometer). A 10 µL glycerol (≥ 99.0%, Sigma-Aldrich) drop was placed on the wound dressing substrates. The acquisition time was extended up to 12 seconds with a frame interval of 300 ms. Each frame was retrieved to MatLab R2012b (MathWorks).

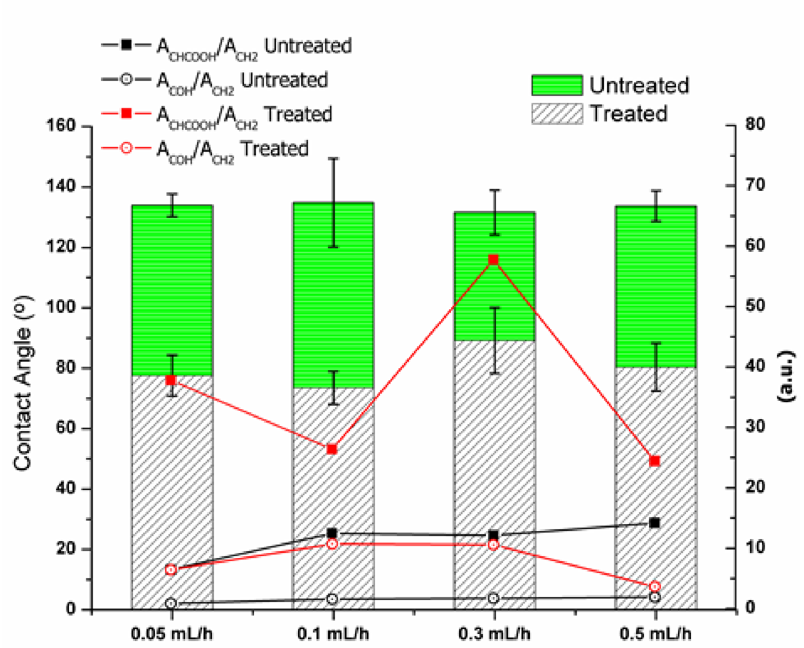

Figure 3C.3 Inter and intra-correlation between the contact angles and FTIR of untreated and NaOH treated wound dressing substrates. FTIR peak ratios referent to δ_{CHCOOH} vs. δ_{CH2} and δ_{COH} vs. δ_{CH2} in order to demonstrated the generation of –C–OH according to the NaOH treatement executed. Samples portions were delaminated and separately milled in KBr (1:200 w/w) being posteriorly pressed to form a disk. For each sample, a FTIR spectrum was recorded at a resolution of 1 cm-1 with a total of 128 scans (Spectrum 1000, Perkin Elmer).

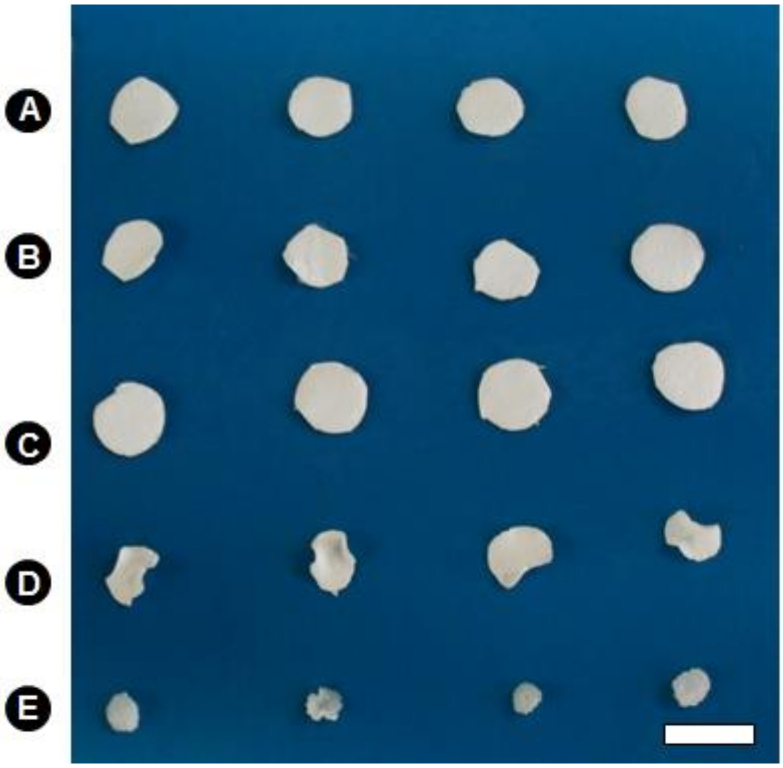

Figure 3C.3 Photographs of wound dressing substrates differently treated to enhance hydrophilicity. **A**, Samples with no further treatment. **B**, Samples plasma treated (80 W during 5 min in an Ar atmosphere, followed by exposition to air). **C**, Samples plasma treated (80 W during 10 min in an Ar atmosphere, followed by exposition to air). **D**, Samples plasma treated (80 W during 5 min in an Ar atmosphere, followed by immersion in ultra-pure water). **E**, Samples plasma treated (80 W during 5 min in an Ar atmosphere, followed by immersion in hydrogen peroxide (30 % v/v)).